

2007-2010

CHINA NATIONAL REPORT

ON

GEOMAGNETISM AND AERONOMY

for XXV General Assembly of International
Union of Geodesy and Geophysics (IUGG)
Melbourne, Australia, June 2011

Prepared by China National Committee on International
Association of Geomagnetism and Aeronomy

National Report List of Chinese Committee for
IAGA/IUGG

- 1、Preface ----- LIU Zhenxing
- 2、Achievement of Double Star ----- LIU Zhenxing, SHI Jiankui,
ZHANG Yongcun
- 3、Introduction to Chinese Meridian Project ----- WANG Chi
- 4、Progress in Geomagnetism Research ----- XU Wenyao, DU Aimin
- 5、Progress in middle and upper atmospheric research ----- HUANG
Kaiming, YI Fan
- 6、Progress in ionospheric research ----- SHI Jiankui, XIAO Zuo
- 7、Progress in Magnetospheric Research ----- PU Zuyin, LIU Zhenxing
- 8、Progress in Coronal and Interplanetary Research ----- ZHAO Xinhua,
FENG Xueshang

PREFACE

The present reports summarize contributions to geomagnetism and aeronomy study by Chinese researchers during the past quadrennial period 2007-2010. There are seven reports included. One paper is on study of geomagnetism in China, one is an introduction to the Chinese Meridian Project. One is on some achievements of the China-ESA Double Star Program. The other four present progresses in the research on the solar-terrestrial physics, including middle-upper atmospheric physics, ionospheric physics, magnetospheric physics, and solar upper atmosphere and interplanetary physics.

The Double Star Program (DSP) has successfully completed its mission. The two satellites of DSP, named TC-1 and TC-2, and four satellites of Cluster made coordinated observations and formed six point measurements in Geospace. They have continuously provided spatial and temporal multi-scale science data for about 4 years. Some important achievements have been obtained with the DSP data. The data will be continuously used by the science community and some more achievements will be obtained in the further studies, I believe. Therefore, here, we give a report on some research results using the DSP data and Cluster coordinated observation data. At present, all the DSP science data have been public. As DSP chief scientist, I would like to announce that every one is welcome to use the DSP data to research.

Also, I would like to show my deep thanks to Prof. Wang Chi, Prof. Xu Wenyao, Prof. Yi Fan, Prof. Xiao Zuo, Prof. Shi Jiankui, Prof. Pu Zuyin, Prof. Feng Xueshang, Prof. Du Aimin, Prof. Huang Kaiming, Dr. Zhaoxinhua, and other co-authors for their contribution to these reports.

Prof. LIU Zhenxing
Chairman, Chinese National Committee for IAGA

ACHIEVEMENTS OF DOUBLE-STAR PROJECT

LIU Zhenxing, SHI Jiankui and ZHANG Yongcun

Center for Space Science and Applied Research, Chinese Academy of Science, Beijing 100190, China

Abstract The Chinese Double Star Programme (DSP) is a cooperation space science mission with ESA. In this report, some main results concerning DSP/Cluster data are presented. It including: global Front-Triggering progress of substorm, magnetic reconnection in the magnetotail, structure of magnetic field and distribution of electric field in the magnetotail, new discoveries of DSP-Cluster coordinated observations of magnetic reconnection at the magnetopause and of substorm dynamics in the magnetotail, bursty bulk flows and related geomagnetic signatures, the neutral sheet oscillations observed by DSP and Cluster, properties of the FAC connecting the ionosphere and magnetosphere, attitude determined by magnetometer and the characteristics dawn side electron and wave burst, research on substorm mechanism and retrieval of RC ion distributions by 3-D CT technique from TC-2/ IMAGE ENA data, coordinated satellite and ground-based observations of dayside magnetic reconnections.

INTRODUCTION

The Chinese Double Star Programme in concert with the ESA Cluster Program provided an unprecedented measurement capability of geospace. The Double Star Programme consisted of two spacecraft, TC-1 and TC-2, which flew in equatorial and polar orbits near the earth. The Cluster mission is comprised of four identical spacecraft and flies in a higher altitude polar orbit. Together, the six spacecraft enabled the first coordinated six-point measurements of the Earth magnetosphere. During the overlapping period of the two missions from 2004 to 2007, they drew significant attention from both the research community and public, providing many scientific discoveries including: the extent of oscillations in the tail of the magnetosphere, density holes in the solar wind, pulsed magnetic reconnection

observed for several hours and crustal cracking of a neutron star. Together with the NASA IMAGE spacecraft, it also provided the first image of the inner magnetosphere, from both the north and the south poles simultaneously.

The International Academy of Astronautics (IAA) has awarded The Laurels for Team Achievement Award to the Double Star/Cluster Team in 2010. This Award is one of two major awards given by the IAA every year, the other being for individual recipients. The Laurels for Team Achievement Award were given to the Russian Mir Space Station team in the first time. In the following, the awardees of the Laurels included the Space Shuttle, SOHO and Hubble Space Telescope teams. Also the Double Star obtained a first level of China national award named National Science and Technology Progress Award. Here we show some main results obtained by Double Star Program and Cluster coordinated six-point measurements.

I . GLOBAL FRONT-TRIGGERING PROGRESS OF SUBSTORM

1. Substorm Front-Trigging Model

Magnetospheric substorm is the most important energy storage and release process. One of the significant scientific objects of the Double-Star Project is to study the triggering mechanism of the substorm expansion phase. Based on the Double-Star satellite observation results and synthesize the characteristics of the global development of the substorm driving and triggering physical process, Liu et al.(2007) puts forward the global “substorm front-triggering model”. In this model, the importance of the interaction between the near-Earth tailward flows and the earthward flows on the substorm triggering is firstly proposed. The “substorm front-triggering model” supplies new thinking to study the substorm triggering. The role of the near-Earth tailward flows (NETFs) in the substorm triggering is significant to understand the coupling between the Magnetosphere-Ionosphere.

The main observation results include that (Zhang et al., 2007a, 2007b): (1) On July 11, 2004, a substorm process in the period of continuous tailward flow was observed by the joint exploration of the TC-1, IMAGE and ACE satellites. The tailward flow continuous 45 min, and company the tailward stretching of the

magnetic field lines. (2) The further statistical analysis shows that the NETFs is characteristic of the low-temperature and high-density plasma. (3) With TC-1 observations in the near-Earth magnetotail from 1 July, 2004 to 31 October, 2004, there are in total 629 tailward flow events observed.

In the GSM X-Y plane, the speed of the earthward flow decreases while getting close to the Earth. In the region near the equator, the flow is mainly in the X component, but the Y component of the flow velocity increases with the distance away from the midnight region. In general, the flow is stronger in the dawn and dusk region than that in the midnight region. The flow tends to drift away from the midnight into the dawn and dusk sides.

In the GSM X-Z plane, the distribution and speed of the flow in the dawn and dusk region have a good symmetry. The flow velocity has a larger Z component. The flow in the Southern Hemisphere moves towards the equator while the plasma flow in the northern hemisphere tends to drift away from the equator into the high latitude.

2 . Plasma Instabilities and Magnetic Disturbance during Substorm

The observation result from TC-1 shows that the ion flow reversal from tailward to earthward is likely to be in close relation with the substorm expansion initiation and might play an important role in triggering the substorm expansion onset (Duan et al., 2008a; Duan et al., 2008b). Duan et al. (2011a) adopted joint observations of TC-1 and Geotail in the near-Earth plasma sheet in the magnetotail to investigate the plasma instabilities in the vicinity of substorm onset. The observation results indicate that the lower-hybrid instability is incited in the substorm triggering region and the lower-hybrid waves with the quasi-perpendicular propagation occur during substorm onset. The magnetic dipolarization and the magnetic disturbance in the outside of near-Earth plasma sheet are very weak during substorm onset. On the base of multiple spacecrafts observations, the magnetic field dipolarization in the vicinity of substorm onset was investigated (Duan et al., 2011a; Duan et al., 2011b). These results reveal that there is no one-to-one relationship between the near-Earth magnetic dipolarization and the earthward ion bulk flow. In particular, the magnetic

dipolarization occurring in the inner edge of the near-Earth plasma sheet is not accompanied by high speed earthward ion bulk flow. The dipolarization at substorm onset is a local and small scale phenomenon. There are multiple magnetic dipolarizations occurring during the substorm expansion phase. The dipolarization process is very complex and is not simply an MHD process. It is accompanied by some kinds of plasma instabilities, the plasma sheet azimuthal expansion not only by earthward ion bulk flow during substorm.

II . MAGNETIC RECONNECTION IN THE MAGNETOTAIL

With TC-1, Cluster, and Geotail observations, Zhang et al. (2010) statistically analyzed earthward and tailward convective bursty flows (CBFs) from 7 to 31 R_E to understand the distribution of X-lines in the magnetotail.

It is found that the earthward and tailward CBFs could occur in both the midnight and the dawn-dusk sides. The earthward CBFs are widely distributed outside 7 R_E . The tailward CBFs are mainly located outside 15 R_E which suggests that magnetic reconnection could hardly occur inside 15 R_E . Assuming that the X-line distribution is the function of the location in X, then the distribution function of the X-line, $F(x)$ satisfies the formation in the paper (Zhang et.al. (2010)). It is clear that the ratio of the number of tailward flows to the number of all flows explored by Cluster(3) is small and constant at $X = 13$ to 17 R_E . The ratio of tail/all has a distinct increase outside 17 R_E . Especially, the ratio reaches highest at $X = 19 R_E$. The ratio of tail/all flows shows a jump between $X = -19$ and $X = -21$. This is fairly consistent with the Cluster results. Outside 22 R_E , the ratio of tail/all flows gradually increases with a radius distance. Finally, with ACE satellite Data, they further analyzed the effect of the solar wind condition on the X-lines. The total number of tailward CBFs explored from 2001 to 2005 by Cluster and Geotail under different solar wind conditions is shown in Table 1. The occurrences of the X-line inside and outside 20 R_E both tend to increase under the strong solar wind and decrease under the weak solar wind, which suggests that the occurrence of X-line is closely related with the solar wind condition. The occurrence of the X-line may be higher under strong solar wind conditions and lower under weak solar wind conditions.

III. NUADU OBSERVATION

The NUADU (Neutral Atom Detector Unit) experiment, developed by a joint project of China and Europe, flight on the TC-2 spacecraft and it has the capability to remote sensing global characterization of the Earth's magnetosphere (McKenna-Lawlor et al., 2004, 2005a and 2005b). The main explorative achievements are shown as following:

The NUADU experiment aboard TC-2, recorded charged particles spiraling around geomagnetic field lines could forms 'ring like' and 'dumbbell-type' pitch angle distributions (PADs) in the region sampled, during its, in-orbit, commissioning phase (Lu, et al., 2005). With variations of PADs, Lu et al. (2007) found that the plasma sheet was stretched accompanying by field aligned energetic ion fluxes. It was the first time the NUADU instrument recorded the ENA aurora near the perigee around the South Pole for about 10 minutes (Liu et al., 2008).

In accordance with designing features, Lu et al. (2005) developed an iterative inversion method autonomously which may effectively improve the temporal resolution and the accuracy of those inverted results. By the iteration technique, it is possible for the first time to simultaneously retrieve the magnetospheric ion distribution and the exospheric neutral density, and further to recover global ENA emissions in three-dimensions (Lu et al., 2008b). Their inversion results agreed with a comprehensive ring current model both in the morphology and the magnitude (Tang et al., 2008). By comparisons between ion distributions retrieved from ENA images of the ring current and contemporaneous, multipoint ion measurements recorded in situ during a major magnetic storm, Lu et al. (2010) first obtained a global estimation of the magnetospheric ion distribution inversion.

IV. STRUCTURE OF THE MAGNETIC FIELD AND DISTRIBUTION OF ELECTRIC FIELD IN THE MAGNETOTAIL

1. Magnetic Flux Rope in the Magnetotail

Zhang et al. (2007a) analyzes Double Star TC-1 magnetic field data from July to

September in 2004 and find that plasmoids exist in the very near-Earth magnetotail. It is the first time that TC-1 observes the plasmoids in the magnetotail at $X > -13 R_E$. According to the difference of the magnetic field structure in plasmoids, they choose two typical cases for their study: the magnetic flux rope on August 6 with the open magnetic field and the magnetic loop on September 14 with the closed magnetic field. Both of the cases are associated with the high speed earthward flow and the magnetic loop is related to a strong substorm. The ions can escape from the magnetic flux rope along its open field line, but the case of the closed magnetic loop can trap the ions.

Using the observations from TC-1, Cluster and Themis, the structure and the configuration of the magnetic fields in magnetic flux rope at the magnetotail are investigated. Zhang et al. (2007b) applied the Grad-Shafranov (GS) technique to reconstruct the transverse magnetic fields distribution perpendicular to the flux rope axis. They found that the distribution of the transverse magnetic fields on the cross section is the asymmetric circles, which requires that the reconnections at multiple X-line points occur. According to the AE index, there is no obvious substorm associated with this magnetic flux rope. Based on the results from the GS analysis, Zhang et al. (2011) check if the magnetic fields in the flux rope is force-free or not, which is a key problem in the study of magnetic flux rope. The results show that the magnetic fields at the central region of magnetic flux rope can be described by force-free, while with the increase of radial distance, the fields display no force-free at the region where the magnetic fields deviate from the axial symmetric distribution. Their results also give the characteristic physics parameters such as the invariant axis direction, the cross scale length, the magnetic flux in flux rope and provide the distribution of the electric current density in magnetic flux rope.

2 . Electric Field at the Magnetotail

He et al. (2010) studied the relationship between the average structure of the inner magnetospheric large-scale electric field and geomagnetic activity levels with Double Star TC-1 data for radial distances between $4.5R_E$ and $12.5R_E$ and magnetic local time (MLT) between 18:00 h and 06:00 h and $Z(\text{GSM})$ between $-1.5R_E$ and

1.5 R_E from July to October in 2004 and 2005. The sunward component of the electric field decreases monotonically as increases and approaches zero as the distance off the Earth is greater than 10 R_E . The dawn-dusk component is always duskward, scaling in the magnitude from 0 mVm^{-1} to 0.7 mVm^{-1} as Kp increasing from 0 to 5. It decreases at about 6 R_E where the ring current is typically observed to be the strongest and shows strong asymmetry with respect to the magnetic local time. Surprisingly, the average electric field obtained from TC-1 for low activity is almost comparable to that observed during moderate activity, which is always duskward at the magnetotail (8 R_E -12 R_E).

3 . Plasma Injection

He et al. (2008a) investigated the plasma injection boundary and source region during the magnetospheric substorms on measurements of energetic particles obtained by the two geosynchronous satellites (1991-080 and LANL-97A). The measurement method is developed to allow remote sensing of the plasma injection time and the radial distance of injection boundaries by using measured energy dispersion and modelling particle drifts within the Volland–Stern electric field and the dipole magnetic field model. The radial distance of the injection boundary deduced from a dispersion event observed by the LANL-97A satellite on 14 June 1998 is 7.1 R_E , and the injection time agrees well with the substorm onset time identified by the Polar Ultraviolet Imager. The method has been applied to an event happened at 22.9 UT on 11 March 1998, when both the satellites (1991-080 and LANL-97A) observed the dispersionless character. The results indicate that the radial distance of injection source locates at 8.1 R_E at magnetotail, and particles move earthward from magnetotail into inner magnetosphere at 22.5 UT.

He et al. (2008b) studied the properties of proton (0eV<E<40keV) in the plasma sheet by means of a superposed epoch analysis, using 115 magnetotail plasma injection events which are identified from Cluster magnetotail orbit time in between 2001 and 2004. All events distribute in magnetic local time from 20 p.m. to 04 a.m. Five classes of magnetotail injection events are found to be similar with the geosynchronous observation: (1) pure ion injections; (2) ion injections followed a few minutes later by an electron injection; (3) simultaneous ion and electron

injections; (4) electron injections followed a few minutes later by an ion injection; (5) pure electron injections. Proton shows a significant increase in temperature and density at the onset, and injects earthward with an increasing velocity more than the pre-injection average one. Superposed epoch analysis on the simultaneous observation data of dusk-dawn electric field from the EFW (Electric Field and Waves) instrument, they found two different electric field configurations: (1) electric field increases suddenly at the onset and the value is positive; (2) electric field changes the direction at the onset, and turns into a negative value. The simulation results of velocity vector after injection in equatorial plain, calculated in static magnetic (T89c) and electric (Volland-Stern) field models, agree with the statistical results mostly, and that suggests the electric drift caused by dawn-dusk convection electric field is one of the mechanisms of the particles injected earthward in magnetotail ($-18R_E < R < -10R_E$).

4. Cluster-DSP Conjunction Observations of the Solar Wind Transport into Magnetosphere

Yan et al. (2008) reported an event of Cluster-Double Star conjunction observations of magnetic reconnection at high latitude magnetopause nightside of both cusps and solar wind transport into magnetosphere caused by such reconnection process. During northward IMF, Cluster/SC1 observed accelerated flows and ion heating associated with magnetic reconnection at high latitude magnetopause nightside of southern cusp. And Double Star observed cold dense solar wind plasma transported into dayside magnetosphere. The analysis on such conjunction observations shows that: (1) during northward IMF, magnetic reconnection occurs at high latitude nightside of southern cusp, accompanied by accelerated flows that are observed by Cluster/SC1; (2) the direction of the accelerated flows, with its sunward component V_x , dawnward component V_y , northward component V_z , is quite consistent with the theoretical anticipation under the condition of northward IMF with dawnward component B_y ; (3) reconnection can heat plasma more in parallel direction than in perpendicular direction, to a level of about 4 keV; (4) with reconnection taking place at high latitude magnetopause nightside of the southern cusp, TC-1 observed cold and dense plasma transported into magnetosphere; (5) by reconnection at high latitude magnetopause nightside of both cusps, solar wind flux tube can be captured

by magnetosphere and pulled into dayside magnetosphere. This event presents further observational evidence for magnetic reconnection at high latitude magnetopause nightside of both cusps as an important mechanism of solar wind transport into magnetosphere.

5. Solar Wind Entry via Flux Tube into Magnetosphere

By analyzing hot ion and electron parameters together with magnetic field measurements from Cluster, Yan et al. (2009) investigated an event of magnetopause crossing of the spacecraft. At the latitude of about 40° and magnetic local time (MLT) of 13:20 during the southward interplanetary magnetic field (IMF), a transition layer was observed, with the magnetospheric field configuration and cold dense plasma features of the magnetosheath. The particle energy-time spectrograms inside the layer were similar to but still a little different from those in the magnetosheath, obviously indicating the solar wind entry into the magnetosphere. The direction and magnitude of the accelerated ion flow implied that reconnection might possibly cause such a solar wind entry phenomenon. The bipolar signature of the normal magnetic component B_N in magnetopause coordinates further supported happening of reconnection there. The solar wind plasma flowed toward the magnetopause and entered the magnetosphere along the reconnected flux tube. The magnetospheric branch of the reconnected flux tube was still inside the magnetosphere after reconnection and supplied the path for the solar wind entry into the dayside magnetosphere. The case analysis gives observational evidence and more details of how the reconnection process at the dayside low latitude magnetopause caused the solar wind entry into the magnetosphere.

6. Component Reconnection Observed by TC-1 at the Dawn Flank Magnetopause

Generally, the component reconnection process tends to occur near the sub-solar point magnetopause. In this work, an event of component reconnections observed by TC-1 has been investigated. During the interval of IMF $B_z \approx 0$, at the dawn flank of the magnetopause, TC-1 observed a series of accelerated flows of plasma, with the velocity of up to 500 km/s, even more than twice of the background of the

magnetosheath flow. The negative V_z component and negative V_x component were the dominant components of the flows. By using MVA method, a series of bipolar signatures were found in the normal component B_N in local magnetopause coordinates (LMN), corresponding to the series of the high-speed flows. The negative V_L component was dominant in the accelerated flows in the LMN coordinates, indicating that the merging happened in -L direction (southward and anti-sunward). The analysis of the observed features of the high-speed flows shows that a sequence of reconnection pulses happened at the dayside flank magnetopause during the interval of IMF $B_z \approx 0$. The shear angle between the IMF and the magnetospheric field is estimated to be about 62° , much smaller than 180° , which implies the component reconnection happened at the dawn flank of the magnetopause. Furthermore, good results of the Walén test using deHoffmann-Teller analysis further support the existence of component reconnection with such a small shear angle. The observation of TC-1 presents new observational evidence of component reconnection at the flank magnetopause far away from the sub-solar point, and also indicates that the component reconnection could occur at the flank magnetopause with the dawnward dominated IMF. In this case, the X-lines are discrete and local in the flank. (Yan et al., 2010)

V. NEW DISCOVERIES OF DSP-CLUSTER COORDINATED OBSERVATIONS OF MAGNETIC RECONNECTION

1. New Discoveries of DSP-Cluster Coordinated Observations of Magnetic Reconnection at the Magnetopause

Magnetic reconnection at the magnetopause is the primary mechanism responsible for the transfer of solar wind energy into the magnetosphere. From January to April the apogee of TC-1 is in the dayside solar wind or magnetosheath at low latitudes, there are numerous opportunities for TC-1 to measure the low-latitude reconnection signatures and make coordinated observations with Cluster at high-latitudes (Liu et al., 2005). Several interesting studies have been done based on these measurements.

Wang et al. (2007) reported an observation of FTE signatures at the dayside

magnetopause on 4 January 2005 at the northern-dusk magnetopause. The event occurred as a magnetosheath FTE first at the Cluster spacecraft at about 07:13 UT, and then observed by TC-1 108s later. All findings including magnetic fluxes, orientations and hot ion velocity distributions strongly suggest that Cluster and TC-1 encountered the magnetosheath branch of the same flux tube at two different positions along its length. The following features of the flux rope are obtained (in GSM coordinates). The scale size: 1-2 R_E ; the axis orientation: (-0.545, 0.184, 0.818); convection velocity: (-44, 340, 178) km/s; magnetic flux contained in the flux rope: $\sim 15 \times 10^5$ Wb. This study suggests that the FTE flux ropes move dominantly in the azimuthal direction, not in the Z-direction as the present models of FTEs assumed.

The global pattern of reconnection line at the dayside magnetopause is a fruitarian subject of the solar wind-magnetosphere coupling. Pu et al. (2007) have studied 290 fast flow events measured by TC-1 and Cluster with the $-y$ dominated IMF. The main results are as follows: (1) Consistent with either the anti-parallel or the component MR hypotheses, the majority of the fast flows at the high-latitude MP and outer cusps are primarily dawnward and duskward. (2) Possible X-Lines could be statistically constructed with a tilt angle of $\sim 155^\circ$ in/near the subsolar region and of $\sim 100^\circ$ and $\sim 86.9^\circ$ respectively in the northern and southern hemispheres. The above results suggest that both anti-parallel and component MR may occur at the MP under the same IMF conditions. A global S-shaped configuration of the possible X-line could be drawn by interconnecting the possible X-line in/near the subsolar region and those at high-latitudes.

2 . New Discoveries of DSP-Cluster Coordinated Observations of Substorm Dynamics in the Magnetotail

The launch of the two Chinese–ESA Double Star spacecraft provided a unique opportunity for coordinated multipoint measurements of substorms in the magnetotail with four Cluster satellites. Cao et al. (2007) study the substorm dipolarization occurring on Sep 14, 2004 based on DSP/TC1, Cluster and Polar data observations. Substorm onset started at about 1822 UT. Three minute later TC1 at $(-10, -2, 0) R_E$ (GSE) saw a sharp decrease of magnetic B_x component,

accompanied by sudden increases in both the ion temperature and thermal pressure. About 23 minutes later at ~1850 UT, similar signatures were observed by Cluster at $(-16, 1, 3) R_E$ (GSE). In addition, POLAR at $(-7.5, 3.5, -4.0) R_E$ (GSE) saw a sudden change in the elevation of the magnetic field at about 1855UT. This substorm time sequence indicates that the source of the dipolarization was situated at about $X = -(8.5-8.7) R_E$ and dipolarization was progressed tailward at a speed of (70-82) km/s. A substorm paradigm is proposed based on this observation: Earthward flow produced by magnetic reconnection in the mid-tail creates favorable conditions for substorm initiation in the near-Earth; after the expansion onset the substorm current wedge progresses down to the tail. Zhang et al. (2007) studied 53 substorms measured by Double Star/TC-1 occurring from July to October, 2004. The main features of these events are: (a) Magnetic flux pileup characterized by continuous enhancement of B_z is observed, which starts almost simultaneously with aurora breakup within 1-3 minutes, indicating that substorm onset is in close relation to flux pileup. (b) Sudden plasma sheet expansion with sharp increases in ion temperature and density is seen in all events, which occurs typically ~11 minutes after the beginning of pileup. The plasma sheet expansion is shown to be in close relation with the primary substorm dipolarization. (c) Evidence indicates that the substorm current wedge first forms earthward of TC-1 position, inward of the flow braking region, and then progresses tailward with an expansion in the Z-direction. Similarly, Cao et al. (2008) present two case studies of substorm timing with TC1, Cluster, Polar, IMAGE, LANL satellites, and ground-based measurements. They show that 8-10 min ahead of the auroral breakup, Cluster measured an earthward flow associated with plasma sheet thinning. A couple of minutes after the breakup, TC1 detected plasma sheet expansion and subsequently the geostationary satellites measured energetic electron injections. About 20 min later, Cluster and Polar successively observe plasma sheet expansion. Substorm dipolarization seems to begin around $X \sim -(8-9) R_E$, then progresses both earthward and tailward. They also found that auroral bulge is quickly expanding poleward when the open magnetic flux in the polar cap is rapidly dissipated during tail lobe reconnection.

VI. BURSTY BULK FLOWES AND RELATED GEOMAGNETIC

SIGNATURES

Cluster and Double Star Discover Density Holes in the Solar Wind

Based on recent observations by the Cluster and the Double Star TC-1 satellites, a team of American, European and Chinese scientists have discovered the presence of ion density holes in the solar wind, upstream of the Earth's bow shock, of thousands kilometers in size. More than 140 of such density holes were found, always observed with upstream particles (propagating against the solar wind flow), suggesting that backstreaming energetic particles interacting with the solar wind are important. This new discovery illustrates the unique capability of Cluster and Double star to provide the microscope into shock physics necessary to understand fundamental physical phenomena at the Earth's bow shock and extrapolate to the more distant planetary and astrophysical shocks.

On the sunward side of each planet of the Solar System, a shock is present due to a constant flow of particles emitted by the Sun: the solar wind. The bow shock of a planet slows down the solar wind and deflects the bulk of this plasma flow around the planet. The solar wind particles passing through the bow shock are both decelerated and heated rather rapidly. More surprisingly, some of the solar wind particles are reflected and stream away from the shock towards the Sun. These backstreaming particles travel upstream, along the interplanetary magnetic field lines. The role of these particles and their interaction with the incoming solar wind is still unclear.

2. Geomagnetic Signatures of Current Wedge Produced by Fast Flows in Plasma Sheet

Using the plasma data from Cluster and TC-1 and geomagnetic data, Cao et al. (2010) study the geomagnetic signatures of the current wedge produced by fast flow braking in the plasma sheet. The three fast flows studied here occurred in a very quiet background and are accompanied by no (or weak) particle injections, thus avoiding the influences from other disturbances. All the geomagnetic signatures of substorm current wedge can be found in the geomagnetic signatures

of current system produced by the braking of fast flows, indicating that the fast flows can produce a complete current wedge which contains post-midnight downward and pre-midnight upward field aligned currents, and westward electrojet. The Pi2 precursors exist not only at high latitudes, but also at mid-latitudes. The starting times of mid-latitude Pi2 precursors can be identified more precisely than those of high latitude Pi2 precursors, providing a possible method to determine the starting time of fast flows in their source regions. The AL drop that a BBF produces is proportional to its velocity and duration. In three cases, the AL drops are smaller than 100 nT. Since the AE increase of a typical substorm is larger than 200 nT, whether a substorm can be triggered depends mainly on the conditions of the braking regions prior to fast flows. The observations of solar wind prior to the three fast flows suggest that it is difficult for the fast flows to trigger a substorm when the IMF Bz of solar wind is weakly southward.

3. Magnetosheath Excursion and the Relevant Transport Process at the Magnetopause

A large-amplitude excursion of the magnetosheath (MS) in quiet solar wind conditions on 17 March 2004 was recorded simultaneously by the Cluster and TC-1 spacecraft. During this period, the IMF Bz was entirely northward. The coherence between the bow shock motion and magnetopause (MP) motion is revealed and the excursion velocities of the bow shock motion are analyzed. In addition, the relevant plasma transport phenomenon in the form of flux fluctuations below the ion gyrofrequency at the MP is exposed and is interpreted as manifestation of the drift instability. Correlated observations on charge accumulation and electrostatic potential perturbation are recorded by electron measurements in high energy regime, and also the eventual cross-field vortex motion in the nonlinear stage and the consequential mass exchange are exhibited. The present investigation gives some new insight into the MS plasma transport mechanism across the subsolar MP region in quiet solar wind conditions during a period of northward IMF. (Cai et al., 2009)

4. Characteristics of Mid-low Latitude Pi2 Excited by Bursty Bulk Flows

The characteristics of low latitude Pi2s generated by a earthward BBF in the near Earth tail plasma sheet are studied based on the data of Cluster, TC-1, GOES and eight ground stations on Oct. 22, 2004. The BBF excited simultaneously two distinct classes of Pi2s: one is long period Pi2 (90-130s), and the other is short period Pi2 (~50s). The long period Pi2 is transient response type Pi2 associated with field aligned current produced by the braking of BBFs. The spectrum analysis show that the amplitude spectrum peak of long period Pi2 increases with increasing latitude, indicating that the source is at higher latitudes. The time delay for the propagation of Alfvén waves from Cluster to the Earth is very close to the time difference between the onset time of the BBFs at Cluster and the starting time of the long period Pi2 on the ground. The short period Pi2 is a global cavity mode since the Pi2s in H components at eight stations have almost the same starting time, same oscillation period and same waveform, which are all typical characteristics of cavity mode. The amplitude spectrum peak of short period Pi2 at NCK (N42.7) is larger than those at higher station UPS (N56.5) and lower station CST (N40.8). The polarization analysis at three lower latitude stations shows that the polarization underwent two reversals. The major axis of the polarization ellipse points to approximately the north, indicating that the short period Pi2s are not excited by night side current system. TC-1 observed transverse mode Pi2s, Its period is almost identical with the periods of Pi2 on the ground, indicating they belong to the same wave. (Cao et al., 2008)

VII. THE NEUTRAL SHEET OSCILLATIONS OBSERVED BY DSP AND CLUSTER

The newly launched Double Star Program (DSP) TC-1 satellite allows Zhang et al. (2005) to investigate neutral sheet at 10–13 Re in the tail. Using DSP with Cluster simultaneously observations at 10–13 and 16–19 Re, these flapping motions are studied and the first results of neutral sheet oscillations are presented.

VIII. PROPERTIES OF THE FAC CONNECTING THE IONOSPHERE AND MAGNETOSPHERE

The data from the coordinated observation of the TC-1, TC-2 and Cluster in the

nightside magnetosphere are used for analysis the large scale Field Aligned Current (FAC) along the field lines between the magnetotail and the auroral region. Two cases during the substorm times were chosen to do study. One was on the September 14, 2004 and the other was on the September 17, 2004. It is first time to give the observation evidence of the large scale Field Aligned Current (Shi et al. 2010a). Furthermore, features of the Field Aligned Current (FAC) distribution in plasma sheet boundary layers in the magnetotail were statistically investigated using the multi-point magnetic field measurements. The current was calculated with the so called “Curlometer” technique. The results show that the FAC distribution in the plasma sheet boundary layers in the magnetotail not only has dusk-dawn asymmetry and Earthward-tailward (polarity) asymmetry, but also has north-south asymmetry. The occurrence and polarities of FACs in the northern hemisphere are different from that in the southern hemisphere. The average density and the standard deviation of the FACs whose are most likely to be Earth connected are 4.90 nAm^{-2} and 2.55 nAm^{-2} in the northern hemisphere, and are 4.21 nAm^{-2} and 1.80 nAm^{-2} in the southern hemisphere. For investigating the mechanism of the north-south asymmetry, FACs in the plasma sheet boundary layers in the magnetotail were mapped along the field line into the polar ionosphere. The footprints of the FACs also show a difference between the southern and northern hemispheres (as a function of mapped latitude). These characteristics suggest a north-south asymmetry of the FACs in the magnetosphere (Shi et al., 2009; Shi et al., 2010b). The properties of the FAC in storm time are also studied using the DSP and Cluster data. And the FACs distribution functions were also studied (Cheng et al., 2007 and 2008).

IX. ATTITUDE DETERMINED BY MAGNETOMETER AND THE CHARACTERISTICS DAWN SIDE ELECTON AND WAVE BURST

DSP aboard magnetometer can determine the parameters of DSP satellite spin axis with a method developed by a special scientist group whose leader is Dr. Tao Chen. The attitude parameter is very importance to scientific exploration and satellite running, especially in the field that determine the direction of physical parameter such as magnetic vector, electric vector and velocity vector. The accuracy and application effect on TC1 satellites and TC2 satellite by the method are illustrated

and compared (Chen et al., 2007). It can be concluded that this method and emergent operation is very effective in satellite experiments. It shows greatly important meaning in scientific analysis and future satellite application.

Data recorded aboard TC2 during the geomagnetic storm of 15 May 2005 show that there was some intermittent occurrence of bursts of electrons and VLF electromagnetic waves in dawn side boundary layer. The characteristics of these burst events are: (1) Flux of the high energy electrons increased by a factor of one hundred. (2) The velocity, density and temperature of low energy (1eV-26 keV) electrons increase. (3) The pitch angle of the burst electrons are mainly 90° (Chen et al., 2011). (4) The frequency of the burst electromagnetic waves is mainly below 100Hz. (5) The cyclotron resonance made by burst electrons and VLF waves cause former local magnetic field drastically debate in magnitude that it is called local magnetic storm (Chen et al., 2009).

X. RESEARCH ON SUBSTORM MECHANISM AND RETRIEVAL OF RC ION DISTRIBUTIONS BY 3-D CT TECHNIQUE FROM TC-2/IMAGE ENA DATA

1. Research on Substorm Mechanism

With favorable constellations of TC-1/ Cluster/GOES/Geotail/CHAMP, and ground stations, studies have been made on the global manifestations of substorm onsets for some typical events (Wang et al., 2008). Their onsets all occurred in both hemispheres simultaneously and conjugately, confirmed by observations of the auroral breakup from IMAGE FUV-WIC and a sudden intensification of a westward electrojet from ground-based magnetometers. Concurrently with the onset, field-aligned and Hall currents in the auroral ionosphere are observed by CHAMP, which are consistent with the signature of a Harang discontinuity. The time difference of depolarization can be explained either by a dawnward propagation of the substorm current wedge at a speed of about 300 km/s, or by the earthward or tailward propagation in the radial direction (Wang et al., 2006). The earthward dipolarization front was found in one case to bounce back and forth at TC-1. One substorm event has been simulated with SWMF (Space Weather

Modeling Framework) (Wang et al., 2009).

2. Retrieval of RC Ion Distributions by 3-D CT Technique from TC-2/ IMAGE ENA Data

With multi-satellite ENA (Energetic Neutral Atom) remote imaging data, including images from coordinated Chinese TC-2 NUADU and American IMAGE-HENA measurements as well as that from the Two Wide-angle Imaging Neutral-atom Spectrometers (TWINS) mission, the ENA sources of ions in the inner magnetosphere have been retrieved for the first time by using volumetric pixel (voxel) computed tomography (CT) inversion technique (Ma et al., 2009). The 3-D distributions of energetic ion intensity in the ring currents during some storms have been reconstructed reliably, showing a reasonable consistent with satellite in situ measurements. It is found that the main part of the RC in some storm tends to appear in the post-midnight sector toward to dawn rather than in the pre-midnight sector as expected by the conventional concept (Yan et al., 2010).

XI. COORDINATED SATELLITE AND GROUND-BASED OBSERVATIONS OF DAYSIDE MAGNETIC RECONNECTIONS

Liu et al. (2005) reported that ground-based observations can be used to provide substantial support for Cluster/Double Star measurements and greatly enhance the mission's scientific return. There are six Chinese ground stations involved in coordinated cluster/Double Star and ground-based instrument observations. Among them, the Chinese Zhongshan Station in Antarctica and the Yellow River Station on Svalbard are closely magnetic conjugate and are situated under the ionospheric projection of the magnetospheric cusp regions, which, combined with satellite data, provide a perfect configuration to conduct conjugate studies of cusp phenomena. Here they present the ground-based instrumentation at these stations, discuss the restriction which is applied to the optical sites and present an overview of the occurrences for conjunctions of these instruments with the spacecraft. Samples of data products are given to illustrate the potential use of these instrumentations in coordination with Cluster/Double Star measurements.

Zhang et al. (2010) analyzed a number of flux transfer events (FTEs), which were observed between 09:00 and 12:00 UT on 11 February 2004, during southward and dawnward IMF, while the Cluster spacecraft array was outbound through the northern, high-altitude cusp and dayside, high-latitude boundary layer, and the Double Star TC-1 spacecraft was crossing the dayside low-latitude magnetopause into the magnetosheath south of the ecliptic plane. The motion of several medium to large scale FTEs are analyzed in some detail to compare to simultaneous, poleward-moving plasma concentration enhancements recorded by EISCAT Svalbard Radar (ESR) and “poleward-moving radar auroral forms” (PMRAFs) on the CUTLASS Finland and Kerguelen Super Dual Auroral Radar Network (SuperDARN) radar measurements. Conjugate SuperDARN observations show a predominantly two-cell convection pattern in the Northern and Southern Hemispheres. The results are consistent with the expected motion of reconnected magnetic flux tubes, arising from a predominantly sub-solar reconnection site. Here, they are able to track north and south in closely adjacent intervals as well as to map to the corresponding ionospheric footprints of the implied flux tubes and demonstrate these are temporally correlated with clear ionospheric velocity enhancements, having northward (southward) and eastward (westward) convected flow components in the Northern (Southern) Hemisphere. The durations of these enhancements imply that the evolution time of the FTEs is about 8 minutes from their (referring to the FTEs) observation by the spacecraft around the magnetopause to their addition to the magnetotail lobe. However, the ionospheric response time in the Northern Hemisphere is about 6 minutes longer than the response time in the Southern Hemisphere.

Dunlop et al. (2009) reported that new investigations have renewed the debate on the occurrence of magnetic reconnection of Earth's dayside magnetopause. Here, they show for the first time strong evidence for a high-latitude reconnection site, located on initially closed field lines, where the magnetic field orientations inside and outside the magnetopause are close to antiparallel. The evidence centers on repeated sampling of the ion diffusion region and associated null magnetic field by four spacecraft in formation, together with simultaneous monitoring of the local magnetosheath behavior by a fifth spacecraft.

Zhang et al. (2009) analyzed the observations of the FGM and PEACE on TC-1 and Cluster Spacecraft between 12:15 and 12:25 UT on 13 March 2004. In this interval, the TC-1 spacecraft located in the magnetosheath southward the sub-solar magnetopause, and observed a standard magnetosheath FTE with a positive to negative bipolar characters at about 12:19 UT. The Cluster spacecraft array was encountering the plasma boundary layer near the high-latitude magnetopause in the northern hemisphere, crossing the magnetopause into the magnetosheath at about 12:23 UT, and also observed a standard magnetospheric FTE with a positive to negative bipolar characters at about 12:21 UT. With the similar features of the magnetic field structures and the plasma data, these two FTEs might be the same FTE moving through TC-1 and then Cluster. Since all 4 Cluster spacecraft observed the FTE, they applied the four-spacecraft techniques “Minimum Directional Derivative (or Difference)” (MDD) and “Spatio-temporal Difference” (STD) to calculate the dimension, motion and scale of these FTEs. The inferred northwardly reconnected flux tube for the FTE is shown to move north-east and tailward with a quasi-2-D structure and a scale of 1.21 RE. Whilst, the FTE motions are shown to be consistent with the expected motion of reconnected magnetic flux tubes over the surface of the magnetopause, arising from a predominantly low-latitude reconnection site during the prevailing upstream conditions. According to the predictions of the Cooling model, they inferred the motion of the FTE observed by TC-1 spacecraft, and implied that the speed and size of flux tube increase with its poleward moving.

References

- Cai C L, Dandouras I, Rème H, Cao J. B., Zhou G. C, Shen C., Parks G., and Fontaine, D. (2009), Magnetosheath excursion and the relevant transport process at the magnetopause, *Ann. Geophys.*, 27, 2997-3005
- Cao J B, et al. (2008), Characteristics of mid-low latitude Pi2 excited by Bursty Bulk Flows, *J. Geophys. Res.* 113, A07S15, doi:10.1029/2007JA012629
- Cao J.B., et al. (2010), Geomagnetic signatures of current wedge produced by fast flows in a plasma sheet, *J. Geophys. Res.*, 115, A08205, doi:10.1029/2009JA014891
- Cao X., Z.Y. Pu, H. Zhang et al (2007), Dipolarization observed by TC1 and Cluster during substorm on September 14, 2004, *Chinese J. Geophys.*, 50(4): 995-1004.

- Cao, X., Z. Y. Pu, H. Zhang et al (2008), Multi-spacecraft and ground-based observations of substorm timing and activations : Two case studies, *J. Geophys. Res-Space Physics*, 113, doi:10.1029/2007JA01276
- Chen, T., X. Zhang, W. Li, N.Wang (2007), Spin Satellite Attitude Determined by Aboard Magnetometer, *Chin. J. Space Sci.* 0254-6124/2007/27 (4), 303-308 in Chinese
- Chen, T., D. Xu, Z. X. Liu, T. L. Zhang, S. McKenna-Lawlor , A.N. Fazakerley, Y. Bogdanova, S. J.Wang (2009), The bust Characteristics of electron and wave recorded aboard TC2 in the vicinity of the northern cusp during the geomagnetic storm of 15 May 2005, DSP-Cluster Workshop, Qindao, China , September, p22, JGR reviewed
- Chen, T., Z. X. Liu, S. McKenna-Lawlor, L. Lu (2011), Pitch angle determination of the high-energy electron bursts near the dawnside boundary layer by the payloads on TC2, *Science Technology and Engineering* , Vol. 11, No. 4, PP 698-704.
- Cheng ZW; Shi J K; Zhang T L; Liu Z X. (2007), Probability of Field-Aligned Currents Observed by the Satellite Cluster in the Magnetotail. *Chin Phys Lett*, 24(4): 1125-1127.
- Cheng ZhengWei, Shi JianKui, Zhang TieLong, Dunlop M, Liu Zhenxing (2008), relationship between FAC at plasma sheet boundary layers and AE index during storms of August and October, 2001, *Science in China Series E: Technological Sciences*, Vol.51, No.5:1-7
- Duan SuPing, Liu ZhenXing, Cao JinBin, et al. (2008a), TC-1 observation of ion high-speed flow reversal in the near-Earth plasma sheet during substorm, *SCIENCE IN CHINA SERIES E-TECHNOLOGICAL SCIENCES*, 51 (10): 1721-1730.
- Duan S.P., Liu Z.X., Cao J.B., Reme H., Dandouras I., Carr C.M.(2008b), Observation and theoretic Analysis of ion-ion two-streaming instability during substorm expansion phase, Ninth International Conference on Substorms (ICS-9), ICS9-A-00072, Graz, Austria, May.
- Duan, S. P., Liu, Z. X., Liang, J., Zhang, Y. C., and Chen, T. (2011a), Multiple magnetic dipolarizations observed by THEMIS during a substorm, *Ann. Geophys.*, 29, 331-339, doi:10.5194/angeo-29-331-2011
- Duan Su-Ping, LIU Zhen-Xing, LU Li, et al. (2011b), TC-1 and Geotail joint observations of magnetic disturbances in the near-Earth plasma sheet during a substorm, *Chin. J. Space Sci.*, in press (in Chinese)
- Dunlop M. W., Zhang, Q. H., Xiao C. J., He J. S., Pu Z. Y., Fear R. C., Shen C., Escoubet C. P. (2009), Reconnection at High Latitude: Antiparallel Merging, *Physical Review Letters*, 102, 075005.
- He, Z. H., Liu, Z. X., Chen, T., Shen, C., Li, X., Carr, C., and Rème, H. (2010), The large-scale magnetospheric electric field observed by Double Star TC-1, *Ann. Geophys.*, 28, 1625-1631, doi:10.5194/angeo-28-1625-2010.

- He, Z. H., Liu, Z. X., Shen, C., Duan, S. P., Zhang, Y. C., Reeves, G. D. (2008a), Identify the radial distance of plasma dispersionless injection boundary from injection source, *Chinese Physics Letters*, Vol.25, No.2, 783-786
- He, Z. H., Liu, Z. X., Shen, C., Duan, S. P., Liu, X., Zhang, Y. C., Yao, L., Zong, Q. G., Rème, H., Gustafsson G (2008b), Characters of the magnetotail plasma injection surveyed from Cluster observation, *Chinese J. Geophys.*(in Chinese), 51(2), 15-23.
- Liu R Y, et al. (2005), The Chinese Ground-based Instrumentation in Support of the Combined Cluster/Double Star Satellite Measurements, *Annales Geophysicae*, 23(8), 2943-2951.
- Liu, Z. X. et al. (2005), The Double Star Mission, *Ann. Geophys.*, 23:2707–2712.
- Liu Zhenxing, Pu Zuyin, Cao Jinbin, Shen Chao, Lu Li and Zhang Lingqian (2008), New progress of Double star—Cluster joint exploration and study, *Chin. Sci.*, 51(10), 1565-1579.
- Liu Zhen Xing, Zhang Ling Qian, Ma Zhi Wei, Wang Ji Ye, Pu Zhu Yin, Shen Chao, Guo Jiu Ling. (2007), The statistical characteristics of the tailward flows in the near-Earth region explored by TC-1. *Chinese J. Geophys.* (in Chinese), 50(3): 655-661
- Lu, L., S. McKenna-Lawlor, S. Barabash, J. Balaz, Z. X. Liu, C. Shen, J. B. Cao and C. L. Tang (2008b), Iterative inversion of global magnetospheric information from energy neutral atom (ENA) images recorded by the TC-2/NUADU instrument, *Chin. Sci.*, 51 (10), 1731-1744
- Lu, L., S. McKenna-Lawlor, S. Barabash, P. C. Brandt, J. Balaz, Z. X. Liu, Z. H. He, G. D. Reeves (2010), Comparisons between ion distributions retrieved from ENA images of the ring current and contemporaneous, multipoint ion measurements recorded in situ during the major magnetic storm of 15 May, 2005, *J. Geophys. Res.*, doi:10.1029/2010JA015770
- Lu Li, Susan McKenna-Lawlor, Stas Barabash, Liu Zhenxing, Jan Balaz, Klas Brinkfeldt, Igor Strhansky, Shen Chao, Shi Jiankui, Cao Jinbin, Fu Suiyan, Herbert Gunell, Karel Kudela, Edmond C. Roelof, Pontos C;son Brandt, Ilannis Dandouras, Zhang Tielong, and Chris Carr (2005), Electron pitch angle variations recorded at high magnetic latitudes by the NUADU instrument on the TC-2 spacecraft, *Ann. Geophys.* 23, 2953-2959.
- Lu Li, Susan McKenna-Lawlor, Stas Barabash, LIU Zhenxing, CAO Jinbin, Jan Balaz, Karel Kudela, Tielong Zhang, Chris Carr (2007), Plasma sheet Stretching accompanied by field aligned energetic ion fluxes observed by the NUADU instrument aboard TC-2, *Chin. Sci. Bull.*, 52(12), 1719-1723.
- Lu. Li, S. McKenna-Lawlor, S. Barabash, J. Balaz, I. Strharsky, Z. X. Liu, C. Shen, K. Kudela, P. C. Brandt and C. L. Tang (2008a), Iterative inversion of global magnetospheric ion distributions using energetic neutral atom (ENA) images recorded by the NUADU/TC2 instrument, *Ann. Geophys.*, 26 (6), 1641-1652.
- Ma S. Y., W. N. Yan, Xu L., A proposal for retrieval of ion distributions in RC by CT technique using

- joint ENA Images from TC-2 and IMAGE, DSP/Cluster-2009 International Scientific Workshop, QingDao, China, November, 2009.
- McKenna-Lawlor Susan, Jan Balaz,, Stas Barabash,, Klas Johnsson, Lu Li, Chao Shen, Jiankui Shi, Qingang Zong, Karel Kudela, Suiyan Fu, Edmond C. Roelof, Pontus C:son Brandt, and Iannis Dandouras (2004), The energetic NeUtral Atom Detector Unit (NUADU) for China's Double Star Mission and its calibration, *Nuclear Inst. & Methods*, A(503) 311-322.
- McKenna-Lawlor Susan, Jan Balaz,, Stas Barabash,, Klas Johnsson, Lu Li, Chao Shen, Jiankui Shi, Qingang Zong, Karel Kudela, Suiyan Fu, Edmond C. Roelof, Pontus C:son Brandt, and Iannis Dandouras (2005a), An overview of the scientific objectives and technical configuration of the NeUtral Atom Detector Unit NUADU for the Chinese Double Star Mission, *Planet.& Space Sci.* 53, 335-348.
- McKenna-Lawlor Susan, Lu Li, Stas Barabash, Karel Kudela, Jan Balaz, Igor Strharsky, Klas Brinkfeldt, Herbert Gunell, Chao Shen, Jiankui Shi, Jin-Bin Cao, Qiugang Zong, Sui-Yan Fu, Edmond C. Roelof, Pontus C. Brandt and Iannis Dandouras (2005b), The NUADU experiment on TC-2 and the first Energetic Neutral Atom (ENA) images recorded by this instrument, *Ann. Geophy.* 23, 2849-2852.
- Pu, Z. Y., X. G. Zhang, X. G. Wang et al. (2007), Global view of dayside magnetic reconnection with the dusk-dawn IMF orientation: a statistical study for Double Star and Cluster data, *Geophys. Res. Lett.*, 34, L20101, doi:10.1029/2007GL030336..
- Shi, J. K., Z. W. Cheng, Z. X. Liu, M. Dunlop, T. L. Zhang (2010a), Simultaneous observation of large scale FAC connecting ionosphere and magnetosphere by double star and cluster, COSPAR10, Bremen, Germany.
- Shi Jian-Kui, CHENG Zheng-Wei, T. L. Zhang, M. Dunlop, LIU Zhen-Xing (2009), Properties of Field Aligned Current in Plasma Sheet Boundary Layers in Magnetotail: Cluster Observation, *CHIN. PHYS. LETT.* Vol. 26, No. 2, 029401.
- Shi, J. K., Z. W. Cheng, T. L. Zhang, M. Dunlop, Z. X. Liu, K. Torkar, A. Fazakerley, E. Lucek, H. Rème, I. Dandouras, A. T. Y. Lui, Z. Y. Pu, A. P. Walsh, M. Volwerk, A. D. Lahiff, M. G. G. T. Taylor, A. Grocott, L. M. Kistler, M. Lester, C. Mouikis, and C. Shen (2010b), South-north asymmetry of field-aligned currents in the magnetotail observed by Cluster, *J. Geophys. Res.*, 115, A07228, doi:10.1029/2009JA014446.
- Tang, C. L., L. Lu, S. McKenna-Lawlor, S. Barabash, Z. X. Liu, M.-C. Fok, Z. Y. Li (2008), A comparison of NUADU neutral atom image inversion with a comprehensive ring current model, *J. Geophys. Res.*, 113, A07S32, doi:10.1029/2007JA012680.

- Wang H., S. Y. Ma, H. Luehr, Z. X. Liu, Z. Y. Pu, C. P. Escoubet, H. U. Frey, Reme H. and P. Ritter (2006), Global manifestations of a substorm onset observed by a multi-satellite and ground station network, *Ann. Geophys.*, 24, 3491-3496
- Wang H., Lüth H., Ma S. Y., Ridley A. J. (2008), Substorm dynamics in the magnetotail as derived from TC1 and Cluster coordinate observations, *Earth, Planets and Space*, 60: 613-621.
- Wang H., S. Y. Ma, and A. J. Ridley (2009), Comparative study of substorm dynamics by satellite observation and Space Weather Modeling Framework simulation, *Chinese Science Bulletin (Chinese and English)* , 54(17), 10.1007/s11434-009-0282-4
- Wang, J., M.W. Dunlop, Z.Y. Pu et al. (2007), TC1 & Cluster Observation of an FTE on 4 January 1, 2005: A Close Conjunction, *Geophys. Res. Lett.*, 34, L03106, doi:10.1029/2006GL028241.
- Yan, G. Q., C. Shen, Z. X. Liu, H. Rème, M. Dunlop, E. Lucek, C. M. Carr, and T. L. Zhang (2008), Solar wind transport into magnetosphere caused by magnetic reconnection at high latitude magnetopause during northward IMF: Cluster-DSP conjunction observations, *Sci. in China (E)* , 51, 1677-1684.
- Yan, G. Q., Z. X. Liu, C. Shen, M. Dunlop, E. Luseck, H. Rème, and Y. V. Bogdanova (2009), Solar wind entry via flux tube into magnetosphere observed by Cluster measurements at dayside magnetopause during southward IMF, *Sci. in China (E)* , 52, 2104-2111
- Yan, Guang Qing, Chao Shen, Zhen Xing Liu, Macholm Dunlop, H. Rème, Chris Carr, Qing He Zhang, Yulia V. Bogdanova, Zhi Qing Chen, Zhao Xian Zeng (2010), Component reconnection observed by TC-1 at the dawn flank magnetopause with IMF $B_z \approx 0$, submitted
- Yan W. N., S. Y. Ma, Xu L., J. Goldstein, L. Lu, Z. X. Liu, Retrieval of ion distributions in RC from TWINS ENAI and joint TC-2/ IMAGE HENA measurements by CT technique, *Geophysical Research Abstracts*, Vol. 12, EGU2010- 11237, report at EGU-10, Vienna Austria, May 2-7, 2010.
- Zhang, H., Z. Y. Pu, X. Cao et al. (2007), TC-1 observations of flux pileup and dipolarization-associated expansion in the near-Earth magnetotail during substorms, *Geophys. Res. Lett.*, 34, L03104, doi:10.1029/2006GL028326
- Zhang Ling Qian, Liu Zhen Xing, Ma Zhi Wei, Pu Zu Yin, Wang Ji Ye, Shen Chao.(2007a), The continuous tailward flow in the near-Earth magnetotail explored by TC-1. *Chin Sci Bulletin.*, 52(1), 1-6
- Zhang Ling Qian, Liu Zhen Xing, Wang Ji Ye, Ma Zhi Wei, Pu Zu Yin, Shen Chao, Guo Jiu Ling.(2007b), The distribution characteristics of the near-Earth plasma flow explored by TC-1. *Chin Sci Bulletin.*, 53(7): 843-847
- Zhang, L. Q., Z. X. Liu, Z. W. Ma, W. Baumjohann, Z. Y. Pu, M. W. Dunlop, H. Reme, and J. Y. Wang (2010), X line distribution determined from earthward and tailward convective bursty flows in the

- central plasma sheet, *J. Geophys. Res.*, 115, A06218, doi:10.1029/2009JA014429
- Zhang Qing-He, Dunlop M. W., Liu R. Y., Hu H. Q., Huang J. Y., McCrea I. W., Bogdanova Y. V., Lester M., Yang H. G., Zhang B. C., Hu Z. J., Crothers S. R., La Hoz C., and Nielsen C. P. (2010), Coordinated Cluster/Double star and ground-based observations of dayside reconnection signatures on 11 February 2004, Submitted to *Annales Geophysicae*.
- Zhang Qing-He, Liu R. Y., Huang J. Y., Dunlop M. W., Hu H. Q., Hu Z. J., Bogdanova Y. V., Walsh A. (2009), Simultaneous TC-1 and Cluster observations of FTEs on 13 March 2004, *Chinese Journal of Space Science*(in Chinese), 29(2):166-174.
- Zhang, T. L., R. Nakamura, M. Volwerk, A. Runov, W. Baumjohann, H. U. Eichelberger, C. Carr, A. Balogh, V. Sergeev, J. K. Shi, and K.-H. Fornacon (2005), Double Star/Cluster observation of neutral sheet oscillations on 5 August 2004, *Annales Geophysicae*, 23, 2909–2914.
- Zhang Yongcun, Liu Zhenxing, et al. (2007a), Double Star TC-1 observation of the earth-ward flowing plasmoids in the nearmagnetotail, *Chinese.Sci.Bull.*,52(13), 1843-1848
- Zhang, Y. C., Z. X. Liu, et al. (2007b), The magnetic structure of an earthward-moving flux rope observed by Cluster in the near-tail, *Ann. Geophys.*, 25, 1471 -1476
- Zhang Yong-Cun, Shen Chao, Liu Zhen-Xing, (2011), The characteristics and structure of magnetotail flux rope recovered from Grad-Shafranov method, *ACTA PHYS SIN-CH ED*, to be published.

INTRODUCTION TO CHINESE MERIDIAN PROJECT

WANG Chi

State Key Laboratory of Space Weather, Center for Space Science and Applied Research, Chinese
Academy of Sciences, Beijing, 100190, China

ABSTRACT The Meridian Project is a ground-based network program to monitor Solar-Terrestrial space environment, which consists of a chain of ground-based observatories with multiple instruments including magnetometers, ionosondes, HF and VHF radars, Lidars, IPS monitors, sounding rockets etc. The chain is mainly located in the neighborhood of 120 °E meridian, and is thus named the Meridian Project. The Meridian Project has officially been approved and supported by the Chinese government and will be finished by the end of 2010. This report gives an overview of the Meridian Project, and reports the recent development since 2008.

I OVERVIEW OF THE MERIDIAN PROJECT

Meridian Space Weather Monitoring Project (for short, Meridian Project), is a Chinese multi-station chain along 120 °E longitude to monitor space environment, starting from Mohe, the most northern station in China, through Beijing, Wuhan, Guangzhou and extending to Chinese Zhongshan station in the Antarctic. The meridian project consists of 15 observational stations (see Table 1), the instruments include magnetometers, ionosondes and digisondes, incoherent scattering radar, HF back-scattering radar, VLF receiver, lidar, Fabry-Perot Interferometer(FPI).

It has been officially approved by Chinese government. The total budget is about 24M US dollars. The construction phase started from January, 2008, and is expected to be finished by December, 2010. The lifetime is designed to be at least 11 years.

The Meridian Project is going to build three systems (see Figure 1):

(1) Space Environment Monitoring System

- Radio monitoring subsystem.
- Geomagnetic (Goelectronic)-monitoring subsystem.
- Optical-atmospheric monitoring subsystem.
- Rocket sounding monitoring subsystem.

(2) Data and communication system

- Collect, transfer, process, store and distribute data.
- International data exchange.
- Coordinate stations, instruments and operating personnel.

(3) Research and Modeling and forecast system

- Coordinating observations, research and management.
- Developing space weather modeling.
- Jointly forecasting space weather.
- Promoting international cooperation.

The key parameters will be observed by the Meridian Project include:

- Earth Surface: Geomagnetic field, Goelectronic field, Cosmic Rays.
- Middle-Upper Atmosphere: density, temperature, composition, electric current.
- Ionosphere: density of electron and proton, temperature, irregular structures, electric current.
- Interplanetary Space: solar wind plasma speed.

The main goal of the Meridian Project is to monitor the geospace environment continuously using multiple ground-based instruments, and its response to interplanetary disturbances.

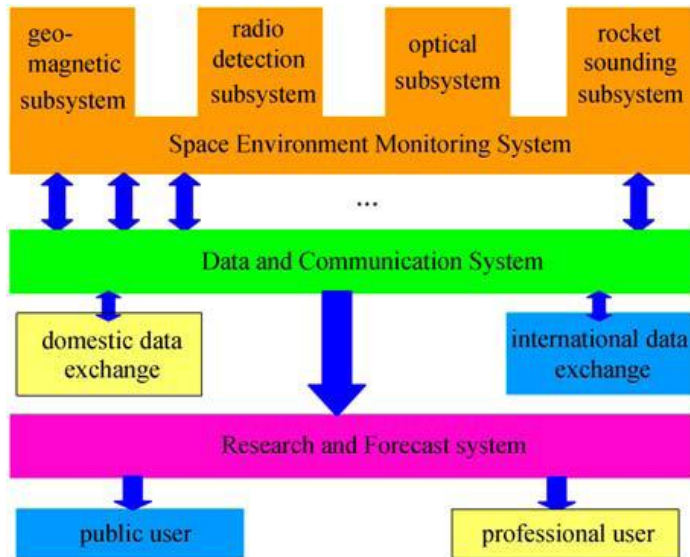


Figure 1 Meridian Project Framework

II RECENT DEVELOPMENT OF THE MERIDIAN PROJECT

The construction phase of the Meridian Project officially started in January, 2008. Two of the three systems, namely the Research and Forecast system and the Data and Communication system, and part of the Space Environment Monitoring system have been finished.

The Research and Forecast system has built up the high performance computing equipment, which has 15T flops computing power. The science operation center has the capability of making the observational plan for each instrument in both short and long term. Five space weather forecast models, including the L1-magnetosphere-ionosphere coupling model, numerical magnetosphere database, cosmic ray based magnetic storm forecast model, ionospheric TEC forecast model, and the atmospheric climate model, have been finished coding.

The Data and Communication system has established the internet connection from each station to the Meridian Project Data Center in Beijing. The data center

has also been ready for operation.

Two of the four subsystems, namely the geomagnetic monitoring subsystem and the optical-atmospheric monitoring subsystem, have completed construction. Especially the Lidar Chain from the north to south, *i.e.* Beijing–Wuhan–Hefei–Hainan, has been finished. Up to date, the geomagnetic measurements, the lidar observations, the cosmic ray conservations, the digisonde ionospheric measurement have been in operation. The other instruments are currently under construction, and are expected to be ready by the end of 2010.

III INTERNATIONAL SPACE WEATHER MERIDIAN CIRCLE PROGRAM

The International Space Weather Meridian Circle Program (IMCP) is proposed to connect 120 °E and 60 °W meridian chains of ground based monitors all over the world, which will enhance the ability of monitoring space environment worldwide in a significant way (see Figure 2).

Countries near this circle which may have interests include:

- Russia,
- Canada,
- USA,
- Brazil,
- Argentina,
- Japan,
- Australia.

The multilateral activities to be promoted include:

- Extending the International Meridian Circle Project to include stations along existing parallel meridian circles in order to get the most scientific benefits.
- Establishing a close collaboration among the existing magnetometer chains run by USA, Canada, Japan, Russia, China and other possible countries in the region. Establishment of new stations is suggested to fill the gaps along the full meridian circle, such as Siberia, South East Asia.
- Encouraging collaboration among various ionospheric, magnetospheric and interplanetary observatories.

The main functions of the IMCP should include:

- Coordinating observational campaigns.
- Making data available to the scientific community.
- Encouraging collaboration on scientific research and observations.
- Promoting education and public outreach on space science and technology.



Figure 2 International Space Weather Meridian Circle

IV SUMMARY

The Meridian Project is a ground-based network program to monitor space environment, which consists of a chain of ground-based observatories with multiple instruments. It has officially been approved by the Chinese government, and will be finished by 2010. The international collaboration will make it possible to constitute the first complete environment monitoring chain around the globe.

References

The Meridian Project Team. 2005. Proposal of the Meridian Space Weather Monitoring Project [R].

Internal Report

The Meridian Project Team. 2006. The Feasibility Study of the Meridian Space Weather Monitoring Project [R]

The Meridian Project Team. 2007. The Preliminary Design of the Meridian Space Weather Monitoring Project [R]

PROGRESS IN GEOMAGNETIC RESEARCH

Wen-Yao XU and Aimin DU

(Institute of Geology and Geophysics, Chinese Academy of Sciences, Beijing, 100029,China)

Abstract The advances of geomagnetic science in China during the period of 2006-2011 is briefly summarized in following aspects: China Meridian Chain of Magnetometers (CMCM), magnetic survey, modeling and compilation of magnetic charts for epochs of 2005 and 2010, the main magnetic field and its origin, the crustal field and regional anomalies, spatial and temporal characteristics of variation magnetic field and their relationship with solar activity and interplanetary disturbances, possible correlation between magnetic variations and earthquakes, and other applications of geomagnetism.

□

The Earth's magnetic field includes important information on both Earth's interior and space environment. The main magnetic field, as the most predominant part, originates from magnetohydrodynamic (MHD) processes in the liquid outer core, and is affected by the thermal structure and dynamic processes in the mantle and the core-mantle boundary (D" layer). The crustal magnetic anomalies reveal magnetic properties of the crust material. The transient magnetic variations are caused by current systems in the solar-terrestrial space (mainly in the ionosphere and magnetosphere), and correlated with space weather.

In this paper the researches in geomagnetism carried out in China during 2006-2011 are briefly summarized in several respects, including the project of meridian chain of magnetometers, magnetic survey and regional magnetic chart compilation, the main magnetic field and its secular variations, the origin of the Earth's magnetic field and geodynamo, geomagnetic transient variations and their connection with solar activity. Besides, possible relationship between magnetic variations and earthquake occurrence are also summarized.

I. THE CHINA MERIDIAN CHAIN OF MAGNETOMETERS (CMCM)

As one of the important parts of The Meridian Project (ZIWU Project), the China Meridian Chain of Magnetometers (CMCM) along 120° E longitude has been established [Wu et al. 2006].

Early in 1994, sponsored by Chinese Academy of Sciences (CAS) and then the State Science and Technology Commission of China (SSTC, now Ministry of Science and Technology), Chinese space scientists gathered together to discuss issues of development of space physics research in China. Several special seminars were held to continue the discussion, which led finally to put forward a proposal to establish a station chain along the 120° E to monitor the geo-space environment. This proposal was highly reviewed and evaluated by quite a lot of scientists from high level community and then listed in the national plan by the Chinese Government. From that time on, the project has been formally called as ZIWU Project, since in Chinese ZIWU means meridian.

This north-south meridian chain includes 8 magnetic observatories, covering a latitudinal span of 35° from Mohe station (geographic latitude 53.5° N, geographic longitude 122.4° E, geomagnetic latitude 43.3°), the northernmost station in China, through Manzhouli (gglat 49.6° N, gglong 117.4° E), Changchun (gglat 44.0° N, gglong 125.2° E), Beijing (gglat 40.3° N, gglong 116.2° E), Xinxiang (gglat 34.6° N, gglong 113.6° E), Wuhan (gglat 30.5° N, gglong 114.6° E), Guangzhou (gglat 23.1° N, gglong 113.3° E), to Sanya station (gglat 18.4° N, gglong 110.4° E, gmlat 7.3°), the southernmost station in the continent. Actually the chain is extended to Chinese Zhongshan Station in the Antarctic (gglat 69.4° S, gmlat -77.1°). The stations of the chain are equipped with modern ground-based magnetometers and networked as a system to coordinately monitor a variety of processes in space environment, especially, during the period of disturbances.

As a complement of CMCM, an additional latitudinal chain of magnetometers (CLCM) has been also established along 30° N latitude, including 4 stations from Shanghai (gglat 31.1° N, gglong 121.2° E), the easternmost station, through Wuhan (gglat 30.5° N, gglong 114.6° E), Chengdu (gglat 31.0° N, gglong 103.7° E), to Lhasa (gglat 29.6° N, gglong 91.0° E), the westernmost station, covering a longitudinal span of 30°. Combined this latitudinal chain with the meridian chain stations, a crosswise station array is formed in middle-low latitudes in Eastern Asia continent.

Extending northward, the CMCM connects with Russian stations in East Siberia, while extending southward, the CMCM connects with stations in Indonesia and Australia, approaching Antarctica.

Continuing the extension to the western hemisphere, the CMCM connects with magnetic stations around 60°W longitude, forming a closed circle of stations. This international complete meridian chain will greatly enhance the ability of space environment monitoring.

Cooperating with other magnetic meridian and latitudinal chains existing at high latitudes and mid-low latitudes, we have a worldwide network of magnetic stations, continuously monitoring global magnetic activity.

The main task of the CMCM is to continuously record magnetic field variations at mid-low latitudes from the subauroral zone to the equatorial anomaly zone. In addition, the CMCM will accumulate historical data which are necessary supplements for space weather researches. These historical and modern data are used to study and understand the physical mechanism of solar wind-magnetosphere-ionosphere coupling responsible for space weather processes, and to develop regional/global cause-effect models for diagnosing space weather environment. These data are also applied to routine forecast and nowcast of space weather events, such as magnetic storms and substorms.

On the basis of the meridian chain data, several research programs have been carried out, such as magnetosphere-ionosphere-thermosphere coupling processes and their responses to solar wind storms, equatorward and poleward transportation of mass, energy and momentum injected into geo-space during space weather events, global 3D semi-empirical background (quiet) model for space environment, time-varying cause-effect model for space weather events, and relationship between regional and global models.

Besides, more than one hundred magnetic stations are routinely operating in China, among which 15 observatories are assessed as the “first class” stations. In the second class there are 19 stations. The data from the 34 observatories have been submitted to World Data Center A in Boulder, USA for international exchange. In addition, there are two permanent stations, Great Wall and Zhongshan, in Antarctica, and one station, Huanghe, in Arctic. During the 23rd solar cycles, the data from these magnetic stations played an important role in studying solar-terrestrial coupling.

II. THE CHINA-GRF MODELS AND NATIONAL MAGNETIC CHARTS FOR

2005 AND 2010

Magnetic field survey and charting is a routine work in China since the early days of global exploration during early last century.

After the seventh generation of China Geomagnetic Reference Field model (China-GRF for the sake of shortness) for the epoch 2000 [Xu et al., 2003], compilation of the eighth and ninth generations of China-GRF have been carried out for 2005 and 2010.

For compiling the eighth generation of China-GRF for 2005, an extended magnetic survey was carried out at a relatively denser network in 2002-2004. In addition, GPS (Global Positioning System) technique was used to positioning of repeat station (longitude, latitude and elevation) and azimuth measurement of the reference mark for determining declination [Gu et al., 2005]. The statistical results of the GPS data at 135 stations indicate that at a single station the difference between two measurements of GPS azimuth is less than 5.9" with an average 1.6", showing accurate and reliable azimuth measurements. The standard deviation of declination D thus obtained based on the GPS azimuth measurement is less than 0.4'.

Several techniques, such as SCHA (spherical cap harmonic analysis), RHA (rectangular harmonic analysis), Taylor polynomial, spline functions, have been used for data fitting and empirical modeling. Their differences are discussed.

The magnetic chart compilation, instead of a mere collection and organization of data, concerns many aspects of geomagnetism: selection and reduction of data, estimation and analysis of error, assessment and comparison of methods, establishment and choice of mathematical models, and evaluation of final results. The magnetic charts are essential base for studying magnetic field source and secular variation. Different users need different kind of magnetic charts and models, but what should be commonly considered in chart compilation are (1) physical reasonableness, (2) proper accuracy, (3) complete information, and (4) convenience in use.

Following the eighth generation of China-GRF for 2005, the ninth generation of China-GRF for 2010 has been accomplished in 2010.

III. THE MAIN MAGNETIC FIELD

The dipole field is the predominant part of the main magnetic field. However, the complexities of the main field in both spatial pattern and temporal evolution are mostly attributed to the non-dipole field, which exhibits as 5 planetary-scale magnetic anomalies in Australia, Africa, Southern Atlantic Ocean, Eurasia continent, and North America, as well as a few minor anomalies. Xu and Bai [2009] focused on the African anomaly, the only anomaly in the equatorial region, and found that the African anomaly affects seriously the shape and position of the magnetic equator, pushing the equator northward for 15° at maximum. The fast westward drift of African anomaly results in a remarkable secular variation cell ($Z_{\max} > 200$ nT/a for 1900~2005) in Central America on the west of the anomaly. In addition, the secular variations of African and Southern Atlantic Ocean anomalies strongly distort the geomagnetic field of the western hemisphere, implying its relationship with the polarity reversed patches on the core-mantle boundary

Another effect of the non-dipole field is seen in determination of the virtual geomagnetic pole (VGP). It is pointed out that the VGP calculated under the assumption of a central dipole field is generally different from the real geomagnetic pole (RGP) since effect of the non-dipole field [Xu et al., 2007]. In order to quantitatively examine the effects, the VGP and RGP are calculated at $5^\circ \times 5^\circ$ virtual sites by using the IGRF 1900~2000 models. The results show significant departures of VGP from RGP in some major magnetic anomaly regions. The latitude departures of VGP from the RGP are as large as 25° in these anomaly regions, although they are acceptable in most sites on the earth's surface (less than 10°), mainly confined in the regions with a weak intensity of the non-dipole field, such as Pacific Ocean. The longitude departures of VGP from RGP are much more remarkable, scattering in a wide range from -180° to 180° in Eurasian continent. The angle distance between VGP and the RGP are generally within a range of 15° ; except the Antarctica, South Atlantic Ocean and Eurasia regions

In addition, a comparative study is carried out in planetary magnetic fields. Based on the fact that Mars has an ionosphere, but has no intrinsic magnetic field, a model for solar wind-Marian ionosphere interaction and Martian induced magnetic field is proposed by Tong and Chen [2010]. According to

the principle of current conservation and a proper assumption on current distribution in the Martian Magnetosphere, they obtained an expression of Martian magnetic field and a magnetic field line distribution, which are in good agreement with other models and observations.

Secular variation (SV) is the dynamic characteristics of the main magnetic field, which bring the convection flow and dynamo process in the Earth's core to light.

Based on the historical geomagnetic models GUFM1 and the 10th International Geomagnetic Reference Field models (IGRF10), Kang et al. [2008] studied the secular variation (SV) of several parameters describing the main field, such as the geomagnetic moment, magnetic energy, and westward drift rate etc. The method of wavelet transform was applied in their work. The results show that during the period of 1800~2005, the quasi-periodic components of 82 and 48 years are predominant in the SV of the dipole magnetic field, while in the SV of non-dipole magnetic field the quasi-periodic components of 66 and 32 years are principle. The authors correlated the main field SV with variations of the length-of-day (LOD), and suggested that the decadal variations of LOD seem to have no direct relation with the SV in the dipole magnetic field.

Using POMME-4.2S model derived from CHAMP satellite data, Kang et al. [2009] calculated annual rates of all 7 magnetic elements and secular acceleration for X , Y , and Z components. Their results indicate that the quadrupole field dominates the SV of the main field, while the octupole field has a great contribution to the secular acceleration.

For detecting the periodicities in the secular variations of the main geomagnetic field, the technique of wavelet transform is applied to analyze the gufm1 models during 1590~1990 A.D [Bai and Xu, 2010]. Three principal periodic components are identified in the annual mean values of the total Pole-strength of the magnetic field. The first is a stable 30-year periodic component, mainly seen in the equatorial component g_1^1 of the dipole field, and also in the non-dipole field. The second is a dispersive component with a quasi 50-year period, typically contributed by the axial component of the dipole field g_1^0 , and also by the quadrupole field. The third one is a centennial component with varying intensity and 110 year period, which seems to be from the equatorial

component of the dipole field, and the octupole field also has a contribution.

A comparative analysis of global and regional secular variations is conducted by Chen et al. [2010], Using the geomagnetic daily means at 34 permanent observatories in China during 2000~2004, they calculated the average annual variation rates for each of stations on quiet days and all days, on the basis of which a regional SV models for 2000.0~2005.0 were established by using Taylor polynomial and spline function fitting. The regional SV model generally coincides with the IGRF-SV model in both magnitude and pattern. However, the authors pointed out some local features in the model, and intended to correlate these features with geological structure and tectonic movement in this area.

IV. THE CRUSTAL MAGNETIC ANOMALIES

The crustal geomagnetic field has been extensively studied from the early age of geomagnetism, and has become one of the most important parts in the whole realm of solid-earth geophysics. Knowledge of vertical gradient of the magnetic field over anomalous regions is necessary for upward continuation. Yu et al. [2009] theoretically studied the spatial variations of anomaly. And then they adopted the curved surface upward continuation method to analyze the vertical variation of a marine magnetic anomaly with two sets of real marine magnetic survey data. Finally, they suggested a reduction condition.

Based on POMME-4.2S model, a geomagnetic field model with high truncation level from CHAMP satellite data, Kang et al. [2011] calculated 7 elements of the magnetic anomaly field at the satellite altitude (~400 km) up to $n=90$. They analyzed the relationship of the anomaly field in China/adjacent area and the lithosphere structures, and noted that the satellite magnetic anomalies have no direct relation with the topography, the rupture zone, the Moho discontinuity depth and the lithosphere thickness, but they are related with the depth of the Curie isotherm surface and the thickness of the magnetic layer: the anomalies are positive (negative) in the areas with deeper (shallower) Curie isotherm surface and thicker (thinner) magnetic layer. They also noted that in the principle anomaly areas of Sichuan, Tarim and Songliao basins, a pair of anomaly foci of X (or Y) component with opposite sign appear to the south and north (or west and east) sides of an Z

anomaly focus. Their examination indicates that the spherical harmonics with degrees higher than 90 in POMME-4.2S model have only minor modification to the magnetic anomaly.

V. TRANSIENT MAGNETIC VARIATIONS

Transient variations in the magnetic field, including regular variations and irregular disturbances, arise from the currents in the ionosphere and magnetosphere, as well as induced currents in the Earth's interior. Consequently, their characteristics depend on both near-Earth space environment and electromagnetic properties in the Earth.

The quiet solar diurnal variation (Sq) is the most important type of regular variations in the magnetic field, and it is also the basis of scaling magnetic indices and studying magnetic disturbances, including storms and substorms. Zhao et al. [2008] used the geomagnetic field data observed by ground-based observatories to analysis the configuration of Sq, the prenoon-postnoon asymmetry, and the daily variations of Sq depended on the latitude and solar zenith. The results indicate that the asymmetry of Sq is resulted from interaction between the current systems in low and high latitude regions

One of the most important databases for space physics research and space weather prediction is a long and complete catalogue of magnetic storms, which comes only from the long history stations. The oldest observatory in China, Sheshan station in Shanghai holds a successive geomagnetic field data set more than one-hundred years from 1877 on, which is benefit for geomagnetic activity research. On the basis of the hundred-year long records, the total 3247 magnetic storms are identified for 1908-2007, with 1% super storms (31 in total, $\Delta H_{\max} > 400\text{nT}$) [Tschu et al., 2010]. A comparison with other three catalogues of super storms, determined by different geomagnetic activity indices, shows that the super storms defined by the main phase amplitude in Sheshan are consistent with them.

By using time series superposition, Fourier and wavelet spectrum analysis, Wu et al. [2009] analyzed magnetic storms recorded at Sheshan during one hundred years from 1908 to 2007. The results show that prominent 11-year,

22-year and semiannual cycles are clearly seen in strong storm activity, but less conspicuous for moderate and weak storms. Furthermore, the semiannual variation of the strong storm shows differences between the odd and the even solar cycle, with a remarkable semiannual variation in high solar activity years and complicated variations in the even solar cycle years.

Using the data of the geomagnetic meridian observatories in China, Wu et al. [2007,2008] analyzed 25 geomagnetic storms in the period of 1997 to 1999. Three methods were used in their research: Natural Orthogonal Components (NOC), Correlation Analysis, and Fourier Analysis. Three steps have been done to decompose the storm-time variation (Dst) correlating with the universal time (UT), the solar daily variation (Sq) and the disturbance daily variation (S_D) depending on the local solar time (LT). The results show that the spatial distribution and the temporal evolution characteristic of equatorial symmetric ring current are reflected clearly by Dst variation. The amplitude of Sq reached maximum or minimum during most main phases in MZL, BMT and QGZ observatories. It reflects the variation of the geomagnetic field from the motion of the Sq focus with latitude. During main phases, the amplitude of S_D was the largest. It decreased slowly during the recovery phase. Correlation Analysis and Fourier Analyses offer a useful way to extract the Sq and S_D variations.

Magnetic pulsation (or ULF waves) is a special type of transient variations. Du et al. [2010] reported a pulsation event, which was simultaneously recorded in the upstream solar wind by ACE craft and in the magnetosphere by GOES12 satellite. Their spectra show similar structures with the maximum frequency band around 2.20–2.44 mHz. The upstream ULF waves are highly correlated with the Pc5 waves with a correlation coefficient of 0.82 for a time lag of 28.5 min. Both the interplanetary and the magnetospheric waves had intense radial components with very large-amplitude $\delta B_r / B > 40\%$, which indicated characteristic of the compression waves. Furthermore, variations of the plasma density were in phase with those in the magnetic field, suggesting that they were essentially magnetosonic waves. The results demonstrated that upstream magnetosonic waves in the solar wind can directly penetrate into the magnetosphere and cause the Pc5 ULF waves during a big magnetic storm. The penetration of the magnetosonic waves seems to be occurred merely around the noon sector.

Magnetic activity indices have been widely used to describe disturbances in the solar-terrestrial space. However, the indices suffer from various uncertainties resulted from data processing, uneven station distribution, and physical assumption [Xu, 2008]. One of the key points to improve magnetic index scaling is to identify and remove the regular solar daily variation (S_R). Elimination of regular solar daily variation is also necessary in marine magnetic survey [Bian et al., 2009]. However, it is not a straightforward issue due to the day-to-day variability of S_q [Chen, 2007]. Qi et al. [2010] used FMI method to effectively eliminate S_R for k -index scaling. In order to solve the problem of time delay inherent in the method and to give real-time K index, they propose a new method based on radial basis neural network. This method can produce the real-time S_R with a standard error of 3.9 nT, and therefore real time K -index. Examination shows that about 70% of the real-time K -indices are in agreement with the standard K -indices, only 0.77% have errors greater than one unit.

One of the most popular magnetic indices is auroral electrojet index (AE), which is used to quantitatively describe the activity of the geomagnetic field in the polar region and to measure the level of a substorm. Wang et al [2009] analyze variations in AE index, and correlated them with auroral display and ionospheric current system. It is noted that for pseudo-breakup events ($AE > 500$ nT) the variations of AE index clearly show a sudden increase phase followed by a slow recovery phase. At same time, however, aurora does not expand poleward or equatorward, and the ionospheric currents present the features of the magnetic convection. On the basis of the relation of AE with the current intensity and its configuration, a “ Key point model ” for polar region currents has been established and used to space weather prediction [Xu et al, 2008].

Both aurora display and auroral electrojet, as the most important manifestations of the energy coupling between the magnetosphere and the ionosphere, are resulted from particle precipitation, and greatly enhanced during substorms. However, they have rather different behaviors and AE-dependences. Xu [2009] analyzed the dynamic characteristics of the auroral electrojet belt by using equivalent current systems deduced from ground-based magnetic records. The results show that the electrojet belt is divided by Harang discontinuity into two parts: the minor eastward electrojet in afternoon sector and the major westward

electrojet in midnight-morning sector. The former shifts equatorward when AE increases, just as the auroral oval does; the latter is divided into two sections: the midnight section shifts poleward when AE increases, while the morning section shifts equatorward. A study on physical mechanism responsible for these differences reveals that the principal factor controlling the midnight-morning westward electrojet is ionospheric conductivities, while the principal factor controlling the afternoon eastward electrojet is electric field, instead of conductivities.

Analyzing the data of the estimated power input (EPI) of auroral particles from NOAA/POES (Polar orbiting environmental satellite) for some 30 years, Liu et al. [2008] obtained the annual variation of EPI, which shows equinox peaks, and an asymmetric activity with a higher peak in the winter-hemisphere. These characteristics in EPI generally coincide with *aa*, *AE* and *Dst* indices. The correlations of hourly mean EPI with *AE* (correlation coefficient $r=0.76$) and with *Dst* ($r=-0.55$) suggest a close correlation among the auroral particle precipitation, aurora display, and magnetic storms. The authors also examined time delays of EPI with respect to magnetic indices, and found that the time delay $\tau=0$ for *AE*, suggesting a synchronism of auroral electrojet and auroral particle precipitation, while $\tau=1\sim 2$ hours for *Dst*, suggesting that the activity of auroral particle precipitation may influence the ring current.

Geomagnetic storms are mainly resulted from the ring current, the decay rate of which is one of the key parameters for estimating energy budget of the magnetosphere and for storm prediction. Xu and Du [2010] proposed two new criterions for evaluating the decay rate: (1) the E-criterion: the total energy balance for a storm event, (2) the L-criterion: the total energy balance for a long interval. Several models of decay rate are examined by using 44 selected storms during 1998~2003 and an 11-year-long continuous record for the 23rd solar cycle. The results show that the models PA1978 and XD2010 show fairly well energy balance for all the storm events, satisfying the E-criterion. In addition, the two models fairly well satisfy the L-criterion, exhibiting enhanced energy dissipation during major storm events and long-term energy balance.

The dependence of the storm-time amplitude on longitude and latitude was statistically analyzed by Li et al. [2009]. The storm-time ranges observed at

Beijing Observatory (BJI) and San Juan Observatory (SJG) were compared to reveal their longitudinal dependence. It was found that the difference between BJI and SJG could be fitted by the 4-order Fourier series and the storm-time H range at dawn is less than that at dusk. The case studies of two typical storms confirm the above conclusion. A statistical study was conducted for all magnetic storms observed at the 120°E magnetic chain in eastern China for 1995–2004 to reveal the latitudinal dependence of storm-time ranges. It is found the relationship depends on the activity of storms and becomes complicated for giant storms with $Dst \leq -300$ nT.

Characteristics and strength of a magnetic storm depends on the topology of the equatorial ring current and its evolution, which are strongly controlled by injection and dissipation of charged particles. In order to trace evolution of the ring current, Chen et al. [2010] analyzed a series of energetic neutral atom (ENA) images obtained by the NUADU instrument aboard TC-2 satellite during a long duration strong magnetic storm in November 2004. It is shown that the southward IMF B_z component plays a key role in facilitating ion injection from the magnetotail into the inner magnetosphere with consequent enhancement of the ring current. Ion injection stopped soon after the IMF turned from southward to northward. In ion injection episodes, the ion drift paths are open and the ring current ions are lost at the noon-dusk magnetopause soon after they are injected at the dusk side. Consequently, the ring current is greatly intensified after, instead of before, the ion drift paths become closed. In storm main phase, ions are injected mainly between 17 : 00~22 : 00 LT, leading to an extremely asymmetric ring current. In the recovery phase, however, ion injection region reaches the post-midnight sector, which may be attributed to a significant positive IMF B_y component. The ring current becomes more symmetrical after ion drift paths become closed due to decrease in tail convection. When the storm enters its recovery phase, the ring current fades away, while the Dst still indicates a strong magnetic disturbance, suggesting the important contribution of the cross tail current.

Saw tooth events (periodic variation of energetic particle flux with a rapid increase followed by a gradual recovery) are often observed at synchronous orbit of the Earth, and are always associated with substorms. Lin et al. [2010] analyzed

ionospheric equivalent current system during a saw tooth event observed by LANL satellites on 30 September 2000. The authors compared the nightside westward electrojets with positive magnetic bays recorded at middle and low latitudes on the ground, and pointed out that a current wedge with a local time width of several hours is formed after each saw tooth injection.

Field-aligned currents (FACs) play an important role in the energy, momentum, and mass coupling between magnetosphere and ionosphere. Wang et al. [2010] statistically investigates the characteristics of polar ionospheric FACs during substorms by using high resolution magnetic field measurements on board CHAMP. Obvious day-night and dusk-dawn asymmetries are noted in both FACs density and location. The FACs densities in dusk and night sectors are correlated well with AL , but the densities in dawn and dayside are less correlated with AL . The location of the peak densities is not correlated with AL .

Dynamic pressure of solar wind on the front magnetopause constantly changes and results in variations of Chapman-Ferarro currents, which in turn cause changes of the resultant magnetic field in the magnetosphere. Ding et al. [2011] analyzed 123 events of solar wind dynamic pressure change and showed that the magnetic field Z component near the geosynchronous orbit presents strong positive response to the dynamic pressure changes. For pressure increase events, the largest increase of geosynchronous magnetic field Z component occurs in pre-noon region, while for pressure decrease events the largest decrease of Z is in post noon region. Dependence of SYM-H index on the solar wind dynamic pressure varies with local time, with the highest correlation at daytime and almost no correlation in midnight sector.

New magnetic indices are also studied [e.g. Yang et al.,2010].

VI. OTHER TOPICS

1. Observation and studies of seismomagnetic effects

Seismomagnetic effects have been extensively studied from last century on, especially, after the great Sichuan earthquake ($M_s=8.0$) occurred in southwest China on 12 May, 2008. Most of studies are focused to magnetic background of the earthquake area, anomalous VLF-ULF signal emission, magnetic disturbances and abnormal S_q .

The great Sichuan earthquake occurred at the Longmenshan fault zone in the east edge of Qinghai-Tibet plateau, where the magnetic field exhibits negative anomaly against the positive magnetic background in Chengdu basin. Wang et al. [2009] attribute this negative anomaly to thrust faults, which result in strata overturn, and therefore, a reversal magnetization forms.

Fan et al [2010] analyzed peculiar variations in the maximum entropy spectrum of geomagnetic and geoelectric fields recorded prior to the Sichuan earthquake at 5 geoelectric stations and 2 geomagnetic stations (epicenter distance less than 500km), and concluded that (1) A significant enhancement of the power spectral density (PSD) of geoelectric field is recorded prior to the earthquake at the northeast edge of the Tibet plateau. The most dramatic increases occur in low frequency components (period $T < 3h$). (2) The pattern of Sq variation in this area is distorted 19 days before the earthquake. (3) Other great earthquakes also show that the temporal and spatial characteristics of geoelectric and geomagnetic fields prior to earthquakes in and around Tibet Plateau show some relationship with the earthquake occurrences in this area.

Magnetic jerk is a kind of rapid variations in the core. Zhang et al. [2008] analyzed the jerks occurred in 1991 and 1999, and examined its possible relation with earthquakes.

2. Geomagnetic navigation

Magnetic compass has been applied in navigation from early days. Geomagnetic field, as a natural reference frame, is thought to be used in modern navigation since Psiaki and Martel's suggestion on autonomous magnetic navigation for Earth orbiting spacecraft in 1989. Wang and Tian [2010] derived both the system state equation and the observation equation, respectively based on the dynamic equation of satellite orbit and geomagnetic vector/magnitude. Considering nonlinearity of the system, they applied the Extended Kalman Filter (EKF), instead of traditional Kalman Filter (TKF), to linearize the system equations. The simulation shows that the EKF has good stability and rapid convergence.

3. Effects of geomagnetically-induced currents on power grid

Liu et al. [2008] collected events of severe transformer vibration and enhanced noise in power stations. They studied the transformer neutral current data and concluded that the disturbances in power lines are caused by geomagnetically-induced current (GIC), which may influence the normal operation of power grid.

Methodology in analysis of geomagnetic data is discussed [Asimopulos et al., 2010]. They compare several commonly used methods and algorithms, such as polynomial regression, correlation factor, spectral analysis and wavelet technique.

Acknowledgement This study is supported by the National Key Basic Research Program (grant number 973 Plan-2008CB425704) and National Natural Science Foundation of China (grant number 40874089).

References

- Asimopulos L, Pestina A M, Asimopulos N S. Considerations on geomagnetic data analysis. *Chinese J. Geophys.*, 2010,V53(3): 765-772
- Bai Chun-Hua, Xu Wen-Yao. Multi-decadal to centennial secular variation of the main geomagnetic field. *Chinese J. Geophys.*, 2010,V53(4): 904-911
- Bian Gang, Liu Yan-Chun, Bian Guang-Lang, Yu Bo. Research on computation method of multi-station diurnal variation correction in marine magnetic surveys. *Chinese J. Geophys.*, 2009,V52(10): 2613-2618
- Chen Bin, Gu Zuo-Wen, Gao Jin-Tian, Yuan Jie-Hao, Di Chuan-Zhi. Study of geomagnetic secular variation in China. *Chinese J. Geophys.*, 2010, V53(9): 2144-2154
- Chen Bo, Xu Wen-Yao, Chen Geng-Xiong, Du Ai-Min, Wu Ying-Yan, and Liu Xiao-Can. Latitudinal shift and tilt of the ring current during magnetic storms, *Chinese Sci. Bull.*, 2008, 53:1-9
- Chen Geng-Xiong, Xu Wen-Yao, Du Ai-Min, Wu Ying-Yan, Chen Bo, and Liu Xiao-Can. Statistical characteristics of the day-to-day variability in the geomagnetic Sq field, *J. Geophys. Res.*, 2007, 112(A5), A06320
- Chen Zhi-Qing, Shen Chao, Lu Li, McKenna-Lawlor S., Liu Zhen-Xing, Yan Guang-Qing. Evolvement

- of the ring current during a magnetic storm: TC-2 neutral atom imager observations. *Chinese J. Geophys.*, 2010, V53(10): 2271-2279
- Ding Liu-Guan, Jiang Yong, Li Chuan-Qi, Yu Chao. Response of geosynchronous magnetic field Z component and geomagnetic field to solar wind dynamic pressure change. *Chinese J. Geophys.*, 2011, V54(1): 6-13
- Du A M, Xu W Y, and Feng X S. Dependence of the IMF sector structure on the solar dipole tilt angle. *J. Geophys. Res.*, 2008, 113:A07105
- Du A M, Tsurutani B T, and Sun W. Anomalous geomagnetic storm of 21–22 January 2005: A storm main phase during northward IMFs. *J. Geophys. Res.*, 2008, 113:A1024
- Du A M, Xu Wen-Yao, and Sun W., Experimental evidence of direct penetration of upstream ULF wave from the solar wind into the magnetosphere during the strong magnetic storm of November 9, 2004, *Planet. Space Sci.*, 2010, 58: 1040-1044,
- Fan Ying-Ying, Du Xue-Bin, Zlotnicki J, Tan Da-Cheng, Liu Jun, An Zhang-Hui, Chen Jun-Ying, Zheng Guo-Lei, Xie Tao. The electromagnetic phenomena before the Ms8.0 Wenchuan earthquake. *Chinese J. Geophys.*, 53(12): 2887-2898, 2010.
- Feng Yan, Pan Jian-Jun, An Zhen-Chang, Sun Han, Mao Fei. Calculation and analysis of geomagnetic field horizontal gradients in China. *Chinese J. Geophys.*, 2010, V53(12): 2899-2906
- Guo Feng-Xia, Zhang Yi-Jun, Yan Mu-Hong. The secular variation characteristics and mechanisms of geomagnetic field. *Chinese J. Geophys.*, 2007, **50**(6): 1649-1657
- Kang Guo-Fa, Bai Chun-Hua, Gao Guo-Ming. Periodical characteristics of the geomagnetic secular variation and length-of-day variation *Chinese Journal Geophysics*. 2008, **51**(2): 369-375
- Kang Guo-Fa; Gao Guo-Ming¹; Bai Chun-Hua²; Di Chuan-Zhi¹ Characteristics of the secular variation and secular acceleration distributions of the main geomagnetic field for the CHAMP satellite, *Chinese Journal Geophysics*, 2009, **52**(8) 1976-1984
- Kang Guo-Fa, Gao Guo-Meng, Bai Chun-Hua, Wang Jun, Shao Dan. Distribution of the magnetic anomaly for the CHAMP satellite in China and adjacent areas. *Chinese J. Geophys.*, 2010, V53(4): 895-903
- Li Qi, Gao Yufen, Wang Jianjun, and Han De-Sheng. Local differences in great magnetic storms observed at middle and low latitudes. *Earth Planets Space*, 2009, **61**:995–1001,

- Liu Lian-Guang, Liu Chun-Ming, Zhang Bing, Wang Ze-Zhong, Xiao Xiang-Ning, Han Li-Zhang. Strong magnetic storm influence on China Guangdong power grid. *Chinese J. Geophys.*, 2008, **51**(4) 968-975, 2008
- Lin Min-Hui, Deng Xiao-Hua, Yuan Zhi-Gang, Wang Jing-Fang. Characteristics of magnetic variations and current wedge in the sawtooth event on 30 September 2000. *Chinese J. Geophys.*, 2010, **V53**(10): 2280-2290
- Liu Xiao-Can, Chen Geng-Xiong, Xu Wen-Yao, Du Ai-Min, Wu Ying-Yan, Chen Bo, Wang Yuan, Zhao Xu-Dong. Relationships of the auroral precipitating particle power with AE and D_{st} indices. *Chinese J. Geophys.*, 2008, **51**(4): 968-975
- Qi Wei, Wang Xiu-Fang, Li Xi-Hai, Liu Dai-Zhi. A real time K -indices scaling method based on radial basis neural network. *Chinese J. Geophys.*, 2010, **V53**(1): 147-155
- Tong Dong-Sheng, Chen Chu-Xin. A model of Martian induced magnetic field and the distribution of magnetic field lines. *Chinese J. Geophys.*, 2010, **V53**(9): 2155-2160
- Wang Hui, Mao Dan-Dan, Ma Shu-Ying, Luehr H. Substorm time ionospheric field-aligned currents as observed by CHAMP. *Chinese J. Geophys.*, 2010, **V53**(6): 1256-1262
- Wang Qiu-Jun, Du Ai-Min, Zhao Xu-Dong, Luo Hao, Xu Wen-Yao. Manifestation of the AE index in substorms on August 6, 1998. *Chinese J. Geophys.*, 2009, **V52**(12): 2943-2950
- Wang Xiang-Lei and Tian Yan-Feng. Autonomous navigation based on geomagnetic research. *Chinese J. Geophys.*, 2010, **53**(11): 2724-2731
- Wang Y, Hong M H, Chen G X, et al. Nightside field-aligned current during the April 6, 2000 superstorm. *Chinese Sci Bull*, 2010, **55**(14): 1409-1415
- Wu Ji, Wang Chi, Fan Quanlin. Introduction to Meridian space weather monitoring project. *Chin. J. Space Sci.*, 2006, **26**(Supp):17-24
- Wu Ying-Yan, Xu Wen-Yao, Chen Geng-Xiong, Chen Bo, and Liu Xiao-Can. The evolution of the characteristics of magnetic disturbances during magnetic storms. *Chinese J. Geophys.*, 2007, **50**(1):1-9,.
- Wu Ying-Yan, Xu Wen-Yao, Chen Geng-Xiong, Chen Bo, Liu Xiao-Can. The evolution characteristics of geomagnetic disturbances during geomagnetic storms. *Chinese J. Geophys.*, 2007, **50**(1) 1-9
- Wu Ying-Yan, Xu Wen-Yao, Chen Geng-Xiong, Chen Bo, and Liu Xiao-Can, Ground magnetic characteristics of the storm-time ring current asymmetry, *Science in China D: Earth Science*, 2008,

51(5):686-693

- Wu Ying-Yan, Tschu Kang-Kun, Xu Wen-Yao, Xu Yuan-Fang. Sheshan hundred years data of geomagnetic storms. 1. solar cycle variations. *Chinese J. Geophys.*, 2009, V52(10): 2595-2601
- Xiao, Z., S. G. Xiao, Y. Q. Hao and D. H. Zhang. The morphological features of ionospheric Response to typhoon. *J. Geophys. Res.*, 2007 .
- Xu Wen-Yao, Geng-Xiong Chen, Ai-Min Du, Ying-Yan Wu, Bo Chen, and Xiao-Can Liu. Key points model for polar region currents, *J. Geophys. Res.*, 2008, 113(A3), A03S11
- Xu Wen-Yao. Uncertainty in magnetic activity indices. *Science in China (E)*, 2008, 51(10), 1659-1664
- Xu Wen-Yao, Xia Guo-Hui, An Zhen-Chang, Chen Geng-Xiong, Zhang Feng-Yu, Wang Yue-Hua, Tian Yu-Gang, Wei Zi-Gang, Ma Shi-Zhuang, Chen Hong-Fei. Magnetic survey and ChinaGRF 2000. *Earth Planets Space*, 2003, 55(4):215-217
- Xu Wen-Yao, Henri-Claud Nataf, Aimin Du, Zi-Gang Wei. Thirty-year period in secular variation rate of the main geomagnetic field. *Chinese J. Geophys.*, 2006, 49(5):1210-1219
- Xu Wen-Yao, Du Ai-Min. Effects of the ring current decay rate on the energy state of the magnetosphere. *Chinese J. Geophys.*, 2010, V53(6): 1247-1255
- Xu Wen-Yao. Variations of the auroral electrojet belt during substorms. *Chinese J. Geophys.*, 2009, 52(3): 607-615
- Xu Wen-Yao, Bai Chun-Hua. Role of the African magnetic anomaly in controlling the magnetic configuration and its secular variation. *Chinese J. Geophys.*, 2009, 52(8): 1985-1992
- Xu Wen-Yao, Du Ai-Min, Chen Geng-Xiong. Effect of non-dipole field on VGP estimation *Chinese J. Geophys.*, 2007, 50(5): 1298-1303
- Yang D, He Y, Chen C and Qian J, Vr: A new index to represent the variation rate of geomagnetic activity, *Earth Sci.*, 2010, 23(4): 343-348
- Yu Bo, Liu Yan-Chun, Zhai Guo-Jun, Bian Gang. Analysis of vertical space variation of marine magnetic field. *Chinese J Geophys.*, 2009, 52(1): 169-175
- Zhang Ji-Sheng, Gao Rui, Zeng Ling-Sen, Li Qiu-Sheng, Guan Ye, He Ri-Zheng, Wang Hai-Yan, Lu Zhan-Wu. Relationship between characteristics of gravity and magnetic anomalies and the earthquakes in Longmenshan range and adjacent areas. *Chinese J. Geophys.*, 2009, 52(2):572-578

Zhang S, Yang D, Li Q and Zhao Y . The 1991 and 1999 Jerks in China, *Earthquake Research in China*, 2008, 24(3): 253-260 (in Chinese)

Zhao Xu-Dong, Du Ai-Min, Xu Wen-Yao, Hong Ming-Hua, Liu Li-Bo, Wei Yong, Wang Cheng-Gong. The origin of the prenoon-postnoon asymmetry for Sq current system. *Chinese J. Geophys.*, 2008, 51(3) :643-649

Zhu Gang-Kun, Wu Ying-Yan, Xu Yuan-Fang. Studies on super storms of So-S é hundred-year data. *Chinese J. Geophys.*, 2010, V53(4): 782-786

PROGRESS IN MIDDLE AND UPPER ATMOSPHERIC RESEARCH

HUANG Kaiming and YI, Fan

School of Electronic Information, Wuhan University, Wuhan 430072

Abstract There has been much progress in studying the middle and upper atmosphere in China due to the joint efforts of scientists and engineers. The characteristics of the atmospheric density, temperature and wind have been revealed by the various lidar and radar observations. The seasonal/annual variation patterns of the mesospheric metal layers at 30°N are established based on the simultaneous and common-volume Fe and Na lidar measurements. Theoretical and modeling efforts have given us an insight into the dynamical processes in the middle and upper atmosphere. Many new facilities under construction promise a bright and prosperous future in this field.

I. INTRODUCTION

The middle and upper atmosphere comprises the stratosphere, mesosphere and thermosphere. As an important link in the solar-terrestrial system, it has been attracting a great attention of Chinese scientists. In the past four years, significant progress has been made in understanding the dynamical and photochemical processes in this region. The structure and variation of the middle atmospheric temperature and wind field have been presented. The features of planetary waves, tidal waves and gravity waves, and the nonlinear interactions among these atmospheric waves are clarified based on the observational data and model works. The essential characteristics of the regular and sporadic metal layers, including their seasonal variation, layer borders, and small-time-scale processes, are revealed. Some of them cannot be explained by the current metal layer theory, which calls for further experimental and modeling efforts.

Supported by the Natural National Science Foundation of China and the Meridian Project of China, both the passive and active ground-based facilities for measuring the middle and upper atmosphere have been set up and put into operation, which greatly improve the observational competence for the middle and upper atmosphere in China mainland. Recently new lidars and MF/VHF radars have been put into operation in China, for instance, Fe/Ca resonance fluorescence lidars and Fe Boltzmann lidar in Wuhan, Na fluorescence lidar and mobile Rayleigh/Mie Doppler wind lidars in Hefei, and Na narrowband Doppler lidar in Beijing. Many valuable studies can be conducted by coordinated campaigns of these instruments.

This review summarizes the advances in the middle and upper atmospheric studies in China from 2007 to 2010, with an emphasis on the upper stratosphere, mesosphere and lower thermosphere.

II. INSTRUMENT DEVELOPMENT AND OBSERVATION

Two independent Fe and Na resonance fluorescence lidars were established in Wuhan University. The two lidar systems have the same altitude and time resolutions as well as the identical starting and ending times for each sampling. This allows a detailed comparison between Fe and Na density profiles based on simultaneous and nearly common-volume Fe and Na lidar measurements. It was found that the sporadic Fe and Na layers occurred in overlapping altitude ranges and moved following almost the same track, moreover on occasion, they exactly simultaneously reached their maximum peak densities at nearly the same altitude, which strongly suggest that the sporadic Fe and Na layers are formed via the same or very similar mechanisms [Yi et al., 2007]. The extremely high sporadic Na and Fe layers above 105 km occurred mostly during the summer [Ma and Yi, 2010]. The sporadic Na layer characteristics on small time scale were investigated based on the 8-s resolution lidar measurements. The observation shows that each sporadic Na consists of a sequence of small-timescale density enhancement bursts, which may imply that there exists a very rapid atom removal process corresponding to the dramatic burst density enhancement [Liu and Yi, 2009]. Yi et al. [2009] established the complete seasonal variation patterns of the nocturnal mesospheric

Na and Fe layers at 30°N on the basis of several years of Na and Fe lidar measurements. Both the Na and Fe layer column abundances show strong annual variations as well as moderate semiannual variations with maxima in winter and double minima from late spring to midautumn. The seasonal variation in the Fe abundance is evidently stronger than that of Na. The Na and Fe centroid heights are dominated by semiannual oscillations with similar phases. The mean centroid heights are about 91.4 km for Na and about 88.7 km for Fe. The Na RMS width exhibits a strong semiannual oscillation with the layer slightly broader in winter, whereas the Fe width varies principally annually with a maximum in winter. By analyzing the high-accuracy Fe and Na atom density profiles, Yi et al. [2008] revealed some ubiquitous features of the Fe and Na layer borders. The Fe and Na lower boundaries show consistently a delicate stratification in which the lower boundary of the Fe layer is in general slightly higher than or coincident with that of the Na layer, with an overall mean altitude difference being about 0.2 km. Despite the existence of considerable vertical displacements, the two lower boundaries vary always following almost the same track. The overall correlation coefficient between them is as high as 0.96. This ubiquitous delicate stratification of the measured lower boundaries with nearly coincident density cutoff suggests strongly that the undersides of Fe and Na layers are controlled by the same or very similar processes. The upper boundary of the Na layer is always several kilometers higher than that of the Fe layer and a relatively weak positive correlation is also persistently observed between the two upper boundaries. Both the Fe and Na layers often show an evidently steeper density gradient on the underside than on the upper extent, and the borders of the Fe layer are clearly steeper than those of the Na layer. The explanation to these ubiquitous features needs further experimental and modeling efforts. In addition, the Na lidar with an integration period of 3.2 s have measured Na atom meteor trails, and the relation between the Na meteor trails and the regular and sporadic Na layers was explored [Xie and Yi, 2010].

Based on the data observed by a sodium fluorescence lidar in Hefei, a meteor radar in Wuhan and the FORMOSAT - 3/COSMIC constellation, Dou et al. [2009, 2010] reported the sodium lidar observations of sporadic sodium layers (SSLs) at a mid-latitude location and studied the possible relations between incoming meteors, sporadic E layers, and sporadic (or sudden) sodium atom layers. From a statistical

point of view, a seasonal dependence of SSL observed by the Hefei lidar between December 2005 and November 2008 correlates well with the annual variation of Es and is also consistent with meteor seasonal deposition, except for February and March. It suggests that a meteor - Es - SSL chain could be reasonable if the recombination process were taken into consideration.

By combining three different lidar techniques, i.e., the N₂ vibrational Raman backscatter, the standard Rayleigh scattering method and the Fe Boltzmann technique, simultaneous and complete temperature profiles from near ground to about 100 km over Wuhan are acquired, which are in good agreement with the radiosonde and satellite data, as well as the model results [Yu and Yi, 2008]. A new sodium narrowband Doppler lidar to measure atmospheric temperature in the mesopause region has been developed in China and comparisons between the lidar temperatures and SABER temperatures show good agreement [Hu et al., 2011].

A double edge Mie Doppler lidar was established in Hefei, China in 2005 for low tropospheric wind measurement. The instrument has demonstrated the capability of atmospheric wind field measurement from 0.2 to 5 km altitude with an accuracy of ~2m/s under the condition of 1-min time and 21.2-m range resolutions [Shen et al., 2008]. A mobile Rayleigh Doppler wind lidar based on double-edge technique was also successfully developed [Tang et al., 2010a]. A preliminary observation of stratospheric wind profiles in field operation was conducted and some wind data at altitudes from 10 to 40 km were obtained. The observational results showed a good agreement with the colocated wind profile radar measurements in the low troposphere [Tang et al., 2010b; Dong et al., 2010].

A new mountain-based GPS radio occultation technique for exploring the lower atmospheric refractivity profile is developed in China [Hu et al., 2008]. The inversion errors of the ionosphere GPS radio occultation are investigated by Wu et al. [2009a]. A new correction method for the errors due to the sphere asymmetry has been proposed by Wu et al. [2009b]. The simulation study of the Martian ionosphere radio occultation experiments with a new sat-to-sat link (Chinese YH-1 and Russian Phobos-Grunt) has been completed by Hu et al. [2010].

There has been significant progress for the atmospheric ground-based observations in China, supported by the Meridian Project of China. Both passive and active instruments for the middle and upper atmosphere observations have been set up and put into operation, which include all sky airglow cameras, an FP interferometer, lidars, and a meteor radar [Wang, 2010]

III.DYNAMICS OF THE MIDDLE AND UPPER ATMOSPHERE

Knowledge of the mean wind and temperature is fundamental for studies of atmospheric dynamics since it represents the basic state. The atmospheric waves are the important dynamical processes, which play a crucial role in determining large-scale circulations, thermal states and dynamics of the middle and upper atmosphere.

The TIDI and SABER data aboard satellite TIMED were used to study the global structure and long-term variations of tides [Xu et al., 2009a] and background atmospheric temperature [Xu et al., 2007a]. The tidal damping in MLT region, which is described by equivalent Rayleigh friction (ERF), was studied. The results show that the seasonal variation of the ERF is consistent with the seasonal variation of the zonal mean wind and the maximum ERF generally coincides with the altitudes of strongest wind reversal in the mesopause region [Xu et al., 2009b]. The evidence of the modulations of migrating and non-migrating tides on the airglow emission was given [Gao et al., 2010; Xu et al., 2010] from the similarity between the airglow emission and the temperature distributions observed by TIMED/SABER. The results show that the airglow layers in mesopause region were strongly modulated by tides. The seasonal variations of the global distribution of the mesopause altitude and structure and the modulation by tides were also investigated [Xu, et al., 2007b]. They found that the mesopause structure was obviously modulated by tides. They have studied the nighttime equatorial mass anomaly (NEMA) of the thermospheric density observed by CHAMP [Ma et al., 2010]. They found that the mass density had longitudinal structures with 2, 3, or 4 peaks, depending on season and solar activity. The results show evidence that the NEMA was probably the results of upward propagating migrating and non-migrating tides from the lower atmosphere. The features of the sources of tides

produced by ozone heating in stratosphere have been studied as well [Xu et al., 2010]. Based on the analysis of the satellite observations, an empirical model of the tidal forcing induced by ozone heating was constructed. This model can be used as input for the simulation study on tides. The ground-based observation data were also utilized to study the seasonal variation of tides and planetary waves [Jiang et al., 2008, 2009].

The global distribution of the stationary planetary waves in the lower thermosphere particularly up to 120 km height and to 80° latitude in both hemisphere was newly investigated by Xiao et al., [2009] with the temperature data from SABER instrument on board of TIMED satellite. The global morphologies of stratospheric gravity wave activity, and the influences of the origins and the background winds and the modulation of the planetary waves on the gravity wave activity, are investigated with the temperature data of COSMIC GPS radio occultation in [Xiao et al., 2010].

Xue et al. [2008] used a canonical correlation analysis (CCA) method to investigate the semi-diurnal tidal winds in mesosphere and low thermosphere (MLT) region, observed by the meteor radar at Wuhan. By analyzing the data from the Colorado State University sodium lidar during the 9-day continuous campaign in September 2003, Li et al. [2009] presented the significant short-term tidal variability in both diurnal and semidiurnal tides above 85 km on days 265–268, and proposed that gravity wave/tidal interaction at least was partially responsible for the observed variability. The seasonal and interannual variability of gravity wave (GW) variance in the upper stratosphere (35–50 km) and lower mesosphere (48–63 km) has been studied using 10.5 years of temperature profile results obtained with the Jet Propulsion Laboratory Rayleigh lidar at Mauna Loa Observatory, Hawaii [Li et al., 2010]. Seasonal variability with a maximum in winter and a minimum in summer was observed in the upper stratosphere, suggesting dominance of the annual oscillation. In the lower mesosphere the seasonal oscillations of GW variance were dominated by a semiannual oscillation (SAO), likely due to the selective filtering of GWs by the tropical upper stratospheric SAO wind.

Using the long-term temperature data sets observed by six Rayleigh lidars from low (20°S, 20°N) to middle (34°N, 44°N, and 47°N) and high (67°N) latitudes within the NDACC net-work, Dou et al. [2009] derived the temperature AO and SAO oscillations in the stratosphere and mesosphere. The lidar results were also compared with those derived from the SABER zonal mean temperatures (2002–2008). They found that the AO oscillations dominate the seasonal oscillations in both stratosphere and mesosphere at middle and high latitudes with the amplitudes increasing poleward, while the SAO oscillations are weaker at all six sites. The oscillations in the upper mesosphere are usually stronger than those in the upper stratosphere with a local minimum near 50–65 km. The upper mesospheric signals are clearly out of phase with upper stratospheric signals. All these features of seasonal oscillations are consistent with early observations and model simulations.

By using the data from intensive radiosonde observations over Yichang in August 2006 and January 2007 on an eight-times-daily basis, the characteristics of dynamical and thermal structures and inertial gravity waves in the troposphere and lower stratosphere (TLS) are statistically studied by Zhang et al. [2008]. In the summer month, the mean intrinsic frequency and vertical wavelength of the inertial GWs in the troposphere are still larger than those in the lower stratosphere with the absence of intensive tropospheric jets, suggesting that the Doppler shifting due to the tropospheric jets cannot completely account for the differences between the GWs in the troposphere and lower stratosphere. Compared with the observations in the summer month, GWs in the winter month are more and stronger in the troposphere and less and weaker in the lower stratosphere. In both the summer and winter months, the fitted spectral slopes of the vertical wave number spectra for GWs are generally smaller than the canonical spectral slope of -3 . The correlation analyses suggest that the tropospheric jet induced wind shear is the dominant source for GWs in both the troposphere and lower stratosphere. Huang et al. [2009] further investigate the activity of diurnal tide and planetary waves (PWs) in the troposphere and lower stratosphere over Yichang, moreover, the spectral analyses reveal that some waves with periods around that of the diurnal tide are generated due to the interactions of the diurnal tide and PWs and the tidal amplitudes are modulated by the PWs, indicating the extensive coupling between the diurnal tide

and PWs. The intensive radiosonde observations also show two lower tropospheric inversion layers over Yichang, which is revealed to be closely related to the intensive inertial gravity waves propagating in winter tropospheric jets [Zhang, et al., 2009]. Based on the routine radiosonde observations over 92 United States stations in the Northern Hemisphere, Zhang et al. [2010] reveal the latitudinal and seasonal variations of gravity wave potential energy density, kinetic energy density, and total energy density. The striking differences between GW activity in the troposphere and lower stratosphere are not likely explained only by the background wind Doppler shifting due to strong tropospheric jets, indicating that the region around tropopause, roughly from 10 km to 18 km, is an important source region. The studies strongly suggest that in order to fully understand the global GW activity in the lower atmosphere, the GW kinetic energy and its geographical and seasonal variations should be included, and more attention should be given to GWs in the troposphere and GW sources within the intermediate region, especially the upper troposphere.

In the propagation processes of the atmospheric waves, the various complicated nonlinear phenomena generally occur in the middle and upper atmosphere. The numerical simulation is the most effective method in dealing with the nonlinear problem. Starting from a set of fully nonlinear basic atmospheric kinetic equations, Zhang and Yi [2008] numerically study the response of wave number spectra for atmospheric gravity wave fields to different excitation sources. The simulation results show that only when excited by a localized random momentum source, the horizontal and vertical wave number spectra of the gravity wave fields exhibit a “quasi-universal” spectral structure, indicating that the random characteristic of the source may play an important role in forming a “universal” spectrum. The intermittency and asymmetry of wave sources and a sheared background wind will lead to shallower wave number spectra. Apart from these differences, vertical wave number spectra arising from different sources and background conditions exhibit some conformities. Generally, the spectral slopes for the vertical wind fluctuations are larger (in magnitude) than those for the horizontal wind and temperature fluctuations, and the slopes for the horizontal wind fluctuations are usually slightly smaller than those for the temperature fluctuations. Huang et al. [2008, 2010] research the characteristics of gravity wave propagation in the meridionally and vertically sheared zonal background wind. The

whole processes of gravity wave packet reflection transmission in the meridionally and vertically sheared wind fields are numerically exhibited, and the reflection and transmission coefficients are quantitatively discussed, which will help us to improve the gravity wave drag parameterization of the general circulation models. By developing a GWD parameterization scheme with continuous wave spectrum, Huang et al. [2009] successfully simulate a more realistic equatorial quasi-biennial oscillation. Furthermore, Huang et al. [2007, 2009] numerically investigate the resonant and nonresonant interactions of the gravity waves in the atmosphere, which suggests that this strong nonlinear interaction may be an important factor in determining the atmospheric wave spectrum and play a significant role in the momentum budget well into the thermosphere. A detuning degree of interaction is proposed, which may be applied to measure whether or not the effective energy exchange occurs in the nonlinear interactions of gravity waves.

IV. PHOTOCHEMISTRY OF THE MIDDLE AND UPPER ATMOSPHERE

The first atmospheric gravity wave imaging observations with a new OH* airglow imager in Langfang site (39N,116E) has been made in 2009 [Tu et al., 2010]. Quasi-monochromatic gravity waves (QMGWs) are found clearly in the observation data. Case studies show that their horizontal wavelengths, horizontal phase velocities, azimuth angles of horizontal propagation directions and periods of three QMGW examples are about 12.3 km, 41 m/s, 327°, 5 min; 25 km, 35 m/s, 68°, 12 min; and 10 km, 48 m/s, 341°, 3.5 min respectively.

Based on 5 years of OH imager data between September 2003 and September 2008 over Yucca Ridge Field Station, CO (40.7°N, 104.9°W), Dou et al. [2010] presented the variation of gravity wave (GW) occurrence frequency and propagation direction in the upper mesosphere. In summer the GW occurrence frequency was extremely high at above 95% compared to other seasons (around 85%). The GW propagation direction showed a strong northward (poleward) preference in summer and a southward (equatorward) preference in winter.

VI. DIRECTIONS FOR FUTURE STUDY

Many new observation facilities under construction in China promise great

advances in the studies of the middle and upper atmosphere. Some new lidar systems will help scientists research the physical and chemical processes in the mesopause region, and some new VHF and MF radar systems will enable scientists to probe the wind and waves in the mesosphere and lower thermosphere, to further understand its responses to the various driving forces from the solar activity and anthropogenic perturbations, and to investigate the coupling mechanisms and processes among the different atmospheric layers. With the development in the ground-based observation capability and the theoretical study, Chinese scientists will devote their efforts to establish cause/effect model on space weather events in the middle and upper atmosphere, and to seek their prediction techniques. It is also a scientific objective of Chinese scientists to identify the long-term variations of the middle and upper atmosphere.

References

- Dong, J. H., Cha, H., Kim, D., Baik, S. H., Wang, G. C., Tang, L., Shu, Z. F., Xu, W. J., Hu, D. D. and Sun, D. S. (2010), Doppler Lidar Measurement of Wind in the Stratosphere, *J. Opt. Soc. Korea*, 14: 199-203.
- Dou, X. K., Xue, X. H., Chen, T. D., Wan, W. X., Cheng, X. W., Li, T., Chen, C., Qiu, S. and Chen, Z. Y. (2009), A statistical study of sporadic sodium layer observed by sodium lidar at Hefei (31.8 ° N, 117.3 ° E), *Ann. Geophys.*, 27: 2247–2257.
- Dou, X. K., Li, T., Xu, J. Y., Liu, H. L., Xue, X. H., Wang, S., Leblanc, T., McDermid, I. S., Hauchecorne, A., Keckhut, P., Heinselman, C., Steinbrecht, W., Mlynarczyk, M. G. and Russell, J. M. (2009), Seasonal oscillations of middle atmosphere temperature observed by Rayleigh lidars and their comparisons with TIMED/SABER observations, *J. Geophys. Res.*, 114: doi:10.1029/2008JD011654.
- Dou, X. K., Xue, X. H., Li, T., Chen, T. D., Chen, C. and Qiu, S. C. (2010), Possible Relations between Meteors, Enhanced Electron Density Layers and Sporadic Sodium Layers, *J. Geophys. Res.*, 115: A06311.
- Dou, X. K. and Li, T. (2010), Yihuan Tang, Jia Yue, Takuji Nakaruma, Xianghui Xue, Bifford P. Williams, and Chiao-Yao She, Variability of gravity wave occurrence frequency and propagation direction in the upper mesosphere observed by the OH imager in Northern Colorado, *J. Atoms. Sol. Terres. Phys.*, 72: 457-462.

- Gao, H., Xu, J. and Wu, Q. (2010), Seasonal and QBO Variations in the OH Nightglow Emission Observed by TIMED/SABER, *J. Geophys. Res.*, 115: doi:10.1029/2009JA014641.
- Hu, X., Wu, X., Gong, X., Wang, X. and Xu, Q. (2010), An Emulation Research on the Radio Occultation Exploration of Martian Ionosphere, *Chinese Astronomy and Astrophysics* 34: 100–112.
- Hu, X., Wu, X. C., Gong, X. Y., Xiao, C. Y., Zhang, X. X., Fu, Y., Du, X. Y., Li, H., Fang, Z. Y., Xia, Q., Yang, G. L. and Mao, J. T. (2008), An introduction of mountain-based GPS radio occultation experiments in China. *Adv. Space Res.*, 42: 1723-1729.
- Hu, X., Yan, Z. A., Guo, S. Y., Cheng, Y. Q. and Gong, J. C. (2011), Sodium fluorescence Doppler lidar to measure atmospheric temperature in the mesopause region, *Chinese Sci. Bull.*, 56: 417–423.
- Huang, C. M., Zhang, S. D. and Yi, F. (2009), Intensive radiosonde observations of the diurnal tide and planetary waves in the lower atmosphere over Yichang (111 ° 18 ' E, 30 ° 42 ' N), China, *Ann. Geophys.*, 27: 1079–1095.
- Huang, K. M., Zhang, S. D. and Yi, F. (2010), Reflection and transmission of atmospheric gravity waves in a stably sheared horizontal wind field, *J. Geophys. Res.*, 115, D16103: doi:10.1029/2009JD012687.
- Huang, K. M., Zhang, S. D. and Yi, F. (2009a), Simulation of the equatorial quasi-biennial oscillation based on the parameterization of continuously spectral gravity waves, *Chinese Science Bulletin*, DOI: 10.1007/s11434-008-0409-z.
- Huang, K. M., Zhang, S. D. and Yi, F. (2009b), Gravity wave excitation through resonant interaction in a compressible atmosphere, *Geophys.Res.Lett.*, 36, L01803: doi:10.1029/2008GL035575.
- Huang, K. M., Zhang, S. D. and Yi, F. (2008), Propagation and reflection of gravity waves in a meridionally sheared wind field, *J.Geophys.Res.*, 113, D09106: doi: 10.1029/2007JD008877.
- Huang, K. M., Zhang, S. D. and Yi, F. (2007), A numerical study on nonresonant interactions of gravity waves in a compressible atmosphere, *J.Geophys.Res.*, 112, D11115: doi:10.1029/2006JD007373.
- Jiang, G., Xu, J., Xiong, J., Ma, R., Ning, B., Murayama, Y., Thorsen, D., Gurubaran, S., Vincent, R. A., Reid, I. and Franke, S. J. (2008), A case study of the mesospheric 6.5-day wave observed by radar systems, *J. Geophys. Res.*, 113, D16111: doi:10.1029/2008JD009907.
- Jiang, G., Xu, J. and Franke, S. J. (2009), The 8-h tide in the mesosphere and lower thermosphere over Maui (20.75° N, 156.43°W), *Ann. Geophys.*, 27: 1989–1999.
- Li, T., She, C. -Y., Liu, H. -L., Yue, J., Nakamura, T., Krueger, D. A., Wu, Q., Dou, X. and Wang, S. (2009), Observation of local tidal variability and instability, along with dissipation of diurnal tidal harmonics in the mesopause region over Fort Collins, CO (41°N, 105°W), *J. Geophys. Res.*, 114, D06106: doi:10.1029/2008JD011089.
- Li, T., Leblanc, T., McDermid, I. S., Wu, D. L., Dou, X. and Wang, S. (2010), Seasonal and inter-annual

- variability of gravity wave activity revealed from long-term lidar observations over Mauna Loa Observatory, Hawaii, *J. Geophys. Res.*, 115, D13103: doi:10.1029/2009JD013586.
- Liu, Y. J. and Yi, F. (2009), Behavior of sporadic Na layers on small time scale, *J. Atmos. Sol. Terr. Phys.*, 71: 1374-1382.
- Ma, R., Xu, J., Wang, W., Lei, J., Liu, H.-L., Maute, A. and Hagan, M. E. (2010), Variations of the nighttime thermospheric mass density at low and middle latitudes, *J. Geophys. Res.*, 115: doi:10.1029/2010JA015784.
- Ma, Z. Z. and Yi, F. (2010), High-altitude sporadic metal atom layers observed with Na and Fe lidars at 30°N, *J. Atmos. Sol. Terr. Phys.*, 72: 492-497.
- Shen, F. H., Cha, H., Sun, D. S., et al. (2008), Low tropospheric wind measurement with Mie Doppler lidar, *Opt. Rev.*, 15: 204-209.
- Tang, L., Shu, Z., Dong, J., Wang, G., Wang, Y., Xu, W., Hu, D., Chen, T., Dou, X., Sun, D. and Cha, H. (2010a), Mobile Rayleigh Doppler wind lidar based on double-edge technique, *Chinese Opt. Lett.*, 8: 726-731.
- Tang, L., Wang, Y., Shu, Z., Dong, J., Wang, G., Xu, W., Hu, D., Chen, T., Dou, X., Sun, D. and Cha, H. (2010b), Analysis of Detectors and Transmission Curves Correction of Mobile Rayleigh Doppler Lidar, *Chinese Phys. Lett.*, 27: 1142071-1142074.
- Tu, C., Hu, X., Yan, Z. A., et al. (2010), First imaging observation of the gravity waves in the mesopause region in China, *Chinese Sci. Bull.*, 55: 539-543.
- Wang, C. (2010), New Chains of Space Weather Monitoring Stations in China, *Space Weather*, 8, S08001: doi:10.1029/2010SW000603.
- Wu, X., Hu, X., Gong, X., Zhang, X. and Wang, X. (2009a), An asymmetry correction method for ionospheric radio occultation, *J. Geophys. Res.*, 114, A03304: doi:10.1029/2008JA013025.
- Wu, X., Hu, X., Gong, X., Zhang, X. and Wang, X. (2009b), Analysis of the inversion errors of ionospheric radio occultation, *GPS solutions*, 13: 231-239.
- Xiao, C., Hu, X. and Tian, J. (2009), Global temperature stationary planetary waves extending from 20 to 120 km observed by TIMED/SABER, *J. Geophys. Res.*, 114, D17101: doi:10.1029/2008JD011349.
- Xiao, C. Y. and Hu, X. (2010) Analysis on the Global Morphology of Stratospheric Gravity Wave Activity Deduced from the COSMIC GPS Occultation Profiles. *GPS Solutions*, 14: doi: 10.1007/s10291-009-0146-z.
- Xie, Q. H and Yi, F. (2010), Preliminary lidar observations of Na meteor trails at Wuhan (30.5 degrees N, 114.4 degrees E), China, *Chinese Sci. Bull.*, 55: 2422-2427.
- Xu, J., Smith, A. K., Liu, H.-L., Yuan, W., Wu, Q., Jiang, G., Mlynczak, M. G., M. Russell III, J. and

- Franke, S. J. (2009a), Seasonal and quasi-biennial variations in the migrating diurnal tide observed by Thermosphere, Ionosphere, Mesosphere, Energetics and Dynamics (TIMED), *J. Geophys. Res.*, 114 D13107: doi:10.1029/2008JD011298.
- Xu, J., Smith, A. K., Liu, H.-L., Yuan, W., Wu, Q., Jiang, G., Mlynczak, M. G. and M. Russell III, J. (2009b), Estimation of the equivalent Rayleigh friction in MLT region from the migrating diurnal tides observed by TIMED, *J. Geophys. Res.*, 114: doi:10.1029/2009JD012209.
- Xu, J., Smith, A. K., Yuan, W., Liu, H.-L., Wu, Q., Mlynczak, M. G. and Russell III, J. M. (2007a), Global structure and long-term variations of zonal mean temperature observed by TIMED/SABER, *J. Geophys. Res.*, 112, D24106: doi:10.1029/2007JD008546.
- Xu, J., H.-L. Liu, W. Yuan, A. K. Smith, R. G. Roble, C. J. Mertens, J. M. Russell III, and M. G. Mlynczak (2007b), Mesopause structure from Thermosphere, Ionosphere, Mesosphere, Energetics, and Dynamics (TIMED)/Sounding of the Atmosphere Using Broadband Emission Radiometry (SABER) observations, *J. Geophys. Res.*, 112, D09102: doi:10.1029/2006JD007711.
- Xu, J., Smith, A. K., Jiang, G., Gao, H., Wei, Y., Mlynczak, M. G. and Russell III, J. M. (2010), Strong longitudinal variations in the OH nightglow, *Geophys. Res. Lett.*, 37, L21801, doi:10.1029/2010GL043972.
- Xu, J., Smith, A. K., Jiang, G. and Yuan, W. (2010), Seasonal variation of the Hough modes of the diurnal component of ozone heating evaluated from Aura Microwave Limb Sounder observations, *J. Geophys. Res.*, 115, D10110, doi:10.1029/2009JD013179.
- Xue, H., Wan, W., Xiong, J. and Dou, X. (2008), The characteristics of the semi-diurnal tides in mesosphere/low-thermosphere (MLT) during 2002 at Wuhan (30.6°N, 114.4°E) using Canonical Correlation Analysis technique, *Adv. Space Res.*, 9: 1415-1422.
- Yi, F., Zhang, S. D., Yu, C., He, Y., Yue, X., Huang, C. and Zhou, J. (2007), Simultaneous observations of sporadic Fe and Na layers by two closely collocated resonance fluorescence lidars at Wuhan (30.5 °N, 114.4 °E), China, *J. Geophys. Res.*, 112, D04303: doi:10.1029/2006JD007413.
- Yi, F., Yu, C., Zhang, S. D., Yue, X., He, Y., Huang, C., Zhang, Y. and Huang, K M. (2009), Seasonal variations of the nocturnal mesospheric Na and Fe layers at 30°N, *J. Geophys. Res.*, 114, D01301: doi:10.1029/2008JD010344.
- Yi, F., Zhang S. D., Yue, X., He, Y., Yu, C., Huang, C. and Li, W. (2008), Some ubiquitous features of the mesospheric Fe and Na layer borders from simultaneous and common-volume Fe and Na lidar observations, *J. Geophys. Res.*, 113, A04S91: doi:10.1029/2007JA012632.
- Yu, C. M. and Yi, F. (2008), Atmospheric temperature profiling by joint Raman, Rayleigh and Fe Boltzmann lidar measurements, *J. Atmos. Sol. Terr. Phys.*, 70: 1281– 1288.
- Zhang, S. D., Yi, F., Huang, C. M. and Chen, Z. (2008), Intensive radiosonde observations of gravity

- waves in the lower atmosphere over Yichang (111°18 ' E, 30° 42 ' N), China, *Ann. Geophys.*, 26: 2005–2018.
- Zhang, S. D., Yi, F., Huang, C. M. and Zhou, Q. (2010), Latitudinal and seasonal variations of lower atmospheric inertial gravity wave energy revealed by US radiosonde data, *Ann. Geophys.*, 28: 1065–1074,
- Zhang S. D. and Yi, F. (2008), A numerical study on the response of wave number spectra of atmospheric gravity waves to lower atmospheric forcing, *J. Geophys. Res.*, 113, D02102: doi:10.1029/2007JD008957.
- Zhang, Y. H., Zhang, S. D. and Yi, F. (2009), Intensive radiosonde observations of lower tropospheric inversion layers over Yichang, China, *J. Atmos. Sol. Terres. Phys.*, 71: 180-190.

PROGRESS IN IONOSPHERE RESEARCH

SHI Jiankui¹ and XIAO Zuo²

¹State Key Laboratory of Space Weather, CSSAR, Chinese Academy of Sciences, Beijing 100190,
China

²Peking University, Beijing 100871, China

Abstract The progresses in the ionospheric research in china since last IAGA/IUGG assembly are reported as five divisions: (1) ionospheric properties and models, (2) ionosphere in storm time, (3) ionospheric coupling with atmosphere, (4) ionosphere – magnetosphere coupling, (5) ionospheric response to solar activities. The corresponding papers are given in the reference.

I. INTRODUCTION

Since last IAGA/IUGG assembly, the ionospheric researches in China have made great progresses both in the observation and theoretical study or modeling. All of the researches can be divided into five aspects. In this report, the progress of researches on ionospheric properties and models will be given directly after the introduction, the progress of the researches on ionosphere in storm time will be showed in the third paragraph, then is the progress of the researches on ionospheric coupling with atmosphere, and then is the progress of the researches on ionosphere – magnetosphere coupling, in the last, the progress of the researches on ionospheric response to solar activities are introduced.

II. IONOSPHERIC PROPERTIES AND MODELS

1 Ionospheric properties

A 30-day Incoherent Scatter Radar (ISR) experiment was conducted at Millstone Hill (288.5 °E, 42.6 °N) from Oct.4, to Nov. 4, 2002. The altitude profiles of electron

density N_m , ion and electron temperature T_i and T_e , and line-of-sight velocity during this experiment were processed by Liu et al [2007] to deduce the topside plasma scale height H_m , Vertical Scale Height VSH), Chapman scale height H_m , ion velocity, and the relative altitude gradient of plasma temperature T_p , as well as the F2 layer electron density N_mF2) and height $hmF2$.

GPS L-band scintillations and TEC were recorded at Sanya (18.33°N, 109.52°E) during the period July 2004-July 2005. Automatic recorded raw digital scintillation data are analyzed by Li et al [2007] to obtain the spectral characteristics of irregularities producing ionospheric scintillations and to estimate the correlation between amplitude scintillation and power spectral density.

The spatial correlations of ionospheric day-to-day variability are investigated by Yue et al [2007a] with the statistical analysis on GPS and Incoherent Scatter Radar observations.

Yu et al [2007b] used the data of ionospheric F2-layer peak electron density, N_mF2 , obtained from 22 European stations. The authors used an exponential function to describe the correlation coefficient as a function of spatial distance, then studied the diurnal variation of correlation distance versus universal time for different seasons, geomagnetic and solar activity levels. Yue et al [2007c] used a middle and low latitude ionospheric model to model the relationship between vertical drift velocity and time rate of change of $hmF2$ over the magnetic equator.

Shang et al. (2008), using the data observed at Hainan station, studied the response of Hainan L-band GPS ionospheric scintillations to different strong magnetic storm conditions.

A 10-year (1996-2005) database of measurements of total ion density N_i from the DMSP spacecraft at 09:30LT and 21:30LT has been analyzed by Liu et al [2007] to investigate the yearly variations of global plasma densities in the topside ionosphere at magnetic latitudes from 60°S to 60°N. Zhao et al [2007] use the NASA-JPL global ionospheric maps of TEC, firstly to construct TEC maps in the interval from 1999 to 2005.

Monthly median values of f_0F_2 , h_mF_2 and $M(3000)F_2$ parameters, with hourly time interval resolution for the diurnal variation, obtained with DPS-4 digisonde observations at Hainan (19.4°N, 109.0°E) are used by Zhang et al [2008] to study the low latitude ionospheric variation behavior. B_0 , B_1 parameters deduced from the electron density profiles that are inverted from the ionograms recorded at Hainan, China during a three year period from March 2002 to February 2005 are used by Zhang et al [2007] to study the diurnal and seasonal variation of B_0 , B_1 parameters at low latitude.

Liu [2007a] statistically analyzed the ionospheric scale heights in the lower topside ionosphere based on the electron density N_e and temperature profiles observed from the ISR radar at Arecibo (29.32°E, 18.3°N), Puerto Rico. A ten-year (1996-2005) total ion density N_i measurements from DMSP in the morning and evening (09:30LT and 21:30LT) sectors have been analyzed by Liu et al [2007b] to explore the dependence of plasma densities in the topside ionosphere at middle and low latitudes on the solar activity level.

She et al [2008] calculated the ionospheric Global Electron Content (GEC) from the GPS TEC data along the geographic longitude 120°E during the period of 1996-2004, and investigated the relationship between GEC and 10.7 μ m solar radio flux $F_{10.7}$ and its seasonal dependence with partial correlation analysis. Half-hourly TEC from Faraday rotation measurement in the EST-II satellite and half-hourly f_0F_2 ionosonde data obtained at Wuhan from 1980 to 1990 are analyzed by Xiong et al [2007] to show the seasonal variation of TEC, N_mF_2 and the slab thickness.

Wang et al [2007] investigated the low-latitude ionospheric drift responses to the solar activity index $F_{10.7}$ from drift data obtained in Hainan during March, 2002 to March 2004. A mid- and low-latitude ionospheric theoretical model is used by Yue et al [2008] for the first time to assess the effects of the secular variations of geomagnetic field orientation on ionospheric long-term trends over the past century. In order to improve the spatial resolution of ionospheric virtual height in vertical ionospheric sounding, Zhu et al [2007b] carried out a high precision virtual height

measurement experiment by means of ionospheric echo phase measurement and corresponding data analysis processing arithmetic with modern digital ionosonde. Ding et al [2007a,b] applied a method based on Empirical Orthogonal Function (EOF) analysis to automatically scale the F2-layer parameters obtained from ionograms.

Li et al. (2008a) studied the effects of geomagnetic storm on the ionospheric scintillations by using GPS scintillation data recorded at Sanya Station, the southernmost station in the Chinese longitude region. GPS data (scintillation and TEC) and DMSP data were utilized to show the development of irregularities during 2005 (solar minimum). Li et al. (2008b) investigated the correlation of seasonal/longitudinal variations of PB occurrence, evening EIA, and pre-reversal $E \times B$ drifts on magnetically quiet days during the solar maximum years (2000--2002). Using the data from a multi-instrument network operated in Southeast Asia, Li et al. (2009a) also investigated the development and dynamics of ionospheric plasma bubble irregularity during the super storm of 7-11 November 2004. The dependence of PB occurrence in the evening side ionosphere, with magnetic activity during the period years 2001-2004, was also studied by Li et al. (2009b) based on the TEC observations gathered by ground-based GPS receivers which are located in the equatorial and low-latitude regions in East Asia. Li et al. (2010a) investigated the ionospheric observations from a set of in situ satellites and ground-based GPS (TEC and scintillation) receivers, a VHF radar, and two chains of ionosondes that provide the evolutionary characteristics of equatorial and low-latitude ionospheric irregularities versus longitude during these storm periods. Based on GPS observation, Li et al. (2010b) also statistically studied the occurrence of ionospheric scintillation and irregularity in an Arctic station at Ny-Alesund, Svalbard and an Antarctic station at Larsemann Hills, East Antarctica during 2007--2008.

Using the DPS-4 ionosonde data observed from February 2002 to December 2007, Luo et al. [2010] statistically studied the influence of geomagnetic storm on the ionospheric Spread-F (SF) in Hainan Using the data of (B0, B1) parameters deduced from the electron density profiles that were inverted from the ionograms recorded at Hainan, China during a three year period from March 2002 to February 2005, Zhang et al. (2008) studied the diurnal and seasonal variation of B0, B1) parameters at low latitude. Gong et al (2007), using the DPS-4 ionosonde data observed from February 2002 to December 2007, statistically studied the properties of ionospheric Es in Hainan Region.

Liu et al (2008a) derived the Vertical Scale Height (VSH) in the topside ionosphere from the electron density profiles retrieved from the C/F Ionospheric Radio Occultation (IRO) observations to investigate the local time, seasonal, latitudinal, and longitudinal variations of the VSH. With the data of COSMIC electron density (Ne profiles, TOPEX/Jason TEC, and GPS-TEC, as well as global ionosonde measurements of the F2 layer peak electron density (NmF2), Liu L. et al. (2010) investigated the behaviors of the daytime ionosphere around equinoxes during low Solar Activity (LSA).

More than two years of COSMIC electron density profiles at low solar activities were collected by He et al. (2009) to study the evolution of the Weddell Sea Anomaly (WSA), which appears as an evening enhancement in electron density during local summer.

Zhao et al. (2008b) investigated an event of anomalous enhancement in ionospheric electron content on 28 June 2002 from a network of 70 GPS receivers and a chain of ionosondes distributed around the Asian-Australian sector. Zhao et al. (2009b) studied the ionospheric TEC of the equatorial ionization anomaly (EIA)

with the data of GPS network around the Asian-Australian region during 1996-2004.

Using the data from the DPS-4 digisoude located at the low latitude region Hainan (19.3° N, 109.2° E), Shi et al (2009) make an investigation on properties of ionospheric sporadic E phenomenon in the ionosphere over Hainan region.

Wang et.al (2007a) studied the seasonal variation of ionospheric spread-F which is an important irregularity in the ionosphere using the data from Hainan station in 2003.

Wang et.al (2008) also make statistic study the seasonal variation of ionospheric spread-F using the data from Hainan station in 2003.

Wang et al (2010) made a statistical study on the properties of spread F observed at Hainan station during the declining period of the 23rd solar cycle using the data observed at Hainan station from 2002 to 2007,

Wang et al (2007b) divided the SF into four types and studied the properties of different type of SF, especially the strong range spread-F characteristics observed in Hainan during intense storm time.

Wang et al also (2009) studied the correlations between strong range spread-F and GPS L-Band scintillations observed in Hainan in 2004 using the data from digisoude and scintillation monitor.

With the latitudinal profiles of GPS-TEC around 120E longitude, Zhang et al. (2009a) also studied the variability of the equatorial ionization anomaly, focusing on the analysis of the crest-to-trough TEC ratio (TEC-CTR) which is an important parameter representing the strength of EIA. By analyzing the winter data from DPS-4 in 1996--1998 and 2002, Zhu et al. (2008) compared the diurnal variations of ionospheric F2 layer at Zhongshan (Jun) and Tromsø (Dec). Combining the results of the numerical simulation, the authors analyzed the main physical

processes responsible for the F region ionosphere over Zhongshan and Tromsø Liu et al (2008b) analyzed three low latitude pre-storm enhancement events that occurred on 21 April 2001, 29 May 2003, and 22 September 2001, respectively, in the Asia-Australia sector. Liu et al. (2008c) also investigated the characteristic TEC enhancements during low geomagnetic activities before storms. Using regional and global TEC data, the authors analyzed the low-latitude TEC enhancement events that occurred around longitude 120°E on 10 February 2004, 21 January 2004, and 4 March 2001, respectively.

Monthly median NmF2 data at Okinawa, Yamagawa, Kokubunji, and Wakkanai have been collected by Chen et al. (2008) to investigate the solar activity dependence of the nighttime ionosphere. Chen et al. (2009) also investigated the solar activity dependence of the topside ionosphere with ROCSAT-1 observations.

By collecting the FORMOSAT-3/COSMIC radio occultation measurements, Liu et al. (2009a) investigated the seasonal behaviors of daytime ionospheric electron density (Ne) in the altitude range of 200-560km. With 11 years' (1998--2008) worth of GPS-TEC data derived at the JPL, Liu et al. (2009b) also investigated the overall climatological features of the ionosphere in a new way. The global ionospheric maps (GIM) of JPL TEC were averaged globally and over low-, mid-, and high-latitude ranges in the southern (northern) hemisphere and both hemispheres to identify their capability of capturing the overall features of the ionosphere.

Liu and Chen (2009) analyzed the data series of GPS-TEC to investigate the solar activity effects of TEC on a global scale. The daily values of the solar extreme ultraviolet (EUV) fluxes in 0.1–50 nm wavelengths, 10.7 cm radio flux F10.7, and F10.7P (the average of daily F10.7 and its 81-day mean F107A) were adopted to represent the solar EUV variability, respectively.

Based on the data observed at 11 ionosonde stations in the East Asia/Australia sector during 1969-1980, Ma et al. (2009) analyzed the characteristics of the quasi-27-day variations of daytime NmF2 and the relation between NmF2 and the solar activity index F10.7.

2. Ionospheric Modeling and prediction

Yue et al [2008] develop a middle and low latitude theoretical ionospheric model (TIME-IGGCAS) to solve the equations of mass continuity, motion and energy of electron and ions self-consistently and uses an eccentric dipole field approximation to the Earth's magnetic field.

Hu et al [2007] compare the Global Ionospheric Scintillation Model (GISM) predictions with observations over Hainan region by using a one-year database.

Wang et al (2010) using the data from low latitude stations to studied the parameter B2bot for the NeQuick model during high solar activity at Hainan station.

By using an Ensemble Kalman Filter (EnKF) technique, Yue et al [2007d] performed the calculation which assimilated the electron densities during 25-28 September 2000 observed by the Millstone Hill Incoherent Scatter Radar (ISR) into a one-dimensional mid-latitude ionospheric theoretical mode.

A climatology model of TEC over China has been developed by Mao et al [2007, 2008] on the basis of the Empirical Orthogonal Function (EOF) analysis and Kriging method using GPS data from the IGS and CMONOC covering almost the whole Chinese sector during 1996-2004.

Liu C et al [2007] also use the EOF analysis, combined with a regression analysis, to construct an empirical model for the ionospheric propagation factor M(3000)F2.

Liu et al [2008] also proposed CRI based Kriging method has for reconstruction of the ionospheric f0F2 in China region.

The relationship of daily accumulated cycle slip occurrence with the season is analyzed by Zhang et al [2007] using the GPS data observed in six GPS stations located in China low latitude region in 2001.

Ren et al. (2008) deduced a theoretical electric field model for ionospheric dynamo at mid- and low-latitude which adopt a modified magnetic apex coordinates system. Ren et al. (2009c) introduced a new theoretical ionospheric model: the Global Coupled Ionosphere– Thermosphere- Electroynamics Model developed at Institute of Geology and Geophysics, Chinese Academy of Sciences.

A middle and low latitude ionospheric model was used by Yue et al (2008) to model the relationship between $E \times B$ vertical drift velocity and time rate of change of hmF2 ($\Delta hmF2/\Delta t$) over the magnetic equator. F10.7 is chosen to be equal to 100, 150, and 200 to represent low, middle, and high solar activities, respectively,

An Empirical Orthogonal Function (EOF) analysis, combined with a regression analysis, was conducted by Liu C. et al [2008] to construct an empirical model for the ionospheric propagation factor M(3000)F2. An algorithm has been developed by Zhang et al. (2009) to derive the ionospheric TEC and to estimate the resulting instrumental biases in GPS data from measurements made with a single receiver. Zhang et al. (2009b) set up an empirical global model of the ionospheric F2 peak height.

She et al (2008) calculated the ionospheric Global Electron Content (GEC) from the GPS TEC data along the geographic longitude 120 E during the period of

1996--2004, and investigated the relationship between GEC and 10.7cm solar radio flux and its seasonal dependence with partial correlation analysis.

Yue et al. (2010) constructed an ionospheric data assimilation system based on Gauss-Markov Kalman filter and give some test results. The ionosphere stations are chosen to be located in China including the Meridional Project ionosondes, the Lithosphere deformation GPS network, and a part of IGS stations.

Based on the China Reference Ionospher (CRI), Liu et al. (2008) proposed a method (Kriging) for reconstruction of ionospheric foF2 in China region.

Wang et al. (2009) investigated the low-latitude ionospheric variations and comparisons with the International Reference Ionosphere (IRI) model predictions. The data used for the present study covers the period from February 2002 to April 2007, which is characterized by a wide range of solar activity, ranging from high solar activity (2002) to low solar activity (2007).

Huang et al. (2009) discussed the accuracy of the model to see if there is regional restriction by comparing the actual observation data of spread-F occurrence at African sectors with prediction made from this model.

Using the GPS Cycle Slip (CS) data detected from the observation of six GPS stations in 2001 over the China low-latitude region, Zhang et al. (2010) analyzed the temporal dependence of CS occurrence during solar active year.

Shi et al (2008) established a physical model for the existence of bipolar structures in the electric field that are parallel to the magnetic field and observed in the auroral ionosphere by deriving the "Sagdeev potential" from the two-fluid equations in a cylindrical coordinate system.

Shi et.al. (2009) made a theoretical study on density distribution of He⁺ ions

originating from the polar region and up-flowing to the magnetosphere along the magnetic field line during quiet and weakly disturbed geomagnetic conditions.

III. IONOSPHERE IN STORM TIME

Using 8-year Global Ionosphere Maps (GIMs) of TEC products from the Jet Propulsion Laboratory (JPL), Zhao et al [2007] make a statistical study on the morphology of the global ionospheric behaviors with respect to the geomagnetic disturbances.

The global Traveling Ionospheric Disturbances (TIDs) during the drastic magnetic storms of October 29--31, 2003 were analyzed by Wang et al [2007] using also the GPS TEC data observed in the Asian-Australian, European and North American sectors.

From the measurements by the accelerometer on board CHAMP during the severe geomagnetic storm occurring on November 20-21, 2003, Zhou et al [2007] calculated and analyzed the global distribution of the storm-time changes in thermospheric total mass density at about 400 km height. The mutual relations of the storm-time changes with the global integrated Joule heating power produced by large convective electric field, as well as with the ring current index of SYM-H are investigated.

Based on a large data base from 15 ionosonde stations and 36 GPS stations combining with TEC data measured from the Oceanic satellite Jason-1, a case study is made by Zhu et al [2007] on the ionospheric responses at Western Pacific area to the magnetic storm triggered by coronal hole high-speed streams during 13-17 April 2006.

With the observed critical frequencies of F2 layer at Kokubunji (139.5°E, 35.5°N) during 1959 to 2004, Zhan et al [2007] statistically investigated the dependence of the variations of NmF2 on the geomagnetic activity, solar activity, season and local time.

Wang et al [2008] investigated the responses of low-latitude f0F2 to geomagnetic activities during 2002-2005. Le et al [2007] investigated the solar flare effects of the ionosphere at middle latitude with a 1-D ionosphere theoretical model. The measurements of solar irradiance from the SOHO/Solar EUV Monitor (SEM) and GOES satellites have been used to construct a simple time-dependent solar flare spectrum model. Zhao et al. (2008a) investigated the ionospheric disturbances in Southeast Asian region during the super magnetic storm of 20--22 November 2003.

Zhao et al. (2009a) presented an investigation of geomagnetic storm effects in the equatorial and mid-low latitude F-region in the West Pacific sector during the intense geomagnetic storm on 13--17 April, 2006.

On the basis of the f0F2 data observed at 4 ionosonde stations in the East-Asian sector during, Gao et al. (2008) statistically studied 515 geomagnetic storms from 1957 to 2006. They analyzed the types, the onset times and the time delay of the ionospheric storms, and then revealed the distribution of ionospheric responses to storms related to geomagnetic latitude, season and local time.

Using the 10-year Global Ionosphere Maps (GIMs) of Total Electron Content (TEC) retrieved at Jet Propulsion Laboratory (JPL), Liu J. et al. (2010) conducted a statistical study of the time delay of the ionospheric responses to geomagnetic disturbances.

Ding et al. (2008) plotted two-dimensional TEC perturbation maps and investigated the statistical characteristics of Large-Scale Traveling Ionospheric Disturbances (LSTIDs) during the major magnetic storms occurred during 2003 to 2005.

IV. IONOSPHERIC COUPLING WITH ATMOSPHERE

Xiao et al [2007] collected complete records of 24 strong typhoons from 1987 to 1992 and compare them with corresponding ionospheric HF Doppler shift data. On the basis of the statistical analyses, the authors reveal the common features of ionospheric responses to typhoon. In order to study the filter effect of the background winds on the propagation of gravity waves, a three dimensional transfer function model is developed by Sun et al [2007a,b] on the basis of the complex dispersion relation of internal gravity waves in a stratified dissipative atmosphere with background winds.

Xu [2008] reports a study on the relationship between ionospheric TEC over East Asia and the tropospheric circulation around the Qinghai-Tibet Plateau. Ionospheric TEC over East Asia are obtained from 25 observatories during 1996-2004.

Based on the DMSP F13 Satellite observations from 1995 to 2005, Ren et al [2008] examined the longitudinal distributions of the electron temperature and total ion density in the sunset equatorial topside ionosphere.

The Global Ionospheric Maps (GIMs) produced by JPL are used by Wan et al [2008] to investigate the longitudinal structure of the low latitude ionosphere.

Ren et al. (2009a) studied the intra-annual variation of the WN4 structure in the equatorial vertical $E \times B$ drifts at high solar flux level based on of the ROCSAT-1 observations during the interval from 1999 to 2004. On the basis of the measurements from the ion drift meter on the DMSP F13 Satellite from 2000 to 2002, Ren et al. (2009b) also examined the relative longitudinal variations of $E \times B$ vertical plasma drifts in the pre-sunset equatorial topside ionosphere at 17:45LT. Using the TIDM-IGGCAS model and the DE3 TIDI/TIMED tidal wind observations, Ren et al. (2010) simulated the WN4 longitudinal structure in equatorial vertical $E \times B$ plasma drifts.

Zuo and Wan (2008) studied the relationship between quasi 6-day oscillations of planetary wave (PW) and Es occurrence observed at Wuhan, China (30.6°N, 114.5°E).

The 6.5-day planetary waves over Wuhan were investigated by Jiang et al. [2008] on the basis of the meteor radar measurements within 78-98 km height region during February 2002 to December 2005.

With GPS-TEC data from the International GNSS Services (IGS), Wang et al. [2009] analyzed the medium scale traveling ionospheric disturbances (MSTIDs) which were generated by the moving Solar Terminator (ST) during the quiet days in 2005.

Xiao et al (2009) provided observational phenomena which show a close relation between acoustic-gravity waves (AGWs) and blurred traces of HF Doppler shifts. This relationship is regarded as observational evidence of a close connection of AGWs with mid-latitude spread F (MSF), analyzed with six years of HF Doppler records.

On 12 May 2008 at 0628 UT a major earthquake $M_s = 8.0$ struck Wenchuan County (31.0°N, 103.4°E) in southwest China. Zhao et al. (2008c) investigated the ionospheric effects associated with this major earthquake.

V. IONOSPHERE - MAGNETOSPHERE COUPLING

Dang et al [2007] draw out for the first time the morphologic features of quiet-time ionospheric O⁺ ion upflowing at altitudes from 2000 to 4000 km.

Starting from the Boltzmann equation and with some reasonable assumptions, Cai et al [2008] derived a 1-D transport equation of charged energetic particles by

taking account of major interactions with neutral species in the upper atmosphere, including the processes of elastic scattering, the excitation, the ionization and the secondary electron production. The transport equation is numerically solved for a simplified atmosphere consisting only of nitrogen molecules N_2 and to obtain the electron fluxes as a function of altitude, energy and pitch angle. Cai et al [2007b] investigated the climatological features of the polar F2-region electron density N_m by using long-term EISCAT and ESR observations during periods of quiet to moderate geomagnetic activity.

Guo et.al. (2007) made a statistical study on the properties of ions (O^+ , He^+ and H^+) measured by the Cluster-II in cusp region as a function of the solar wind dynamic pressure and geomagnetic index . Guo et.al. (2008) also studied the dipole tilt angle effect on the latitude of the mid-altitude cusp.

Zhang et al [2008] present features of two typical strong FTEs which were simultaneous conjugatively observed by Cluster and Super-DRAN radar on 1 April 2004. Cai and Ma [2007a] suggest a principle and method to estimate auroral precipitating particle energy spectra from electron density observations of ground-based radar. In the energy range of 4-30,keV.

Convection data from Super-DARN radars in the northern hemisphere are utilized by Xu et al [2007] to investigate the response of high-latitude ionospheric convection during a southward IMF turning event, focused on the response timescale.

An unusually long lasting multiple penetration of interplanetary electric field to equatorial ionosphere under oscillating IMF B_z was investigated by Wei et al [2008] During November 11-16, 2003.

With observations of the Interplanetary Electric Field (IEF), solar wind pressure obtained from the Wind satellite, and the geomagnetic field on four magnetometers from high latitudes to magnetic equator, Yuan and Deng [2007a] presented an event of a long-lasting penetration of the IEF into the dayside equatorial ionosphere during the main phase of a magnetic storm on April 17, 1999.

By using the network GPS data, Yuan et al [2007b] studied the ionospheric response of the three isolated substorms occurred during April 28-29, 2001.

With geomagnetic measurements on board of CHAMP satellite, Wang et al [2007a] investigated the characteristics of global large-scale Field-Aligned Currents (FACs) in the topside ionosphere along with their responses to interplanetary conditions for the superstorm of November, 2003. Based on 2760 well-defined substorm onsets in the northern hemisphere and 1432 in the southern hemisphere observed by the FUV (Far Ultraviolet) Imager on board IMAGE (Imager for Magnetosphere-to-Aurora Global Exploration) spacecraft, Wang et al [2007b] performed a statistical study of the seasonal-longitudinal variation of substorm occurrence for both hemispheres.

Cheng et.al. studied the FAC with polar ionospheric AE index by analysis the observation data when the Cluster satellites crossed the plasma sheet boundary layer (PSBL) in the magnetotail during the two magnetic storms in August to October 2001.

Shi et.al. (2009, 2010) investigated the features of FAC connecting the ionosphere and magnetosphere in plasma sheet boundary layers using the data measured with Cluster in 2001 and FAC distribution in the plasma sheet boundary layers in the magnetotail which has north-south asymmetry not only in the magnetotail, but also in the ionosphere.

VI. IONOSPHERIC RESPONSE TO SOLAR ACTIVITIES

The longest total solar eclipse of this century occurred in East and South Asia on 22 July 2009. Using TEC data from 60 GPS stations, Ding et al. (2010) constructed differential TEC maps to investigate the ionosphere response to this solar eclipse in Central China.

Le et al. (2008a) studied a total eclipse which occurred on 11 August 1999 with its path of totality passing over central Europe in the latitude range 40°N. The ionospheric responses to this eclipse were measured by a wide ionosonde network. On the basis of the measurements of f₀E, f₀F₁, and f₀F₂ at sixteen ionosonde stations in Europe, the authors statistically analyzed the variations of these parameters with a function of eclipse magnitude. Based on the data derived from 23 ionosonde stations, Le et al. [2008b] conducted a statistical analysis on the changes in f₀F₂ during seven eclipse events. To model eclipse effects on the ionosphere, the authors constructed a solar spectrum model for solar eclipses. By using the ionosonde observations during 15 eclipse events from 1973 to 2006 and the GPS TEC observations during six solar eclipse events from 1999 to 2006, Le et al. (2009a) also analyzed statistically the latitudinal dependence of NmF₂ and TEC responses to solar eclipses. Le et al. (2009b) investigated the ionospheric behavior in conjugate hemispheres during the 3 October 2005 solar eclipse, on the basis of observations of electron temperature (T_e) from the DMSP spacecraft, f₀F₂ and hmF₂ at the Grahamstown ionosonde station, and TEC from the GPS station SUTH.

REFERENCES

- Cai H T, Ma S Y. (2007a), Initial study of inversion method for estimating energy spectra of auroral particle from ground-based IS radar observations. *Chin. J. Geophys.*, 50(1):10-17.
- Cai H T, Ma S Y, Yin F, Liu Y C, Schlegel K. (2007b), Climatologic features of electron density in the polar ionosphere from long-term observations of EISCAT/ ESR radar. *Ann. Geophys.*, 50(12):2561-2569.
- Cai H, Ma S, Pu Z. (2008), Numerical study of the auroral particle transport in the polar upper atmosphere. *Sci. China-E.*
- Gao Q, et.al. (2008). Statistical study of the storm effects in middle and low latitude ionosphere in the East-Asian sector. *Chin. J. Geophys.*, 51(3):626-634
- Chen Y, Liu L, Le H. (2008), Solar activity variations of nighttime ionospheric peak electron density. *J. Geophys. Res.*, 113, A11306, doi:10.1029/2008JA013114.

- Chen Y, Liu L, Wan W, Yue X, Su S Y. (2009), Solar activity dependence of the topside ionosphere in low latitudes. *J. Geophys. Res.*, 114, A08306, doi:10.1029/2008JA013957
- Cheng Zhengwei, et.al. (2008), Relationship between FAC at plasma sheet boundary layers and AE index during storms from August to October, 2001. *Sci China Ser E-Tech Sci. Jul. 2008 Vol.51 no. 7* pp 842-848.
- Dang G, Ma S Y, Zhou Y L. (2007), Morphology of polar ionospheric O⁺ ion upflow FAST observations during quiet time. *Chin. Sci. Bull.*, (24):3403-3415.
- Ding F, et.al. (2008), A statistical study of large scale traveling ionospheric disturbances observed by GPS TEC during major magnetic storms over the years 2003-2005. *J. Geophys. Res.*, 113, A00A01, doi:10.1029/2008JA013037
- Ding F, Wan W, Ning B, et al. (2010), GPS TEC response to the 22 July 2009 total solar eclipse in East Asia. *J. Geophys. Res.*, 115.
- Ding Z, Ning B, Wan W, Liu L. (2007a), Automatic scaling of F2-layer parameters from ionograms based on the empirical orthogonal function (EOF) analysis of ionospheric electron density. *Earth Planet Space*, 59(1):51-58.
- Ding Z, Ning B, Wan W. (2007b), Real-time automatic scaling and analysis of ionospheric ionogram parameters. *Chin. J. Geophys.*, 50(4):969-978.
- Gong Y, Shi J K, Wang G J. (2007), Properties of ionospheric Es in Hainan Region, *Chinese Journal of Spacer Science*, 27(3), 198-203
- Guo J G, Shi J K, Zhang T L, et al. (2007) The correlations of ions density with geomagnetic activity and solar dynamic pressure in cusp region. *Chinese Science Bulletin*, 52(7):967-971.
- Guo J. G, Shi Jian-Kui, ZHANG Tie-Long, LIU Zhen-Xing. (2008), Interhemispheric Comparison of Dipole Tilt Angle Effects on Latitude of Mid-Altitude Cusp. *CHIN.PHYS.LETT.* Vol. 25, No. 5 1916-1918.
- He M, et.al., (2009), A study of the Weddell Sea Anomaly observed by FORMOSAT-3/COSMIC. *J. Geophys. Res.*, 114, doi:10.1029/2009JA014175
- Hu L, Ning B, Li G. (2007), Comparison between GISM predictions and ionospheric scintillation measurements over Hainan region. *Chin. J. Space Sci.*, 27(5): 384-390.
- Huang W, Xiao S, Xiao Z, Zhang D, Hao Y. (2009), Comparison study of IRI-2007 spread-F occurrence predictions and observations. *Chin. J. Space Sci.*, 29(3): 275-280
- Jiang G, et.al. (2008), Observation of 6.5-day waves in the MLT region over Wuhan. *J. Atmos. Solar-Terr. Phys.*, 70(1):41-48
- Le H, et.al. (2007), Model responses of middle latitude ionosphere to solar flares. *J. Atmos. Solar-Terr. Phys.*, 69(13):1587-1598.

- Le H, et.al. (2008a), The ionospheric responses to the 11 August 1999 solar eclipse: Observations and modeling. *Ann. Geophys.*, 26(1):107-116
- Le H, et al. (2008b). The mid-latitude F2 region during solar eclipses: observations and modeling. *J. Geophys. Res.*, 113, A08309, doi:10.1029/2007JA013012
- Le H, et.al. (2009a). Latitudinal dependence of the ionospheric response to solar eclipses. *J. Geophys. Res.*, 114, A07308, doi:10.1029/2009JA014072
- Le H, et al. (2009b), The ionospheric behavior in conjugate hemispheres during the 3 October 2005 solar eclipse. *Ann. Geophys.*, 27(1):179–184.
- Li G, et al. (2008a), Effects of geomagnetic storm on GPS ionospheric scintillations at Sanya. *J. Atmos. Solar-Terr. Phys.*, 70(7): 1034-1045.
- Li G, et al. (2008b), Correlative study of plasma bubbles, evening equatorial ionization anomaly and equatorial pre-reversal E×B drifts at solar maximum. *Radio Sci.*, 43, RS4005, doi:10.1029/2007RS003760
- Li G, et al. (2009a), Characterizing the 10 November 2004 storm-time middle latitude plasma bubble event in Southeast Asia using multi-instrument observations. *J. Geophys. Res.*, 114, A07304, doi:10.1029/2009JA014057
- Li G., et al. (2009b), Effect of magnetic activity on plasma bubbles over equatorial and low-latitude regions in East Asia, *Ann. Geophys.*, 27(1), 303-312.
- Li G, et al. (2010a), Longitudinal development of low-latitude ionospheric irregularities during the geomagnetic storms of July 2004. *J. Geophys. Res.*, 115, A04304, doi:10.1029/2009JA014830
- Li G, et al. (2010b), Statistics of GPS ionospheric scintillation and irregularities over polar regions at solar minimum. *GPS Solut*, doi 10.1007/s10291-009-0156-x
- Liu C, Zhang M L, Wan W, Liu L, Ning B. (2007), Modeling M(3000)F2 based on Empirical Orthogonal Function analysis method. *Radio Sci.*, 42, doi: 10.1029/2007RS003694
- Liu C, et al. (2008), Modeling M(3000)F2 based on empirical orthogonal function analysis method. *Radio Sci.*, 43, RS1003, doi:10.1029/2007RS003694
- Liu J, Zhao B, Liu L. (2010), Time delay and duration of ionospheric total electron content responses to geomagnetic disturbances. *Ann. Geophys.*, 28, 795–805
- Li G, Ning B, Yuan H. (2007), Analysis of ionospheric scintillation spectra and TEC in the Chinese low latitude region. *Earth Planets Space*, 59(4):279-285.
- Liu L et al. (2007a), Variations of topside ionospheric scale heights over Millstone Hill during the 30-day incoherent scatter radar experiment. *Ann. Geophys.*, 25:2019-027.
- Liu L, et al. (2007b), Yearly variations of global plasma densities in the topside ionosphere at middle and low latitudes. *J. Geophys. Res.*, 112, A07303, doi:10.1029/2007JA012283.

- Liu L, et al. (2007c), An analysis of the scale heights in the lower topside ionosphere based on the Arecibo incoherent scatter radar measurements. *J. Geophys. Res.*, 112, A06307, doi:10.1029/2007JA012250.
- Liu L, et al. (2007d), The dependence of plasma density in the topside ionosphere on solar activity level. *Ann. Geophys.*, 25(6):1337-1343.
- Liu L, et al. (2008a), Topside ionospheric scale heights retrieved from Constellation Observing System for Meteorology, Ionosphere, and Climate radio occultation measurements. *J. Geophys. Res.*, 113, A10304, doi:10.1029/2008JA013490
- Liu L, et al. (2008b), Prestorm enhancements in NmF2 and total electron content at low latitudes. *J. Geophys. Res.*, 113, A02311, doi:10.1029/2007JA012832.
- Liu L, et al. (2008c), Case study on total electron content enhancements at low latitudes during low geomagnetic activities before the storms. *Ann. Geophys.*, 26(4):893-903.
- Liu L, et al. (2009a), Seasonal variations of the ionospheric electron densities retrieved from constellation observing system for meteorology, ionosphere, and climate mission radio occultation measurements. *J. Geophys. Res.*, 114, A02302, doi:10.1029/2008JA013819
- Liu L, et al. (2009b), Climatology of the mean TEC derived from GPS Global Ionospheric Maps. *J. Geophys. Res.*, 114, A06308, doi:10.1029/2009JA014244
- Liu L, Chen Y. (2009), Statistical analysis on the solar activity variations of the TEC derived at JPL from global GPS observations. *J. Geophys. Res.*, 2009, 114, doi:10.1029/2009JA014533
- Liu L, He M, Yue X, Ning B, Wan W. 2010. The ionosphere around equinoxes during low solar activity. *J. Geophys. Res.*, 115, in press
- Liu R Y, et al. (2008), Ionospheric f0F2 reconstruction and its application to the short-term forecasting in China region. *Chin. J. Geophys.*, 51 (2):300-306
- Liu R, Liu G, Wu J, Zhang B, Huang J, Hu H, Xu Z. (2008), Ionospheric f0F2 reconstruction and its application to the short-term forecasting in china region. *Chin. J. Geophys.*, 2008, 51(2):8-14.
- Luo Z, Shi J, Gao T, Wang G, Shang S, Wang X, Fang H, Wang Z, Zherebtsov G A. (2010), Influence of the storm on the ionospheric Spread-F in Hainan region. *Chin. J. Space Sci.*, 30(1): 23-28
- Ma R, Xu J, Yuan W, Jiang G, Liu X. (2009), Quasi-27-day variations of ionospheric NmF2. *Chin. J. Space Sci.*, 29(4):368-376
- Mao T, Wan W, Sun L. (2007), Central and northern China TEC map using the Kriging method. *Chin. J. Space Sci.*, 27(4):279-285.
- Mao T, Wan W, Yue X, Sun L, Zhao B, Guo J. (2008), An empirical orthogonal function model of total electron content over China. *Radio Sci.*, 43, RS2009, doi:10.1029/2007RS003629
- Ren Z et al. (2008), Longitudinal variations of electron temperature and total ion density in the sunset

- equatorial topside ionosphere. *Geophys. Res. Lett.*, 35, L05108, doi:10.1029/2007GL032998.
- Ren Z, et al. (2008),. A theoretical model for mid- and low-latitude ionospheric electric fields in realistic geomagnetic fields. *Chin. Sci. Bull.*, 53(24):3883-3890
- Ren Z, et al. (2009a), Intra-annual variation of wavenumber-4 structure of vertical $E \times B$ drifts in the equatorial ionosphere seen from ROCSAT-1. *J. Geophys. Res.*, 114, A05308, doi:10.1029/2009JA014060
- Ren Z, et al. (2009b), Influences of geomagnetic fields on longitudinal variations of vertical plasma drifts in the presunset equatorial topside ionosphere. *J. Geophys. Res.*, 114, A03305, doi:10.1029/2008JA013675. doi:10.1016/j.jastp.2009.09.015
- Ren Z, et al. (2009c), GCITEM-IGGCAS: A new global coupled ionosphere-thermosphere-electrodynamics model. *J. Atmos. Solar-Terr. Phys.*, 71: 2064–2076
- Ren Z, et al. (2010), Simulated wave number 4 structure in equatorial F-region vertical plasma drifts. *J. Geophys. Res.*, 115, A05301, doi:10.1029/2009JA014746
- Shang S P, J K Shi, et al. (2008), Response of Hainan GPS ionospheric scintillations to the different strong magnetic storm conditions. *Advances in Space Research* 41 579–586.
- She C, Wan W, Xu G. (2008), Climatological analysis and modeling of the ionospheric global electron content. *Chin. Sci. Bull.*, 53(2):282-288.
- She C, Wan W, Xu G. (2008), Climatological analysis and modeling of the ionospheric global electron content. *Chin. Sci. Bull.*, 53(2):282-288
- Shi J K, and Wang G J. (2009), An Investigation on Properties of Ionospheric Es in Hainan Region, *Progress in electron-magnetism research*. 2009
- Shi J. K. et.al. (2008), An interpretation for the bipolar electric field structures parallel to the magnetic field observed in the auroral ionosphere. *Ann. Geophys.*, 26, 1431–1437, 2008.
- Shi J. K. et.al. (2009), Zhengwei Cheng, T.L. Zhang, M. Dunlop, Zhenxing Liu, Properties of field aligned current in the plasma sheet boundary layers in the magnetotail: Cluster observation, *Chin. Phys.Lett.*, (2009), 26(2): 029401
- Shi J K, et.al. (2010), South-north asymmetry of field-aligned currents in the magnetotail observed by Cluster, *J. Geophys. Res.*, 2010, 115, A07228, doi:10.1029/2009JA014446.
- Shi J. K. et al. (2009), The Ionospheric Up-flowing He⁺ Ion Distribution in the Magnetosphere, *Journal of Atmospheric and Solar-Terrestrial Physics*, DOI information: 10.1016/j.jastp. 71, 1630-1635.
- Sun L F, Wan W, Ding F, Mao T. (2007a), Gravity waves propagation in the realistic atmosphere based on a three-dimensional transfer function model. *Ann. Geophys.*, 25:1979-1986.
- Sun L F, Wan W, Ding F, Mao T. (2007b), Study of internal gravity waves propagation on the basis of the three-dimensional transfer function model. *Chin. J. Space Sci.*, 7(3):211-217.

- Wan W et al. (2008), Wavenumber-4 patterns of the total electron content over the low latitude ionosphere. *Geophys. Res. Lett.*
- Wan W, et al. (2008), Wavenumber-4 patterns of total electron content over the low latitude ionosphere. *Geophys. Res. Lett.*, 35, L12104, doi:10.1029/2008GL033755
- Wang G J, J K Shi, et al. (2008). Seasonal variation of spread-F observed in Hainan. *Advances in Space Research* 41 639–644.
- Wang G J, Shi J K, et al.. (2009), Correlations between Strong Range Spread-F and GPS L-Band Scintillations Observed in Hainan in 2004, *CHIN. PHYS. LETT.* Vol. 26, No. 1 019401.
- Wang G J, J K Shi, X Wang, S P Shang, G Zherebtsov, and O M Pirog. (2010), The statistical properties of spread F observed at Hainan station during the declining period of the 23rd solar cycle, *Ann. Geophys.*, 28, 1263–1271, doi:10.5194/angeo-28-1263-2010
- Wang G J, Shi J K, et al. (2007a), Seasonal variation of ionospheric spread-F observed in Hainan. *Chinese Journal of Radio Science*, 22(4), 583-588.
- Wang G J, Shi J K, et al. (2007b), Strong Range spread-F Characteristics observed in Hainan during intense storm. *Chinese Journal of Space Science*, 27 (5), 379-383
- Wang H, Ma S Y, Luehr H, Zhou Y L. (2007a), Field-aligned current distribution and response to interplanetary conditions during a superstorm-CHAMP observation. *Chin. Sci. Bull.*, 52(2):238-247.
- Wang H, Luehr H. (2007b), Seasonal-longitudinal variation of substorm occurrence frequency: Evidence for ionospheric control. *Geophys. Res. Lett.*, 34, L07104, doi:10.1029/2007GL029423
- Wang M, et al. (2007), Monitoring global traveling ionospheric disturbances using the worldwide iGPS network during the October 2003 storms. *Earth Planets Space*, 59:407-419.
- Wang M, Ding F, Wan W, Ning B, Chen Y. (2009), GPS observations of TID events generated by the moving solar terminator. *Geophys.*, 52(5):1146-1155
- Wang M, Ding F, Wan W, Ning B, Chen Y. (2009), GPS observations of TID events generated by the moving solar terminator. *Geophys.*, 52(5):1146-1155
- Wang S G, J K Shi, X Wang, G J Wang. (2010), Validation of B2bot in the NeQuick model during high solar activity at Hainan station, *Advances in Space Research*, 46, 1096-1101.
- Wang X, Shi J K, Wang G J, Gong Y. (2009), Comparison of ionospheric F2 peak parameters f0F2 and hmF2 with IRI2001 at Hainan station. *Adv. Space Res.*, 43:1812-1820
- Wang X, Shi J, Wu S, Zheng W, Chen L, Pirog O, M, Zherebtsov G A. (2007), Analysis of ionospheric drifts to F10.7 response in Hainan. *Radio Sci.*, 22(3):370-374.
- Wang X, Shi J K, Wang G J, Zherebtsov G A, Pirog O M. (2008), Responses of ionospheric f0F2 to geomagnetic activities in Hainan. *Adv. Space Res.*, 41:556-561.

- Wei Y. (2008), Unusually long lasting multiple penetration of interplanetary electric field to equatorial ionosphere under oscillating IMF Bz. *Geophys. Res. Lett.*, 35, L02102, doi:10.1029/2007GL032305
- Xiao S, Xiao Z, Shi J, Zhang D, Feng X, Hao Y, Huang W. (2009), Observational facts in revealing a close relation between acoustic-gravity waves and midlatitude Spread F. *J. Geophys. Res.*, 114, A01303, doi:10.1029/2008JA013747
- Xiao Z, Xiao S, Hao Y, Zhang D. (2007), Morphological features of ionospheric response to typhoon. *J. Geophys. Res.*, 112, A04304, doi:10.1029/2006JA011671.
- Xiong B, Wan W, Liu L, Ning B, Guo J. (2007), Seasonal variation of the ionospheric total electron content, maximum electron density and slab thickness over Wuhan. *Chin. J. Space Sci.*, 27(2):125-131.
- Xu G, Wan W, She C, Dud L. (2007), The relationship between ionospheric total electron content (TEC) over East Asia and the tropospheric circulation around the Qinghai-Tibet Plateau obtained with a partial correlation method. *Adv. Space Res.*, 42:219-223.
- Xu L J, Koustov A V. (2007), The response of high-latitude ionospheric convection during a southward IMF turning event. *Chin. J. Geophys.*, 50(6):1623-1631.
- Yue X, et al. (2007a), Statistical analysis on spatial correlation of ionospheric day-to-day variability by using GPS and Incoherent Scatter Radar observations. *Ann. Geophys.*, 25(8):1815-1825.
- Yu X, et al. (2007b), A study of correlation distance of the day-to-day variability of F2-layer peak electron density over Europe. *Chin. J. Geophys.*, 50(5):1283-1288.
- Yue X, Wan W, Lei J, Liu L. (2007c), Modeling the relationship between E cross B vertical drift and the time rate of change of hmF2 over the magnetic equator. *Geophys. Res. Lett.*, 35, L05104, doi:10.1029/2007GL033051.
- Yue X, Wan W, Liu L, Zheng F. (2007d), Data assimilation of Incoherent Scatter Radar observation into a 1-dimensional mid-latitude ionospheric model by applying Ensemble Kalman Filter. *Radio Sci.*, 42, doi:10.1029/2007RS003631.
- Yue X, Liu L, Wan W, Wei Y, Ren Z. (2008), Modeling the effects of secular variation of geomagnetic field orientation on the ionospheric long term trend over the past century. *J. Geophys. Res.*, doi:10.1029/2007JA012995.
- Yue X, Wan W, Liu L, Le H, Chen Y, Yu T. (2008), Development of a middle and low latitude theoretical ionospheric model and an observation system data assimilation experiment. *Chin. Sci. Bull.*, 53(1):94-101.

- Yue X, Wan W, Liu L, Le H, Chen Y, Yu T. (2008), Development of a middle and low latitude theoretical ionospheric model and an observation system data assimilation experiment. *Chin. Sci. Bull.*, 53(1):94-101
- Yue X, Wan W, Liu L, Ning B, Zhao B, Li G, Xiong B. (2010), Development of an ionospheric numerical assimilation nowcast system based on Gauss-Markov Kalman filter: An observation system simulation experiment taking example for China and its surrounding area. *Chin. J. Geophys.*, 53(4):787-795
- Yuan Z, Deng X. (2007a), Effects of continuous solar wind pressure variations on the long-lasting penetration of the interplanetary electric field during southward interplanetary magnetic field. *Adv. Space Res.*, 39:1342-1346.
- Yuan Z, Tian A, Deng X. (2007b), Observation and analysis of the ionosphere response to substorms by GPS. *J. Wuhan Univ. Nat. Sci. E*, 53(3):351-355.
- Zhan L, Liu L, Wan W, Zhao B. (2007), Morphology of ionospheric disturbances over Kokubunji during geomagnetic disturbances. *Chin. J. Space Sci.*, 27(5):391-399.
- Zhang D, Feng M, Xiao Z, Hao Y, Shi L, Yang G, Suo Y. (2007), The seasonal dependence of cycle slip occurrence of GPS data over China low latitude region. *Sci. China Ser. E*, 50(4):422-429.
- Zhang D H, Xiao Z, Feng M, Hao Y Q, Shi L Q, Yang G L, Suo Y C. (2010), Temporal dependence of GPS cycle slip related to ionospheric irregularities over China low-latitude region. *Space Weather*, 8, S04D08, doi:10.1029/2008SW000438
- Zhang M.-L., W. Wan, L. Liu, and J. K. Shi. (2008), Variability of the behavior of the bottomside (B_{00} , B_{10}) parameters obtained from the ground-based ionograms at China's low latitude station. *Adv. Space Res.*, 42:695-702
- Zhang M L, Wan W, Liu L, Ning B. (2009a), Variability study of the crest-to-trough TEC ratio of the equatorial ionization anomaly around 120E longitude. *Adv. Space Res.*, 43 (11):1762-1769
- Zhang M L, Liu C, Wan W, Liu L, Ning B. (2009b), A global model of the ionospheric F2 peak height based on EOF analysis. *Ann. Geophys.*, 27:3203-3212
- Zhang M L, W Wan, L Liu, Shi J K. (2008), Variability of the behavior of the bottomside B₀₀, B₁₀ parameters obtained from the ground-based ionograms at China's low latitude station. *Adv. Space Res.*, 42:695-702.
- Zhang, M L, Shi J K, Wang X, Shang S P, Wu S Z. (2007), Ionospheric behavior of the F2 peak parameters f_oF2 and h_mF2 at Hainan and comparisons with IRI model predictions. *Adv. Space Res.*, 39(5):661-667.
- Zhang Q et al, (2008), Simultaneous Cluster and Super-DRAN conjugated observations of two strong FTEs on 1 April 2004. *Ann. Geophys.*

- Zhang W, Zhang D H, Xiao Z. (2009), The influence of geomagnetic storms on the estimation of GPS instrumental biases. *Ann. Geophys.*, 27:1613-1623
- Zhao B, Wan W, Liu L, Mao T. (2007), Morphology in the total electron content under geomagnetic disturbed conditions: results from global ionosphere maps. *Ann. Geophys.*, 25(7):1555-1568
- Zhao B, Wan W, Liu L, Mao T, Ren Z, (2007a), Christensen A B. Features of annual and semiannual variations derived from the global ionospheric maps of total electron content. *Ann. Geophys.*, 2007, 25}:1-15.
- Zhao B, et al. 2008a. Ionosphere disturbances observed throughout South-East Asia of superstorm of 20-22 Nov., 2003. *J. Geophys. Res.*, doi:10.1029/2008JA013054
- Zhao B, et al. (2008b), Anomalous enhancement of ionospheric electron content in the Asia/Australian region during a geomagnetically quiet day. *J. Geophys. Res.*, 113, A11302, doi:10.1029/2007JA012987.
- Zhao B, et al. (2008c), Is an unusual large enhancement of ionospheric electron density linked with 2008 great Wenchuan earthquake. *J. Geophys. Res.*, doi:10.1029/2008JA013613
- Zhao B, et al. (2009a), Ionospheric response to the geomagnetic storm on 13-17 April 2006 in the West Pacific region. *J. Atmos. Solar-Terr. Phys.*, 71(1): 88–100
- Zhao B, Wan W, Liu L, Ren Z. (2009b), Characteristics of the ionospheric total electron content of the equatorial ionization anomaly in the Asian-Australian region during 1996–2004. *Ann. Geophys.*, 27:3861-3873.
- Zhou Y L, Ma S Y, Lü H, Wan H, Dang G. Changes of thermospheric mass density and their relations with joule heating and ring current index during Nov. 2003 Superstorm-CHAMP Observations. *Chin. J. Geophys.*, 2007, 50(4):986-994.
- Zhu A, Zhang B, Huang J, Liu R. 2008. Comparative study of winter polar ionospheric F2 layer in both hemispheres. *Chin. J. Polar Res.*, 20(1):31-39
- Zhu Z, Ning B, Wan W, Zhao B, Wang M. (2007), An investigation of ionospheric responses during 13-17 April 2006 at Western Pacific magnetic storm area. *Chin. J. Geophys.*, 50(4):957-968.
- Zhu Z, Ning B, Wan W. (2007), Measurement and analysis of ionospheric virtual height with high precision. *Chin. J. Space Sci.*, 27(3):204-210.
- Zuo X, Wan W. (2008), Planetary wave oscillations in sporadic E layer occurrence at Wuhan. *Earth Planets Space*, 60 (6):647-652

PROGRESS IN MAGNETOSPHERIC RESEARCH

Zhuyin PU(1), Zhenxin LIU (2), Chao YUE (1) and Biao YANG (1)

(1) School of Earth and Space Sciences, Beijing University, Beijing, 100871, China

(2) Center for Space Science and Applied Research, Chinese Academy of Sciences, Beijing, China

Abstract During the period from late 2006 to early 2011, a lot of works have been done by Chinese magnetospheric physicists based on in situ measurements of two Chinese Double Star satellites, four spacecraft of ESA Cluster and five NASA THEMIS probes, together with ground-based magnetometer and ionospheric radar observations. Meanwhile, plenty of studies were also conducted by computer simulation and theoretical modeling. Progresses have been made in understanding the physics of magnetospheric dynamic under different solar wind conditions. This report presents the advances of the magnetospheric physics researches in China during the past four years, based on reviewing the selected 205 articles published in peer-refereed scientific journals.

I. MAGNETOSPHERIC SUBSTORMS AND STORMS

Based on Double Star and Cluster coordinated measurements, Liu et al. (2008) proposed a global “Front” substorm triggering model. The main features of the model include: (1) The “Ionospheric wind” (IW) manifests tailward flows in the near earth tailward flow (NETF) which has an important effect on the substorm onset. (2) A front region (FR) is formed by interaction of NETE with earthward plasma flow. (3) The triggering process of substorms occurs in the FR. In this article the authors first made detailed analyses of NETFs observed by Double Star TC-1; then presented observations of substorm triggering processes in the FR with a typical example of substorm on 28 Sep. 2004; finally suggested the time sequence of substorm evolution indicated by the Front model. Possible global and multi-temporal/spatial-scale driving processes of substorms were discussed.

Duan et al (2008) studied the substorm on September 14, 2004 and ion high-speed flows in the near-Earth plasma sheet based on measurements of FGM and HIA on board TC-1 at its apogee. Strong tailward high-speed flows ($V_x \sim -350$ km/s) are first seen at about $X \sim -13.2 R_E$; 1 minute later the flows are reversed from tailward to earthward. The reversal process occurs quickly after the substorm expansion onset. This analysis shows that the ion flow reversal from tailward to earthward is likely to be in close relation with the substorm expansion initiation and might play an important role in triggering the substorm expansion onset.

Zhang et al. (2007) studied 53 substorms measured by Double Star/TC-1 in the near-Earth magnetotail from July to October, 2004. The main features of these events are: (a) Magnetic flux pileup characterized by continuous enhancement of B_z is observed, which starts almost simultaneously with aurora breakup within 1-3 minutes, indicating that substorm onset is in close relation to flux pileup. (b) Sudden plasma sheet expansion with sharp increases in ion temperature and density is seen in all events, which occurs typically ~ 11 minutes after the beginning of pileup. The plasma sheet expansion is shown to be in close relation with the primary substorm dipolarization and, hence, can be referred to as 'dipolarization-associated expansion'. (c) Evidence indicates that the substorm current wedge first forms earthward of TC-1 position and, hence, inward of the flow braking region, and then propagates tailward with an expansion in the Z-direction.

Cao et al. (2007, 2008) performed two case studies to investigate substorm timing and activations based on Double Star TC1, Cluster, Polar, IMAGE, LANL geostationary satellites and ground-based geomagnetic field measurements. In both events, an earthward flow associated with plasma sheet thinning is measured by Cluster 8–10 min ahead of the auroral breakup. A couple of minutes after the breakup, either TC1 at $X \sim -10 R_E$ first detects plasma sheet expansion and then the LANL satellites near the midnight measure energetic electron injections at geostationary orbit or the LANL satellites first measure the electron injections and then TC1 detects the plasma sheet expansion. More than about 20 min later, Cluster at $X \sim -16 R_E$ and Polar (at higher latitude) successively observe plasma sheet expansion. The open magnetic flux of the polar cap, Ψ , is found to continually increase during the early substorm phase and then to rapidly fall when

the IMF turns northward. When Ψ reaches its minimum value, bright and broad auroral activities start to decrease. Tailward progression of the magnetic dipolarization and a poleward expansion of auroral bulges are shown to closely map to one another. These results suggest that substorm activations start in the midtail before ground onset and then move earthward, which leads to an expansion onset in the near-Earth tail around $X \sim -(8-9) R_E$. After onset, the activations progress both earthward and tailward. Substorm onset is possibly related to plasma sheet reconnection of close field lines, while tail lobe reconnection of open field lines release more energy to support the full expansion of the substorm. In a fully developed expansion phase, an initial dipolarization in the near-Earth may eventually evolve to enable disruption of the cross-tail current over a wide region of the magnetotail.

Pu et al. (2010) and Chu et al. (2009) studied two substorms occurred at about 04:05 UT and 04:55 UT, respectively on February 26, 2008 observed by THEMIS satellites. They display detailed features of the two substorms with emphasis on the first. In both substorms a distinct auroral intensification occurred during the earliest stage of onset, about 1 to 2 min after midtail reconnection began. This initial intensification was weak and localized and thus had the signatures of a pseudobreakup. In both substorms, a second, major intensification occurred next in the substorm onset sequence, followed by rapid and extensive poleward expansion. This second intensification had the features of the major expansion onset and was nearly co-incident with observations of earthward flows and magnetic dipolarization in the near-Earth tail. During the growth phase of the two substorms, open magnetic flux accumulated in the polar cap; in the expansion/recovery phase the polar cap open flux was quickly reduced. These observations are in agreement with the assertion that tail reconnection initiates the initial pseudobreakup and the ensuing major expansion and releases and transports energy to eventually cause near-Earth dipolarization and the expansion phase onset of these two substorms.

Tang et al. (2009a) investigated the magnetic structures in the near-tail at $X_{GSM} = -17.5 R_E$ in the substorm on September 19, 2003. During the event Cluster observed an earthward propagating plasmoid and two flux ropes, which were embedded within earthward plasma flows. The first flux rope diameter is about $0.7 R_E$ and duration is ~ 20 s, while the second one diameter is about $1.4 R_E$ and duration is ~ 30 s. These observations can be interpreted as evidence for multiple X-lines reconnection in the tail during a substorm time.

Tang et al. (2009b) present observations of a substorm on 13 March 2008 measured by Time History of Events and Macroscale Interactions during Substorms (THEMIS) spacecraft in the near-Earth tail during plasma sheet expansion. The main features of the event are as follows: (1) Cross-tail current disruption (CD) was observed at $X \sim -8.0 R_E$ and $Y \sim 2.0 R_E$. During the plasma sheet expansion, dipolarization was propagated tailward and azimuthally at ~ 48 km/s and ~ 35 km/s, respectively. (2) In the inner edge of the plasma sheet, slow flux pileup is observed which was characterized by continuous enhancement of B_z and B_t and reduction of plasma density and thermal, pressure P_{th} . (3) A sharp decrease in the magnitude of B_x at P1 ($-13.1 R_E$, $2.5 R_E$, $-0.56 R_E$) prior to the dipolarization was also observed which may be caused by inward motion of flux from magnetic reconnection in the midtail.

Tang et al. (2010) analyzed simultaneous THEMIS measurements and ground-based observations during a set of successive auroral activations between 0600 and 0900 UT on 27 February 2009. They found that the first activation (a pseudobreakup) may be related to transient reconnection on closed plasma sheet field lines. At substorm expansion, an abrupt reduction in the lobe field was observed. The rapid lobe flux reduction may indicate the onset of magnetotail lobe magnetic reconnection and the substorm expansion phase.

Aurora display and auroral electrojet are both resulted from particle precipitation and greatly enhanced during substorms. However, they have rather different behaviors and AE-dependences. Xu (2009) studied the dynamic characteristics of the auroral electrojet belt by using equivalent current systems deduced from ground-based magnetic records. The results show that the electrojet belt is divided by Harang discontinuity into two parts: the minor eastward electrojet in afternoon sector and the major westward electrojet in midnight-morning sector. The former shifts equatorward when AE increases, just as the auroral oval does; the latter is divided into two sections: the midnight section shifts poleward when AE increases, while the morning section shifts equatorward. The author further revealed that the principal factor controlling the midnight-morning westward electrojet is ionospheric conductivities, while the principal factor controlling the

afternoon eastward electrojet is electric field, instead of conductivities.

Xu et al. (2008) proposed a “Key-Points model” for outlining the basic features of the polar region current system for different disturbance levels. The “Key-Points model” (or KP model) includes 6 key points of the current system: the centers of two DP2 cells, the maximum densities of the eastward and westward electrojets, and the maximum densities of the northward and southward currents. Each of 6 key points is described by 3 parameters: intensity, local time and latitude. The AE-dependences of the 18 parameters are deduced from the equivalent current systems for every 5 minutes during a 2-day period (March 18~19, 1978). The KP model reveals systematic variations of the current systems. When AE increases, the currents and the current densities are simultaneously enhanced linearly, and most of the key points concentrate towards midnight. In addition, when AE increases, the key points of K2 and K4 for the evening current cell move equatorward, whereas the key points of K1 and K3 for morning cell move poleward.

Based on well-defined substorm onsets in the northern hemisphere and 1432 in the southern hemisphere observed by the FUV Imager on board IMAGE spacecraft, Wang and Luehr (2007) performed a statistical study for both hemispheres. The main emphasis was put on a possible dependence of the substorm occurrence frequency on season and longitude (S/L). It was found that around December solstice UT noon-time and around June solstice UT nighttimes are more favorable for substorms to occur. The occurrence frequency varies by a factor of 2. The sum of ionospheric Pedersen conductance of both hemispheres caused by solar illumination in the nightside auroral regions can account for the S/L dependence. Lower total conductivity seems to reduce the trigger level. The authors found that the IMF threshold for initiating a substorm is on average lower during favorable times, thus, substorms can occur more frequently

Based on 2760 well-defined substorm onsets in the Northern Hemisphere and 1432 in the Southern Hemisphere observed by the FUV Imager on board the IMAGE spacecraft, Wang et al. (2008a) made a detailed statistical study including both auroral regions. This study focused on the hemispheric comparisons. Southward pointing IMF is favorable for substorm to occur, but still 30% of the events are

preceded by northward IMF. The magnetic latitude (MLat) of substorm onset depends mainly on the merging electric field (E_m) with a relationship of $|dMLat| = -5.2E_m^{0.5}$ where $dMLat$ is the deviation from onset MLat. In addition, seasonal effects on onset MLat are also detected, with about 2 degrees higher latitudes during solstices than equinoxes. Both IMF B_y and solar illumination have a significant influence on the magnetic local time (MLT) of onsets and can contribute to hemispheric longitudinal displacements of substorm onset locations from conjugacy.

Wang et al. (2008b) investigated two substorm onset events measured by TC-1 and Cluster. One is believed to be triggered by a northward turning of the IMF, while the other occurs under generally southward IMF. For both events, Cluster was located tailward of TC-1, but observed the depolarization at earlier time for one event while at later time for the other. The timing difference of dipolarization at different positions could be explained by the earthward or tailward propagation of the field disturbances in the radial direction. The earthward dipolarization front was found in one case to bounce back and forth at TC-1. The earthward propagation was accompanied by a fast earthward plasma flow. The event analysis suggests that substorms can be quite different from case to case due to differences in the solar wind condition and magnetotail configuration.

Liu et al. (2010) showed, for the first time, a substorm event with double onsets under northward IMF condition. Magnetic field data from ground stations and from geosynchronous satellite and aurora data from IMAGE satellite are examined. The results show that the intensity and the spatial extent of the event are as large as those of typical substorms. A possible mechanism for the double onsets was proposed. The energy source for the event was also discussed. Further, Liu et al. (2011a) made an attempt to study the difference between the response of the polar ionosphere to “spontaneous” substorms and “trigger - associated substorms” in terms of the ionospheric current vectors, electric potential and the current function. The results show that to the first approximation, the ionospheric parameters for the two types of substorms are quite similar, indicating that spontaneous substorms are

not very different from trigger - associated substorms in the magnetosphere - ionosphere system. The authors demonstrate, however, that spontaneous substorms seem to have a more clearly identifiable growth phase, whereas trigger - associated substorms have a more powerful unloading process. Changes in the current intensity and the electric potential drop across the polar cap in the recovery phase are also quite different. The authors interpret these as an indication of the relative importance of the unloading process and the directly driven process in conjunction with the north - south polarity of the interplanetary magnetic field.

Using the data of LFEW/TC-2, Yang et al. (2008) studied the dawn side 14 chorus around substorm onsets during a strong geomagnetic storm in Nov., 2004. Nine of them occurred within 40 min around the substorm onsets. The frequencies of waves have a good correlation with the half equatorial electron cyclotron frequencies. Chorus can be excited in the region near magnetic equatorial plane and then propagate to the mid and high latitudes. Previous observations show that the chorus can propagate at most to the magnetic latitudes of 40°. LFEW/ TC-2 found for the first time that the chorus can propagate to the magnetic latitude of 70°. Since most of previous chorus observations were made close to the magnetic equatorial plane, the present results are important for the studies of excitation and propagation of whistler mode waves, and relevant relativistic electron acceleration in the magnetosphere.

A comparison between substorm onset times identified by geomagnetic westward electric jet AL index, substorm electric jet AE index and field-aligned current AF index and auroral breakup were conducted by Ding et al. (2010a). They found that if auroral onsets are chosen as zero time, the AL and AE onsets are mainly distributed between (-5, +6) min. Field-aligned current AF onsets are relatively widely distributed as (-8, +7) min. The average AL, AE, AF onsets are 0.5, 0.5, and -0.1 min. The most possible AL onset is at the same time as auroral onset, but that is 1 min before for AE and AF onsets. The substorm onsets identified by geomagnetic indices get closer to auroral onset for more intense substorms. For the 5 super substorms, AL and AE onsets are both before auroral onset, indicating that electric jets are increased before the auroral breakup.

Duan et al (2011a) adopted joint observations of TC-1 at about -12.5 RE and Geotail at about X~-(8-9) RE in the near-Earth plasma sheet to investigate the plasma instabilities in the vicinity of substorm onset which occurred at about 0253:20 UT on September 28 2004. The observations indicate that 1) the location of substorm onset triggering region is within the inner plasma sheet, 2) the lower-hybrid instability is incited in the substorm triggering region and the lower-hybrid waves with the quasi-perpendicular propagation occur during substorm onset, 3) the magnetic dipolarization and magnetic disturbance outside the near-Earth plasma sheet are very weak during substorm onset, and 4) the features of dipolarization at onset and during the expansion phase are found to be different.

Duan et al (2011b) studied magnetic field dipolarization near the substorm onset and during substorm expansion phase in the period of 06:00 -06:40 UT on 15 February 2008 observed by THEMIS. It is found that dipolarization at substorm onset was not accompanied by noticeable ion bulk speed variation, whereas dipolarization taking place during the expansion phase were mostly accompanied by high speed earthward ion bulk flow. Before substorm onset THEMIS P3, P4, P5 all observed fluctuation in the Bx component with a period of ~300 s. After onset earthward ion bulk flow and magnetic disturbances both occurred at P3 and P4 locations. These results indicate that there is no one-to-one relationship between near-Earth dipolarization and earthward ion bulk flow. Dipolarization at substorm onset seems to be a local and small scale phenomenon, associated with some kinds of plasma instabilities.

Zhou et al. (2009c) observed multiple dipolarization fronts by THEMIS spacecraft in the near-Earth magnetotail during a substorm. The dipolarization fronts were located at the leading edge of earthward propagating plasma bubbles. Major energetic electron flux enhancements were observed at the dipolarization fronts, which were also associated with large wave fluctuations extending from below the lower hybrid frequency to above the electron cyclotron frequency. Intense electric field wave packets, primarily contributed by the Hall electric field and lower hybrid drift (LHD) wave, were observed right at the front, which was a thin current

layer with size of the order of the ion inertial length. Electrostatic electron cyclotron harmonic (ECH) waves were detected slightly after the front. The ECH waves were probably generated by the positive slope of the electron perpendicular velocity distribution. Both of these waves are suggested to be able to heat electrons. The observation of these waves at the dipolarization front could be important for the understanding of electron energization during substorm injection, as well as the mechanism of current disruption.

A current disruption and dipolarization scenario associated with island coalescences in the near-Earth region is proposed in Ma and Lu (2009). The thin and elongated current-sheet built up during the growth phase is unstable due to a tearing mode instability that leads to formation of multiple magnetic islands (or magnetic flux ropes in the three dimensional case) in the near-Earth region. The growth rate of the tearing mode should be different in different locations. When the rate of the magnetic MR in the mid-tail region around $20R_E$ is much larger than that in other locations, the strong bulk earthward flows resulting from the fast MR drive the earthward convection and the coalescence of the magnetic islands. Consequently, the cross-tail current in the near-Earth region is suddenly disrupted and the geometry of the magnetic field changes from tail-like to dipolar-like in the ideal time scale. This proposed scenario is tested by Hall MHD simulation and is compared with the observations in the paper.

Current dynamic processes in realistic magnetotail geometry are studied in Lu and Ma (2009) by Hall MHD simulations under various driven conditions and Hall effects. Associated with the external driving force, a thin current sheet with a broad extent is built up in the near-Earth magnetotail. The time evolution for the formation of the current sheet comprises two phases: slow growth and a fast impulsive phase before the near-Earth disruption of the current sheet resulting from the fast magnetic reconnection. The simulation results indicate that as the external driving force increases, the site and the tailward speed of the near-Earth current disruption region are closer to the Earth and faster, respectively. Whether the near-Earth disruption of the current sheet takes place or not is mainly controlled by Hall effects. It is found that there is no sudden disruption of the current sheet in the

near-Earth region if the ion inertial length is below $d_i = 0.04$.

A Hall MHD simulation is used by Ma (2008) to study current dynamic processes with realistic magnetotail geometry. The simulation results indicate that sudden disruption of cross-tail current at the near Earth region inside $15R_E$ is triggered by fast magnetic reconnection with the reconnection rate ~ 0.15 . The cross-tail current density exhibits an impulsive intensification in the late growth phase. The magnitude of the current increases more than one order within a few minutes. After the reconnection onset, the cross-tail current is suddenly disrupted in a few Alfvén times, which is in good agreement with that from the satellite observations. Associated with the current disruption, the tail-like geometry becomes a dipolar-like structure with an impulsive enhancement of the magnetic field B_z . Large increases of the electric field and Earthward bulk flow in this simulation are observed immediately after the reconnection onset.

Geomagnetic storms are mainly resulted from the ring current, the decay rate of which is one of the key parameters for estimating energy budget of the magnetosphere and for storm prediction. Xu and Du (2010) proposed two new criteria for evaluating the decay rate: (1) the E-criterion: the total energy balance for a storm event, or balance between the integrated energy input and output during whole course of the event; (2) the L-criterion: the total energy balance for a long interval, or balance between the integrated energy input and output for a long interval. Several models of decay rate are examined by using 44 selected storms during 1998-2003 and an 11-year-long continuous record for the 23rd solar cycle (1998-2008). The results show that the models PA1978 and XD2010 show fairly well energy balance for all the storm events, satisfying the E-criterion. In addition, the two models fairly well satisfy the L-criterion, exhibiting enhanced energy dissipation during major storm events and long-term energy balance.

Li et al.(2010) showed that the magnetopause (MP) around noon erodes earthward with increasing storm intensity. For superstorms with $S_{YM} \leq -300$ nT, the MP around noon erodes to inside the geosynchronous orbit, which causes reversal of the magnetic B_z component near the local noon. The necessary conditions for

superstorms with $\text{SYM-H} \leq -300$ nT to occur are found to be the following: (1) the interplanetary magnetic field (IMF) $B_z < -27$ nT lasts for at least ~ 1 h; (2) solar wind dynamic pressure, $P_d > \sim 12$ nPa; and (3) the projected interplanetary electric field $E_K - L >$ is greater than ~ 30 mV/m.

Wang et al. (2008) have investigated variations of the location and intensity of auroral currents during two magnetic storms based on measurements from CHAMP. The corresponding auroral electrojet current densities are on average enhanced by about a factor of 7 compared to the quiet time current. The nightside westward current densities are on average 1.8 (2.2) times larger than the dayside eastward current densities in the Northern (Southern) Hemisphere. Both eastward and westward currents are present during the storm periods with the most intense electrojets appearing during the storm main phase, before the ring current maximizes in strength. The eastward and westward electrojet centers can expand to 55 MLat during intense storms. The equatorward shift of auroral currents on the dayside is closely controlled by the southward IMF, while the latitudinal variations on the nightside are better described by the variations of the Dst index. The Space Weather Modeling Framework can capture the general dynamics of the storm time current variations. Both the model and the actual data show that the currents tend to saturate when the merging electric field is larger than 10mV/m .

Cai and Ma et al. (2010) used the NARX neural network for the first time to predict SYM-H index from solar wind (SW) and IMF parameters. In total 73 time intervals of great storm events during 1998-2006, IMF/SW data from ACE satellite are available for establishing the ANN model; out of them, 67 are used to train the network and the other 6 (including two super-storms of min. $\text{SYM-H} < -200$ nT) for test. In addition, the NARX prediction model is also validated with usage of IMF/SW data from WIND satellite for 7 great storms during 1995–1997 and 2005, as well as for the July 2000 Bastille day storm and November 2001 superstorm based on Geotail and OMNI data at 1AU. For the 6 test storms registered by ACE, the correlation coefficient between the observed and NARX network predicted SYM-H is 0.95 as a whole. The prediction for the 7 storms with WIND data is also satisfactory with the averaged correlation coefficient about 0.91. The newly developed NARX model shows much better capability than Elman network for

SYM-H prediction, which can partly be attributed to a key feedback to the input layer from the output neuron with a suitable length (about 120 min). This feedback effect is discussed in detailed in the paper.

Tang et al. (2008) present energetic neutral atom (ENA) images in the energy range 45 to 50 keV for H and 92 to 138 keV for O⁺ measured by the Neutral Atom Detector Unit (NUADU) onboard Double Star TC-2 during a geomagnetic storm on 8 May 2005. They compare the ion fluxes deduced from inversion of the NUADU image with those calculated using the Comprehensive Ring Current Model (CRCM). This comparison shows that the two approaches are consistent for deriving the configuration of the global ion distribution and peak ion fluxes. The deduced peak ion flux is located in the premidnight sector at 1540 UT and in the midnight sector at 1610 UT. There are strong ion fluxes in the region between L = 2 and L = 4 which form a closed loop configuration. The ion peak flux is about $2.2 \times 10^6 / (\text{cm}^2 \text{ sr keV s})$. The agreement between the inverted ion distributions and the CRCM results provides confidence in applying the ENA imaging and modeling techniques to study the inner magnetosphere plasma distribution and the global dynamics of the ring current during magnetic storms.

Xie et al. (2006) conducted an extensive study of ring current injection and intensification of the storm-time ring current with three-dimensional (3-D) test particle trajectory calculations (TPTCs). The TPTCs reveal more accurately the process of ring current injection, with the main results being the following: (1) an intense convection electric field can effectively energize and inject plasma sheet particles into the ring current region within 1–3 h. (2) Injected ions often follow chaotic trajectories in non-adiabatic regions, which may have implications in storm and ring current physics. (3) The shielding electric field, which arises as a consequence of enhanced convection and co-exists with the injection and convection electric field, may cause the original open trajectories of injected ions with higher energy to change into closed ones, thus playing an important role in the formation of the symmetric ring current.

It has been known that the magnetic indices suffer from various uncertainties, which limit their application and even mislead to incorrect conclusion. Recently,

Xu (2008) analyzed three most popular indices, Kp, AE, and Dst. Three categories of uncertainties in magnetic indices are discussed: “data uncertainty” originating from inadequate data processing, “station uncertainty” caused by incomplete station covering, and “physical uncertainty” stemming from unclear physical mechanism. A comparison between magnetic disturbances and related indices indicate that the residual Sq will cause an uncertainty of 1-2 in K measurement, the uncertainty in saturated AE is as much as 50%, and the uncertainty in Dst index caused by the partial ring currents is about a half of the partial ring current.

Considering the KuaFu mission, Shi et al. (2007) reviewed the energy release of substorm and storm in the geo-space. They also made an investigation on the improvements of the energy release by KuaFu mission.

II. RADIATION BELT DYNAMICS AND WAVE-PARTICLE INTERACTION

Zong et al. (2007) studied the electron and ion (electrons: 30 keV to 500 keV, protons: 30 keV to 1.5 MeV) flux variations associated with ultralow frequency (ULF) waves in the dayside magnetosphere observed during the CLUSTER's perigee pass near 0900 MLT on Oct. 31, 2003. In the region from $L \sim 5.0$ to 10, the ion flux modulation and electron flux modulation are out-of-phase with same periods. The observed magnetic ULF pulsations are dominated by the toroidal mode, along with a relatively weaker poloidal wave. A 90° phase shift between the radial electric field and the azimuthal magnetic field indicates that the dominating toroidal standing waves are a fundamental harmonic.

Zong et al. (2009a) reported Cluster observations of an interplanetary shock arrival on 7 November 2004 (with the maximum solar wind dynamic pressure of ~ 70 nPa) which induced significant ULF waves in the plasmasphere boundary and caused simultaneous acceleration of energetic electrons (up to 2 MeV). The relationship between the energetic electron bursts and large shock-induced ULF waves is studied. It is shown that the energetic electrons could be accelerated and decelerated by the observed ULF wave electric fields and that the distinct wave number of the poloidal and toroidal waves at different locations indicates the different energy ranges of electrons resonating with these waves. For comparison,

a rather weak interplanetary shock on 30 August 2001 (dynamic pressure ~ 2.7 nPa) is also investigated in this paper. It is found that interplanetary shocks or solar wind pressure pulses with small dynamic pressure change can also play a non-negligible role in the radiation belt dynamics.

Zhang et al. (2010) have systematically studied ULF waves excited at geosynchronous orbit by both positive and negative solar wind dynamic pressure pulses. They have identified 270 ULF events excited by positive solar wind dynamic pressure pulses and 254 ULF events excited by negative pulses from 1 January 2001 to 31 March 2009. The poloidal and toroidal waves excited by positive and negative pressure pulses oscillated in a similar manner of phase near 06:00 local time (LT) and 18:00 LT, but in anti-phase near 12:00 LT and 0:00 LT. Furthermore, it is shown that the ULF oscillations are in general stronger around local noon than those in the dawn and dusk flanks. It is demonstrated that disturbances induced by negative impulses are weaker than those by positive ones, and the poloidal wave amplitudes are stronger than the toroidal wave amplitudes both in positive and negative events.

Yang et al. (2008) used a dipole model to investigate ULF waves excited by the sudden impulse (SI) of the solar wind dynamic pressure. The numerical results show that for a given SI lasting for 1 min with amplitude of 50 mV/m impinging on the subsolar MP, the total ULF energy transported from the solar wind to the magnetosphere is about 10^{14} J. The efficiency of the solar wind energy input is around 1%. It is also found that the energy of the cavity mode is confined in the region near the MP, whereas the energy of the toroidal mode may be distributed among a few specific L-shells. It is shown that the fundamental eigenfrequency of the cavity mode and the central locations of the field line resonances (FLRs) do not vary noticeably with the power spectrum of the SI. The spectrum of the SI affects the excitation of higher harmonics of the global cavity mode. The broader the bandwidth of the SI is, the higher harmonics of cavity mode could be excited. Meanwhile, the corresponding FLRs regions are broadened at the same time, implying that the global cavity modes and toroidal modes can resonate on more L-shells when more harmonics of the global cavity modes appear.

Yang et al. (2010) reported concurrent flux modulations in both drifting energetic electrons (tens to hundreds of keV) and in bouncing thermal ions (several keV), associated with the fundamental mode poloidal standing wave at 3.3 mHz. It occurred during the early storm recovery phase on 21 Oct 2001 when the Cluster satellites were travelling near the perigee with $L=4.5$ on the dayside (0900 MLT). Based on the observations and theoretical calculations, they suggest the simultaneous drift resonances of electrons (~ 94 keV) and bounce resonances of the O^+ (~ 4.5 keV) and H^+ (~ 0.3 keV) ions with the same ULF Pc5 poloidal standing wave.

Yang et al. (2011a) present the first systematic observational study on pitch angle evolutions of O^+ ions driven by storm-time Pc5 poloidal standing waves. Near the magnetic equator, the O^+ flux oscillation appears only around 0° and 180° pitch angles with no phase delay, which can result from wave-particle interactions in a fundamental mode poloidal standing wave. Away from the equator, however, the flux oscillation appears in a wide range of pitch angles with strong pitch angle dispersion that reverses sign from the southern hemisphere to the northern hemisphere. The latitude dependence of the dispersion signature is explained by combining the ion energy modulation near the equator and the time of flight effect of ion bounce motion.

Yang et al. (2011b) study the drift-bounce resonance process of O^+ ions with the ULF Pc5 standing waves to understand whether the ions could be accelerated or decelerated by ULF waves. Two event studies are performed to address the resonant interactions of the ions with fundamental mode standing waves. They find that drift-bounce resonances of the O^+ ions with ULF waves can be excited at some specific energy that satisfying the resonance condition. The phase space density spectra at the resonant energy range deviates remarkably from the background power-law distribution. The observations thus reveal the effective role of ULF standing waves in accelerating /decelerating the ring current O^+ ions during storm times.

Using data from low altitude polar orbit satellite of NOAA and ACE, Xie et al. (2007) investigated the possible sources of the enhancement of relativistic

electron in the magnetosphere. The observation from NOAA for the different geomagnetic activity period show that substorm injections provide seed electrons for MeV electron enhancement associated with geomagnetic storms and that energetic electrons in the solar wind provide an alternative sources for the relativistic electrons in the magnetosphere during the SEP (Solar Energetic Proton) events.

Xie et al. (2009) studied the formation and loss mechanism of the new proton belt in the Halloween storm of 2003 by using the NOAA/POES data. The results show that the formation of new proton belts is the result of the cooperation of various effects, including strong SPEs (Solar Proton Events), big magnetic storms, and IP shock waves. All these are the preconditions for the formation of the new proton belt, especially the IP is indispensable. The authors newly address the effective role of storm main phase which helps to drive protons inward to the stably trapped region. They also demonstrated that the magnetic field perturbation of sufficient magnitude due to ring current build up could cause the destruction of adiabatic invariant conservation, which lead to the losses of the new belt particles

Zheng et al. (2008) developed a two-dimensional (2-D) numerical model to investigate the in-situ wave-particle interactions in the radiation belt. Based on the solution of Fokker-Planck equation including pitch-angle and momentum diffusion, they calculated the temporal evolution of electron phase space density due to gyro-resonant interactions with a band of chorus waves in the heart of outer radiation belt $L = 4.5$. Their results show that the phase space density at energies of 0.5–1 MeV can increase by a factor of 10 or above in one day, supporting the previous finding that the gyro-resonance with whistler-mode chorus waves can contribute significantly to the buildup of energetic outer radiation belt electron flux during geomagnetic storms.

Zong et al. (2009b) reported two vortex-like plasma flow structures observed in the outer radiation belt and/or the ring current region on 11 April 2002, when the Cluster fleet entered (in the southern hemisphere) and exited (from the northern hemisphere) the boundary layer of the inner magnetosphere near 2130 MLT. A pair of bidirectional current sheet and bipolar electric field (E_y) are found to be closely associated with these vortices. The fact that vortices are observed both inbound and outbound at the boundary of the radiation belt at nearly the same L

shell suggests that they may last for more than 140 min. The scale sizes of the two vortices are about 810 km and 1138 km, respectively. These plasma flow vortices are suggested to be formed at the interface between the enhanced ionospheric outflow stream from the polar ionosphere and a sudden braking and/or azimuthal deflection of bursty bulk flows generated by the tail reconnection. The observed flow vortices provide a link among the inner magnetosphere, the tail plasma sheet, and the Earth's ionosphere by coupling magnetic shear stresses and plasma flow momentum.

Xiao et al. (2009) constructed a 2D diffusion model for the evolution of radiation belt electron phase space density based the bounce-averaged Fokker-Planck equation. The diffusion of energetic electrons in pitch-angle, momentum and cross-pitch-angle-momentum driven by gyro-resonance with various electromagnetic waves were fully taken into account. This numerical model was implemented via a hybrid finite difference scheme, which can successfully overcome the numerical difficulty caused by the inclusion of cross diffusion terms. Using this diffusion model, the authors and Su et al. (2009c, 2011c) performed many test simulations to investigate the influence of the cross diffusion on the efficiency of wave-particle interactions. The ignoring of cross diffusion was found to generally overestimate the \sim MeV electron phase space density by \sim 5 times for chorus alone, \sim 3.5 times for combination of chorus and hiss, and 5 – 10 times for combination of chorus, hiss, and EMIC, suggesting that cross diffusion terms are crucial in wave-particle interaction.

Xiao et al. (2010b) further developed a three-dimensional (3D) code to solve a fully bounce-averaged pitch-angle and energy diffusion equation including radial diffusion and particularly the cross diffusion terms. They presented one of the first simulations to examine the effects of radial diffusion and chorus-electron interaction with/without cross diffusion terms on the radiation belt electron dynamics. Simulated results demonstrated that chorus waves can produce significant accelerations of energetic (\sim MeV) electrons, leading to peaks in phase space density (PSD) in the center of outer radiation belt, which are subsequently smoothed by inward and outward radial diffusion. Moreover, neglecting cross diffusion process generally resulted in relatively large overestimates in the PSD

evolution, implying that cross diffusion terms are very critical in the 3D modeling of radiation belts dynamics. However, their test case simulations also showed that such overestimates are sensitive to the initial conditions and wave models.

Su et al. (2009a) constructed a 3-D realistic electron density model in the plasma trough region. Using the previously developed two-dimensional diffusion model, they examined the influence of field-aligned density variation on the acceleration efficiency of chorus waves in the outer radiation belt. Ignoring the density variation along the magnetic field lines was found to generally result in overestimates of relativistic electrons PSD due to an underestimate of the plasma parameter f_{pe}/f_{ce} . Particularly, such overestimates of PSDs tend to become more significant at larger kinetic energies and L-shells. In two days, the maximum overestimate factors over all the pitch angles were found to be 1.5 (1.5), 2.1 (18) and 4.7 (47) for energies of 1.0, 2.0 and 3.0MeV at $L = 4.5$ ($L = 6.0$), respectively. Their results demonstrated that incorporation of field-aligned density variation is very important to quantify the in-situ wave-particle interactions in the outer radiation belt.

Su and Zheng (2009) studied the resonant scattering of radiation belt electrons by EMIC waves in the plasmaspheric plume. It was found that the EMIC waves can deplete the relativistic electron fluxes by one to three orders of magnitude in 5 hours. The contribution of EMIC waves in different bands to the dropouts of relativistic electrons was differentiated: (1) the significant precipitation loss of \sim MeV electrons is primarily induced by the EMIC waves in H^+ and He^+ bands; (2) the rapid remove of highly relativistic electrons (>5 MeV) is mainly driven by the EMIC waves in O^+ band at lower pitch-angles, as well as the EMIC waves in H^+ and He^+ bands at larger pitch-angles. Moreover, the dependence of scattering efficiency on the spectral characteristics of EMIC waves in each band was also investigated. It was found that stronger depletion of relativistic electrons can occur over a wider pitch angle range when EMIC waves centering relatively higher in the band.

Su et al. (2010d) evaluated the energetic outer zone electron PSD evolution due to local resonant interaction with various waves and azimuthal advection around the Earth at a constant L-shell. They showed that \sim MeV electron PSD can decrease by

about three orders of magnitude over all pitch angles with a visible azimuthal asymmetry during the main phase, and increase by about 30 times with a weak azimuthal asymmetry during the recovery phase. The incorporation of multiple types of waves resulted in considerable differences between MLT-averaged and MLT-dependent simulations. MLT-averaged simulations can overestimate the ~MeV electron PSD by a factor of 5–50 during the main phase, and 9–13 during the recovery phase. Larger drift speed tends to diminish the azimuthal asymmetry of MLT-dependent simulations. These results suggest that azimuthal advection can play an important role in the radiation belt electron dynamics, which should be incorporated in future radiation belt models for space weather application.

Su et al. (2010a) presented a 3-D physics-based electron radiation belt model (STEERB) based on the solution of 3-D modified Fokker-Planck equation. The STEERB model covers the inner and outer radiation belts with incorporation of radial diffusion due to magnetic and electric field perturbations, and local pitch-angle, energy and cross-pitch-angle-energy diffusion due to various wave-particle interactions. It was implemented by a split operator technique, in conjunction with the recently developed hybrid finite difference method for local wave-particle interaction, and the fully implicit finite difference method for radial diffusion. The resulting numerical model was robust, efficient and easily parallelizable. Test simulations were performed to evaluate the respective roles of radial diffusion, gyro-resonant interaction with chorus and plume waves, and the sensitivity of numerical results to the uncertainty of wave spectrum, and the importance of cross-pitch-angle-energy diffusion.

Su et al. (2010b) simulated the storm-time radial diffusion of radiation belt electrons with arbitrary pitch-angles in a time-varying geomagnetic field using STEERB code. In particular, the adiabatic response of energetic electrons to the variation of geomagnetic field was self-consistently incorporated. Simulation results showed that the outward adiabatic transport is primarily responsible for the main phase depletion of energetic electron fluxes at large pitch-angles beyond $5R_e$. However, combined radial diffusion and adiabatic transport contributes insignificantly to the main phase depletion of energetic electron fluxes within $5R_e$, or the recovery phase enhancement of energetic electron fluxes in the outer

radiation belt. Moreover, the simulation with both radial diffusion and adiabatic transport showed that the pitch-angle distribution of energetic outer zone electrons can evolve from a rounded 90° -peaked distribution to a butterfly-shaped distribution during the main phase, and back to a rounded 90° -peaked distribution during the recovery phase.

Su et al. (2011b) introduced the adiabatic transport process into the 3-D STEERB model via adopting a time-varying Hilmer-Voigt geomagnetic field, which then contains more complete physical processes: adiabatic transport, radial diffusion, and various in-situ wave-particle interactions. It was found that the adiabatic transport alone (without plume hiss and EMIC waves) is unable to reproduce the observed main phase loss of energetic outer radiation belt electron fluxes in the presence of a strong chorus-driven acceleration process. However, after coupling with non-adiabatic processes, the adiabatic transport, together with radial diffusion and cyclotron resonant interactions with chorus, plume hiss and EMIC waves, contributes significantly to the main phase loss and the recovery phase enhancement of energetic electron fluxes. In the absence of adiabatic transport, the energetic outer radiation belt electron fluxes were found to be overestimated by a factor of 5–30 over all the pitch-angles during the main phase, and be underestimated by a factor of 2–5 at larger pitch-angles ($>50^\circ$) during the recovery phase. Their numerical results suggest that the adiabatic transport in the time-varying geomagnetic field should be incorporated into the future radiation belt models for space weather application.

Su et al. (2011a) examined and simulated the electron radiation belt dropout event on 9 October 1990. CRRES observations showed that significant depletions of electron fluxes occurred at energies ~ 0.1 – 1.0 MeV beyond $6 R_e$ and at energies $> \sim 0.4$ MeV within $6 R_e$. The 3-D radiation belt model STEERB was used to simulate this dropout event, taking into account the magnetopause (MP) shadowing, adiabatic transport, radial diffusion, and plume and chorus wave-particle interactions. Their results showed that STEERB code can basically reproduce the observed depletion of ~ 0.1 – 1.0 MeV electron fluxes throughout the outer radiation belt, suggesting that the competition and combination of all these physical mechanisms can well explain this electron radiation belt dropout event.

Xiao et al. (2007a) investigated the propagation characteristic of the superluminous wave (R-X and L-O) modes. They found that both modes can propagate down and even through the equatorial plane in the radiation belts during high geomagnetic activity without reflection. Xiao et al. (2007b) studied the higher-order harmonic resonances and found that the R-X, L-O and L-X modes have the potential for producing significant acceleration of electrons over their respective regions of parameter space. In particular, Xiao et al. (2006a) constructed expressions of the local diffusion coefficients in both pitch angle and momentum resulted from gyro-resonant interactions between electrons and superluminous mode waves. Xiao et al. (2011a) evaluated bounce-averaged diffusion coefficients of superluminous wave (R-X and L-O) modes at $L = 6.5$ and 4.5 . They showed that bounce-averaged momentum diffusion coefficients play a dominant role for pitch angles above a critical angle. They also demonstrated that for a Gaussian distribution of wave normal angle, diffusion coefficients are sensitively dependent on the peak normal angle. They estimated wave amplitudes for particular stochastic acceleration timescale for 1MeV electrons and found that the required wave amplitudes $\sim 86\text{--}170$ pT for a timescale 1 day. Their results indicate that superluminous wave modes may have a significant potential for both stochastic acceleration of trapped electrons (with higher pitch angles) and loss process of un-trapped electrons (with smaller pitch angles).

Xiao et al. (2010a) studied the temporal evolution of PSD of the outer radiation belt energetic electrons driven by the superluminous right-hand extraordinary (R-X) mode waves at $L = 4.5$. Bounce-averaged diffusion rates in pitch angle and momentum were calculated. Those diffusion rates were used as inputs to solve a 2-D momentum-pitch angle diffusion equation. In particular, three cases are considered: momentum diffusion rates alone, momentum pitch angle diffusion rates, and momentum +pitch angle +cross diffusion rates. Numerical results showed that at 24 h, electron PSDs can enhance substantially for 1 MeV energy at higher pitch angles. Momentum diffusion dominates the dynamic evolution of energetic electrons, whereas the contribution of pitch angle or cross-diffusion rates is insignificant. In addition, PSD evolutions are sensitively dependent on the assumed different wave normal angle distributions and tend to be located in lower

pitch angles when wave normal angles move to smaller regions. Diffusion coefficients and PSD evolution are largely determined by the wave latitudinal distributions. High-latitude R-X mode waves primarily contribute to pitch angle scattering of energetic electrons, whereas equatorial (or lower latitude) R-X mode waves yield efficient acceleration of electrons.

Xiao et al. (2011b) examined the precipitation loss of ring current protons produced by the EMIC waves at the location $L = 3.5$ where the symmetrical ring current primarily occurs. Using a recently introduced hybrid finite difference (HFD) method, they solve the standard Fokker-Planck diffusion equation with incorporation of the cross diffusion terms that were often ignored in the previous work. They show that EMIC waves can produce efficient pitch angle scattering of energetic (tens of keV) protons, yielding a rapid decrement in the flux with a time scale of a few hours, consistent with observational data. They also demonstrate that omission of the cross diffusion terms generally overestimates the decrement in the flux, typically by a factor of ~ 2 after a few hours at lower pitch angles, suggesting that the cross terms also play an important role in precipitation loss of ring current protons.

Cao et al. (2007) presented observations of long duration loss of high energetic electrons and relevant waves in the recovery phase of a substorm, that are made by LFEW and HEED of the polar satellite of DSP /TC-2. The HEED of TC-2 observed a loss event of high energetic electrons which lasted about 240 s. At same time, the LFEW of TC-2 observed a wave burst. The wave burst began 60s earlier than the loss event. The frequency of waves ranges from 300 Hz to over 10 kHz. The analyses of wave characteristics indicate that the wave was whistler-mode. Thus it is likely that the loss of high energy electron was caused by wave activities through wave particle interaction.

Yang et al. (2007) have studied acceleration of energetic electrons associated with chorus observed by TC-2. Data of Low frequency waves and high energy electron fluxes from TC-2 during the Nov. 7th-11th storm in year 2004 were used, Evidence that relativistic electrons were accelerated from seed electrons of a few hundred KeV are observed.

Li et al. (2009) investigated the total flux variations of the entire outer zone relativistic electrons in substorms occurring from August 1990 to March 1991. The statistical results indicate that continuous intense substorm activity (average AE > 200 nT) can lead to net increases of the relativistic electrons; the more intense the substorm activity, the larger the increases of the relativistic electrons, suggesting that the continuous intense substorm activity can effectively supply relativistic electrons for the entire outer zone.

Li et al. (2008) tried to establish a global quasi-linear diffusion model of electrons by combining the whistler-mode wave amplitude distribution model, the electron density distribution model and the IGRF10 magnetic field model in the $1 < L < 7$ region. Numerical results show that the variation of plasmopause location changes the electron loss region (which is controlled by whistler-mode hiss) and acceleration region (which is controlled by whistler-mode chorus) through changing electron density and wave intensity. The variation of the electron loss region is consistent with variation of the slot region, while the variation of the electron acceleration region is consistent with the variation of the outer radiation belt.

Su et al. (2009b) quantitatively analyzed the pitch-angle distribution (PAD) evolution of substorm-injected electrons at $L = 6$ due to interactions with upper and lower band chorus waves. The PADs of >0.1 keV electrons were found to be able to develop into the pancake-shaped distributions due to the combined resonant scattering by upper and lower band chorus; and the pancake index PI, defined as the flux ratio between pitch-angles 90° and 70° , can reach 6 after 5 hours since substorm injections. These numerical results suggest that the resonant scattering of electrons by the whistler-mode chorus waves be a substantial mechanism responsible for the formation of a pancake distribution outside $L = 6$, and that the rapid precipitation of electrons (\sim keV) driven by resonant scattering of chorus waves may be also responsible for the diffuse aurora. Test simulations were conducted to differentiate the contributions of chorus waves in both upper and low bands. The upper band chorus can efficiently scatter the electrons with energies 0.1–2keV into loss cone, and drive the electrons with energies above 2keV toward

loss cone. The lower band chorus can only cause precipitation loss of the electrons with energies above 1keV.

Su et al. (2010c) studied the dependence of chorus-driven diffuse auroral precipitation on the spatial position L , normal-angle and frequency distribution of both upper band chorus (UBC) and lower band chorus (LBC). It was found that whistler-mode chorus waves are more effective in the production of diffuse aurora at larger L -shells. The normal angle and frequency distribution of UBC can significantly affect the diffusion rates for \sim keV electrons and the consequent diffuse aurora precipitation. The strong diffusion limit for \sim keV electrons can be reached up to large pitch-angles closer to 90° , and the diffuse auroral precipitation can be remarkably enhanced when the UBC waves are possessing a larger normal angle range or centering higher in the band. In contrast, the diffusion rates and diffuse auroral precipitation of 2keV electrons were found to be largely independent of the normal angle and frequency distribution of LBC waves. Enhanced precipitations of \sim 5keV electrons can occur when the LBC waves centering higher in the band.

III. MAGNETIC RECONNECTION IN THE MAGNETOTAIL AND AT THE MAGNETOPAUSE

On 1 October 2001, the four Cluster spacecraft were flying in the magnetotail and meandered several times around a magnetic reconnection (MR) region over a period of nearly 15 minutes. The magnetic field, plasma density and flow velocity data collected during this event have already been studied extensively under the assumption of 2D Hall MR. Xiao et al. (2007a) challenged this result under the assumption of 3D MR. They found a null-null line with a length of $\sim 860 \pm 340$ km and showed that the fans and spines structure in the vicinity of the null-null line is consistent with the prediction of the theoretical 3D MR model, and can readily be reduced to the previously reported 2D 'X-line' geometry when projecting on the plane perpendicular to the null-null line. Moreover, they found that the null pair is related to wave activities in the lower-hybrid frequency range, which is in agreement with some past results from laboratory experiments and Cluster

measurements.

He et al., (2008a) proposed a novel method to reconstruct the 3D magnetic field structure in the vicinity of a MR null based on Cluster 4-satellite measurements. This method is to fit the measured magnetic field vectors by using a new fitting function, which involves 10 spherical harmonic functions, a Harris current sheet function, and a constant field. The method has been successfully applied to reconstruct the 3D MR structures at the magnetopause (MP) and in the magnetotail. The typical 3D MR structure, such as the null-pair geometry as predicted by theoretical studies, has also been successfully reconstructed (He et al., 2008b). He et al., (2008b) further studied the electron dynamics around the null pair, proposing a new scenario of micro-physics in the null region: electrons are temporarily trapped in the central reconnection region and accelerated by the parallel electric field and electron pressure gradient and reflected from the magnetic cusp mirrors, leading to the bi-directional energetic electron beams which excite the high-frequency electrostatic waves.

Xiao et al. (2007b) report a multi-spacecraft measurement of fast MR rate of $\sim (0.07-0.15)$ based on directly measurements of the plasma flow into the diffusion region. It falls into the range of $\sim (0.03-0.2)$ predicted in the steady state MR simulations. The characteristic sizes for the diffusion region of the width $L_z \sim 0.9d_i$ ($= 460$ km) and the length $L_x \sim (3.3-5.1)d_i$ ($=1680-2597$ km) were measured as well. The length of the diffusion region L_x is determined for the first time based on the in situ observations.

Deng et al. (2009) provided Cluster in situ observation of a spiral magnetic null pair and the associated waves in the MR diffusion region. A close relation among the null points, the bipolar signature of the Z component of the magnetic field, and enhancement of the flux of energetic electrons up to 100keV are found. Near the null structures, whistler-mode waves were identified by both the polarity and the power law of the spectrum of electric and magnetic fields. It is shown that the angle between the fans of the nulls is quite close to the theoretically estimated

maximum value of the group-velocity cone angle for the whistler wave regime of MR.

Zhou et al. (2009a) presented an observation of electromagnetic and electrostatic wave enhancements near lower hybrid (LH) frequency associated with MR process around a null pair. The quasi-perpendicular propagated LH waves were identified by the power law of the spectrums of electric and magnetic fields. They estimated the anomalous resistivity based and found that its contribution from LH wave in the current sheet is small. However, LH drift instability may heat electrons anisotropically and increase the peak current density; and both anisotropic heating and current peaking could enhance the growth rate of the tearing instability.

Zhou et al. (2009b) reported the Cluster observations of electrostatic and electromagnetic waves near the LH frequency in the MR region within a thin current sheet. During the crossing of the separatrix, strong electrostatic waves near the LH frequency were observed which were polarized with a large angle to the ambient magnetic field. Strong electromagnetic fluctuations were observed in the center of the current sheet in the diffusion region. The dispersion properties of the electromagnetic wave are studied and compared with the properties of lower hybrid drift instability. For the first time the authors directly observed the electromagnetic mode of LH drift instability in the neutral sheet around the MR X-line. The estimated anomalous resistivity could not provide the electric fields observed in the current sheet.

Huang et al. (2010) analyzed the properties of low frequency waves in a magnetotail MR diffusion region with a small guide field and high beta. Using the k -filtering method on the magnetic field data measured by Cluster spacecraft, they found that the dominated low frequency waves in the diffusion region were highly oblique propagating Alfvén-whistler mode.

In Wang et al. (2010b, c) an anti-parallel MR event in the magnetotail and a secondary island with a strong core field near the center of the ion diffusion region were identified. Within the island, the electron density peaks in the outer region and dips in the core region. A strong electron beam (current) parallel (anti-parallel)

to the magnetic field are observed in the outer region of the island. This suggests that the strong core magnetic field inside the island is likely to be generated by the electron beam (current) in the outer region of the island. The electron density dip in the core region is formed due to the existing strong core field. The electron flat-top distributions are detected in the ion diffusion region except the core area of the island, and the shoulder energy range of the flat-top distributions is from 100 eV to 4 keV. An enhancement of the energetic electron flux up to 200 keV is found in the ion diffusion region. Waves at the lower hybrid frequency are intensified in the ion diffusion region, while the intensification is strong in the outer region of the island and becomes very weak in the core region.

Xiao et al. (2010c) showed that strong whistler-mode electromagnetic waves were indeed found around the magnetic null in a 3-D MR event. They proposed a new electron acceleration scenario of trapped electrons near the magnetic null points driven by the whistler-mode waves, which was confirmed by numerical results. It was demonstrated that whistler waves can enhance the electrons phase space density for energies of ~ 2 keV by a factor of 100 at lower pitch angles very rapidly, typically within 2 seconds. The accelerated electrons may escape from the loss-cone of the magnetic cusp mirrors around the magnetic null, leading to the observed energetic beams.

Yuan et al., (2007) report observations from Geotail satellite showing that large Poynting fluxes associated with Alfvén waves in the plasma sheet boundary layer (PSBL) occurred in the vicinity of the near-tail MR region on December 10, 1996. During the period of large Poynting fluxes, Geotail also observed strong tailward plasma flows. These observations demonstrate the importance of near-tail MR in generating the energy source of Alfvén waves in the PSBL. Strong tailward (earthward) plasma flows ought to be an important candidate on explaining the generating Alfvén waves. Furthermore, the strong perturbations not only in the magnetic field but also in the electric field observed in PSBL indicate that PSBL can be the carrier of the energy flux associated with the Alfvén waves.

Wei et al. (2007) presented Cluster observations of waves in the whistler frequency range during MR in the Earth's magnetotail. On 21 August 2002 the Cluster

spacecraft encountered a MR event when it crossed the plasma sheet. Prior to the southward turning of magnetic field in the tailward flow, the weak whistler waves were first observed. The burst of whistler waves appeared about 30 s earlier than the southward turning. During the MR event, the waves in the whistler frequency range were greatly enhanced. It is found that the waves in the higher-frequency range are mainly quasi-parallel propagating right-hand polarized whistler waves, while those in the lower frequency range are quasi-perpendicular propagating linear polarized waves,. The combined observations of energetic electrons and waves show that the waves in the MR process are greatly enhanced by energetic electron beams.

Using the data from four Cluster satellites prior to a magnetospheric MR event on 13 September 2002, Wei et al. (2010) utilized the wave telescope technique to obtain the wave number which corresponding to peak of power spectral density. The wave length is about 18 RE and consistent with previous theoretic and numerical results. After substituting the wave vector and other necessary parameters of observed current sheet into the triggering condition of tearing mode instability, the authors found that the near-Earth current sheet prior to MR is unstable to tearing mode.

With TC-1, Cluster, and Geotail observations, Zhang et al. (2010) statistically analyzed earthward and tailward convective bursty flows (CBFs) from 7 to 31 RE to understand the distribution of X lines in the magnetotail. They also analyzed the effect of the solar wind condition on the X lines with ACE satellite observations. The statistical results show that the earthward CBFs can be distributed widely, from 7 to 31 RE. TC-1 exploration shows that tailward CBFs with negative Bz in the central plasma sheet can seldom be observed inside 13 RE. Tailward CBFs with negative Bz are mainly distributed outside 17 RE, thus indicating that near-Earth X lines are most likely to occur outside 17 RE. According to Cluster observations, the occurrence of tailward CBFs has a sudden increase from 17 to 19 R_E. Geotail observations show a slow increase of tailward CBFs outside 20 R_E. Both Cluster and Geotail observations indicate that the near-Earth X lines could occur inside 20 R_E. The solar wind condition has a significant effect on the occurrence of the X

line in the magnetotail. The occurrence of the X line can increase under strong solar wind and decrease under weak solar wind.

Cai et al. (2009) reported a novel density depleted cavity in the outflow region of MR observed by Cluster satellites. Reflected field-aligned proton beams and magnetic-mirror loss-cone proton distributions were observed. The reflected field-aligned particles are produced by a generation mechanism similar to that of the terrestrial foreshock. In addition, magnetic field fluctuations, especially quasi-monochromatic oscillations, were also recorded. The underline physics and MR acceleration processes is discussed

The quadrupole out-of-plane magnetic field and electron density depletions along the separatrices are characteristics of collisionless MR. Lu et al (2010; 2011) investigated the features of MR separatrix regions and the relations between the electron density depletions and the out-of-plane magnetic field with both 2D particle-in-cell simulations and Cluster observations. They concluded that the electron density depletions are formed because of the magnetic mirror, and they are outside the peaks of the out-of-plane magnetic field. Such a prediction is confirmed by both simulations and observations. When the initial guide field is sufficiently large, the electron density depletion layers along one pair of the separatrices disappear. The parallel electric field in guide field MR was found to play an important role in forming such structures. The out-of-plane magnetic field and electron depletion layers in anti-parallel and guide field MR are both found to be related to the electron flow or in-plane currents in the separatrix regions.

Fu et al. (2006) and Huang et al. (2010) investigated electron acceleration in MR with 2D particle-in-cell simulations by tracing typical electron trajectories. When there is no initial guide field, the electrons can be accelerated in both the X-type and O-type regions. In the X-type region, the electrons can be reflected back and enter the acceleration region several times before leaving from the diffusion region. In this way, the electrons can be accelerated by the inductive electric field to high energy. In the O-type region, the trapped electrons can be accelerated when they are trapped in the magnetic island. On the other hand, when there is an initial guide

field, the electrons can only be accelerated in the X-type region; no obvious acceleration is observed in the O-type region. In the X-type region, the electrons are not demagnetized and they gyrate with the force of the guide field. Although no electron reflection is observed, the acceleration efficiency can be enhanced through staying longer time due to their gyration motion. Wang et al. (2010a) studied pitch angle distributions of energetic electrons in the vicinity of the X line and the outflow region based on a Cluster observation of anti-parallel MR in the magnetotail. At lower energies the electron distributions are highly anisotropic (field-aligned bidirectional); while at higher energies, electrons are observed to flow away from the X line along the magnetic field lines. At the edge of the outflow region, at lower energies, the electrons flow toward the X line; while at higher energies the electrons are flow away from the X line. Near the center of the current sheet, at lower energies, the electrons have field-aligned bidirectional distributions; while at higher energies, the electron distributions are isotropic.

Li and Ma (2010) investigated nonlinear evolution of resistive tearing mode with different sub-Alfvénic shear flow by using incompressible MHD simulations. The sub-Alfvénic shear flow can have either stabilization or destabilization effects on the tearing mode development, which is mostly determined by the shear flow thickness (a_v). The shear flow tends to boost the tearing mode instability when the thickness of the shear flow is above $a_v \sim 0.35a$ (where a is the normalization unit). The boosting effect of the shear flow on the tearing mode becomes strongest at $a_v \sim 0.6a$. But the strength of the boosting and suppressing effects is controlled by the asymptotic velocity (V_0) of the shear flow. The suppressing and boosting effects of the shear flow increase with increase of the shear flow velocity. The kinetic energy associated with initial shear flow is reduced when the shear flow has a boosting effect on the tearing mode growth.

Ma and Feng (2008) studied generation of Hall electric field and net charge associated with magnetic MR under different initial conditions of plasma density and magnetic field. With inclusion of the Hall effects, decoupling of the electron and ion motions leads to the formation of a narrow layer with strong electric field and large net charge density along the separatrix. The asymmetry of the plasma density or magnetic field or both across the current sheet will largely increase the

magnitude of the electric field and net charge. The results indicate that the asymmetry of the magnetic field is more effective in producing larger electric field and charge density. The electric field and net charge are always much larger in the low density or/and high magnetic field side than those in the high density or/and low magnetic field side. Both the electric field and net charge density are linearly dependent on the ratios of the plasma density or the square of the magnetic field across the current sheet. For the case with both initial asymmetries of the magnetic field and density, rather large Hall electric field and charge density are generated.

Huang et al. (2008) studied generation of electric fields at the scale of the local electron Debye length in collisionless magnetic MR through two-dimensional Darwin particle-in-cell simulation. For asymmetric initial temperature and density profile across the Harris current sheet, intense perpendicular electrostatic structure with the local electron Debye-length scaling ($\sim 2.9\lambda_{De}$) is observed near the edge of the magnetic island in the high-temperature/low-density region. It is also found that a weak electron jet with return electron flow on the high-density side results in the formation of an electron current loop. However, in the low density region only a strong electron outflow is detected. Because of a single-looped electric current on each side of the outflow region, the usual quadrupole structure appearing in the earlier symmetric-profile simulations is replaced by a dipole-like structure of the guiding magnetic field. Possible applications of the present results in the dayside magnetopause are discussed.

Huang and Ma (2008) studied collisionless magnetic MR by using two-dimensional Darwin particle-in-cell simulations with different types of open boundary conditions. The simulation results indicate that MR rates are strongly dependent on the imposed boundary conditions of the magnetic field B_x in the inward side. Under the zero-gradient B_x boundary condition, the MR rate quickly decreases after reaching its maximum and no steady-state is found. Under both electromagnetic and magnetosonic boundary conditions, the system can reach a quasi-steady state. However, the MR rate $E_r \sim 0.08$ under the electromagnetic boundary condition is weaker than $E_r \sim 0.13$ under the magnetosonic boundary condition.

A 3D Hall MHD simulation was carried out by Zhang et al. (2008) to study roles of initial current carrier on the topology of magnetic field, generation and distribution of FACs and the appearance of Alfvén waves. The initial equilibrium of magnetic field is determined by one dimensional Harris current sheet with maximum variation in x direction. The initial current density is in +y direction. Several interesting features occur owing to the inclusion of initial ion current carrier in the initial conditions. First, motions of electron and ion are decoupled from each other in the small plasma region (Hall effect region) with a scale comparable with the ion inertial length or ion skin depth $d_i = c / \omega_{pi}$. In the non-Hall effect region, the global magnetic structure is shifted in +y direction under the influence of ions with initial y directional motion. However, in the Hall effect region, magnetic field lines are bent in -y direction affected by the motion of electrons. Therefore, B_y is generated. Second, FACs emerge as a result of B_y . Compared with the prior Hall MHD simulation results, the FACs shift in +y direction as well as the dawn-dusk symmetry is broken. Third, electron and ion Walén relations in Hall plasma are $A_e \equiv \Omega_{e//} / \Omega_{A//}$ and $A_i \equiv \Omega_{i//} / \Omega_{A//}$ respectively. Here $\Omega_{e//}$, $\Omega_{i//}$ and $\Omega_{A//}$ are the electron, ion and Alfvén parallel vortex. We got $A_e \approx 1.36$, $A_i \approx 0.76$ and $A_e A_i \approx 1.03$ in our simulation, which is consistent with the Walén relation in Hall plasma and presents an evidence of Alfvén wave.

Pu et al. (2007) studied 290 fast flow events measured by TC-1 and Cluster with the B_y dominated IMF. They found that in agreement with the component MR scenario, fast flows in the region near the subsolar point are directed mainly north-east or south-west. Consistent with the anti-parallel or the component MR hypotheses, the majority of the fast flows at the high-latitude MP and outer cusps are primarily dawnward and duskward, but having a wide spread of directions into the z direction. Possible X-Lines could be statistically constructed with a tilt angle of $\sim 155^\circ$ in/near the subsolar region and of $\sim 100^\circ$ and $\sim 86.9^\circ$, respectively in the northern and southern hemispheres. These results suggest that both anti-parallel and component MR may occur at the MP under the same IMF conditions. A global S-shaped configuration of the possible X-line could be drawn by interconnecting

the possible X-line in/near the subsolar region and those at high-latitudes.

Wang et al. (2007) reported a FTE at the dayside MP consecutively observed on 4 January 2005 by both the Double Star/TC1 and the Cluster quartet. The event occurred as a magnetosheath FTE first at the Cluster spacecraft at about 07:13 UT and crossed each of the others within 2 minutes. TC1 observed the FTE signature about 108 s after Cluster. All findings including magnetic fluxes, orientations and hot ion velocity distributions suggest that Cluster and TC1 encountered the magnetosheath branch of the same flux tube at two different positions along its length. A globally bended flux rope was reconstructed for the first time based on the five-point measurement.

Wang et al. (2008) reported a conjunction of FTEs on the dayside MP observed on 6 April 2004 by Double TC1 in the equatorial orbit and Cluster tetrahedron in the high latitude. The tube axes of the TC1 FTEs were orientated along the predicted the MR X-line, indicating that they are likely to be generated through Multiple X-line MR or Single X-line Bursty MR near the subsolar MP. The axes of magnetosheath FTEs encountered with Cluster were pointing roughly along the IMF direction, implying that they can either be the extended MR structure originally formed in the low latitudes or the magnetosheath branch of open flux tubes produced via high-latitude MR. A global FTE configuration was proposed based on this conjunction FTEs observation.

Previous theoretical and simulation studies have suggested that anti-parallel and component MR can occur simultaneously on the dayside magnetopause. Certain observations have also been reported to support global conjunct pattern of magnetic reconnection. Wang et al. (2011) show direct evidence for the conjunction of anti-parallel and component MR using coordinated observations of Double Star TC-1 and Cluster under the same IMF condition on 6 April, 2004. The global MR X-line configuration constructed is in good agreement with the “S-shape” model.

Pang et al. (2010a, b) studied the generation and structure of MR in the magnetosheath due to interaction of an interplanetary tangential discontinuity (TD)

with the bow shock and magnetosphere with 3-D global hybrid simulations. As the TD propagates through the bow shock toward the MP, it is greatly narrowed. In cases with a relatively thin solar wind TD, 3-D patchy MR is initiated in the transmitted TD, forming magnetosheath flux ropes. For cases with a relatively wide initial TD, a dominant single X line appears in the subsolar magnetosheath after the transmitted TD is narrowed. A shock analysis is performed for the detailed structure of MR in the magnetosheath. Rotational discontinuity/time-dependent intermediate shock is found to dominate the MR layer.

Zhang et al. (2007) studied configuration of flux ropes observed by TC-1, Cluster and THEMIS in the magnetotail, with application of the Grad-Shafranov (GS) technique to reconstruct the magnetic field component perpendicular to the rope axis. They found that the transverse magnetic field on the cross section is an asymmetric circles, which requires operation of multiple X-line MR. Together with a further application of GS method, Zhang et al. (2010) evaluated the magnetic helicity in the flux rope and discussed the conservation of magnetic helicity in multiple X-line MR and transport of magnetic helicity between different magnetic field configuration. Zhang et al. (2011) further checked if the magnetic field in the flux rope is force-free, a key problem in the study of magnetic flux ropes. The results show that the magnetic fields in the central region of magnetic flux ropes can be regarded as force-free, while with increasing distance from the center, the fields display non force-free feature in the region where the magnetic fields deviate from axial symmetric. The invariant axis direction, cross scale length, and the amount of magnetic flux and current density inside flux rope were also obtained.

Zhang et al. (2010a) studied three typical flux transfer event (FTE) signatures observed by Cluster near the high-latitude magnetopause on 16 January 2004 and simultaneous observations of moving auroral forms (PMAFs) at Yellow River Station, Svalbard. FTEs were shown to mainly move northward with duskward and tailward velocity components, roughly consistent with the observed moving direction of the PMAFs. This provides evidence for an equatorward eroding and poleward moving open-closed boundary associated with a variable magnetopause MR rate under variable IMF conditions.

Zhang et al. (2008a) analyzed the Cluster in situ measurements and CUTLASS Finland radar observations 11 February 2004. In this event, Cluster was crossing the magnetopause into the magnetosheath in the northern high altitude cusp, and encountered three FTEs which were moving northward or northeastward with a scale of $0.87\sim 1.81R_E$. The motion of the flux tubes is consistent with their formation via sub-solar MR and moving away from the source region. It is of interest to show that the ionospheric footprint of the Cluster spacecraft during their boundary passage is found to map centrally within the field-of-view of the CUTLASS Finland radar and the CUTLASS radar auroral features subsequently propagated poleward, forming classic “poleward-moving radar auroral form” structures. Underline physics has been discussed in the paper.

A series FTEs are reported by Zhang et al. (2008b) observed by Cluster spacecraft when they were located near the high-latitude magnetopause, between 11:30-13:00 UT on 1 April 2004. During this pass, simultaneous and conjugated SuperDARN measurements were available that showed a global flow pattern consistent with the expected northwest motion of (predominantly subsolar) reconnected, magnetic flux at the magnetopause. The authors focus on tracking the FTEs’ magnetopause motion together with their corresponding ground mapped motions. It is shown that Flux tube motion, both measured and modeled from the inferred X-line, qualitatively matches the velocity enhancements in the ionospheric convection flows in the northern hemisphere simultaneously measured by SuperDARN, and also roughly matches the observed, south-eastward ionospheric flow in the southern hemisphere. The observed evolution time of the FTEs and ionospheric response time are also reported in the paper.

Based on the simultaneous FGM observations by 4 Cluster satellites, Zhang et al. (2007) calculated and analyzed the current density of FTEs occurred between 12:24 and 12:54UT on 1 April 2004 by using the Curlometer analyzer. It is showed that an intense current flows inside the flux tubes with the current density reaching as high as about $10^{-7}A/m^2$. With the Minimum Directional Derivative (or Difference) (MDD) analysis, the authors found that the FTEs are of the quasi-2D structure, and the direction of the current is almost parallel to the plasma flows and the axes of the flux tubes.

Zhang et al. (2009) reported the observations of TC-1 and Cluster Spacecraft between 12:15 and 12:25 UT on 13 March 2004. In this interval, TC-1 observed a FTE at about 12:19 UT in the magnetosheath to the south of the sub-solar magnetopause and Cluster observed a FTE at about 12:21 UT near the northern high-latitude magnetopause. With the similar features of the magnetic field structures and the plasma data, the authors inferred that these two FTEs might be the same structure moving through TC-1 and then Cluster. Detailed analysis shows that the FTE flux tube was moving northeast and tailward with a quasi-2-D structure of scale of $\sim 1.21 R_E$, which is consistent with its arising from MR at a low-latitude site. More detailed features of the FTE are studied in the paper with usage of the Cooling model.

IV. WAVES AND INSTABILITIES IN THE MAGNETOSPHERE

Du et al. (2009) studied the Mirror waves and mode transition observed in the magnetosheath based on Double Star TC-1 measurements made on 26 February 2004. Strong compressional signatures lasting for more than an hour were found near the magnetopause (MP) behind a quasi-perpendicular bow shock. These compressional structures are most likely mirror mode waves. There is a clear wave transition in the magnetosheath which probably results from the change of the IMF cone angle. The wave characteristics in the magnetosheath are strongly controlled by the type of the upstream bow shock.

Du et al. (2008) studied low-frequency fluctuations (in the range of time periods from 4 s to 240 s) in the magnetosheath observed by Double Star TC-1 and Cluster in 2004. The characteristics of the magnetic field fluctuations are strongly controlled by the angle between the upstream IMF and the normal of the bow shock. Generally the magnetic field fluctuations in the quasi-parallel magnetosheath are more intense than those in the quasi-perpendicular one. Almost purely compressional waves are found in the quasi-perpendicular magnetosheath. With the increase of the local plasma β , both the magnitude and direction of the magnetic field fluctuate more intensely. An inverse correlation between the local temperature anisotropy T_{\perp}/T_{\parallel} and the plasma β is found.

Xiao et al. (2006c) used a linear theory to study the instability threshold of whistler-mode for two typical plasma regions: the higher density (or a weakly magnetized) region, and the lower density (or a strongly magnetized) region. They found that (a) in the case of a regular bi-Maxwellian, the instability threshold obeys a general form of $T_{\perp}/T_{\parallel} - 1 = S/\beta_{\parallel}^{\alpha}$, with a narrow range of the fitting parameter: $0.25 \leq \alpha \leq 0.52$ over $0.01 \leq \beta_{\parallel} \leq 2.0$; (b) the instability threshold in the higher density (or a weakly magnetized) region is generally lower than that in the lower density (or a strongly magnetized) region, with the fitting parameter range $0.3 \leq S \leq 5.0$ in the higher density (or a weakly magnetized) region and $0.32 \leq S \leq 6.94$ in the lower density (or a strongly magnetized) region; (c) the instability threshold for the kappa distribution generally decreases as the spectral index κ increases, and tends to the lowest limiting values of the bi-Maxwellian as $\kappa \rightarrow \infty$. These results may present a further insight into the instability threshold condition for the whistler-mode waves in the outer radiation belts of the Earth, the inner Jovian magnetosphere, and other space plasmas where an anisotropic hot electron component and a cold plasma component are both present.

Xiao et al. (2007c) examined the EMIC instability driven by the temperature anisotropy condition ($T_{\perp}/T_{\parallel} > 1$) of superthermal protons modeled with a typical kappa distribution in a cold multi-species plasma (electron, H^+ , He^+ and O^+). The instability threshold condition, as in the case for a regular bi-Maxwellian, was found to follow a typical form $T_{\perp}/T_{\parallel} - 1 = S/\beta_{\parallel}^{\alpha}$, with higher values in the He^+ band than those in the H^+ band in the case of the strong wave instability. As the spectral index κ increases, the instability threshold generally decreases and tends to the lowest limiting values of the bi-Maxwellian. The densities of the cold components (particularly protons) have impacts on the threshold condition primarily in the H^+ band, with a higher density of cold protons, a lower value of the threshold condition. These results may further reveal the nature of this instability threshold condition for the EMIC waves in any space plasmas where an anisotropic superthermal ion component and cold multi-components are present together.

Xiao (2006) and Xiao et al. (2008a) suggested a fully relativistic kappa-type (KT) distribution to model the highly energetic particles in plasmas where magnetic

mirror geometries occur. The new KT distribution combines the features of the well-known kappa type and loss-cone type, and follows the power-law at both the lower energies and the relativistic energies. Furthermore, such kappa-type distribution is found to fit very well with the solar energetic particles (Xiao et al., 2008c), and well with the geostationary orbit electrons (Xiao et al., 2008b).

Xiao et al. (2006b) investigated the growth rate of field-aligned whistler-mode waves in space plasmas by using a fully relativistic treatment, including a recently developed relativistic kappa-loss-cone (KLC) distribution and a fully relativistic growth rate formula. They found that, in the lower wave frequency, the wave growth by the KLC distribution is generally higher than that by the kappa distribution, due to a larger fractional number of the resonant electrons η_{rel} (which controls the wave growth) for the KLC distribution; but is lower in the higher wave frequency. The growth rates tend to increase with the thermal anisotropy A , and the peak wave growth increases more rapidly for the kappa distribution. The relativistic anisotropy A_{rel} basically decreases as the thermal parameter θ^2 increases; whereas the fractional number of the resonant electrons η_{rel} is found to be large in the case of $\theta^2 \sim 150$ keV, and results in a large wave growth. This indicates that hot electrons with typical energies of hundreds of keV may play a dominant role on the instability of whistler-mode waves. The results above have applications to plasma wave instability in the outer radiation belts of the Earth, the Jovian inner magnetosphere, and other astrophysical plasmas where relativistic electrons are present.

Zhou et al. (2008) study the generation mechanism of modulated electron plasma waves with different polarizations via two dimensional particle-in-cell simulations. Modulated electron plasma waves are often observed in space plasma. It is shown that weak beam instability could generate the modulated Langmuir wave and the ambient magnetic field plays an important role in the formation of modulation. When the weak beam has loss cone distribution, highly modulated upper hybrid waves are generated and propagate with large angle to the ambient magnetic field.

Lu et al. (2008) and Wu et al. (2010) studied transverse instability and perpendicular electric field in 2D electron phase-space holes by performing 2D

electrostatic particle-in-cell simulations. Evolution of E_{\perp} in such electron holes under different plasma conditions was investigated and the generation mechanism of the uni-polar structures of E_{\perp} was discussed.

Han et al. (2007b) studied a typical Pi3 pulsation based on magnetic field measurements from multiple satellites and ground stations. Low - latitude ground observations with a wide longitudinal span indicate that the amplitude of the Pi3 pulsation peaks on the dayside and is gradually decreasing toward the nightside, implying that the source of the Pi3 lies on the dayside. Variations in solar wind dynamic pressure observed by the GEOTAIL satellite (just outside of the magnetosphere) are highly correlated with these ground magnetic field variations. The authors argue that this global Pi3 pulsation is directly driven by impulsive variations in the solar wind dynamic pressure. The Pi3 pulsation observed along the latitudinal magnetometer chain at 0930LT shows significant equatorial enhancement. The low - altitude polar orbiting satellite Oersted also observed this pulsation in the dayside inner magnetosphere. The B_{\parallel} (northward) component at Oersted is strictly out of phase with the X component observed at the dip equator below the spacecraft path, which indicates that the Pi3 pulsation at the dip equator is caused by oscillation of an ionospheric current. The authors propose that the Pi3 pulsations at different latitudes are generated by different mechanisms.

Han et al. (2008b) investigated frequency differences of Pi2 pulsations between the dayside and the nightside with two case studies. Firstly, it is found that the dominant frequency peaks at the dayside showed latitudinal dependence, i.e., the higher (lower) frequency peak was predominant at lower (higher) latitude. Meanwhile, the dominant Pi2 frequency on the nightside was apparently higher than that on the dayside. The authors argue that the multiple frequency peaks observed on the ground are harmonics of a plasmaspheric cavity resonance mode (CRM) and that the latitudinal dependence of the dominant frequency peaks may result from the energy coupling between the CRM and field line resonance (FLR) occurred in the near Earth space. Furthermore, the frequency difference between the dayside and the nightside could be caused by the fact that a higher harmonic was observed in the nightside plasmasphere but was not effectively observed in the dayside. In addition, the authors statistically examined 829 Pi2 events that were

simultaneously recorded at Kakioka (KAK, Maglat=27.2°) and Jicamarca (JIC, Maglat=0.0°). They found that the statistical results are consistent with the facts reflected by case studies.

Liu et al. (2008) studied phase structure of Pc3 waves simultaneously observed from 09:20 to 10:10 UT on 1 April 2004 by Cluster satellites and Zhongshan, Davis and Mawson magnetometers, Antarctica. When Cluster was located on closed field lines equatorward of the exterior northern cusp, Zhongshan and Davis were near the ionospheric footprint of the southern cusp. The Pc3 waves observed by Cluster spacecraft with a frequency of about 25 mHz have a wavelength of about 5200 ± 2400 km and wave vector is directed almost perpendicular to the geomagnetic field ($94.6^\circ \pm 10.4^\circ$). The wave Poynting flux indicates that wave energy is transported predominantly along the magnetic field line toward the ionosphere. These results show that the Pc3 waves near the cusp are shear Alfvénic waves guided by closed field lines in the low-latitude boundary of the cusp and reflected from the ionosphere. The authors suggest that these waves may result from incoming MHD fast waves from the upstream solar wind that couple to shear Alfvén waves guided by the magnetic field at high latitudes and excite field line resonance in various harmonics at middle and low latitudes.

Liu et al. (2009) utilized the wave coherency methods to analyze ULF waves in the Pc3 band that were simultaneously observed by the Cluster satellites near the exterior cusp and by ground stations at local magnetic noon near the footprint of the cusp. The results show that the coherency of waves observed at the ground on the H component is much larger than on the D component, opposite to that seen by Cluster in space. The coherency between the H component on the ground and the y component in space is higher than the other combination of pairs, with the coherency between the satellite and the Daneborg (DNB) station having the maximum value. These results suggest that the polarization of the waves is rotated by 90° after propagating through the ionosphere, and the magnetic footprint of Cluster is closest to the DNB station at this time. The coherency of the Pc3 waves between the satellites is highly related to the alignment of satellite pairs with respect to the geomagnetic field direction. This alignment may provide a transverse scale size of the geomagnetic Pc3 ULF waves near the exterior cusp at about

900km with a coherency of 0.65.

V. MAGNETOSPHERIC CONFIGURATION

1. The plasma sheet and bursty bulk flows

Basing on the data from three satellites of Cluster (C1, C3 and C4) in the year of 2001 and 2002, Ma et al. (2007) examined the relationship between the rapid convection event (RCE) and substorm. The observation of RCE measured by single satellite is not exactly what happened in the magnetotail. For instance, both C1 and C3 observed the event occurring on July 25, 2002, but C4 did not. Among the 306 RCEs jointly measured by three satellites, 215 ones were observed by C1. C3 and C4 obtained 266 and 227 ones respectively. The average duration of RCE in the magnetosphere can't be really represented by the outcome surveyed by single satellite. The present analysis has shown that RCE transports more fractions of energy and magnetic flux than what had calculated by single satellite in the central plasma sheet.

Cao et al. (2008) found that bursty bulk flows (BBFs) in the near earth plasma sheet can excite simultaneously long period Pi2 (90-130s) and short period Pi2 (~50s). The long period Pi2 is transient response type associated with FAC produced by the braking of BBFs. The time delay for the propagation of Alfvén waves from Cluster to the Earth is very close to the time difference between the onset time of the BBFs at Cluster and the starting time of the long period Pi2 on the ground. The short period Pi2 is a global cavity mode since the Pi2s in H components at eight stations have almost the same starting time, same oscillation period and same waveform, which are all typical characteristics of cavity mode.

A statistical study is performed by Ma et al. (2009) on the velocity distribution, density, duration and energy transport of earthward flow bursts in the inner plasma sheet (IPS) during three substorm phases using the data of Cluster in 2001 and 2002. The mean peak velocity of earthward flow bursts in recovery phases (390 km/s) is smaller than those in growth and expansion phases (490 km/s and 520 km/s). The super earthward flow bursts ($V > 1000$ km/s) appear more frequently in the expansion phase. The average ion density of earthward flow bursts in the recovery phase is 0.14 cm^{-3} , much smaller than those in the growth phase and expansion phase (0.28 and 0.21 cm^{-3}), indicating that lobe MR most likely occurs in the recovery phase. The average durations of earthward flow bursts in recovery phase is 48 s, smaller than those in growth and expansion phases (99 s and 103 s), suggesting that the MR occurring in the recovery phase is rather short lived. The earthward flow bursts in the expansion phase have largest capability of the transport of energy, about 7 times that in the recovery phase. Thus the earthward

flow bursts in the expansion phase have largest capability of the transport of energy and can produce largest impact effects to the inner magnetosphere

Cao et al. (2010) used plasma data from Cluster and TC-1 and geomagnetic data to study the geomagnetic signatures of the current wedge produced by fast flow braking in the plasma sheet. Three fast flows were adopted which occurred in a very quiet background, accompanying by no (or weak) particle injections and under weakly southward IMF condition. It is shown that the fast flows can produce a complete current wedge which contains post-midnight downward, pre-midnight upward field aligned currents, and westward electrojet. It has been known that the AL drop that a BBF produces is proportional to its velocity and duration. In the three cases, the AL drops are smaller than 100 nT. Since the AE increase of a typical substorm is larger than 200 nT, whether a substorm can be triggered depends mainly on the conditions of the braking regions prior to fast flows. The observations of solar wind prior to the three fast flows suggest that it is difficult for the fast flows to trigger a substorm when the IMF B_z is weakly southward.

Cao et al. (2010a) compared the observations of BBF by single satellite with those by Cluster multi satellites. Their results showed that there exists remarkable difference between observations of BBF by single satellite and multi satellites. The observations of BBF by a single satellite depend on its position relative to the flow channel. The difference is caused by the localization characteristics of fast flows, and can lead to diverging views about substorm and causal relations among substorm phenomena.

Ma et al. (2010) studied the occurrence rate, probability function of velocity and duration of earthward BBFs in the Inner Plasma Sheet (IPS, $\beta > 0.5$) using the data of Cluster in 2001 and 2002. The occurrence rate of earthward BBFs increases with distance from the Earth up to -19 RE, which is in agreement with the previous observations of the radial evolution of BBFs. About 54% of earthward BBFs in expansion phase have a velocity larger than 600 km/s, whereas only 38% of earthward BBFs in growth and recovery phases have a velocity larger than 600 km/s. The average velocity of earthward BBFs in expansion phase is 732 km/s, larger than those in growth phase (631 km/s) and recovery phase (617 km/s). The

durations of earthward BBFs decrease with the decrease of downtail distance from Earth due to the braking of earthward BBFs. The duration of earthward BBFs in expansion phase is larger than that in growth and recovery phases. The average durations in growth, expansion, and recovery phases are respectively 49.3, 71.5, and 47.6 s. Therefore, the ratios of transports of energy of earthward BBFs in growth, expansion, and recovery phases can be estimated to be 0.51:1:0.47. Thus, the earthward BBFs in the expansion phase have the largest capability of the transport of energy and can produce the largest braking effects.

With the 4-s resolution Double Star TC-1 data from June to November of each year during the period of 2004-2006, Zhang et al. (2009) statistically analyzed the occurrence rate of both convective and field-aligned bursty flows. In the region $-13 R_E < X < -9 R_E$, $|Y| < 10 R_E$, $|Z| < 4 R_E$, there are in total 80 convective bursty flow events and 430 field-aligned bursty flow events with a criterion that the duration time of both $V_{\perp x} > 180$ km/s and $V_{\parallel x} > 180$ km/s exceeds 30 s, where $V_{\perp x}$ and $V_{\parallel x}$ are irrespectively the X component of the velocity vector perpendicular and parallel to the local magnetic field. The statistical results show that the occurrence rate of the convective bursty flow (CBF) reached a minimum around $-11.5 R_E$; the occurrence rate of the field-aligned bursty flow (FABF) has a sudden decrease around $-11.5 R_E$, but has no clear increase inside $-11.5 R_E$. The spatial distribution of the all types of bursty flows shows that there had no deflection flows in the azimuthal direction related to the absence of the convective bursty flows inside $13 R_E$ explored by TC-1. The magnetic field analysis indicates that there exists a minimum in B_z around $12 R_E$. The minimum B_z may have close relation with the flow braking.

Deng et al. (2010) show the THEMIS observation of the electron injection, which was closely associated with a dipolarization front and bursty bulk flows. The electron injection occurred within a thin plasma boundary layer and had both perpendicular and parallel energization with very little energy dispersion. The thin plasma boundary layer had a thickness comparable to the ion inertial length and displayed different plasma characteristics at different locations. Strong electromagnetic waves between the lower hybrid frequency and the electron

gyrofrequency, and electrostatic waves up to the electron plasma frequency were observed within the thin plasma boundary layers. Near the electron injection region, nonlinear electrostatic structures such as electrostatic solitary waves and double layers were also observed. The observations show that non-ideal MHD, non-linear and kinetic behavior is intrinsic to the electron injections with multi-scale coupling.

The effect of guiding field to low-frequency electromagnetic instabilities in the collisionless current sheet was studied by Wei et al (2007) with the dispersion relation obtained by collisionless and compressible MHD model. The result show that (1) if there is not guiding field on the middle plane of current sheet ($z=0$), no instability observed; whereas if there is guiding field, instabilities take place. (2) Near the middle of current sheet ($z=0.2$), instabilities of whistler or low-hybrid mode occur. The grow rate is increasing with increasing of guiding field. (3) Near the edge of current sheet ($z=0.8$), the effects of guiding field become not clearly.

A magnetotail event on 15 September 2001 is analyzed by Cai et al. (2008), during which the Cluster spacecraft observed both embedding and bifurcation of the Thin Current Sheet (TCS). It is indicated that the ion anisotropy and non-gyrotopropy are responsible for those new equilibrium features that represent deviations from the conventional Harris model. Measurements show that an embedded proton TCS manifests a pressure anisotropy with $p_{\parallel} > p_{\perp}$, associated with a density embedding; while a bifurcated oxygen ion TCS exhibits a pressure anisotropy with $p_{\parallel} < p_{\perp}$ and non-gyrotopropy, except at the edges where $p_{\parallel} > p_{\perp}$ is necessary for marginal firehose stability condition. The local flapping motion of the TCS was observed, and some particular features such as the solitary wave-like behavior and the kink motion in the plane perpendicular to the Sun-Earth direction were revealed. The present investigation intimates the complexity of equilibria of the magnetotail current sheet and declares the crucial role played by the ion kinetics in the dynamics of TCSs.

Using the data of Cluster on 8 November 2004, Wang et al. (2010) analyze the ULF waves associated with earthward periodical high speed flow in magnetotail plasma sheet. The results show that the ULF waves enhance and end at the same times as the periodical high speed ion flow does. Particularly, the oscillation frequencies in ion flow velocity and magnetic field are both between 60~70 mHz,

i.e. in the frequency range of Pi1. These observations show that there is a close correlation among the ULF waves in periodical high speed flow, magnetic field and ion temperature. The oscillation of the high speed flow is approximately out of phase with the ULF wave in magnetic field and in phase with the ion temperature. The results of Minimum Variance Analysis show that although the wave propagation direction includes earthward component, the major propagation direction is towards the centre of plasma sheet and perpendicular to both the high speed flow velocity and magnetic field. All these observations indicate that periodical high speed flows can generate ULF waves at the same frequency.

Xu and Li (2006) studied the 3D configuration of the non-adiabatic region and the magnetic field lines (MFLs) in the magnetosphere based on the Tsyganenko magnetic field model. According to the parameter $d = dB/B$, the magnetosphere can be divided into the adiabatic and non-adiabatic region. A thin non-adiabatic region has been found in the near tail, which moves toward to the Earth during the geomagnetic disturbance. Pitch angle scattering occurs when particles go through the non-adiabatic region, which is expected as the source region of the precipitating particles. Moreover, by investigating the 3D configuration of MFLs, the authors find that MFLs remain in the noon meridian plane if their foot prints are in the noon meridian plane; but leave from the foot print plane and are swept tailward if their foot prints are not in the noon meridian plane. The characteristics of the MFLs suggest that the precipitation region is almost in the nightside, centered near midnight.

Based on the theory of magnetospheric particle dynamics, the guiding center and magnetic field line tracing methods are used by Huang et al. (2008) to calculate the drift shell splitting of particle motion in the radiation belt. The initial location of the particles is $\leq 9R_E$ with different initial pitch angles. Different Kp index and solar wind pressure, corresponding to T89c and T96 magnetic field model, are compares to each other. The results show that drift shell splitting varies with initial position, pitch angles, Kp index and solar wind pressure. The details are (1) the drift shell splitting is stronger when the radius distance increases. Particles starting from noon will be trapped stably; otherwise, particles starting from night will escape from the magnetopause, when the initial radius distance and pitch angle are

large. (2) When the initial pitch angle on the magnetic equatorial plane increases, the drift shell of particles starting from noon align inward, but from night align outward. (3) Drift shell splitting becomes obvious when Kp index or solar wind pressure increases, and the basic character and trend under these two disturbance parameters are the same.

Ding et al. (2010) studied the plasma sheet ion boundary in the (U,B) coordinates based on the drift path theory. The open and close drift path and their variations with Kp index are discussed. In high energy situation, the radial distance from the Earth to the boundary is increasing with increasing of energy, and the distance in dawn side is much larger than that in dusk side. On the other hand, in the low energy situation, the radial distance is decreasing with increasing energy, and the radial distance in the dusk side is larger than in the dawn side. Their results also show that with the increase of Kp index, all boundaries of various energy particles move towards the Earth, with the shape of the boundary keeping unchanged in low energy situation, and changed remarkably in high energy situation. But performances of ion boundaries in high and low situations are different. To, the inner boundary shape of ion almost keeps constant with the increase of Kp index. To high energy situation, its shape will with Kp index.

Cao et al. (2011) used the ion data recorded by TC-1 from 2004 to 2006 to study the distribution of inner boundary of ion plasma sheet (IBIPS) and for the first time show the observational distribution of IBIPS in the equatorial plane. The IBIPS has a dawn-dusk asymmetry, being farthest to the Earth in the 0600-0800 LT and closest to the Earth in the 1800-2000 LT. Besides, the IBIPS has also a day-night asymmetry, which may be due to the fact that the ions on the dayside are exposed more time to loss mechanisms on their drift paths. The radial distance of IBIPS (R_i) decrease generally with the increase of Kp index. The mean radial distance of R_i basically larger than 6.6 RE during quiet times and smaller than 6.6 RE during active times. When the convection electric field increases, the inward shift of IBIPS is most significant on the night side (2200-0200 LT). For $K_p \leq 0+$, only 16% of IBIPSs penetrate inside the geosynchronous orbit. For $2 \leq K_p < 3+$, however, 70% of IBIPSs penetrate inside the geosynchronous orbit. The IBIPS has weak

correlations with the AE and Dst indexes. The average correlation coefficient between Ri and Kp is -0.58 while the correlation coefficient between Ri and AE/Dst is only -0.29/0.17. Particularly, Ri and Kp are highly correlated ($r=-0.72$) in the night sector, meaning that Ri in the night sector has the good response to the Kp index. These observations indicate that Kp plays a key role in determining the position of IBIPS.

Based on the geometrical features of the tail current sheets deduced from the multiple spacecraft data analysis, Shen et al. (2008a) found that the tail current sheets may be divided into three types: the normal current sheet, the flattened current sheet (Shen et al., 2008b) and the tilted sheet (Shen et al., 2008c). The normal current sheet is typically observed, in which the MFLs are plane curves with constant binormals parallel to the equatorial plane; the current density is normal to the magnetic field lines (MFLs) and lies along the binormal.

In Shen et al. (2008b) the features of the flattened current sheet are thoroughly studied. The flattened current sheet (FCS) has a strong guide field, or B_y component. In the corresponding neutral sheet, the magnetic field lean towards the equatorial plane and rotate around the normal direction from tailward in the southern hemisphere to earthward in the northern hemisphere. In the FCS, the MFLs are spiral-like. The half-width of the corresponding neutral sheet is much less than the minimum radius of curvature of the MFLs and the current density in the neutral sheet is duskward and nearly field-aligned. The curvature current makes little contribution to the total current in the flattened current sheet. The main current carriers in the neutral sheet of the flattened current sheet are electrons. A statistical survey shows that, there is a positive correlation between B_y in the FCS and IMF B_y . FCS may occur in both quiet and disturbed periods and may appear at all phases of the substorms. During the growth phase of substorms, the neutral sheet of the FCS is shown to become progressively thinner, while the associated current density is increasing gradually. It is found that the northern turning of the IMF may lead to an explosive growth phase at the end of the growth phase which lasts for several minutes, during the explosive growth phase the FCS becomes much thinner and the current density in the neutral sheet increases considerably. Just after the onset of the substorms, the current density in the neutral sheet drops

abruptly and varies turbulently.

Shen et al. (2008c) analyzed the geometrical structures of tilted current sheet (TCS) and tail flapping waves based on Cluster multiple spacecraft measurements. Some features of the TCSs have been made clear for the first time. The geometrical features of the TCS are as follows: (1) The MFLs in the TCS are generally plane curves and the osculating planes in which the MFLs lie are about vertical to the equatorial plane, while the normal of the TCS leans severely to the dawn or dusk side. (2) The TCS may become very thin, the half thickness of its neutral sheet is generally much less than the minimum radius of the curvature of the MFLs. (3) In the neutral sheet, the FAC density becomes very large and has a maximum value at the center of the current sheet. (4) In some cases, the current density is a bifurcated one, and two humps of the current density often superpose two peaks in the gradient of magnetic strength, indicating that the magnetic gradient drift current is possibly responsible for the formation of the two current humps. Moreover, TCSs often appear along with tail current sheet flapping waves. In the tail flapping current sheets, the current sheet is tilted substantially, and the minimum curvature radius of the MFLs is rather large being around $1R_E$; while the neutral sheet may be very thin, with its half thickness being several tenths of R_E . The phase velocities of these flapping waves are several tens km/s; their periods and wavelengths are several tens of minutes and several earth radii, respectively. These tail flapping events generally last several hours, occur during quiet periods or weak magnetospheric activity.

Sun et al. (2010) made a statistical study by using Cluster data on the flapping motion of the magnetotail current sheet. Their results showed that although most flapping motions were propagating toward the tail flanks, which is consistent with previous studies, the proportions of the flapping motion propagating toward midnight (where $|Y_{GSE}|=0$) were found to be higher than in previous studies. Flapping motions of the current sheet in the middle area ($|Y_{GSE}|<8 R_E$) of the magnetotail were investigated. Relatively high value of the Z component of the velocity further confirms that the middle area of the magnetotail might be a source region for the flapping motion propagating towards the tail flanks. They found that the way that the flapping motion propagate toward midnight area differs

significantly from that toward dusk and dawn, indicating that there might be two different kinds of flapping motion originated from different sources.

Zong et al. (2008a) showed two extreme oxygen-rich BBFs with predominant ionospheric O^+ ions observed on 8 November 2004 by the Cluster and Double Star spacecraft during a strong magnetic storm time period with $Dst = -373$ nT. The O^+ densities in two BBFs are found to be 3–5 times larger than the H^+ densities and the oxygen thermal pressures in the BBFs are 8 times higher than the hydrogen thermal pressure. These BBFs are associated with nested magnetic structures and are observed simultaneously by the Cluster and the Double TC-1 spacecraft. Thus, the flow braking region should be greatly pushed inside the usual pressure balance region (even inside the inner magnetosphere) since the BBF is dominated by oxygen ions. Results in this paper indicate that O^+ dominated BBFs can be formed during a strong magnetic storm time period. The observations made in this paper suggest that O^+ embedded in the BBFs could be carried into the ring current region by bursty flows during very intense magnetic storms.

Tian et al. (2010) showed a series of earthward-moving (~ 140 km/s) plasma flow vortices with anticlockwise (when viewed from above the ecliptic plane) rotation in the dawnside tail plasma sheet between 1255 and 1400 UT on 6 July 2003. These flow vortices were observed under the condition of northward IMF with an enhanced solar wind dynamic pressure. Analyzing the plasma and magnetic field data from the Cluster spacecraft and using the Grad-Shafranov streamline reconstruction technique, the authors show that the vortex-like plasma structures have a very similar shape: a V_x component dominant in the dawnside, while a distinct V_y component appears in the duskside, and each structure has a size of about $1.8 \times 0.68 R_E$, approximately in the xy plane of GSM coordinates. It is found that the vortices contain both magnetosphere-originated hot ($N \sim 0.1 \text{ cm}^{-3}$, $E > 3$ keV) and magnetosheath-originated denser and colder ($N > 0.2 \text{ cm}^{-3}$, $E < 1$ keV) populations on the closed field lines. The vortices involve fast earthward flows ($V_x > 200$ km/s) of mainly sheath-originated plasmas. The authors suggest that these observed plasma flow vortices are generated inside the magnetotail during the prolonged and intensified compression of the magnetosphere by the enhanced solar wind dynamic pressure.

2. Plasmasphere

Xie et al. (2008) presented a study of the characteristic and properties of ULF waves in the plasmasphere boundary layer during two very quiet periods. The ULF waves were detected by Double Star TC-1 when the spacecraft passed through the plasmasphere in an outbound and inbound trajectory, respectively. A clear association between the ULF waves and periodic variations of energetic ions fluxes is observed. The observations show that the wave frequency is higher inside the plasmasphere than outside. The mechanism generating these ULF waves and possible diagnosing of the “classical plasmopause” location with the ULF wave are discussed.

Yuan et al. (2010) report observations of ULF wave from a Cluster satellite in the outer boundary of a plasmaspheric plume on September 4, 2005. The band of observed ULF waves is between the He⁺ ion gyrofrequency and O⁺ ion gyrofrequency at the equatorial plane, implying that these ULF waves can be identified as EMIC waves generated by ring current ions in the equatorial plane and strongly affected by rich cold He⁺ ions in plasmaspheric plumes. During the interval of observations, the footprint of Cluster SC3 lies in a subauroral proton arc observed by the IMAGE FUV instrument, demonstrating that the subauroral proton arc was caused by energetic ring current protons scattered into the loss cone under the Ring Current-EMIC interaction in the plasmaspheric plume. This paper provides an evidence that EMIC waves can be generated in the plasmaspheric plume and scatter ring current ions to cause subauroral proton arcs.

Fu et al. (2010a) reported coordinated observations of a density trough within the plasmasphere using the measurements from the radio plasma imager (RPI) and extreme ultraviolet imager (EUV) on the IMAGE satellite and the measurements from DMSP F - 15. The density trough inside the plasmasphere with a width of ~ 0.7 RE from $L \sim 2.3$ to $L \sim 3.0$ was observed in ~ 2130 magnetic local time (MLT). The plasmasphere images taken by the IMAGE EUV confirm that the density trough is inside the plasmasphere. The RPI active sounding measurements

reveals that the density trough extends along the magnetic field from the IMAGE orbit to at least 41° magnetic latitude. Meanwhile, the DMSP - F15 satellite detected a light ion density trough at the same time on the same L shells and similar MLT sector. These coordinated observations demonstrate, for the first time, that the density trough is a low - density plasmaspheric structure extending from the plasmasphere to the topside ionosphere along the geomagnetic field lines.

By analyzing the sounding measurements from the IMAGE Radio Plasma Imager, Fu et al. (2010b) studied two cases concerning the nightside - to dayside evolution of the corotating inner magnetosphere. One, under a quiet geomagnetic condition, shows a typical evolution process during which the plasmopause was observed on both the nightside and the dayside. The other, during the recovery phase of a magnetic storm, shows a different inner magnetospheric structure in which the distinct plasmopause observed on the nightside becomes unidentifiable on the dayside as the density in the nearly empty nightside plasma trough increases to a level similar to that of the plasmasphere. It is shown that the evolutions of the inner magnetosphere in both cases were primarily controlled by the fast plasma refilling of the flux tubes from the ionosphere as the flux tubes drift from the nightside to the dayside. In the former case the fast refilling was confined inside $L \sim 6.3$, while in the latter case the fast refilling extended to at least $L = 10$. The present observations provide an example for fast refilling as a possible cause of the smooth density transition from the plasmasphere to the subauroral region and demonstrate the importance of the plasmasphere - ionosphere coupling in controlling the structures of the inner magnetosphere.

Huang et al. (2009) studied the deduction of the global density of the Earth plasmasphere from the column density by using Computer Tomography (CT) technique, which has been achieved by the well known Filtered Back Projection (FBP). Due to the Earth's shelter, using this method, there will be a gradual deviation from the original Phantom Diagram, especially in the dayside area near the Earth. This deviation can be acknowledged through further quantitative analysis. An improved accuracy of reconstruction is achieved by using Algebraic Reconstruction Technique (ART). Their reconstruction quality has been analyzed through the correlation coefficient between the Phantom Diagram and the

reconstruction results, the value of ART approach is 0.98, while FBP approach is only 0.86. The result has established that the ART is more efficient than the FBP when the Phantom Diagram includes Earth's shelter.

Li et al. (2009) introduced a new topic for imaging plasmasphere density with CT techniques. Both parallel-beam and fan-beam reconstruction formulas are derived with a special weighting function. Different from the traditional X-ray CT, the extreme ultraviolet (EUV) radiation may be totally absorbed by the Earth. Only the portion between the Earth and the detector enters the EUV sensor and be measured. The key step in our derivation is to remove the complete absorption effect with a specific weighting function. Computer-simulation studies are present to verify our formulas for the plasmasphere density

A 3D phantom for the density distribution of the plasmasphere is established by Chen et al. (2010). The imaging processes of the extreme ultraviolet (EUV) Imager are computer simulated, in which the Earth shelter is treated as a main problem. A modified ART method is devised to resolve the incomplete data reconstruction problem to validate and evaluate the proposed methods. The cone-beam EUV data are simulated based on the 3D phantom from both a circular and semi-circular trajectories. Quantitative reconstruction results demonstrate the correctness of the proposed modified ART algorithm. The CT technique can be used to calculate the global density of the plasmasphere from the EUV data.

3. Cusp

Zong et al. (2008) reported four cusp-like regions observed consecutively in about five hours by all four Cluster spacecraft when the IMF was northward with a significant B_y component. All four cusp-like encounters were characterized by turbulent magnetic fields, high-density plasma, and plasma flow significantly slower than the magnetosheath level. The cusp-like regions are associated with thermalized, bidirectional distributed plasma electrons. The first encountered cusp is the main cusp; the other three cusp-like regions are temporal effects. The boundary normal, velocity, and timing analysis for six clear boundaries of the last

three cusps indicates that they are most likely one boundary shifting in the dawn-dusk direction between the dayside magnetosphere/trapping region and the cusp region. All these indicate that the Cluster spacecraft have been observing the same cusp, and it appeared as four cusp-like regions due to possible magnetospheric oscillations. Oscillations with a period of 22 min are observed by the Cluster spacecraft in the high-latitude region, which is in agreement with the cold-dense plasma sheet fluctuations (20 min period) observed by the Geotail satellite.

Cai et al. (2009) made a study of the cusp behavior during a four hours interval on 12 February 2003 characterized by a series of rapid reversals in the B_z -dominated IMF. During this interval the IMF B_z underwent four reversals, remaining for around 30 min in each orientation. The Cluster spacecraft were on an outbound trajectory through the Northern Hemisphere magnetosphere. Both Cluster and the EISCAT radar were observing the cusp region. The series of IMF reversals resulted in a sequence of poleward and equatorward motions of the cusp; consequently Cluster crossed the high altitude cusp twice before finally exiting the dayside MP, both times under conditions of northward IMF B_z . The first magnetospheric cusp encounter showed reverse ion dispersion typical of lobe reconnection (MR); subsequently, Cluster spacecraft 1 and 3 (only) crossed the cusp for a second time. The cusp in the first crossing is a “typical” northward-IMF one, with short-lived ion injections of evident “reversed” dispersion signatures. In the second crossing, however, the cusp appears to be a region reminiscent of the Stagnant Exterior Cusp (SEC). In addition, evident upward-flowing O^+ ion bursts, possibly original from polar ionosphere, are also detected during the second cusp crossing, together with enhancement of trapped magnetospheric-like electron fluxes. We suggest that the SEC-like cusp is likely on newly closed field lines, which were first reconnected (being opened) at low latitudes and later reconnected again (being closed) poleward of the northern cusp.

Guo et.al. (2007) made a statistical study on the properties of ions (O^+ , He^+ and H^+) measured by the Cluster in cusp region as a function of the solar wind dynamic pressure and geomagnetic index. The main results are that O^+ density responds in a significant way to Kp but He^+ doesn't. Both of them have a significant positive

correlation with solar wind dynamic pressure. The H^+ density is increased with solar wind dynamic pressure, and not correlated with K_p .

Guo et.al. (2008) studied the dipole tilt angle effect on the latitude of the mid-altitude cusp. The results show that the dipole tilt angle has a clear control of the cusp latitudinal location. When the dipole tilts sunwards, the cusp is shifted poleward. The northern cusp moves 1° ILAT for every 15.4° increase in the dipole tilt angle, while the southern cusp moves 1° ILAT for every 20.8° increase in the dipole tilt angle.

Shi et al. (2009a) studied Magnetic depression structures (magnetic holes) of short time duration from seconds to minutes using Cluster data in the high-latitude cusp. Their multi-spacecraft analysis revealed that the magnetic depressions are spatial structures. They showed that multiple properties of the magnetic depressions are consistent with those of mirror structures observed in the magnetosheath or solar wind. The plasma in the cusp is rarely unstable with respect to mirror instability. However, as has been shown by previous studies, once a large magnetic hole is created by mirror instability, it becomes relatively stable and can survive for extended periods of time even if surrounding plasma conditions drop well below the mirror threshold. Although local generation of these structures cannot be completely ruled out in some cases, they proposed an interpretation of the magnetic depressions observed in the cusp as mirror structures generated in the magnetosheath and enter the cusp due to the open geometry of the cusp magnetic field.

In contrast to the southward IMF cases, in which a turbulent and diffusive entry layer is present equatorward of the cusp, Shi et al. (2009b) found a transition layer (without significant turbulence and diffusive properties) that shows clear differences in plasma parameters compared to the adjacent regions. They suggested that this transition layer, which contains both magnetosheath and magnetospheric populations, is the entry layer during northward IMF conditions. This transition layer is possibly formed by dual-lobe MR when the IMF is northward. The plasma property and the closed field line geometry of this layer indicate that it is possibly linked to the low-latitude boundary layer. The width of this layer varies from 480

to 2200 km. These results support the notion that high-latitude dual-lobe MR is a potential mechanism of the transport of solar wind into the magnetosphere during northward IMF through the formation of a high-altitude entry layer. Their observations of different sub-layers with evident density and temperature differences are consistent with the view that the reconnection process at the magnetopause is not steady.

4. Magnetospheric modeling

Zhang et al. (2010b) investigated the effects on the Earth's magnetic field of the externally driven current systems connecting the ionosphere, cusp and ring current regions. This study extends previous works to cover a greater range of orbit location and external conditions. The authors compared the modeled magnetic field from different global field models (Tsyganenko 1989, 1996, and 2001, hereafter T89, T96 and T01) with data from the four Cluster spacecraft, which allows not only characterizing each model's performance, but also providing insight into the physical sources of observed signals. The data generally deviate much less from the expected model field during the years close to the solar minimum, implying that the models perform better during weaker geomagnetic activity. There are particular deviations from the models associated with the ring current (well-defined smooth trends) and region 2 field aligned currents (FACs) or low-altitude cusp FACs (sharp bipolar signatures). During the ring current crossings (through perigee, at 4-5 R_E), the T96 model always overestimates the ring current, while the T01 and T89 models sometimes underestimate it. The sharp bipolar signatures are not always sampled, implying a localized extent, but only the T96 and T01 models include forms for the region 2 FACs and T01 appears to model these better. Overall, all deviations from T01 are much smaller than for the other models, indicating that this model achieves the best fit to the data. The 4 Cluster spacecraft observe nearly the same signatures at small separations (during the early years of the mission) but do sample different signatures at the large separations (during the later years). Using the four-spacecraft technique, the authors infer that the region 2 FACs, with a transverse thickness of $\sim 0.17-0.54 R_E$, and cusp FACs, with a thickness of $\sim 0.06-0.12 R_E$, are very stable in size and location.

5. Bow shock, magnetosheath and outer boundaries of the magnetosphere

Li et al. (2008) reported a case of shrinkage of the magnetosphere observed by TC-1. During the period of 06:14-07:30 UT on August 24, 2005, the Earth's magnetopause (MP) was suddenly compressed by a persistent high-speed solar wind stream with the southward component of IMF. The magnetopause moved inward about 3.1 RE; in the meantime, TC-1 satellite shifted from northern plasma sheet to the northern lobe/mantle region. The observation indicates that enhanced solar wind dynamic pressure may also cause significant inward displacements of the plasma sheet and near-Earth lobe/mantle.

A large-amplitude excursion of the magnetosheath in quiet solar wind conditions on 17 March 2004 recorded simultaneously by the Cluster and TC-1 was reported by Cai et al. (2009). During this period, the IMF B_z was northward. Coherent bow shock motion and MP motion are observed. The relevant plasma transport phenomenon in the form of flux fluctuations below the ion gyrofrequency at the MP is detected and interpreted as the manifestation of the drift instability. Correlated observations on charge accumulation and electrostatic potential perturbation are recorded in high energy regime, and the consequential mass exchange is also exhibited. The present investigation gives some new insight into the plasma transport mechanism across the subsolar MP in quiet solar wind conditions during a period of northward IMF.

Although the solar wind deceleration in the terrestrial foreshock was noticed three decades ago, previous studies show some conflicting results. Cao et al.(2009) presents direct evidence of solar wind deceleration in the foreshock of the Earth by using the data of two Cluster satellites. On 2 February 2003, the two satellites (C1 and C3) of Cluster missions are inside and outside the foreshock, respectively, approximately along the solar wind flow line. Comparison of the plasma data recorded by two satellites shows that the solar wind velocity decreases in the foreshock and the largest deceleration reaches 22 km/s. The velocity distribution of ions in the phase space indicates that the solar wind ions undergo pitch angle

scattering in the foreshock. The solar wind deceleration is associated with diffuse ions and ULF wave activities. The diffuse ion density reached 0.25 cm^{-3} , about 7% of the solar wind density. The interaction of ULF waves with solar wind also deflects the solar wind away from the bow shock in both the ecliptic and the meridian planes. Meanwhile, the solar wind deceleration is accompanied by thermalization during which the solar wind temperature can reach 240 eV.

The characteristics of ULF waves associated with the solar wind deceleration in the Earth's foreshock on 6-7 April 2003 was further studied by Fu et al.(2009) studied using the wave telescope technique. In the satellite frame, the ULF waves are the left-handed polarized and quasi anti-parallel propagating mode, with a power peak at $\sim 18.63 \text{ mHz}$. The wave vector in the GSE coordinates is estimated as $k = (-4.29, 2.28, 1.21) \times 10^{-4} \text{ km}^{-1}$. In the solar wind frame, the frequency of waves becomes -9.39 mHz after the Doppler shift correction. The propagation direction of the waves is thus reversed and correspondingly the polarization of the waves becomes right-handed. The above mentioned characteristics of the ULF waves in the solar wind frame indicate that the ULF waves associated with the solar wind deceleration are the Alfvén-whistler waves, which have been frequently reported in both the observations and computer simulations.

The data from two Cluster satellites (C1 and C3) were used by Fu et al.(2009a) to make a statistical study of the solar wind deceleration and deflection in the Earth's foreshock region. In the foreshock coordinates, the magnitude of deceleration is inversely proportional to DBS (the distance between the satellite and the bow shock) along the IMF, and also inversely proportional to θ_{BN} (the angle between the IMF and the bow shock normal). The decelerations mainly occur when DWS (the distance from satellite to the ULF wave boundary along X direction) is less than 6RE. On the other hand, the solar wind deflection displays a similar feature. The largest values of deceleration and deflection are, respectively, estimated as 10 km/s and 3° . These decelerations and deflections not only lead to a variation of the magnetopause's position and shape, but also support a possible generation mechanism of the diffuse ions in the foreshock region.

Sun et al.(2007) studied the energetic particle acceleration mechanism at

perpendicular shock with particle simulation. Large amount of test particles trajectories at perpendicular shock with magnetic turbulence are calculated. The effect of shock strength and particles initial energy on the average energy change per shock-crossing is also studied. Furthermore, the test particle energy gain from Shock Drift Acceleration (SDA) under different conditions is analyzed, as well. In addition, a theoretical formula is given for SDA, which agrees with the simulation results. The results show that, although magnetic turbulence is included, particles would still be accelerated mainly by SDA at perpendicular shock, while the diffusive shock acceleration, based on the guiding center assumption, is not valid.

VI. SOLAR WIND-MAGNETOSPHERE-IONOSPHERE COUPLING

On the basis of the principle of energy conservation, Xu (2011) reviews the aspects on energy input and dissipation in the coupling processes of the Solar wind, Magnetosphere and Ionosphere (SMI coupling). He focus on the following nine principle issues: (1) solar wind energy input, (2) magnetosphere response to solar wind energy injection, (3) ring current dissipation, (4) Joule heating in the polar ionosphere, (5) auroral particle precipitation, (6)energy dissipation and storage in the magnetotail, and energy returning from the magnetosphere to solar wind, (7) energy accumulation and dissipation during quiet periods, (8) energy partitioning in different sinks, (9) the criterions and methods for assessing energy function.

Yue et al. (2009) used the magnetic field data of GOES satellites from 1997 to 2007 and the plasma data of MPA on the LANL satellites from 1997 to 2004 to study the properties of magnetic field and plasma at the geosynchronous orbit within 3 hours before and after the arrival of shock front at the geosynchronous orbit. It is found that following the arrival of shock front at the geosynchronous orbit, the magnetic field magnitude and GSM B_z component increase significantly on the dayside (8-16 LT), while the B_y component has almost no change before and after shock impacts. The proton becomes much denser, and the proton temperature increases sharply on the dusk and night side. The electron density also increases dramatically on the night side. The peak of the anisotropy of proton's temperature is located at the noon sector, and the anisotropy decreases towards the

dawn and dusk side with the minimum on the night side. It is suggested that the electromagnetic ion cyclotron (EMIC) wave and whistler wave can be stimulated by the proton and electron temperature anisotropy respectively.

Yue et al. (2010) analyzed 106 IP shock events based on OMNI data, GOES, and Los Alamos National Laboratory (LANL) satellite observations during 1997-2007. It was shown that IP shocks with southward IMF are likely to increase AE (AL, AU) and PC indices significantly. The amplitude of AE index increases from 200 to 600 nT, AU from 100 to 200 nT, AL from 50 to 400 nT, and PC from 1.5 to 3 approximately in 10 min, which could be a signature of geomagnetic activity/substorms onset (or substorm further intensification). Meanwhile, there is a strong injection of energetic electrons in the dawn region following the shock arrival and a strong depletion in the dusk region 30 min later, showing a clear dawn-dusk asymmetry. On the other hand, there is only the typical shock compression effect for IP shocks with northward IMF. These results indicate that the magnetosphere-ionosphere (M-I) system must be preconditioned for a substorm-like geomagnetic activity to be triggered by an IP shock with southward IMF impact, whereas IP shock with northward IMF precondition shows only compression effect.

Wang et al.(2007) did a statistical survey of solar wind dynamic pressure (P_d) pulses and geosynchronous magnetic fields observed between 1998 and 2005. In geomagnetic quiet times with $Dst > -50$ nT, they found 111 p_d pulses which produce geosynchronous responses. The magnitudes of the geosynchronous magnetic field changes (δB_z) have a peak near the noon meridian. However, the relative change of the geosynchronous magnetic field $\delta B_z / \overline{AV-Bz}$ (where $\overline{AV-Bz}$ is the average of the geosynchronous magnetic field B_z observed during the response to the pressure pulse) depends weakly on the local time. As the magnitude of the relative change of solar wind P_d (dP_d/P_d) increases, the rate of geosynchronous magnetic field variation increases correspondingly. These results imply that the magnitude of the geosynchronous response could be determined by $\overline{AV-Bz}$. In addition, the interplanetary field orientation does not affect the response significantly. Using an MHD code which models the global behavior of the SMI system, the authors reproduced the main characteristics of the observations.

Wang et al.(2009) performed a statistical survey of geospace magnetic field responses to IP shocks. The magnitude of the geosynchronous magnetic field (dBz) responses to IP shocks peaked near the noon meridian and varied weakly on local time. Negative responses (dBz<0) were sometimes observed in the nightside.. It was shown that 75% of negative responses in the midnight sector are associated with southward IMF. For a moderately compressed magnetosphere, the amplitude of the geosynchronous response dBz could be determined by the average value of the background local magnetic field. As the upstream solar wind dynamic pressure increases, the rate of response increases correspondingly. The dBz at the geosynchronous orbit near local noon and the amplitude of sudden impulses on the ground are found to be highly correlated.

Wang et al. (2010a) extended the previous statistical study and showed that sudden impulses (SIs) could be used to estimate key parameters at L1 point and geosynchronous orbit, including the arrival time of an IP shock at L1 point, the change of the solar wind dynamic pressure across the shock, and the associated geosynchronous magnetic field changes near noon. Empirical formulae deduced from observations can be used to estimate certain IP shock characteristics and geosynchronous magnetic field changes from SI data on the ground, with prediction efficiency as high as 90% and 86%, respectively. These estimates are useful for studying historic, pre-space era data, or if L1 and geosynchronous data are not available at some time.

The magnetospheric response at the geosynchronous orbit near midnight to two IP shocks passing observed by the GOES spacecraft is studied in Wang et al.(2010b). Observations show that one shock produced a decrease in B_z and the other an increase in B_z . A global 3D MHD code was run to reproduce these responses and to provide further information on the initiation and development of B_z variations in the entire magnetosphere. The simulation reveals that when a fast forward shock (FFS) sweeps over the magnetosphere, there exist a positive response region caused by the compressive effect of the shock, and a negative response region probably associated with the temporary enhancement of earthward convection in the nightside magnetosphere. A spacecraft may observe an increase or decrease of

the magnetic field depending on which region it is in. The numerical results reproduce the main characters of the geosynchronous magnetic field response to IP shocks for these two typical cases.

Yuan and Deng (2007) presented an event of a long-lasting penetration of the interplanetary electric field (IEF) into the dayside equatorial ionosphere during the main phase of a magnetic storm on April 17, 1999. In the event, variations of the geomagnetic field at both high latitudes and magnetic equator show coherence with those of the solar wind pressure, indicating that enhancements of solar wind pressures can drive those coherent increases of the penetrated electric field in dayside equatorial ionosphere during stable and southward interplanetary IMF. Therefore, not only the dawn-dusk component of the IEF, but also the solar wind pressure can strongly control the long-lasting penetration of the magnetospheric electric field into low-latitude or equatorial ionosphere during southward IMF.

In order to study the response of auroral electrojets for a sawtooth event observed by LANL satellites on 30 September 2000, Lin et al. (2010) obtained large scale 2D ionospheric equivalent current systems by using spherical elementary current system method with data of high-latitude magnetometers in the Northern Hemisphere. Comparing enhancements of nightside ionospheric westward electrojets with positive magnetic bays in middle/low-latitude ground magnetic field H components after each sawtooth injection, they demonstrated that there were current wedges formed during the sawtooth event. The width of current wedges suggested by the observations is around 11 hours (MLT). Time durations for middle/low-latitude magnetic bays to reach maximum variations are found to be longer than those for high-latitude electrojets, implying that source currents for middle/low-latitude magnetic bays are multiple.

Guo et al.(2008) reported that under strong southward IMF conditions, the bow shock contributes significantly to the region 1 field-aligned current (FAC). More than 50 percent of the total region 1 FAC may originate from the bow shock in certain circumstances. Stronger southward IMF, higher solar wind speed, or larger ionospheric Pedersen conductance, leads to greater contribution from the bow shock to the region 1 current.

Shi et al. (2009a) made a theoretical study on density distribution of He^+ ions originating from the polar region and up-flowing to the magnetosphere along the magnetic field line during quiet and weakly disturbed geomagnetic conditions. The main results show that the up-flowing He^+ mainly resides in inner magnetosphere and their density has a negative radial gradient. The up-flowing He^+ ion distributions along the magnetic field line are mainly controlled by gravity and the geomagnetic field configuration.

Shi et al. (2009b, 2010) investigated the features of FAC distribution in plasma sheet boundary layers using the data measured with Cluster in 2001. The main results show that the FAC distribution in the plasma sheet boundary layers in the magnetotail not only has dusk-dawn asymmetry, earthward- tailward (polarity) asymmetry, but also has north-south asymmetry. That the FAC densities are different between the hemispheres suggests that an important source of these currents must be a voltage generator.

Using Cluster multi-measurement data, Cheng et al. (2007) studied the field-aligned current density distribution at the plasma sheet boundary layers. The results show that the FAC occurrence versus its density has a distribution consisting of a Gaussian distribution with an additional decreasing exponential distribution. The most probable value of the FAC density is 3.45pT/km.

Cheng et al. (2008) analyzed the observation data when the Cluster satellites crossed the plasma sheet boundary layer in the magnetotail during the two magnetic storms in August to October 2001. The main results show that, in the storm time, the FAC density was approximately negatively correlated with AE index from the sudden commencement to the early main phase, was approximately positively correlated during the late main phase and early recovery phase, and was no apparent correlation during the late recovery phase.

Tang et al.(2009) studied the closure of the cross-tail current in the magnetotail under different solar wind conditions. The cross-tail current closes totally within the magnetopause, forming the classical θ structure when IMF is set to be zero. The

situation changes for southward IMF cases: part of the cross-tail current passes through the magnetosheath and closes across the bow shock, forming an overlapped θ structure of the cross-tail current, when viewed from the Sun. Quantitative analysis shows that a larger strength of the southward IMF B_z results in a higher percentage of current closed through the bow shock. Nearly a constant quantity of the cross-tail current comes from the bow shock despite variations in the solar wind speed. An increase in the ionospheric Pedersen conductance leads to an increase in the bow shock contribution and a decrease in the MP contribution to the cross-tail current. Cross-tail current that closes across the bow shock rather than the magnetopause can be classified as the magnetic MR current, providing energy supply for dissipation needed in the magnetic MR region in the magnetotail.

On the basis of the steady state results in global SMI MHD simulation, Guo et al. (2010a) traced streamlines of FAC from the ionosphere to draw the global geometry of current streamlines. When the IMF B_y is dominant, the topology of the current streamlines is found to significantly change. Cusp and mantle currents arise, and the symmetry of the FAC across the noon-night meridional plane breaks in the ionosphere. In addition to the self-closed currents in the Northern or Southern hemispheres, three more types of current streamlines connecting the two ionospheres appear. The first current, including the cusp current, originates from the southern ionosphere and flows into the northern ionosphere. The second current, mainly the mantle current, and the tail current are connected to form a single current system. The third current flowing out of the southern and into the northern ionosphere connects the two ionospheres by finally closing through the bow shock. The results indicate that for the dominant IMF B_y conditions the bow shock current should be included among the magnetosphere-ionosphere (M-I) current system.

Guo et al. (2010b) studied the Kelvin-Helmholtz instability (KHI) at the MP based on global 3D simulation. The KHI is found to occur at the low-latitude MP during a period of northward IMF. At the low-latitude boundary layer (within the latitude of about 30°), vortices are generated at the dayside MP and transported to the far distant magnetotail along the flanks; two modes of surface waves propagate along the inner and outer edge of the magnetopause boundary layer, respectively, from the initial point to the tail region. The wavelengths of the inner and outer modes are

estimated to vary from 1 to 8 R_E as the longitude increases. The vortices are initiated at a longitude of about 28° relative to the Sun-Earth line in the equatorial plane. Different behaviors of the fast-mode surface waves on the two sides of the magnetopause boundary were investigated in the paper.

Peng et al.(2010) studied the role of IMF B_x in the SMI coupling using global MHD simulations and presented an examination of the effects of the IMF B_x on the geometry of the MP, the ionospheric transpolar potential, and the MP MR rate under low Alfvén Mach numbers. The role of the IMF B_x is found to manifest in three aspects: (1) the MP shifts toward either north or south, depending on whether B_x/B_z is negative or positive, whereas the bow shock expands in the opposite direction; (2) during southward IMF, the magnetic merging line shifts northward (southward) on the day side and southward (northward) on the night side for $B_x > 0$ ($B_x < 0$); (3) both the ionospheric transpolar potential and the magnetopause MR rate decrease with increasing B_x , and the relative reduction may reach as high as 20% under extreme cases. The physical mechanism for this reduction is attributed to the change in the width of the magnetosheath, which is sensitive to the variation of B_x under low Alfvén Mach numbers.

Hu et al.(2007) proposed three methods to calculate the MR potential based on data obtained by global MHD simulations of the Earth's magnetosphere-ionosphere system. The three methods are all based on the line integration of electric field and differ in the choice of integration path. For a properly selected numerical resistivity, the MR potentials obtained from the three methods are reasonably close to each other. The MR voltage is found to be larger than the transpolar potential, and the ratio between them increases with increasing ionospheric conductance. The appearance of parallel electric field along the last closed magnetic field lines is found to be responsible for the difference between the ionospheric and the MR potentials and between the transpolar potential and the MR voltage as well.

Hu et al.(2009) propose diagnosis methods to trace the magnetic merging line and to calculate the electric potential along it obtained by global MHD simulations of

the solar wind-magnetosphere-ionosphere (SMI) system. The merging line is found to be similar in geometry to that of the compound field superposed by the Earth's dipole field and the IMF, whereas the MR voltage is approximately fitted by $\sin^{3/2}(\theta_{IMF}/2)$. It is shown that the ionospheric transpolar potential and the voltage along the polar cap boundary cannot be taken as substitutes for the MR voltage and that the electric fields along the merging line cannot characterize the total MR rate and the coupling strength between the solar wind and the magnetosphere. The MR nearby magnetic nulls closest to the subsolar point are found to be negligible, which gives support to the component MR hypothesis for dayside MR of quasi-steady states of the SMI system.

Hu and Wang (2010a) presented a brief summary of their global MHD simulations results of the SMI system with emphasis on the electrodynamic coupling. The main conclusions obtained are summarized as follows. (1) As a main dynamo of the SMI system, the bow shock contributes to both region 1 FAC and cross-tail current. Under strong interplanetary driving conditions and moderate Alfvén Mach numbers, the bow shock's contribution may exceed more than fifty percent of the total of either region 1 or cross-tail currents. (2) In terms of more than 100 simulation runs with due southward IMF, they found a combined parameter $f = E_{sw}P_{sw}MA^{-1/2}$. Both the ionospheric transpolar potential and the magnetopause MR voltage vary linearly with f for small f , but saturate for large f . (3) The MR voltage is approximately fitted by $\sin^{3/2}(\theta_{IMF}/2)$ where θ_{IMF} is the IMF clock angle. The ionospheric transpolar potential, the voltage along the polar cap boundary, and the electric fields along the merging line respond differently to θ_{IMF} , so it is not justified to take them as substitutes for the reconnection voltage.

Tang et al. (2008) simulates the penetration of energetic particles into the magnetosphere. They developed a code to calculate the trajectories of energetic particles penetration into the magnetosphere based on T89 model with different energies and pitch angles. The preliminary results show that only those particles moving along the magnetic field lines can penetrate into the magnetosphere and reach the earth's surface. The particles with larger deviation angle with respect to the magnetic field lines will be reflected earlier. The particles with higher energies can penetrate into the magnetosphere with larger distribution of the pitch angle.

Cai et al. (2008) made a numerical study of the auroral particle transport in the polar upper atmosphere. A 1D transport equation of charged energetic particles is derived by taking account of major interactions with neutral species in the upper atmosphere. The transport equation is numerically solved, for a simplified atmosphere consisting only of nitrogen molecules (N₂), to obtain the variations of incident electron fluxes as a function of altitude, energy and pitch angle. The model results can describe fairly the transport characteristics of precipitating auroral electron spectra; meanwhile the N₂ ionization rates calculated from the modeled differential flux spectra also exhibit good agreements with existing empirical models. Taking the energy flux spectra of precipitating electrons observed by FAST satellite flying over EISCAT site on May 15 1997 as model inputs, the model-calculated ionization rate profile of neutral atmosphere consists reasonably with that reconstructed from electron density measurements by the radar.

Han et al. (2010) examine an unusual geomagnetic sudden impulses (SIs) event observed at the dayside dip equator, which shows a clear precursor ~1 min before the preliminary reverse impulse (PRI) onset. The precursor was observed simultaneously at both the dayside dip equator and in the southern polar region but was not at all in the northern polar region. The global ground variations after the PRI onset were, however, consistent with a conventional SI model of the magnetospheric response to a sudden enhancement of the solar wind dynamic pressure. The authors suggest that the SI precursor in the event was caused by high - latitude magnetic MR that occurred only (or first) in the dawn quadrant of the southern hemisphere, This implies that electric field effects occurring in the polar ionosphere due to magnetopause MR may be rapidly monitored at the dayside dip equator. In addition, they argue that the reported observations lend strong evidence for validity of the waveguide model in generation of SIs.

Using the magnetic field measurements by Oersted, Han et al. (2007a) identified more than 20 geomagnetic sudden commencement (SC) events on both dayside and nightside. The SCs observed in the B_∥ (compressional) component on the nightside had the nearly same waveforms as those observed on the ground in the H (northward) component. The authors suggest that the SCs on the nightside were

dominantly caused by the enhanced MP currents, which were transmitted by the compressional MHD waves, and the effects of the ionospheric current (IC) were negligible. On the other hand, near the dayside dip equator (DDE), Oersted always observed positive impulses in the $B_{//}$ component, which suggest that the PRIs at the preliminary reverse impulses (DDE) are generated by westward ICs; while the Oersted $B_{//}$ component on the dayside always present clear decreases, implying that an eastward IC was excited after the PRI. The authors suggest that the waveforms observed both on the ground and at Oersted during the time period of PRI and MI were superposition of the incident compressional waves and the disturbance fields caused by the ICs. They concluded that features observed by Oersted just above the ionosphere are significant complementary to the empirical knowledge for SCs.

Han et al. (2008a) presented the first evidence for particle injection in the dawn-side equatorial plane caused by a sudden enhancement of the solar wind dynamic pressure (SEPdyn). The observations demonstrate that the SEPdyn caused two effects: (1) instantaneous particle energization in the dayside, and (2) particle injection in the dawn side at approximately 7 min later. The former has been suggested to be energization of the preexisting particles by the sudden compression of the magnetosphere. The latter was argued by the authors to be due to acceleration of relatively hot ions in the dawn-side plasma sheet by a bipolar electric field caused by the SEPdyn.

Liu et al. (2009) calculated the height-integrated conductance and the electron density in the F-layer of the polar ionosphere, based on one self-consistent model of the polar ionosphere, which takes the ionization of the precipitation electrons with different energy spectrum into account. It is found that the energy spectrum of the electrons doesn't have an obvious effect on the conductance. The average energy of the electrons is the determinant factor of the conductance. The relative magnitude of the conductance deduced using the different energy spectrum of the electrons also depends on the average energy. On the other hand, the electron density in the F-layer is well affected by the energy spectrum of the precipitation electrons. The larger the average energy of the precipitation is, the more notable the effect is.

Pang et al. (2008) reported that Cluster crossed the dayside magnetopause boundary and observed a series flux transfer events (FTEs) during the interval from 0630 to 0730 UT on April 15th 2003. During this period, the IMF showed a negative z component and a positive y component. Simultaneous corresponding transient plasma flows were identified in the near-conjugate polar ionosphere by the CUTLASS Finland HF radar, and the geomagnetic field disturbances were observed by the IMAGE ground-based magnetometers. By combining these data and applying the Cooling model, we show that the transient plasma flows and the geomagnetic field disturbances are closely related to the dayside FTEs.

Hu et al. (2009) used the observations acquired from three-wavelength (427.8, 557.7 and 630.0 nm) all-sky imagers (ASIs) at Yellow River Station (YRS) in Ny-Ålesund, Svalbard to examine the synoptic distribution of dayside aurora. The results demonstrate that the maximum emission regions (MERs) at each wavelength are all located in the postnoon sector, but have rather different magnetic local time (MLT) distributions from each other. The so-called 15 MLT “hot spot” is the overlapping region of the MERs at three wavelengths, and the prenoon “warm spot” is characterized uniquely by an increase of emissions at the 557.7 nm wavelength. The detailed dayside auroral spectra and morphology as a function of MLT are discussed.

Hu et al. (2010) made a survey of dayside aurora excitation at 557.7 nm, which was acquired from an all-sky imager at Yellow River Station in Ny-Ålesund, Svalbard. He suggested that there are 4 intense emission maxima in the dayside oval, centered near 0630/76, 0830/76, 1400/75, and 1600/75 (unit: MLT/MLAT), respectively. Tracing the magnetospheric sources of these cores along geomagnetic field lines, the 0830- and 1400-MLT cores correspond with the prenoon and postnoon magnetospheric boundary layers (MBLs), and the 0630- and 1600-MLT cores are located at the dusk and dawn MBLs, respectively. The potential solar wind-magnetosphere dynamic processes resulting in these auroral features are discussed.

Liu et al. (2011b) examined temporal variations of a dayside aurora and corresponding ionospheric plasma convection observed by all-sky camera (ASC)

and Super Dual Auroral Radar Network (SuperDARN) over Zhongshan (ZHS), located at -74.5° in magnetic latitude (MLAT) in Antarctica, during a geomagnetic sudden commencement (SC) event occurred on 27 May 2001. Simultaneous ASC observations at South Pole (SP, -74.3° MLAT) were also analyzed. During the SC time, ZHS and SP were located in the postnoon (1610 MLT) and prenoon (1100 MLT) sectors, respectively. Before the SC onset, the ASC at ZHS observed an auroral arc with moderate intensity in the poleward direction of the field of view, and the SuperDARN radar detected sunward ionospheric plasma flow over ZHS. Just after the SC onset, the auroral intensity over ZHS decreased rapidly and the direction of the plasma flow was reversed to anti-sunward. The authors suggest that these observational results were generated by a downward FAC, and consistent with a physical model of SC which predicts appearance of a pair of FACs flowing downward (upward) in the postnoon (prenoon) sector at the very beginning of SC. Additional observations supporting the validity of the model were also presented in the paper.

Zhang et al. (2011) reported a number of poleward-moving events between 1130-1300 UT on 11 Feb 2004, during periods of southward IMF, while the steerable antenna of the EISCAT Svalbard Radar (ESR) and the Tromsø VHF Radar pointed nearly northward at low elevation. In this interval, simultaneous SuperDARN CUTLASS Finland radar measurements showed poleward-moving radar aurora forms (PMRAFs) which appeared very similar to the density enhancements observed by the ESR northward-pointing antenna. These events appeared quasi-periodically with a period of about 10 minutes. It is inferred that there is an almost one-to-one correspondence between the Poleward- Moving Plasma Concentration Enhancements (PMPCEs) observed by the ESR and the VHF radar, and the PMRAFs measured by the CUTLASS Finland radar. These observations are consistent with the interpretation that the polar cap patch material was generated by photo-ionization at sub-auroral latitudes, and that the plasma was structured by bursts of magnetopause reconnection giving access to the polar cap.

Wang et al. (2008c) used two years of DMSP ion drift meter measurements for a focused study of the subauroral polarization streams (SAPS). The main emphasis is on the effects of the cross-polar cap potential (CPCP) and the subauroral flux

tube-integrated conductivity (that is, whether or not the northern and/or southern ionospheric footprint of the flux tube is sunlit or not) on the SAPS spatial distribution. For higher flux tube-integrated conductivity the SAPS tend to occur more poleward than for lower conductivity. The magnetic latitude (MLAT) difference can reach several degrees at most. The dependence of SAPS location on geomagnetic activity is also studied, and it is found that the SAPS magnetic latitude exhibits an exponential relation with Dst. When Dst < -200 nT the SAPS tend to occur at 48° MLAT. The CPCP averaged over 15 min prior to the SAPS correlates best with the SAPS peak velocities. The high-latitude CPCP has a stronger effect on the SAPS velocities for low integrated conductivity than for high conductivity. Finally, the observations show that there is a good anti-correlation between the subauroral integrated conductivity and the SAPS velocity, which confirms previous model results.

Wang et al. (2010) have shown that the ionospheric azimuthal plasma velocity jets near the open-closed field line boundary on the nightside can be associated with the peak in the ionospheric conductivity gradient. Both model and DMSP observations have been utilized to conduct this investigation. The model tests show that when the gradient of conductivity in the poleward boundary becomes sharper, convection peaks appear around the poleward edge of the aurora. The model results have been confirmed by DMSP observations. Hundreds of large ion flow events are identified from one year DMSP observations, with flow speed larger than 500 m/s that occurred poleward of the aurora. Among them, 280 (74%) events are found to be associated with conductivity gradient peaks. Most of the convection jets occur in winter when conductivity gradients are expected to be large. The convection jets tend to occur at later local times (21:00–22:00MLT) at 70°–72°MLat. These events are preceded by increasing of the merging electric field suggesting that they occur after the expansion of the polar cap. Both observation and model results show that the conductivity gradient at the polar cap boundary is one of the important elements in establishing the convection jets.

Dang et al. (2007) made a study on the morphologic features of quiet-time ionospheric O⁺ ion up-flowing at altitudes of 2000 to 4000 km using energetic (5eV to 12keV) ion measurements on FAST satellite. The pre-noon cusp/cleft is the

predominant region of up-flowing occurrence for O^+ with lower (< 1 keV) energy. Meanwhile the pre-dawn sector near the equatorward edge of the plasma convection dominates the occurrence for the higher (> 1 keV) energy O^+ ions. No matter whether the energy is lower or higher, the up-flows occur often over a wide MLT range of lower latitudes outside the auroral oval. The up-flowing within auroral oval at pre-midnight (21:00—22:00 MLT) carries largest energy fluxes, with extremely large fluxes for higher energy O^+ near the polar cap boundary. For altitudes of 2000—4200 km under observation, the up-flowing ion conics occur much more frequently than ion beams. Ion beams are rarely found below 3000 km, while the conics occur uniformly over the observed altitudes.

Wang et al. (2008d) compared ionospheric outputs from the Space Weather Modeling Framework (SWMF) with magnetic and plasma observations from CHAMP and DMSP satellites under both quiet and storm conditions, emphasizing the dependence of the model's performance for various magnetic local times, solar wind conditions, and seasons. The model predicts the potential better in the dawn-dusk sector than in the noon-midnight sector. For FACs the model performs better on the dayside than on the nightside. In addition, there is a trend toward unsatisfactory behavior in the model as solar activity increases. The model more accurately corresponds to observations during quiet times than disturbed periods. During storms the modeled FACs tend to locate at 40 MLat more poleward than the observations. The present analysis has revealed that the model performance depends strongly on the seasons. The model underestimates the cross polar cap potential (CPCP) by about 50% in the summer hemisphere while overestimating it by 50% in the winter hemisphere. The model calculates the difference between the winter and summer hemisphere CPCP on the order of a factor of 2.5, while DMSP data show that the actual factor is around 1.3. These results reveal that the ionospheric modeling subsets lack appropriate seasonal dependence.

The work from Wang et al. (2008) concentrates on the FACs distribution for the varying northward and duskward IMF conditions when the dipole tilt is nonzero. The SWMF simulation has been used to perform this study. Hemispheric asymmetry of the time evolution of northward IMF B_z (NBZ) FACs is found. As the IMF changes from strictly northward to duskward, NBZ FACs shift

counterclockwise in both summer and winter hemispheres. However, in the winter hemisphere, the counterclockwise rotation prohibits the duskward NBZ FACs from evolving into the midday R1 FACs. In the summer hemisphere, the NBZ FACs can evolve into the DPY FACs, consisting of the midday R0 and R1 FACs, after the counterclockwise rotation. The hemispheric asymmetry is due to the fact that the dipole tilt favors more MR between the IMF and the summer magnetosphere. For the DPY FACs the hemispheric asymmetry emerges. Both IMF By and dipole tilt cause the polar cap hemispheric and local time asymmetric. The polar cap boundary tends to move equatorward as the IMF rotates from northward to duskward.

VII. METHODS OF DATA ANALYSIS AND SIMULATION

Shen et al. (2007) developed a technique, termed MRA (magnetic rotation analysis), to probe 3-D magnetic field topology from in situ magnetic field observations. The method first constructs a symmetrical magnetic rotation tensor and deduces the rotation rate of the magnetic field along one arbitrary direction. The value of curvature of a magnetic field line is given by the magnetic rotation rate along the magnetic unit vector and its corresponding radius of curvature is readily obtained. It is verified that MRA can be applied to analyze the geometrical structure of the tail current sheet and flux ropes. The advantage of the MRA is that not only it can determine the orientation but also the internal geometrical configuration, as well as the spatial scale of the magnetic structures.

Huang et al.(2008) presented a dynamic domain decomposition (D3) technique for implementing the parallelization of the piecewise parabolic method (PPM) for solving the ideal MHD equations. The key point of D3 is distributing the work dynamically among processes during the execution of the PPM algorithm. This parallel code utilizes D3 with a message passing interface (MPI) in order to permit efficient implementation on clusters of distributed memory machines and may also simultaneously exploit threading for multiprocessing shared address space architectures. 3D global MHD simulation results for the Earth's magnetosphere on the massively parallel supercomputers Deepcomp 1800 and 6800 demonstrate the

scalability and efficiency of the present parallelization strategy.

Reference

- Cai Hongtao, MA Shuying and PU Zuyin (2008), Numerical study of the auroral particle transport in the polar upper atmosphere, *Science in China (series E)*, 51(10): 1563-1802.
- Cai L., MA S. Y., and ZHOU Y. L.(2010), Prediction of SYM-H index during large storms by NARX neural network from IMF and solar wind data, *Ann. Geophys.*, 28: 381–393.
- Cai, H. T., Mccrea, I. W., Dunlop, et. al (2009), Cusp observations during a sequence of fast IMF BZ reversals, *Ann. Geophys.*, 27: 2721–2737.
- Cai, H. T., S. Y. Ma, M. W. Dunlop, Y. Bogdanova, J. A. Davies and F. Pitout (2010), Cluster observations of high-altitude cusp during multiple fast-turning IMF, *Chinese Science Bulletin*, 55(12): 1178-1185, DOI: 10.1007/s11434-009-0306-0
- Cai C L, Dandouras I, Rème H, Cao J B, Zhou G C, Shen, C, Parks, G K,(2009). Fontaine D. Magnetosheath excursion and the relevant transport process at the magnetopause, *Ann Geophys.*, 2009, 27, 2997-3005
- Cai C L, Dandouras I, Rème H, Cao J B, Zhou G C, Parks, G K. (2008). Cluster observations on the thin current sheet in the magnetotail, *Ann Geophys.*, 2008, 26(4):929-940
- Cai C L, Dandouras I, Rème H, Cao J B, Zhou G C, Parks G K, (2009). Fontaine D Foreshock-like density cavity in the outflow region of magnetotail reconnection, *Ann Geophys.*, 2009,27:3043-3053.
- Cao, J. B., et al.(2008). Characteristics of mid-low latitude Pi2 excited by Bursty Bulk Flows, *J. Geophys. Res.*, DSP-Cluster special issue, 2007JA012761, 2008.
- Cao J B, Fu H S, Zhang T L, Reme H, Dandouras I, Lucek E. (2009). Direct evidence of solar wind deceleration in the foreshock of the Earth, *J. Geophys. Res.*, 2009,114, A02207, doi:101029/2008JA013524
- Cao et al, (2010). Geomagnetic signatures of current wedge produced by fast flows in plasma sheet, *J. Geophys. Res.*, 2010, 115, A08205,doi:101029/2009JA014891

- Cao, J. B., Ding, W. Z., Reme, H., Dandouras, I., Dunlop, M., Liu, Z. X., and Yang, J. Y. (2011) The statistical studies of the inner boundary of plasma sheet, *Ann. Geophys.*, 29, 289-298, doi:10.5194/angeo-29-289-2011, 2011
- Cao, J.B., Cheng, C., Ma, Y. D., Cai, C. L. (2010a), Comparison of BBFs observed by single and multi satellites, *Chin. J. Space Sci.*, 30(4), 343-348.
- Cao J., J. Yang, C. Yan and L. Li, (2007) The observations of high energy electrons and associated waves by DSP satellites during substorm, *Nuclear Physics B, Supplement*, 166, 56-61, 2007
- Cao, X., Z. Y. Pu, H. Zhang, et al. (2007), Dipolarization observed by TC1 and Cluster during substorm on September 14, 2004, *Chinese J. Geophys* V.50, N.4, 995-1004, 2007.
- Cao, X., Z. Y. Pu, H. Zhang, et al. (2008), Multi-Spacecraft and ground-based observations of substorm timing and activations: Two case studies, *J. Geophys. Res.-Space Physics*, 113, A07S25, doi:10.1029/2007JA012761, 2008
- Chen, Z. Q., Zheng, J., Li, L., and Xu, R.L. (2010), Simulation of EUV Imaging and 3-D Con-Beam CT Reconstruction of Plasmasphere, *Tsinghua Science and Technology*, 15 ,1, 127
- Cheng Z. W, Shi J. K, Zhang T. L., Liu Z. X. (2007), Probability of Field-Aligned Currents Observed by the Satellite Cluster in the Magnetotail. *Chin Phys Lett*, 24(4): 1125-1127.
- Cheng, Z.W., Shi, J. K., Zhang, T.L. et al. (2008), Relationship between FAC at plasma sheet boundary layers and AE index during storms from August to October, 2001. *Sci China Ser E-Tech Sci.*, 51(7), 842-848.
- Chu XN, Pu ZY, Cao X, et al. (2009), THEMIS Observation of two substorms on February 26, 2008, *SCIENCE IN CHINA SERIES E-TECHNOLOGICAL SCIENCES*, May 2010 Vol.53 No.5: 1328-1337 doi: 10.1007/s11431-009-0399-3
- DANG Ge, MA ShuYing and ZHOU YunLiang (2007), Morphology of polar ionospheric O⁺ ion upflow: FAST observations during quiet time, *Chinese Science Bulletin*, 52(24): 3403-3415.
- Deng, X., M. Ashour Abdalla, M. Zhou, R. Walker, M. El - Alaoui, V. Angelopoulos, R. E. Ergun, and D. Schriver (2010), Wave and particle characteristics of earthward electron injections associated with depolarization fronts, *J. Geophys. Res.*, 115, A09225, doi:10.1029/2009JA015107.
- Deng, X.H., et al. (2009), Dynamics and waves near multiple magnetic null points in reconnection diffusion region, *J. Geophys. Res.*, 114, A07216, doi:10.1029/2008JA013197.

- Ding WZ, Cao JB, Zeng L, et al. (2010), Simulation studies of plasma sheet ion boundary, CHINESE JOURNAL OF GEOPHYSICS-CHINESE EDITION , Vol. 53(7): 1505-1514, 2010.
- Ding W Z, Cao J B, Du A M. (2010a) Statistical research of substorm onset identified by geomagnetic indices, Chin. J. Space Sci., 2010,30(1):17-22
- Du, J., C. Wang, T.L. Zhang, M. Volwerk, and C. Carr (2009), Mirror waves and mode transition observed in the magnetosheath by Double Star TC-1, Ann. Geophys., 27, 351-355.
- Du, J., C. Wang, P. Song, and T. L. Zhang (2008), Low-frequency fluctuations in the magnetosheath: Double Star TC-1 and Cluster observations, Sci. China Ser. E, 51(10), 1626-1638.
- Duan SuPing, Liu ZhenXing, Cao JinBin, et al. (2008), TC-1 observation of ion high-speed flow reversal in the near-Earth plasma sheet during substorm, SCIENCE IN CHINA SERIES E-TECHNOLOGICAL SCIENCES, 2008, 51 (10): 1721-1730.
- Duan Su-Ping, LIU Zhen-Xing, LU Li, et al.(2011a), TC-1 and Geotail joint observations of magnetic disturbances in the near-Earth plasma sheet during a substorm, Chin. J. Space Sci., 2011a, in press.
- Duan, S. P., Liu, Z. X., Liang, J., Zhang, Y. C., and Chen, T. (2011b) Multiple magnetic dipolarizations observed by THEMIS during a substorm, Ann. Geophys., 29, 331-339, doi:10.5194/angeo-29-331-2011, 2011b.
- Guo, X. C., C. Wang, Y. Q. Hu, and J. R. Kan (2008), Bow shock contributions to region 1 field-aligned current: A new result from global MHD simulations, Geophys. Res. Lett., 35, L03108:1-4.
- Guo, X. C., and C. Wang (2010a), Effect of the dawn-dusk interplanetary magnetic field By on the field-aligned current system, J. Geophys. Res., 115, A01206:1-10.
- Guo, X. C., C. Wang, and Y. Q. Hu (2010b), Global MHD simulation of the Kelvin-Helmholtz instability at the magnetopause for northward interplanetary magnetic field, J. Geophys. Res., 115, A10218:1-14.
- Guo J G, Shi J K, Zhang T L, Liu Z X, FAZAKERLEY A., RÈME H., DANDOURAS I. and LUCEK E., The correlations of ions density with geomagnetic activity and solar dynamic pressure in cusp region. Chinese Science Bulletin, 2007, 52(7):967-971.
- Guo Jian-Guang, Shi Jian-Kui, Zhang Tie-Long, Liu Zhen-Xing. Inter-hemispheric Comparison of Dipole Tilt Angle Effects on Latitude of Mid-Altitude Cusp. CHIN.PHYS.LETT. Vol. 25, No. 5 (2008) 1916-1918.

- Fu H S, Cao J B, Yang B, Lucek E, Rème H, Dandouras I.(2009) ULF waves associated with Solar wind deceleration in the Earth's Foreshock, *Chin Phys Lett.*, 2009,26(11), 119402, doi: 101088/0256-307X/26/11/119402
- Fu H S, Cao J B, Zhang T L, Reme H, Lucek E.(2009a).Statistical study of the solar wind deceleration in the Earth's foreshock region, *Chinese Journal of Space Science.*, 52(2):361-368
- Fu, H. S., J. Tu, J. B. Cao, P. Song, B. W. Reinisch, D. L. Gallagher, and B. Yang (2010a), IMAGE and DMSP observations of a density trough inside the plasmasphere, *J. Geophys. Res.*, 115, A07227, doi:10.1029/2009JA015104
- Fu, H. S., J. Tu, P. Song, J. B. Cao, B. W. Reinisch, and B. Yang (2010b), The nightside-to-dayside evolution of the inner magnetosphere: IMAGE RPI observations, *J. Geophys. Res.*, 115, A04213, doi:10.1029/2009JA014668.
- Fu, X., Q. Lu, and S. Wang (2006), The process of electron acceleration during collisionless magnetic reconnection. *Phys. Plasmas*, 13, 012309.
- Han, D.-S., H. - G. Yang, J. Liang, T. Iyemori, S. W. H. Cowley, and T. Araki (2010), High - latitude reconnection effect observed at the dayside dip equator as a precursor of a sudden impulse, *J. Geophys. Res.*, 115: A08214.
- Han D.-S., H.-G. Yang, M. Nose, D.-H. Huang, Z.-T. Chen, and H.-Q. Hu (2008a), Dawnside particle injection caused by sudden enhancement of solar wind dynamic pressure, *J. Atmos. Solar Terr. Phys.*, 70: 1995-1999.
- Han DeSheng, Yang HuiGen, Chen ZhuoTian & C. P. NIELSEN (2008b), Coupling of Pi2 wave energy in the inner magnetosphere as inferred from low-latitude ground observations, *Science in China Series E: Technological Sciences*, 51: 10 1745-1758.
- Han De-sheng, Tohru Araki, H-G. Yang, Z-T. Chen, Toshihiko Iyemori, and Peter Stauning (2007a), Comparative study of Geomagnetic Sudden Commencement (SC) between Oersted and ground observations at different local times, *J. Geophys. Res.*, 112: A05226, doi:10.1029/2006JA011953.
- Han D-S., H-G. Yang, Z-T. Chen, T. Araki, M. W. Dunlop, M. Nosé T. Iyemori, Q. Li, Y-F. Gao, K. Yumoto (2007b) : Coupling of perturbations in the solar wind density to global Pi3 pulsations: A case study, *J. Geophys. Res.*, 112: A05217, doi:10.1029/2006JA011675

- He, J.-S., Tu, C.-Y., Tian, H, et al. (2008a), A magnetic null geometry reconstructed from Cluster spacecraft observations, *J. Geophys. Res.*, 113, id.A05205.
- He, J.-S., Zong, Q.-G., Deng, X.-H., , (2008b), Electron trapping around a magnetic null, *Geophys. Res. Lett.*, 35, L14104.
- Hu, Y.Q, and C. Wang (2010a), Electrodynamical coupling in the solar wind - magnetosphere - ionosphere system, *Chinese Journal of Space Science*, 30(4): 321 - 332.
- Hu, Y. Q., Z. Peng, C. Wang, and J. R. Kan (2009), Magnetic merging line and reconnection voltage versus IMF clock angle: Results from global MHD simulations, *J. Geophys. Res.*, 114, A08220:1-11.
- Hu, Y. Q., X. C. Guo, and C. Wang (2007), On the ionospheric and reconnection potentials of the earth: Results from global MHD simulations, *J. Geophys. Res.*, 112, A07215, doi:10.1029/2006JA012145.
- Hu Z.-J., Yang H.-G. et al. (2010), The 4-emission-core structure of dayside aurora oval observed by all-sky imager at 557.7 nm in Ny-Alesund, Svalbard, *J. Atmos. Solar Terr. Phys.*, 72: 638-642.
- Hu Z.-J., Yang H.-G., et al. (2009), Synoptic distribution of dayside aurora: Multiple-wavelength all-sky observation at Yellow River Station in Ny-Alesund, Svalbard, *J. Atmos. Solar Terr. Phys.*, 71: 791-804.
- Huang, C.Y., Xu, R.L. and Hn J. W. (2008), 3-Dimensional Drift Shell Spitting during the Geomagnetic Disturbance, *Chinese Journal of Space Sci*, 28(4), 288.
- Huang, Y., Xu, R.L., Li, L., and Jin, X. (2009), Deduction of the Global Density of the Plasmasphere Reconstructed from the Observation Image using Computer Tomography Technique, *Chinese Journal of Geophysics*, 31,11, 2683.
- Huang, C., Q. Lu, and S. Wang (2010), The mechanisms of electron acceleration in anti-parallel and guide field magnetic reconnection. *Phys. Plasmas*, 17, 072306.
- Huang, S. Y., M. Zhou, F. Sahraoui, X. H. Deng, Y. Pang, Z. G. Yuan, Q. Wei, J. F. Wang, and X. M. Zhou (2010), Wave properties in the magnetic reconnection diffusion region with high beta: Application of the k-filtering method to Cluster multi-spacecraft data, *J. Geophys. Res.*, 115, A12211, doi:10.1029/2010JA015335.

- Huang Z. H., C. Wang, Y. Q. Hu and X. C. Guo (2008), Parallel Implementation of the 3D Global MHD Simulations for Earth's Magnetosphere, *Computers & Mathematics with Applications*, Vol. 55, No. 6, 1094-1101.
- Huang, J. and Ma, Z.W. (2008), Reconnection rate in collisionless magnetic reconnection under open boundary conditions, *CHINESE PHYSICS LETTERS*, 25 (5): 1764-176.
- Huang, J., Ma, Z. W., and Li, D. (2008), Debye-length scaled structure of perpendicular electric field in collisionless magnetic reconnection, *Geophys. Res. Lett.* 35 (10): Art. No. L10105
- Hu Z.-J., Yang H.-G. et al. (2010), The 4-emission-core structure of dayside aurora oval observed by all-sky imager at 557.7 nm in Ny-Alesund, Svalbard, *J. Atmos. Solar Terr. Phys.*, 72: 638-642.
- Hu Z.-J., Yang H.-G., et al. (2009), Synoptic distribution of dayside aurora: Multiple-wavelength all-sky observation at Yellow River Station in Ny-Alesund, Svalbard, *J. Atmos. Solar Terr. Phys.*, 71: 791-804.
- Li, H., C. Wang, and J. R. Kan (2010), Midday magnetopause shifts earthward of geosynchronous orbit during geomagnetic superstorms with $Dst \leq -300$ nT, *J. Geophys. Res.*, 115, A08230:1-6.
- Li, L Y, Cao J B, Zhou G C, Li X L. (2009). Statistical roles of storms and substorms in changing the entire outer zone relativistic electron population, *J. Geophys. Res.*, 2009, 114, A12214
doi:101029/2009JA014333
- Li L Y, Cao J B, Zhou G C. (2008). Whistler-mode waves modify the high-energy electron slot region and the outer radiation belt, *Chin. J. Geophys.*, 2008, 51(2), 361-324
- Li L Y, Cao J B, Zhou G C, Yang J Y, Yan C X, Zhang T L, R àme H, Dandouras I, Carr C M. (2008) Shrinkage of magnetosphere observed by TC-1 during the high-speed solar wind stream, *Sci in China(E)*, 2008,51(10), Special issue, 1695-1703
- Li, L., Chen, Z.Q., Xu, R.L. et al. (2009), A study of the plasmasphere density distribution using computed tomography methods from the EUV radiation data, *Advances in Space Research*, 43, 1143-1147.
- Li, J. H. and Ma, Z. W. (2010), Nonlinear evolution of resistive tearing mode with sub-Alfvénic shear flow, *J. Geophys. Res.*-115: Art. No. A09216.
- Lin M., Deng X., Yuan Z., Wang J. (2010), Characteristics of magnetic variation and current wedge in the sawtooth event on 30 september 2000, *Chinese J. Geophys.* (in Chinese), 2010,53(10):2280-2290, doi:10.3969/j.issn.0001-5733.2010.10.002

- Liu, J. J., H. Q. Hu, D. S. Han, L. Song, Z. J. Hu, Q. H. Zhang, and H. G. Yang (2011b), Diminishment of the auroral luminosity and reversal of the plasma convection associated with shock aurora, *J. Geophys. Res.*, in press.
- Liu, J.-M., B.-C. Zhang, Y. Kamide, Z.-S. Wu, Z.-J. Hu, and H.-G. Yang (2011a), Spontaneous and trigger-associated substorms compared: Electrodynamic parameters in the polar ionosphere, *J. Geophys. Res.*, 116: A01207.
- Liu, J.-M., B.-C. Zhang, et al. (2010), Observation of a double-onset substorm during northward interplanetary magnetic field, *J. Atmos. Sol. Terr. Phys.* 72(11-12): 864-868.
- Liu Jun-Ming, Zhang Bei-Chen, Liu Rui-Yuan, Wu Zhen-Sen (2009), Effects of the precipitation electrons on the polar ionosphere with different energy spectrum, 52(6): 1429-1437.
- Liu Y. H., B. J. Fraser, S.T.Ables, B.C.Zhang, R.Y.Liu, M.W.Dunlop, and J.Waterman (2009), Transverse-scale size of Pc3 ULF waves near the exterior cusp, *J. Geophys. Res.*, 114: A08208, doi: 10.1029/2008JA013971.
- Liu, Y. H., B. J. Fraser, S. T. Ables, M. W. Dunlop, B. C. Zhang, R. Y. Liu, and Q. G. Zong (2008), Phase structure of Pc3 waves observed by Cluster and ground stations near the cusp, *J. Geophys. Res.*, 113: A07S37, doi:10.1029/2007JA012754.
- Liu ZhenXing , ZuYin Pu, JinBin Cao, Chao Shen, Li Lu and LingQian Zhang, (2008). New progress of Double Star-Cluster joint exploration and study, *Science in China Series E: Technological Sciences*, Volume 51, Number 10, 1565-1579, DOI: 10.1007/s11431-008-0267-6, 2008
- Lu et al , Q., C. Huang, J. Xie, R. Wang, M. Wu, A. Vaivads, and S. Wang (2010), Features of separatrix regions in magnetic reconnection: Comparison of 2 - D particle - in - cell simulations and Cluster observations, *J. Geophys. Res.*, 115, A11208, doi:10.1029/2010JA015713.
- Lu, S., Q. Lu Q, Y. Cao et al.(2011), The effects of the guide field on the structures of electron density depletions in collisionless magnetic reconnection. *Chin. Sci. Bull.*, 56: 48–52, doi: 10.1007/s11434-010-4250-9
- Lu, Q. M., B. Lembege, J. B. Tao, and S. Wang (2008), Perpendicular electric field in two-dimensional electron phaseholes: A parameter study, *J. Geophys. Res.*, 113, A11219, doi:10.1029/2008JA013693
- Lu X. Q. and Ma Z. W. (2009), Dynamic Processes of Cross-Tail Current in the Near-Earth Magnetotail,

CHINESE PHYSICS LETTERS, 26 (5): Art. No. 059401

- Ma Yu duan, Jinbin Cao, Guocheng Zhou, Zhenxing Liu, Henri Reme and Iannis Dandouras (2007).
Multi satellite observations of magnetospheric fast convection events, Chinese Journal of
Geophysics, 2007, 50(5), 662-671.
- Ma Y D, Cao J B, R Nakamura, T L Zhang, Reme H, Dandouras I, Lucek E, and Dunlop M W. (2009).
Statistical analysis of earthward flow bursts in the inner plasma sheet during substorms, J.
Geophys. Res., 2009, 114, A07215, doi:10.1029/2009JA014275
- MA YuDuan, CAO JinBin, H. Reme, I. Dandouras, E. Lucek,(2010).The radial evolution of earthward
BBFs during substorm, Science in China (D), 2010, 40 (10) , 1542-1551
- Ma, Z. W. (2008), Sudden disruption of the cross-tail current in the magnetotail, PHYSICS OF
PLASMAS, 15 (3): Art. No. 032906
- Ma Z. W. and Feng S. L. (2008), Generation of electric field and net charge in Hall reconnection,
CHINESE PHYSICS LETTERS, 25 (8): 2934-2937.
- Ma Z. W. and Lu X. Q. (2009), An Island Coalescence Scenario for Near-Earth Current Disruption in
the Magnetotail, CHINESE PHYSICS LETTERS, 26 (8): Art. No. 089401.
- Pang, Y.; Deng, X. H.; Yuan, Z. G.; Zhou, M.; Lin, M. H.; Shu, Z. W.; Li, S. Y.; Wang, J. F.; Balogh, A.
(2008), Polar ionosphere and geomagnetic response for the flux transfer events: A case study,
Advances in Space Research, Volume 43, Issue 6, p. 957-963.
- Pang, Y., Y. Lin, X. H. Deng, X. Y. Wang, and B. Tan (2010a), Three-dimensional hybrid simulation of
magnetosheath reconnection under northward and southward interplanetary magnetic field, J.
Geophys. Res., 115, A03203, doi:10.1029/2009JA014415.
- Pang Ye, Lin Yu, Deng Xiaohua (2010b). Global hybrid simulation of magnetic reconnection in the
magnetosheath. Chinese Journal of Space Science, 2010, 30(4): 333-342.
- Peng, Z., C. Wang, and Y. Q. Hu (2010), Role of IMF Bx in the solar
wind - magnetosphere - ionosphere coupling, J. Geophys. Res., 115, A08224:1-7.
- Pu, Z. Y., et al. (2007), Global view of dayside magnetic reconnection with the dusk-dawn IMF
orientation: A statistical study for Double Star and Cluster data, Geophys. Res. Lett., 34, L20101,
doi:10.1029/2007GL030336.

- Pu, Z.Y., X.N. Chu, X.Cao, V. Mishin, V. Angelopoulos, et al. (2010), THEMIS Observations of Magnetotail Reconnection Initiated Substorms on February 26, 2008, *J. Geophys.Res.-Space Physics*, VOL. 115, A02212, doi: 10.1029/2009JA014217.
- Shen, C. and Dunlop, M. W. (2008a), Geometric structure analysis of the magnetic field, in *Multi-Spacecraft Analysis Methods Revisited*, edited by G. Paschmann and P.W. Daly, ISSI Science Report, SR-008, chap. 3, pp27-32, Kluwer Academic Pub.
- Shen, C., Z. Liu, X. Li, et al. (2008b), Flattened Current Sheet and its Evolution in Substorms, *J. Geophys. Res.*, 113, A07S21,doi:10.1029/2007JA012812.
- Shen C., Z. J. Rong, X. Li, Z. X. Liu, M. Dunlop, E. Lucek, H.V. Malova(2008c), Magnetic Configurations of Tail Tilted Current Sheets, *Ann. Geophys.*, 26, 3525–3543.
- Shen, C., X. Li, M. Dunlop, Q. Q. Shi, Z. X. Liu, E. Lucek, and Z. Q. Chen (2007), Magnetic field rotation analysis and the applications, *J. Geophys. Res.*, 112, A06211, doi:10.1029/2005JA011584.
- Shi, Q. Q. et al. (2009a), Spatial structures of magnetic depression in the Earth's high-altitude cusp: Cluster multipoint observations, *J. Geophys. Res.*, 114, A10202, doi:10.1029/2009JA014283.
- Shi, Q. Q. et al. (2009b), Cluster observations of the entry layer equatorward of the cusp under northward interplanetary magnetic field, *J. Geophys. Res.*, 114, A12219, doi:10.1029/2009JA014475.
- Shi, J.K. (2009a), The Ionospheric Up-flowing He⁺ Ion Distribution in the Magnetosphere, *Journal of Atmospheric and Solar-Terrestrial Physics*, DOI information: 10.1016/j.jastp. 71, 1630-1635.
- Shi Jiankui, Zhengwei Cheng, T.L. Zhang, M. Dunlop (2009b), Zhenxing Liu, Properties of field aligned current in the plasma sheet boundary layers in the magnetotail: Cluster observation, *Chin. Phys.Lett.*, 26(2): 029401
- Shi, K., Z. W. Cheng, T. L. Zhang, M. Dunlop, Z. X. Liu, K. Torkar, et al.(2010), South-north asymmetry of field-aligned currents in the magnetotail observed by Cluster, *J. Geophys. Res.*, 115, A07228, doi:10.1029/2009JA014446.
- Su, Z., Xiao, F., Zheng, H., Wang, S. (2010a), Combined radial diffusion and adiabatic transport of radiation belt electrons with arbitrary pitch-angles, *J. Geophys. Res.* 115: A10249.
- Su, Z., Xiao, F., Zheng, H., Wang, S. (2010b), STEERB: A three-dimensional code for storm-time evolution of electron radiation belt, *J. Geophys. Res.* 115: A09208.

- Su, Z., Xiao, F., Zheng, H., Wang, S. (2011a), CRRES observation and STEERB simulation of the 9 October 1990 electron radiation belt dropout event, *Geophys. Res. Lett.* In press.
- Su, Z., Xiao, F., Zheng, H., Wang, S. (2011b), Radiation belt electron dynamics driven by adiabatic transport, radial diffusion, and wave-particle interactions, *J. Geophys. Res.* In press.
- Su, Z., Zheng, H. (2009), Resonant scattering of relativistic outer zone electrons by plasmaspheric plume electromagnetic ion cyclotron waves, *Chinese Phys. Lett.* 26: 129401.
- Su, Z., Zheng, H., Chen, L., Wang, S. (2010c), Numerical simulations of storm-time outer radiation belt dynamics by wave-particle interactions including cross diffusion, *J. Atmos. Sol.-Terr. Phys.* 73: 95–105.
- Su, Z., Zheng, H., Wang, S. (2009a), Dynamic evolution of energetic outer zone electrons due to whistler-mode chorus based on a realistic density model, *J. Geophys. Res.* 114: A07201.
- Su, Z., Zheng, H., Wang, S. (2009b), Evolution of electron pitch angle distribution due to interactions with whistler-mode chorus following substorm injections, *J. Geophys. Res.* 114: A08202.
- Su, Z., Zheng, H., Wang, S. (2010c), A parametric study on the diffuse auroral precipitation by resonant interaction with whistler-mode chorus, *J. Geophys. Res.* 115: A05219.
- Su, Z., Zheng, H., Wang, S. (2010d), Three dimensional simulations of energetic outer zone electron dynamics due to wave-particle interaction and azimuthal advection, *J. Geophys. Res.* 115: A06203.
- Su, Z., Zheng, H., Xiong, M. (2009c), Dynamic evolution of outer radiation belt electrons due to whistler-mode chorus. *Chinese Phys. Lett.* 26: 039401.
- Sun, P., G. Qin, and C. Wang (2007), Study of energetic particle's acceleration mechanism at perpendicular shock with particle simulation results, *Chin. J. Space Sci.*, 97(6), 441-447.
- Sun, W. J. et al. (2010), Statistical research on the motion properties of the magnetotail current sheet: Cluster observations, *Sci. China Tech. Sci.*, 53: 1732–1738, doi: 10.1007/s11431-010-3153-y.
- Tang, B. B., X. C. Guo, C. Wang, Y. Q. Hu, and J. R. Kan (2009), Bow shock and magnetopause contributions to the cross-tail current from global MHD simulations, *J. Geophys. Res.*, 114, A08203:1-7.

- Tang, C. L., L. Lu, S. McKenna-Lawlor, S. Barabash, Z. X. Liu, M.-C. Fok, and Z. Y. Li (2008), A comparison of Neutral Atom Detector Unit neutral atom image inversion with a comprehensive ring current model, *J. Geophys. Res.*, 113, A07S32, doi:10.1029/2007JA012680.
- Tang, C.L. et al. (2009a), Cluster observations of earthward propagating plasmoid and flux ropes in the near-tail during the course of a substorm event, *J. Adv. Space Res.*, doi:10.1016/j.asr.2008.12.018
- Tang, C. L., Z. Y. Li, V. Angelopoulos, S. B. Mende, K. H. Glassmeier, E. Donovan, C. T. Russell, and L. Lu (2009b), THEMIS observations of the near-Earth plasma sheet during a substorm, *J. Geophys. Res.*, 114, A09211, doi:10.1029/2008JA013729.
- Tang, C. L., V. Angelopoulos, A. Runov, C. T. Russell, H. Frey, K. H. Glassmeier, K. H. Fornacon, and Z. Y. Li (2010), Precursor activation and substorm expansion associated with observations of a dipolarization front by Time History of Events and Macroscale Interactions during Substorms (THEMIS), *J. Geophys. Res.*, 115, A07215, doi:10.1029/2009JA014879.
- Tang P. J. (2008), Simulation on the Penetration of Energetic Particles into the Magnetosphere, *Chin., Space Sci.* 28 (4): 283-287.
- Tian, A. M., Q. G. Zong, Y. F. Wang, Q. Q. Shi, S. Y. Fu, and Z. Y. Pu (2010), A series of plasma flow vortices in the tail plasma sheet associated with solar wind pressure enhancement, *J. Geophys. Res.*, 115, A09204, doi:10.1029/2009JA014989.
- Wang, C., T. R. Sun, X. C. Guo, and J. D. Richardson (2010b), Case study of nightside magnetospheric magnetic field response to interplanetary shocks, *J. Geophys. Res.*, 115, A10247:1-8.
- Wang, C., H. Li, J. D. Richardson, and J. R. Kan (2010a), Interplanetary shock characteristics and associated geosynchronous magnetic field variations estimated from sudden impulses observed on the ground, *J. Geophys. Res.*, 115, A09215:1-10.
- Wang, C., J. B. Liu, H. Li, Z. H. Huang, J. D. Richardson, and J. R. Kan (2009), Geospace magnetic field responses to interplanetary shocks, *J. Geophys. Res.*, 114, A05211:1-8.
- Wang, C., J. B. Liu, Z. H. Huang, and J. D. Richardson (2007), Response of the magnetic field in the geosynchronous orbit to solar wind dynamic pressure pulses, *J. Geophys. Res.*, 112, A12210:1-8.
- Wang H. and LÜHR H. (2007), Seasonal-longitudinal variation of substorm occurrence frequency: Evidence for ionospheric control, *Geophys. Res. Lett.*, 34 (L07104): doi: 10.1029/2007GL029423.

- Wang H., LÜHR H., MA S. Y., FREY H. U. (2007), Interhemispheric comparison of average substorm onset locations: Evidence for deviation from conjugacy, *Ann. Geophys.*, 25: 989-999.
- Wang H., LÜHR H., MA S. Y., RIDLEY A. J. (2008b), Substorm dynamics in the magnetotail as derived from TC1 and Cluster coordinate observations, *Earth, Planets and Space*, 60: 613-621.
- Wang H., LÜHR H., RIDLEY A. J., RITTER P. AND YU Y. (2008c), Storm time dynamics of auroral electrojets: CHAMP observation and the Space Weather Modeling Framework comparison, *Ann. Geophys.*, 26: 555-570.
- Wang H., LÜHR H., RIDLEY A. J. (2010), Plasma convection jets near the poleward boundary of the nightside auroral oval and their relation to Pedersen conductivity gradient, *Ann. Geophys.*, 28: 969-976.
- Wang H., RIDLEY A. J., LÜHR H., LIEMOHN M. W., and MA S. Y. (2008a), Statistical study of the subauroral polarization streams: its dependence on the cross polar cap potential and subauroral conductance, *J. Geophys. Res.*, 113 (A12311): doi: 10.1029/2008JA013529.
- Wang H., RIDLEY A. J. AND LÜHR H. (2008), SWMF simulation of field-aligned currents in the varying northward and dusward IMF with nonzero dipole tilt, *Ann. Geophys.*, 26: 1461-1477.
- Wang H., RIDLEY A. J. AND LÜHR H. (2008d), Validation of the Space Weather Modeling Framework with CHAMP and DMSP observations, *Space Weather*, 6 (S03001): doi: 10.1029/2007SW000355.
- Wang, J., et al. (2007), TC1 and Cluster observation of an FTE on 4 January 2005: A close conjunction, *Geophys. Res. Lett.*, 34, L03106, doi:10.1029/ 2006GL028241
- Wang, J. et al. (2008), Coordinated Cluster/Double Star observations of dayside flux transfer events on 6 April 2004, *Sci China Ser E-Tech Sci.*, 51 (10), 1611-1619.
- Wang, J., Z. Y. Pu, S. Y. Fu, X. G. Wang, C. J. Xiao et al (2011), Conjunction of anti-parallel and component reconnection at the dayside MP: Cluster and Double Star coordinated observation on 6 April 2004, *Geophys. Res. Lett.*, in press.
- Wang, R., Q. Lu, C. Huang, and S. Wang (2010a), Multispacecraft observation of electron pitch angle distributions in magnetotail reconnection, *J. Geophys. Res.*, 115, A01209, doi:10.1029/2009JA014553.

- Wang, R., Q. Lu, A. Du, and S. Wang(2010b), In situ observations of a secondary magnetic island in an ion diffusion region and associated energetic electrons. *Phys. Rev. Lett.*, 104, 0175003.
- Wang, R., Q. Lu, X. Li, C. Huang, and S. Wang (2010c), Observations of energetic electrons up to 200 keV associated with a secondary island near the center of an ion diffusion region: A Cluster case study, *J. Geophys. Res.*, 115, A11201, doi:10.1029/2010JA015473.
- Wang Z Q, Cao J B. (2010) ULF waves associated with the periodical high speed flows in magnetotail plasma sheet, *Chin. J. Geophys.*, 2010, 53 (2): 231-236
- Wei, X. H., J. B. Cao (, G. C. Zhou, O. Santolik, H. Reme, I. Dandouras , N. Cornilleau , E. Lucek, C. M. Carr, A. Fazakerley, (2007). Cluster observations of waves in the whistler frequency range during magnetic reconnection in the Earth's magnetotail, *J. Geophys. Res.*, 2007, 112, doi:10.1029/2006JA011771
- Wei X H, Cao J B, Zhou G C, Fu H S.(2010). Is the Near Earth Current Sheet Prior to Reconnection Unstable to Tearing Mode? , *Chin Phys Lett.*, 2010, 27(2):029401
- Wei Xinhua, CAO Jinbin, (2007). Effect of Guiding Field to Low-frequency Electromagnetic Instabilities in the Collisionless Current Sheet, *Chinese Journal of Space Science* , 2007 , 27(5): 360-367.
- Wu, M., Q. Lu, C. Huang, and S. Wang (2010), Transverse instability and perpendicular electric field in twodimensional electron phase - space holes, *J. Geophys. Res.*, 115, A10245, doi:10.1029/2009JA015235.
- Xiao C. J., X. G. Wang, Z. Y. Pu, et al. (2007a), Satellite Observations of Separator Line Geometry of Three-Dimensional Magnetic Reconnection, *Nature Physics*, 3(9), 609-613, doi:10.1038/nphys342, 2007a.
- Xiao C. J., Z. Y. Pu, X. G., Wang, et al.(2007b), Cluster Measurements of Fast Magnetic Reconnection in the Magnetotail, *Geophys. Rev. Lett.*, 34, L01101, doi:10.1029/ 2006GL028006, 2007b.
- Xiao, F. (2006), Modelling energetic particles by a relativistic kappa loss cone distribution function in plasmas, *Plasma Phys. Control. Fusion*. 48: 203.
- Xiao, F., Chen, L., He, Y. (2011a), Bounce-averaged diffusion coefficients for superluminous wave modes in the magnetosphere, *J. Atmos. Sol.-Terr. Phys.* 73: 88–94.

- Xiao, F., Chen, L., He, Y., Su, Z., Zheng, H. (2011b), Modeling of precipitation loss of ring current protons by electromagnetic ion cyclotron waves, *J. Atmos. Sol.-Terr. Phys.* 73: 106–111.
- Xiao, F., Chen, L., Li, J. (2008a), Energetic particles modeled by a generalized relativistic kappa-type distribution function in plasmas, *Plasma Phys. Control. Fusion.* 50: 105002.
- Xiao, F., Chen, L., Zheng, H., Wang, S. (2007a), A parametric ray tracing study of superluminous auroral kilometric radiation wave modes, *J. Geophys. Res.* 112: 10214.
- Xiao, F., He, H., Zhou, Q., Zheng, H., Wang, S. (2006a), Relativistic diffusion coefficients for superluminous (auroral kilometric radiation) wave modes in space plasmas. *J. Geophys. Res.* 111: 11201.
- Xiao, F., Zhou, Q., He, H., Tang, L. (2006b), Instability of whistler-mode waves by a relativistic kappa-loss-cone distribution in space plasmas, *Plasma Phys. Control. Fusion.* 48: 1437–1445.
- Xiao, F., Shen, C., Wang, Y., Zheng, H., Wang, S. (2008b), Energetic electron distributions fitted with a relativistic kappa-type function at geosynchronous orbit, *J. Geophys. Res.* 113:5203.
- Xiao, F., Su, Z., Zheng, H., Wang, S. (2009), Modeling of outer radiation belt electrons by multidimensional diffusion process, *J. Geophys. Res.* 114: A03201.
- Xiao, F., Su, Z., Zheng, H., Wang, S. (2010a), A parametric study on outer radiation belt electron evolution by superluminous R-X mode waves, *J. Geophys. Res.* 115:A10217.
- Xiao, F., Su, Z., Zheng, H., Wang, S. (2010b), Three-dimensional simulations of outer radiation belt electron dynamics including cross diffusion terms, *J. Geophys. Res.* 115: A05216.
- Xiao, F., Thorne, R. M., Summers, D. (2007b), Higher-order gyroresonant acceleration of electrons by superluminous (AKR) wave-modes, *Planet. Space Sci.* 55: 1257.
- Xiao, F., Zhou, Q., He, H., Tang, L. (2006b), Instability of whistler-mode waves by a relativistic kappa-loss-cone distribution in space plasmas, *Plasma Phys. Control. Fusion.* 48: 1437–1445.
- Xiao, F., Zhou, Q., He, H., Zheng, H., Wang, S. (2007c), Electromagnetic ion cyclotron waves instability threshold condition of suprathermal protons by kappa distribution, *J. Geophys. Res.* 112: A07219.
- Xiao, F., Zhou, Q., Li, C., Cai, A. (2008c), Modeling solar energetic particle by a relativistic kappa-type distribution, *Plasma Phys. Control. Fusion.* 50: 062001.
- Xiao, F., Zhou, Q., Zheng, H., Wang, S. (2006c), Whistler instability threshold condition of energetic electrons by kappa distribution in space plasmas, *J. Geophys. Res.* 111: A08208.

- Xiao, F., Zong, Q., Pu, Z., Su, Z., Cao, J., He, J., Wang, Y., Zheng, H. (2010c), Electron acceleration by whistler-mode waves around the magnetic null during 3D reconnection, *Plasma Phys. Control. Fusion*. 52: 052001.
- Xie, L., Z. Y. Pu, X. Z. Zhou, S. Y. Fu, Q.-G. Zong, and M. H. Hong (2006), Energetic ion injection and formation of the storm-time symmetric ring current, *Ann. Geophys.*, 24, 3547–3556.
- Xie Lun, TU Wei-chao, Zhang Hui, PU Zu-yin (2007), NOAA/POES observation of the sources of the relativistic electron in the magnetosphere, *CHINESE JOURNAL OF GEOPHYSICS* Vol.50, No.6, 1407-1413
- Xie, L, Zhang, X., Pu Z. Y., Wang Y. F., Fu S. Y, and Zong Q. G. (2008), Ultra low frequency waves observed by Double Star TC-1 in the plasmasphere boundary layer, *Science in China Series E: Technological Sciences*, vol. 51, no. 10 , 1685-1694.
- Xie, L., Tu, W.C., Li, X.L., and Pu, Z.Y. (2009), The study for the formation and loss mechanism of new proton radiation belt after Halloween storm in 2003, *Chinese J. Geophys.*, 52 (5), 1138-1145
- Xu, R.-L. and L. Li, 2006 (2006), The 3-dimensional characteristics of the magnetic field lines and the non-adiabatic region in the magnetosphere, *Advances in Space Research* 38, 1647–1651.
- Xu Wenyao (2011), Energy Budget in the Coupling Processes of the Solar Wind, Magnetosphere and Ionosphere *Chinese J. Space Sci.*, 31(1):1-14.
- Xu, W.Y., and Du A. M. (2010). Effects of the Ring Current Decay Rate on the Energy State of the Magnetosphere, *Chinese J. Geophys.* 53(3): 329-338.
- Xu Wenyao (2009), Variations of the auroral electrojet belt during substorms, *Chinese J. Geophys.*, 52(2), 301-310.
- Xu Wenyao (2008), Uncertainty in magnetic activity indices, *Science in China (E)*, 51(10), 1659-1664.
- Xu, W.Y., Ceng, G. X., Du, A.M., Ying-Yan et al. (2008), Key points model for polar region currents, *J. Geophys. Res.*, 113(A3), A03S11, doi:10.1029/2007JA012588.
- Yang .B., Q.-G. Zong, S. Y. Fu, K. Takahashi, X. Li, Y. F. Wang, Z. Y. Pu, H. S. Fu, H. Reme, C. Yue, H. Zheng and C. Sheng (2011a), Pitch angle evolutions of oxygen ions driven by storm-time ULF poloidal standing waves, *J. Geophys. Res.*, 116, A03207, doi:10.1029/2010JA016047.
- Yang B., Q.-G. Zong, S. Y. Fu, X. Li, A. Korth, H. S. Fu, C. Yue, and H. Reme (2011b), The role of ULF waves interacting with oxygen ions at the outer ring current during storm times, *J. Geophys. Res.*, 116, A01203, doi:10.1029/2010JA015683.

- Yang B., Q.-G. Zong, Y. F. Wang, S. Y. Fu, P. Song, H. S. Fu, A. Korth, T. Tian, and H. Reme (2010), Cluster observations of simultaneous resonant interactions of ULF waves with energetic electrons and thermal ion species in the inner magnetosphere, *J. Geophys. Res.*, 115, A02214, doi:10.1029/2009JA014542.
- Yang, B. S. Y. Fu, Q.-G. Zong, Y. F. Wang, X.Z. Zhou, Z.Y. Pu, L. Xie (2008), Numerical study of ULF waves excited by sudden impulse in the dipole model, *Sci Chin Ser E-Tech Sci*, 51(10): 1665–1676.
- Yang J., J. Cao, C. Yan, L. Li and G. Zhou,(2007). The acceleration of energetic electrons associated with chorus observed by TC-2, *Nuclear Physics B, Supplement*, 166, 276-278, 2007.
- Yang J Y, Cao J B, Yan C X, Li L Y, Ma Y D.(2008). The mid-high latitude whistler mode chorus waves observed around substorm onsets, *Science in China (D)*., 2008,51(10), Special issue, 1648-1658.
- Yuan, Z.,X. Deng, X. Lin, Y. Pang, M. Zhou, P. M. E. Dér éau, J. G.Trotignon, E. Lucek, H. U. Frey, and J. Wang (2010), Link between EMIC waves in a plasmaspheric plume and a detached sub - auroral proton arc with observations of Cluster and IMAGE satellites, *Geophys. Res. Lett.*, 37, L07108, doi:10.1029/2010GL042711.
- Yuan Z. , X. Deng, (2007), Effects of continuous solar wind pressure variations on the long-lasting penetration of interplanetary electric field during southward interplanetary magnetic field, *Adv. Space Res.*, 39,1342-1346, dio:10.1016/j.asr.2007.02.033.
- Yuan Z., X. Deng, Y. Pang, S. Li, J. Wang (2007), Alfvén waves in a plasma sheet boundary layer associated with near-tail magnetic reconnection, *Chin. Phys. Lett.*, 24(4), 1122-1124.
- Yue. C., Q.-G. Zong, and Y. F. Wang (2009), Response of the magnetic field and plasmas at the geosynchronous orbit to interplanetary shock, *Chinese Sci Bull*, 54, 4241-425.
- Yue. C., Q.-G. Zong, H. Zhang, Y. F. Wang, C. J. Yuan, Z. Y. Pu, S. Y. Fu, A. T. Y. Lui, B. Yang and C.R. Wang (2010). Geomagnetic activities triggered by interplanetary shocks. *J. Geophys. Res.*, 115, A00I05, doi:10.1029/2010JA015356.
- Zhang Y. C, Z. X. Liu,C. Shen, A.Fazakerley, M.Dunlop, H.R éne, E.Lucek, A.P.Walsh, L.Yao,(2007), The magnetic structure of an earthward-moving flux rope observed by Cluster in the near-tail, *Ann. Geophys.*, 25, 1471 -1476.

- Zhang Y. C., C. Shen, Z. X. Liu, and Y. Narita, (2010), Magnetic helicity of a flux rope in the magnetotail: THEMIS results, *Ann. Geophys.*, 28, 1687–1693.
- Zhang Yong-Cun, Shen Chao, Liu Zhen-Xing, (2011), The characteristics and structure of magnetotail flux rope recovered from Grad-Shafranov method, *ACTA PHYS SIN-CH ED*, to be published.
- Zhang, L. Q., Z. X. Liu, W. Baumjohann, Z. W. Ma, Z. Y. Pu, M. W. Dunlop, L. Lu, J. K. Shi, C. Carr, H. Rème, and J. Y. Wang (2009), Convective bursty flows in the near-Earth magnetotail inside 13 RE, *J. Geophys. Res.*, 114, A02202, doi:10.1029/2008JA013125.
- Zhang, L. Q., Z. X. Liu, Z. W. Ma, W. Baumjohann, Z. Y. Pu, M. W. Dunlop, H. Rème, and J. Y. Wang (2010), X line distribution determined from earthward and tailward convective bursty flows in the central plasma sheet, *J. Geophys. Res.*, 115, A06218, doi:10.1029/2009JA014429.
- Zhang Q. -H., B. -C. Zhang, R. -Y. Liu, et al (2011), On the importance of IMF |BY| on polar cap patch formation, *J. Geophys. Res.*, in press.
- Zhang Q.-H., M. W. Dunlop, M. Lockwood, et al (2010a), Simultaneous observations of reconnection pulses at Cluster and their effects on the cusp aurora seen at Chinese Yellow River Station, *J. Geophys. Res.*, 115: A10237.
- Zhang Q. -H., Dunlop M. W., Holme R., and Woodfield E. E. (2010b), Comparison of eight years magnetic field data from Cluster with Tsyganenko models in the inner magnetosphere, *Ann. Geophys.*, 28(1): 309-326.
- Zhang Qing-He, R. Y. Liu, J. Y. Huang, M. W. Dunlop, H. Q. Hu, Z. J. Hu, Y. V. Bogdanova, and A. Walsh (2009), Simultaneous TC-1 and Cluster observations of FTEs on 13 March 2004, *Chinese Journal of Space Science(in Chinese)*, 29 (2): 166-174.
- Zhang Qing-He, LIU Rui-Yuan, HUANG Ji-Ying, M W Dunlop, HU Hong-Qiao, HU Ze-Jun, Bogdanova Y V and Lester M. (2008a), Simultaneous Cluster and CUTLASS observations of FTEs on 11 February 2004, *CHINESE JOURNAL OF GEOPHYSICS*, 51(1): 1-11.
- Zhang Q. -H., Liu R. Y., Dunlop M. W., Huang J. Y., Hu H. Q., Lester M., Liu Y. H., Hu Z. J., Shi Q. Q., and Taylor M.G. G. T. (2008b), Simultaneous tracking of reconnected flux tubes: Cluster and conjugate SuperDARN observations on 1 April 2004. *Ann. Geophys.*, 26(6): 1545-1557.

- Zhang Qing-He, Liu R. Y., Huang J. Y., Dunlop M. W., Hu H. Q., Shen C., Bogdanova Y. V. (2007), Characteristics of the magnetic flux transfer events on 1 April 2004, Chinese Journal of Polar Research (in Chinese), 19(2): 121-130.
- Zhang, X. Y., Q.-G. Zong, Y. F. Wang, H. Zhang, L. Xie, S. Y. Fu, C. J. Yuan, C. Yue, B. Yang, and Z. Y. Pu (2010), ULF waves excited by negative/positive solar wind dynamic pressure impulses at geosynchronous orbit, J. Geophys. Res., 115, A10221, doi:10.1029/2009JA015016.
- Zhang X. G., Pu Z. Y., Ma Z. W., Zhou X. Z. (2008), Roles of initial current carrier on the distribution of field-aligned current in 3-D Hall MHD simulations, 38 (3), 361 ~ 374.
- Zheng, H., Su, Z., Xiong, M. (2008), Pitch angle distribution evolution of energetic electrons by whistler-mode chorus, Chinese Phys. Lett. 25: 3515–3518.
- Zhou, M., M. Ashour-Abdalla, X. Deng, D. Schriver, M. El-Alaoui, and Y. Pang (2009c), THEMIS observation of multiple dipolarization fronts and associated wave characteristics in the near-Earth magnetotail, Geophys. Res. Lett., 36, L20107, doi:10.1029/2009GL040663.
- Zhou, M., et al. (2009b), Observation of waves near lower hybrid frequency in the reconnection region with thin current sheet, J. Geophys. Res., 114, A02216, doi:10.1029/2008JA013427.
- Zhou Meng et al. (2009a), Observation of the lower hybrid waves near the three-dimensional null pair, Sci China Ser G-Phys Mech Astron, Apr. 2009, vol. 52, no. 4, 626-630
- Zhou M. et al. (2008), Two dimensional simulation of amplitude modulated electron plasma waves, Advances in Space Research 41 (2008) 1305–1309.
- Zong, Q.-G., et al. (2007), Ultralow frequency modulation of energetic particles in the dayside magnetosphere, Geophys. Res. Lett., 34, L12105, doi:10.1029/2007GL029915.
- Zong, Q.-G., et al. (2008), Multiple cusps during an extended northward IMF period with a significant By component, J. Geophys. Res., 113, A01210, doi:10.1029/2006JA012188.
- Zong, Q.-G., H. Zhang, S. Y. Fu, Y. F. Wang, Z. Y. Pu, A. Korth, P. W. Daly, and T. A. Fritz (2008a), Ionospheric oxygen ions dominant bursty bulk flows: Cluster and Double Star observations, J. Geophys. Res., 113, A07S23, doi:10.1029/2007JA012764.
- Zong, Q.-G., X.-Z. Zhou, Y. F. Wang, X. Li, P. Song, D. N. Baker, T. A. Fritz, P. W. Daly, M. Dunlop, and A. Pedersen (2009a), Energetic electron response to ULF waves induced by interplanetary shocks in the outer radiation belt, J. Geophys. Res., 114, A10204, doi:10.1029/2009JA014393.

Zong, Q.-G., et al. (2009b), Vortex-like plasma flow structures observed by Cluster at the boundary of the outer radiation belt and ring current: A link between the inner and outer magnetosphere, *J. Geophys. Res.*, 114, A10211, doi:10.1029/2009JA014388.

PROGRESS IN CORONAL AND INTERPLANETARY RESEARCH

ZHAO Xinhua and FENG Xueshang

(State Key Laboratory of Space Weather, Center for Space Science and Applied Research, Chinese Academy of Sciences, Beijing 100190, China)

Abstract In recent years, considerable progress in the research of solar corona and interplanetary space has been achieved by the space physics community of China. This paper gives a brief report of the progress in this area of China during the period of 2006-2010. The primary achievements can be divided into the following aspects: Solar corona, Solar wind, Interplanetary transients, Energetic particles, MHD simulations, Space plasma, and Prediction methods.

I. SOLAR CORONA

In order to determine whether EIT waves are generated by coronal mass ejections (CMEs) or pressure pulses in solar flares, 14 non-CME-associated energetic flares, which should possess strong pressure pulses in their loops, are studied by Chen (2006). They are selected near solar minimum, as this favors the detection of EIT waves. It is found that none of these flares are associated with EIT waves. Particular attention is paid to AR 0720, which hosted both CME-associated and non-CME types of flares. The *SOHO*/EIT images convincingly indicate that EIT waves and expanding dimmings appear only when CMEs are present. Therefore, it is unlikely that pressure pulses from flares generate EIT waves.

Coronal mass ejections (CMEs) are often categorized into flare-associated and filament-associated types, which logically is incomplete since there are many CMEs of the intermediate type. With this new classification, Chen et al. (2006) reexamined whether flare-associated CMEs and filament eruption-associated CMEs have distinct velocity distributions and to investigate which factors may affect the CME velocities. They divided the CME events observed from 2001–2003 into three types, i.e., the flare-associated type, the filament

eruption-associated type, and the intermediate type. The magnetic environments of the source regions, e.g., the polarity orientation, the chirality of the filaments, etc., are examined. Their results indicate that the P-value of the likelihood between the flare-associated and the filament eruption-associated CMEs is as high as 0.79, which strongly suggests that they are a continuum of events rather than two distinct types. For the filament eruption-associated CMEs, the speeds are found to be strongly correlated with the average magnetic field in the filament channel. It is also found that there is a slight tendency for the filaments with the minority chirality to have weaker magnetic fields, and hence the corresponding CMEs have smaller eruption speeds. A slight tendency is also found for the CMEs associated with non-active region filaments to have higher eruption speeds than those with active region filaments. However, the polarity orientation of the filament channel has little effect on the eruption speed.

By use of the high-resolution spectral data obtained with THEMIS on 2002 September 5, the characteristics of 14 well-observed Ellerman bombs (EBs) have been analyzed by Fang et al. (2006). Their results indicate that 9 of the 14 EBs are located near the longitudinal magnetic polarity inversion lines. Most of the EBs are accompanied by mass motions. The most obvious characteristic of the EB spectra is the two emission bumps at the two wings of both $H\alpha$ and $Ca\ II\ \lambda 8542$. For the first time both thermal and nonthermal semiempirical atmospheric models for the conspicuous and faint EBs are computed. In computing the nonthermal models, they assume that the electron beam resulting from magnetic reconnection is produced in the lower chromosphere. The reasons are that it requires much lower energies for the injected particles and that it gives rise to a more profound absorption at the H line center, in agreement with their observations. The common characteristic is the heating in the lower chromosphere and the upper photosphere. The temperature enhancement is about 600–1300K in the thermal models. If the nonthermal effects are included, then the required temperature increase can be reduced by 100–300 K. These imply that the EBs could probably be produced by the magnetic reconnection in the solar lower atmosphere. The radiative and kinetic energies of the EBs are estimated, and the total energy is found to be 10^{26} to 5×10^{27} ergs. According to the characteristics of EBs, they tentatively suggest that EBs could be called “submicroflares.”

It is generally believed that the magnetic free energy accumulated in the corona

serves as a main energy source for solar explosions such as coronal mass ejections (CMEs). In the framework of the flux rope catastrophe model for CMEs, the energy may be abruptly released either by an ideal magnetohydrodynamic (MHD) catastrophe, which belongs to a global magnetic topological instability of the system, or by a fast magnetic reconnection across preexisting or rapidly developing electric current sheets. Both means of magnetic energy release are thought to be important to CME dynamics. To disentangle their contributions, Chen et al. (2007) construct a flux rope catastrophe model in the corona and solar wind and compare different cases in which they either prohibit or allow magnetic reconnection to take place across rapidly growing current sheets during the eruption. It has been demonstrated that CMEs, even fast ones, can be produced taking the ideal MHD catastrophe as the only process of magnetic energy release. Nevertheless, the eruptive speed can be significantly enhanced after magnetic reconnection sets in. In addition, a smooth transition from slow to fast eruptions is observed when increasing the strength of the background magnetic field, simply because in a stronger field there is more free magnetic energy at the catastrophic point available to be released during an eruption. This suggests that fast and slow CMEs may have an identical driving mechanism.

Previous studies of coronal magnetic flux rope systems indicated that these systems exhibit a catastrophic behavior for background fields with a specific photospheric flux distribution, and that the catastrophic energy threshold exceeds the associated open field energy. Sun et al. (2007) took axisymmetrical bipolar fields in spherical geometry with different flux distributions on the photosphere as the background, and then examine how the flux distribution affects the catastrophic behavior and the energy threshold of a flux rope system. It is found that when the photospheric flux is concentrated too much toward the equator, the flux rope system loses its catastrophic behavior, i.e., that it evolves smoothly with the change of the rope properties. On the other hand, if the flux shifts poleward more than a split monopole field, a catastrophe behavior is recovered, and the catastrophic energy threshold increases in magnitude and percentage relative to the associated open field energy with increasing poleward shift of the flux. As a result, the flux rope erupts upward after catastrophe with a faster acceleration and a larger final speed when the flux is concentrated more toward the solar poles.

With the assumption of radial motion and uniform longitudinal distribution of

coronal mass ejections (CMEs), Song et al. (2007) proposed a method to eliminate projection effects from the apparent observed CME latitude distribution. This method has been applied to *SOHO* LASCO data from 1996 January to 2006 December. As a result, they find that the real CME latitude distribution had the following characteristics: (1) High-latitude CMEs ($\theta > 60^\circ$, where θ is the latitude) constituted 3% of all CMEs and mainly occurred during the time when the polar magnetic fields reversed sign. The latitudinal drift of the high-latitude CMEs was correlated with that of the heliospheric current sheet. (2) Four percent of all CMEs occurred in the range $45^\circ \leq \theta \leq 60^\circ$. These midlatitude CMEs occurred primarily in 2000, near the middle of 2002, and in 2005, forming a prominent three-peak structure. (3) The highest occurrence probability of low-latitude ($\theta < 45^\circ$) CMEs was at the minimum and during the declining phase of the solar cycle. However, the highest occurrence rate of low-latitude CMEs was at the maximum and during the declining phase of the solar cycle. The latitudinal evolution of low-latitude CMEs did not follow the Spörer sunspot law, which suggests that many CMEs originated outside of active regions.

Song et al. (2008) investigate the magnetic evolution of a flare/CME source region to determine the trigger of the flare and the EUV brightening event. Also, they discuss the role of the current helicity (hc) in solar activity. They use the long duration sequences of *SOHO*/MDI magnetograms and *TRACE* 195 Å images for a super active region (AR), NOAA AR 8375. Magnetic field changes in the photosphere and the corona are investigated. In AR 8375, the southwestern and northwestern parts of an overlying loop ($hc < 0$) are influenced by the rising magnetic arcades ($hc > 0$) and the emerging flux region ($hc > 0$). Two collisions make the overlying loop inflate in a bounce interaction. However, the related solar events are triggered by a merge interaction which takes place among the fibers of the rising magnetic arcades and among those of the overlying loop.

Wang and Zhang (2008) present statistical results on the properties of the solar source regions that produced the 57 fastest (≥ 1500 km/s) front-side coronal mass ejections (CMEs) from 1996 June to 2007 January. The properties of these fast-CMEY producing regions, 35 in total, are compared with those of all 1143 active regions (ARs) in the period studied. An automated method, based on *SOHO*/MDI magnetic synoptic charts, is used to select and characterize the ARs. For each, a set of parameters is derived that includes the areas (positive, negative,

and total, denoted A_P , A_N , and A_T , respectively), the magnetic fluxes (positive, negative, and total, F_P , F_N , and F_T), the average magnetic field strength (B_{avg}), a quasi elongation (e) characterizing the overall shape of the AR, the number and length of polarity inversion lines (PILs, or neutral lines, N_{PIL} and L_{PIL} , respectively), and the average and maximum magnetic gradient on the PILs (GOP_{avg} and GOP_{max}). Their statistical analysis shows a general trend between the scales of an AR and the likelihood of its producing a fast CME; that is, the larger the geometric size (A_T), the larger the magnetic flux (F_T), the stronger the magnetic field (B_{avg}), and the more complex the magnetic configuration (N_{PIL} and L_{PIL}), the greater the possibility of producing a fast CME. When all the ARs are sorted into three evenly sized groups with low, intermediate, and high values of these parameters, they find that for all the parameters, more than 60% of extremely fast CMEs are from the high-value group. The two PIL parameters are the best indicators of fast-CME production, with more than 80% coming from the high-value group.

More and more evidence indicates that “EIT waves” are strongly related to coronal mass ejections (CMEs). However, it is still not clear how the two phenomena are related to each other. Chen (2009) investigate a CME event on 1997 September 9, which was well observed by both the EUV Imaging Telescope (EIT) and the high-cadence Mark-III K-Coronameter at Mauna Loa Solar Observatory, and compare the spatial relation between the “EIT wave” fronts and the CME leading loops. It is found that “EIT wave” fronts are cospatial with the CME leading loops, and the expanding EUV dimmings are cospatial with the CME cavity. It is also found that the CME stopped near the boundary of a coronal hole, a feature common to observations of “EIT waves.” It is suggested that “EIT waves”/dimmings are the EUV counterparts of the CME leading loop/cavity, based on which they propose that, as in the case of “EIT waves,” CME leading loops are apparently moving density enhancements that are generated by successive stretching (or opening-up) of magnetic loops.

The kink wave, which has often been observed in coronal loops, is considered as a possibly important energy source contributing to coronal heating. However, its generation has not yet been observed. He et al. (2009) report the first observation of kink-wave excitation caused by magnetic reconnection as inferred from Solar Optical Telescope measurements made in the Ca II line. They observed

transverse-displacement oscillations on a spicule which propagated upwardly along the spicule trace and originated from the cusp of an inverted Y-shaped structure, where apparently magnetic reconnection occurred. Such transverse oscillation of an individual spicule is interpreted by us to be the signature of a kink wave that was excited by magnetic reconnection. They present the height variations of the velocity amplitude, δv , and the phase speed, C_k , of the kink wave, starting from its source region. The kink wave is found to steepen with height and to evolve into a nonlinear state with a large relative disturbance, yielding a $(\delta v/C_k)$ of 0.21 at 5.5 Mm. This nonlinear kink wave seems to be damped in velocity amplitude beyond 5.5 Mm, which may result from the conversion of transverse-fluctuation energy to longitudinal-motion energy required to sustain the spicule. They also estimate the energy flux density carried by the kink wave, and in spite of its attenuation in the transition region conclude it to be sufficient for heating the quiet corona. Their findings shed new light on future modeling of coronal heating and solar wind acceleration involving magnetic reconnection in the chromosphere.

Plasma blobs are observed to be weak density enhancements as radially stretched structures emerging from the cusps of quiescent coronal streamers. Chen et al. (2009) suggested that the formation of blobs is a consequence of an intrinsic instability of coronal streamers occurring at a very localized region around the cusp. The evolutionary process of the instability, as revealed in Their calculations, can be described as follows: (1) through the localized cusp region where the field is too weak to sustain the confinement, plasmas expand and stretch the closed field lines radially outward as a result of the freezing-in effect of plasma-magnetic field coupling; the expansion brings a strong velocity gradient into the slow wind regime providing the free energy necessary for the onset of a subsequent magnetohydrodynamic instability; (2) the instability manifests itself mainly as mixed streaming sausage-kink modes, the former results in pinches of elongated magnetic loops to provoke reconnections at one or many locations to form blobs. Then, the streamer system returns to the configuration with a lower cusp point, subject to another cycle of streamer instability. Although the instability is intrinsic, it does not lead to the loss of the closed magnetic flux, neither does it affect the overall feature of a streamer. The main properties of the modeled blobs, including their size, velocity profiles, density contrasts, and even their daily occurrence rate, are in line with available observations.

Using NSO/Kitt Peak synoptic charts from 1975 to 2003, Song, Feng et al. (2009) group the main solar magnetic fields into two categories: one for active regions (ARs) and the other for extended bipolar regions (EBRs). Comparing them, they find that there exist three typical characteristics in the variability of EBRs: First, there exists a correlation between ARs and EBRs. The phase of EBR flux has a delay nearly two CRs. Second, the EBR flux has two prominent periods at 1.79 years and 3.21 years. The 1.79-year period seems to only belong to large-scale magnetic features. Lastly, the North-South asymmetry of EBR flux is not very significant on a time scale of one solar cycle. However, during solar maxima, its dominance is found to shift from one hemisphere to the other.

Jin et al. (2009) investigated the outflows associated with two halo coronal mass ejections (CMEs) that occurred on 2006 December 13 and 14 in NOAA 10930, using the *Hinode*/EIS observations. Each CME was accompanied by an EIT wave and coronal dimmings. Dopplergrams in the dimming regions are obtained from the spectra of seven EIS lines. The results show that strong outflows are visible in the dimming regions during the CME eruption at different heights from the lower transition region to the corona. It is found that the velocity is positively correlated with the photospheric magnetic field, as well as the magnitude of the dimming. They estimate the mass loss based on heightdependent EUV dimmings and find it to be smaller than the CME mass derived from white-light observations. The mass difference is attributed partly to the uncertain atmospheric model, and partly to the transition region outflows, which refill the coronal dimmings.

EUV Imaging Telescope (EIT) waves are a wavelike phenomenon propagating outward from the coronal mass ejection source region, with expanding dimmings following behind. Chen, Ding and Chen (2010) present a spectroscopic study of an EIT wave/dimming event observed by the *Hinode*/Extreme-ultraviolet Imaging Spectrometer. Although the identification of the wave front is somewhat affected by the pre-existing loop structures, the expanding dimming is well defined. They investigate the line intensity, width, and Doppler velocity for four EUV lines. In addition to the significant blueshift implying plasma outflows in the dimming region as revealed in previous studies, they find that the widths of all four spectral lines increase at the outer edge of the dimmings. They illustrate that this feature can be well explained by the field line stretching model, which claims that EIT waves are apparently moving brightenings that are generated by the successive

stretching of the closed field lines.

“EIT waves” are a wavelike phenomenon propagating in the corona, which was initially observed in the extreme ultraviolet (EUV) wavelength by the EUV Imaging Telescope (EIT). Their nature is still elusive, with the debate on-going between fast-mode wave model and non-wave model. In order to distinguish between these models, Yang and Chen (2010) investigate the relation between the EIT wave velocity and the local magnetic field in the corona. It is found that the two parameters show significant negative correlation in most of the EIT wave fronts, *i.e.*, the EIT wave propagates more slowly in the regions of stronger magnetic field. Such a result poses a big challenge to the fast-mode wave model, which would predict a strong positive correlation between the two parameters. However, it is demonstrated that such a result can be explained by the fieldline stretching model, *i.e.*, that “EIT waves” are the propagation of apparent brightenings, which are generated by successive stretching of closed magnetic field lines pushed by the erupting flux rope during coronal mass ejections (CMEs).

Magnetic reconnection is commonly believed to be responsible for flare-like events and plasma ejections in the solar atmosphere, but the field-line reconfiguration observed in association with magnetic reconnection has rarely been observed before. He et al. (2010) attempt to reconstruct the configuration of the magnetic field during a magnetic reconnection event, estimate the reconnection rate, and analyze the resulting X-ray burst and plasma ejection. They use the local-correlation-tracking (LCT) method to track the convergence of magnetic fields with opposite polarities using photospheric observations from *SOT/Hinode*. The magnetic field lines are then extrapolated from the tracked footpoint positions into the corona, and the changes in field-line connections are marked. They estimate the reconnection rate by calculating the convective electric field in the photosphere, which is normalized to the product of the plasma jet speed and the coronal magnetic field strength inside the inflow region. The observed X-ray burst and plasma ejection are analysed with data from *XRT/Hinode* and *TRACE*, respectively. They find that in this reconnection event the two sets of approaching closed loops were reconfigured to a set of superimposed large-scale closed loops and another set of small-scale closed loops. Enhanced soft X-ray emission was seen to rapidly fill the reconnected loop after the micro-flare occurred at the reconnection site. Plasma was ejected from that site with a speed between 27 and

40 km/s. The reconnection rate is estimated to range between 0.03 and 0.09. Their work presents a study of the magnetic field reconfiguration owing to magnetic reconnection driven by flux convergence in the photosphere. This observation of the magnetic structure change is helpful for future diagnosis of magnetic reconnection. The results obtained for the reconnection rate, the X-ray emission burst, and the plasma ejection provides new observational evidence, and places constraints on future theoretical study of magnetic reconnection in the Sun

Zhao et al. (2010) performed a detailed analysis of a coronal mass ejection (CME) on 2008 January 2. The combination of *SOHO* and the twin *STEREO* spacecraft provides three-point observations of this CME. They track the CME in imaging observations and compare its morphology and kinematics viewed from different vantage points. The shape, angular width, distance, velocity and acceleration of the CME front are different in the observations of these spacecraft. They also compare the efficiency of several methods, which convert the elongation angles of the CME front in images to radial distances. The results of their kinematic analysis demonstrate that this CME experiences a rapid acceleration at the early stage, which corresponds to the flash phase of the associated solar flare in time. Then at a height of about 3.7 Rs the CME reaches a velocity of 790 km/s and propagates outward without an obvious deceleration. Because of its propagation direction away from the observers, the CME is not detected in situ by either *ACE* or *STEREO*.

Between July 5th and July 7th 2004, two intriguing fast coronal mass ejection (CME)-streamer interaction events were recorded by the Large Angle and Spectrometric Coronagraph (*LASCO*). At the beginning of the events, the streamer was pushed aside from their equilibrium position upon the impact of the rapidly outgoing and expanding ejecta; then, the streamer structure, mainly the bright streamer belt, exhibited elegant large scale sinusoidal wavelike motions. The motions were apparently driven by the restoring magnetic forces resulting from the CME impingement, suggestive of magnetohydrodynamic kink mode propagating outwards along the plasma sheet of the streamer. The mode is supported collectively by the streamer-plasma sheet structure and is therefore named "streamer wave" in the present study. With the white light coronagraph data, Chen et al. (2010) show that the streamer wave has a period of about 1 hour, a wavelength varying from 2 to 4 solar radii, an amplitude of about a few tens of

solar radii, and a propagating phase speed in the range 300 to 500 km/s. They also find that there is a tendency for the phase speed to decline with increasing heliocentric distance. These observations provide good examples of large scale wave phenomena carried by coronal structures, and have significance in developing seismological techniques for diagnosing plasma and magnetic parameters in the outer corona

The temperature curve in the solar chromosphere has puzzled astronomers for a long time. Referring to the structure of supergranular cells, Song, Feng and Shen (2010) propose an inductive heating model. It mainly includes the following three steps. (1) A small-scale dynamo exists in the supergranulation and produces alternating small-scale magnetic fluxes; (2) The supergranular flow distributes these small-scale fluxes according to a regular pattern; (3) A skin effect occurs in the alternating and regularly-distributed magnetic fields. The induced current is concentrated near the transition region and heats it by resistive dissipation.

Wang, Cao et al. (2010) present an automated system, which has the capability to catch and track solar limb prominences based on observations from the extreme-ultraviolet (EUV) 304 Å passband. The characteristic parameters and their evolution, including height, position angle, area, length, and brightness, are obtained without manual interventions. By applying the system to the *STEREO-B/SECCHI/EUVI* 304 Å data during 2007 April-2009 October, they obtain a total of 9477 well-tracked prominences and a catalog of these events available online. A detailed analysis of these prominences suggests that the system has a rather good performance. They have obtained several interesting statistical results based on the catalog. Most prominences appear below the latitude of 60° and at the height of about 26 Mm above the solar surface. Most of them are quite stable during the period they are tracked. Nevertheless, some prominences have an upward speed of more than 100 km s⁻¹, and some others show significant downward and/or azimuthal speeds. There are strong correlations among the brightness, area, and height. The expansion of a prominence is probably one major cause of its fading during the rising or erupting process.

Zhang et al. (2010) search for signatures of transition region explosive events (EEs) in hydrogen Lyβ profiles. The relationship between the peak emission of Lyβ profiles and the wing emission of C II and O VI during EEs is investigated. Two rasters made by the *SUMER* (Solar Ultraviolet Measurements of Emitted

Radiation) instrument onboard *SOHO* in a quiet-Sun region and an equatorial coronal hole were selected for their study. Transition-region explosive events were identified from profiles of C II 1037 Å and O VI 1032 Å, respectively. They compared Ly β profiles during EEs with those averaged in the entire quiet-Sun and coronal-hole regions. They find that the central part of Ly β profiles reverses more and the distance of the two peaks becomes larger during EEs, both in the coronal hole and in the quiet Sun. The average Ly β profile of the EEs detected by C II has an obviously stronger blue peak. During EEs, there is a clear correlation between the increased peak emission of Ly β profiles and the enhanced wing emission of the C II and O VII lines. The correlation is more pronounced for the Ly β peaks and C II wings, and less significant for the Ly β blue peak and O VI blue wing. They also find that the Ly β profiles are more reversed in the coronal hole than in the quiet Sun. They suggest that the jets produced by EEs emit the Doppler-shifted Ly β photons, causing enhanced emission at positions of the peaks of Ly β profiles. The more-reversed Ly β profiles confirm the presence of higher opacity in the coronal hole than in the quiet Sun. The finding that EEs modify the Ly β line profile in QS and CHs implies that one should be careful in the modeling and interpretation of relevant observational data.

II. SOLAR WIND

It is well known that the fast solar wind originates from coronal holes (CHs). However, the question whether it can also originate from quiet Sun regions has not yet been answered. To study this problem He et al. (2007) analyzed *SOHO* data obtained from observations made in a quiet Sun area. The data set includes far-ultraviolet data from SUMER, magnetic field data from MDI, and extreme-ultraviolet data from EIT. They make a potential-field extrapolation of the coronal magnetic field and calculate the field lines from the photosphere up to 80 Mm height. Those field lines which can be traced from the bottom to the top of the extrapolation box are called (locally) open field lines. By a combined analysis of the coronal magnetic field structures inferred from MDI data, the flows indicated by the Ne VIII Doppler shifts in the SUMER data, and the Fe XII radiance images from EIT, it is possible to study this problem in depth. They find that most of the sites with plasma outflow, which can be recognized by the Ne VIII blue shift, are

not located in regions with an open magnetic field. Most likely, these outflows just correspond to plasma being delivered to magnetic loops. It is further found that, in a cross-section plane located at a height of 25 Mm, the pattern of open field lines intersecting that plane is consistent with the dark pattern of low radiance in the image of the Fe XII 19.5 nm line. Usually, small dark regions are considered to represent small CHs, and thus are assumed to be sources of the solar wind. However, since here the source of the low emission appears to be located at a height of only 25 Mm, it seems more likely that this radiation originates near the foot points of large coronal loops. Previous results obtained at middle latitudes on the quiet Sun indicated that sizable outflow velocities occur at the intersections of the network boundaries. This finding is also confirmed here. However, they could not identify most of these intersections as sources of the solar wind. Only a few small outflow regions might be sources. Yet, one dark area that they found on the EIT map seems to be connected with open field lines, and therefore it could be a source of the solar wind.

The origin of the solar wind is a long-standing issue in both observational and theoretical studies. To understand how and where in the solar atmosphere the mass and energy of the solar wind are supplied is very important. Previous observation suggests a scenario in which the fast solar wind originates at heights above 5 Mm in the magnetically open funnel, a process that is accompanied by downward flow below 5 Mm, whereby the mass and energy are supplied through reconnection between the open funnel and adjacent closed loops. Based on this scenario, He et al. (2008) develop a fluid model to study the solar wind generation under the assumption that mass and energy are deposited in the open funnel at 5 Mm. The mass supply rate is estimated from the mass loss rate as given by the emptying of the side loops as a result of their assumed reconnection with the open funnel. Similarly, the energy input rate is consistent with the energy release rate as estimated from the energy flux associated with the reconnection between the open magnetic funnel and the closed magnetic loops. Following the observations, they not only simulate the plasma flowing upward to form the solar wind but also calculate the downward flow back to the lower atmosphere. This model is a first attempt to study physically the proposed scenario of solar wind origin and gives a new physical illustration of the possible initial deposition and consequent transportation of mass and energy in the coronal funnel.

The radiance and Doppler-shift distributions across the solar network provide observational constraints of two-dimensional modeling of transition-region emission and flows in coronal funnels. These distributions have not, however, been studied in detail. Tian et al. (2008a) attempt an investigation for a quiet Sun region. Two different methods, dispersion plots and average-profile studies, were applied by them to investigate these distributions for three EUV lines. In the dispersion plots, they divided the entire quiet Sun region scanned by *SUMER* into a bright and a dark part according to an image of Fe XII taken by EIT during the scanning; they plotted intensities and Doppler shifts in each bin as determined according to a filtered intensity of Si II. They also studied the difference in height variations of the magnetic field as extrapolated from the MDI magnetogram, in and outside network, in the two parts. For the average-profile study, they selected 74 individual cases and derived the average profiles of intensities and Doppler shifts across the network. Cases with large values of blue shift of Ne VIII were further studied. The dispersion plots reveal that the intensities of Si II and C IV increase from network boundary to network center in both the bright and dark parts. However, the intensity of Ne VIII shows different trends, namely increasing in the bright part and decreasing in the dark part. In both parts, the Doppler shift of C IV increases steadily from internetwork to network center. The height variations in the magnetic field imply a more homogeneous magnetic structure at greater heights and clearly reflect the different magnetic structures in the two regions. The average-profile study reveals that the intensities of the three lines all decline from the network center to internetwork region. The binned intensities of Si II and Ne VIII have a good correlation. They also find that the large blue shift of Ne VIII does not coincide with large red shift of C IV. Their results suggest that the network structure is still prominent at the layer where Ne VIII is formed in the quiet Sun, and that the magnetic structures expand more strongly in the dark part than in the bright part of this quiet Sun region. The results might also hint for a scenario of magnetic reconnection between open funnels and side loops.

Tian et al. (2008b) study the height variations of the sizes of chromospheric and transition-region features in a small coronal hole and the adjacent quiet Sun, considering images of the intensity, Doppler shift, and non-thermal motion of ultraviolet emission lines as measured by *SUMER*, together with the magnetic field as obtained by extrapolation from photospheric magnetograms. In order to estimate

the characteristic sizes of the different features present in the chromosphere and transition region, they have calculated the autocorrelation function for the images as well as the corresponding extrapolated magnetic field at different heights. The Half Width at Half Maximum (HWHM) of the autocorrelation function is considered to be the characteristic size of the feature shown in the corresponding image. Their results indicate that, in both the coronal hole and quiet Sun, the HWHM of the intensity image is larger than that of the images of Doppler-shift and non-thermal width at any given altitude. The HWHM of the intensity image is smaller in the chromosphere than in the transition region, where the sizes of intensity features of lines at different temperatures are almost the same. But in the upper part of the transition region, the intensity size increases more strongly with temperature in the coronal hole than in the quiet Sun. They also studied the height variations of the HWHM of the magnetic field magnitude B and its component B_z , and found they are equal to each other at a certain height below 40 Mm in the coronal hole. The height variations of the HWHM of B_z/B seem to be consistent with the temperature variations of the intensity size. Their results suggest that coronal loops are much lower, and magnetic structures expand through the upper transition region and lower corona much more strongly with height in the coronal hole than in the quiet Sun.

The physical implication of large blue shift of Ne VIII in the quiet Sun region is investigated in this paper. Tian et al. (2008c) compare the significant Ne VIII blue shifts, which are visible as large blue patches on the Doppler-shift map of a middle-latitude quiet-Sun region observed by *SUMER*, with the coronal magnetic-field structures as reconstructed from a simultaneous photospheric magnetogram by means of a force-free-field extrapolation. They show for the first time that coronal funnels also exist in the quiet Sun. The region studied contains several small funnels that originate from network lanes, expand with height and finally merge into a single wide open-field region. However, the large blue shifts of the Ne VIII line are not generally associated with funnels. A comparison between the projections of coronal loops onto the solar xy -plane and the Ne VIII dopplergram indicates that there are some loops that reveal large Ne VIII blue shifts in both legs, and some loops with upflow in one and downflow in the other leg. Their results suggest that strong plasma outflow, which can be traced by large Ne VIII blue shift, is not necessarily associated with the solar wind originating in

coronal funnels but appears to be a signature of mass supply to coronal loops. Under the assumption that the measured Doppler shift of the Ne VIII line represents the real outflow velocity of the neon ions being markers of the proton flow, they estimate the mass supply rate to coronal loops to be about 10^{34} s^{-1} .

Song, Chen et al. (2009) search for persistent and quasi-periodic release events of streamer blobs during 2007 with the LASCO on *SOHO* and assess the velocity of the slow solar wind along the plasma sheet above the corresponding streamer by measuring the dynamic parameters of blobs. They find ten quasi-periodic release events of streamer blobs lasting for three to four days. In each day of these events, they observe three-five blobs. The results are in line with previous studies using data observed near the last solar minimum. Using the measured blob velocity as a proxy for that of the mean flow, they suggest that the velocity of the background slow solar wind near the Sun can vary significantly within a few hours. This provides an observational manifestation of the large velocity variability of the slow solar wind near the Sun

The origin of the solar wind is one of the most important unresolved problems in space and solar physics. Tian et al. (2010) reported the first spectroscopic signatures of the nascent fast solar wind on the basis of observations made by the EUV Imaging Spectrometer on *Hinode* in a polar coronal hole in which patches of blueshift are clearly present on Dopplergrams of coronal emission lines with a formation temperature of $\lg(T/K) > 5.8$. The corresponding upflow is associated with open field lines in the coronal hole and seems to start in the solar transition region and becomes more prominent with increasing temperature. This temperature-dependent plasma outflow is interpreted as evidence of the nascent fast solar wind in the polar coronal hole. The patches with significant upflows are still isolated in the upper transition region but merge in the corona, in agreement with the scenario of solar wind outflow being guided by expanding magnetic funnels.

Geomagnetic storm intensity, as measured by the Dst (SYM_H) index, shows no limit as the solar wind dawn-to-dusk electric field increases. Li et al. (2010) show that the magnetopause around noon erodes earthward with increasing storm intensity. The panoramic geosynchronous B_z signatures for the magnetic storm groups with different intensity are differ significantly from each other. For superstorms with SYM_H ≤ -300 nT, the magnetopause around noon erodes to

inside the geosynchronous orbit, which causes the BZ reversal near local noon. The necessary conditions for superstorms with $\text{SYM}H \leq -300$ nT to occur include the following: (1) interplanetary magnetic field (IMF) $B_z < -27$ nT lasts for at least ~ 1 h; (2) solar wind dynamic pressure, $P_d > \sim 12$ nPa; (3) the projected interplanetary electric field, $E_K - L > \sim 30$ mV/m.

It has already been established that the solar wind may originate at the edges of active regions (ARs), but the key questions of how frequently these outflows occur, and at which height the nascent solar wind originates have not yet been addressed. He, Marsch, et al. (2010) study the occurrence rate of these intermittent outflows, the related plasma activities beneath in the low solar atmosphere, and the interplanetary counterparts of the nascent solar wind outflow. They use the observations from *XRT/Hinode* and *TRACE* to study the outflow patterns. The occurrence frequency of the intermittent outflow is estimated by counting the occurrences of propagating intensity enhancements in height-time diagrams. They adopt observations of *SOT/Hinode* and *EIS/Hinode* to investigate the phenomena in the chromosphere associated with the coronal outflows. The *ACE* plasma and field in-situ measurements near Earth are used to study the interplanetary manifestations. They find that in one elongated coronal emission structure, referred to as strand, the plasma flows outward intermittently, about every 20 min. The flow speed sometimes exceeds 200 km s^{-1} , which is indicative of rapid acceleration, and thus exceeds the coronal sound speed at low altitudes. The inferred flow speed of the soft-X-ray-emitting plasma component seems a little higher than that of the Fe IX/X-emitting plasma component. Chromospheric jets are found to occur at the root of the strand. Upflows in the chromosphere are also confirmed by blue-shifts of the He II line. The heliospheric plasma counterpart close to the Earth is found to be an intermediate-speed solar wind stream. The AR edge may also deliver some plasmas to a fraction of the fast solar wind stream, most of which emanate from the neighboring CH. The possible origin of the nascent solar wind in the chromosphere, the observed excessive outflow speed of over 200 km s^{-1} in the lower corona, and the corresponding intermediate-speed solar wind stream in interplanetary space are all linked in their case study. These phenomena from the low solar atmosphere to the heliosphere near Earth in combination shed new light on the solar wind formation process. These observational results will constrain future modeling of the solar winds originating close to an AR.

III. INTERPLANETARY TRANSIENTS

Zhao et al. (2007) study the source locations of 130 solar flare-type II radio burst events with the associated interplanetary shocks observed by L1 spacecraft (type A events) and 217 flare-type II events without such shocks observed at L1 (type B events) during February 1997-August 2002. In particular, they investigate the relative positions between the flare sources, the heliospheric current sheet (HCS), and the Earth. They found the following results: (1) Solar flares are usually distributed within $[S30^{\circ}, N30^{\circ}]$ in heliographic latitude and $[S30^{\circ}, N30^{\circ}] \times [E10^{\circ}, W30^{\circ}]$ is the predominant source region on the solar disk that includes the majority of geoeffective solar flares. (2) The shocks with the associated flares located near the HCS would have a lower probability of reaching the Earth. For the Earth-encountered shocks, their initial speeds are distinctly higher when their associated flares are located near the HCS. (3) The angular distance from the flare source to the Earth (defined as Ψ below) also contributes to the probability of the associated shock being observed at the Earth. The shock arrival probability decreases with the increment of Ψ and the mean initial shock speed increases with Ψ for those Earth-encountered shocks. (4) The so-called “same-opposite side effect” of the HCS is confirmed to exist. That is, the shocks whose associated flares are located on the same side of the HCS as the Earth (called as “same side events”) have a greater chance of reaching the Earth than those shocks with their associated flares on the opposite side (“opposite side events”). Here for the first time, a comprehensive sample of solar transient events of both arriving and nonarriving ones (at Earth) is used to testify to the same-opposite side effect. These results would be valuable in understanding the solar-terrestrial relations, and helpful for space weather prediction.

Interplanetary magnetic clouds (MCs) are one of the main sources of large nonrecurrent geomagnetic storms. With the aid of a force-free flux rope model, the dependence of the intensity of geomagnetic activity (indicated by Dst index) on the axial orientation (denoted by θ and φ in GSE coordinates) of the magnetic cloud is analyzed theoretically by Wang, Ye and Wang (2007). The distribution of the Dst values in the (θ, φ) plane is calculated by changing the axial orientation for various cases. It is concluded that (i) geomagnetic storms tend to occur in the region of

$\theta < 0^\circ$, especially in the region of $\theta \leq -45^\circ$, where larger geomagnetic activity could be created; (ii) the intensity of geomagnetic activity varies more strongly with θ than with φ ; (iii) when the parameters B_0 (the magnetic field strength at the flux rope axis), R_0 (the radius of the flux rope), or V (the bulk speed) increase, or $|D|$ (the shortest distance between the flux rope axis and the x -axis in GSE coordinates) decreases, a flux rope not only can increase the intensity of geomagnetic activity, but also is more likely to create a storm, however the variation of n (the density) only has a little effect on the intensity; (iv) the most efficient orientation (MEO) in which a flux rope can cause the largest geomagnetic activity appears at $\varphi \sim 0^\circ$ or $\sim 180^\circ$, and some value of θ which depends mainly on D ; (v) the minimum Dst value that could be caused by a flux rope is the most sensitive to changes in B_0 and V of the flux rope, and for a stronger and/or faster MC, a wider range of orientations will be geoeffective. Further, through analyzing 20 MC-caused moderate to large geomagnetic storms during 1998-2003, a long-term prediction of MC-caused geomagnetic storms on the basis of the flux rope model is proposed and assessed. The comparison between the theoretical results and the observations shows that there is a close linear correlation between the estimated and observed minimum Dst values. This suggests that using the ideal flux rope to predict practical MC-caused geomagnetic storms is applicable. The possibility of the long-term prediction of MC-caused geomagnetic storms is discussed briefly.

Wang and Zhang (2007) examine the two kinds of major energetic phenomena that occur in the solar atmosphere: eruptive and confined events. The former describes flares with associated coronal mass ejections (CMEs), while the latter denotes flares without associated CMEs. They find that about 90% of X-class flares are eruptive, but the remaining 10% are confined. To probe why the largest energy releases could be either eruptive or confined, they investigate four X-class events from each of the two types. Both sets of events are selected to have very similar intensities (X1.0 to X3.6) and duration (rise time under 13 minutes and decay time over 9 minutes) in soft X-ray observations, to reduce any bias due to flare size on CME occurrence. They find that the occurrence of eruption (or confinement) is sensitive to the displacement of the location of the energy release, defined as the distance between the flare site and the flux-weighted magnetic center of the source active region. The displacement is 6-17 Mm for confined events but as large as 22-37 Mm for eruptive events. This means that confined

events occur closer to the magnetic center, while the eruptive events tend to occur close to the edge of active regions. They use the potential field source-surface model to infer the coronal magnetic field above the source active regions and calculate the flux ratio of low ($<1.1 R_s$) to high ($\geq 1.1 R_s$) corona. They find that the confined events have a lower ratio (<5.7) than the eruptive events (>7.1). These results imply that a stronger overlying arcade field may prevent energy releases in the low corona from being eruptive, resulting in flares, but without CMEs.

Coronal shocks are important structures, but there are no direct observations of them in solar and space physics. The strength of shocks plays a key role in shock-related phenomena, such as radio bursts and solar energetic particle (SEP) generation. Shen, Wang et al. (2007) presented an improved method of calculating Alfvén speed and shock strength near the Sun. This method is based on using as many observations as possible, rather than one-dimensional global models. Two events, a relatively slow CME on 2001 September 15 and a very fast CME on 2000 June 15, are selected to illustrate the calculation process. The calculation results suggest that the slow CME drove a strong shock, with Mach number of 3.43–4.18, while the fast CME drove a relatively weak shock, with Mach number of 1.90–3.21. This is consistent with the radio observations, which find a stronger and longer decameter-hectometric (DH) type II radio burst during the first event, and a short DH type II radio burst during the second event. In particular, the calculation results explain the observational fact that the slow CME produced a major solar energetic particle (SEP) event, while the fast CME did not. Through a comparison of the two events, the importance of shock strength in predicting SEP events is addressed.

The chance of a magnetic cloud (MC) being observed by widely separated spacecraft is rare. However, such an event provides us a good opportunity to study the propagation and evolution of magnetic cloud in the interplanetary space. A magnetic cloud event observed by *ACE* at Earth on 4-6 March 1998 is tracked from the location of *ACE* to *Ulysses*. Using a one-dimensional (1-D) MHD solar wind model, Du et al. (2007) propagated the *ACE* data to the location of *Ulysses* and confirm that the two magnetic clouds observed by both spacecraft have the same solar origin. The Grad-Shafranov (GS) reconstruction technique is then employed to recover the 2.5-D cross sections of the magnetic clouds at locations of *ACE* and *Ulysses*, respectively. The magnetic clouds observed at *ACE* and *Ulysses* both show magnetic flux rope configurations of the same chirality and unidirectional

axial magnetic field along approximately the same direction. It is found that the magnetic cloud is expanding while propagating outward. Their relevant toroidal (axial) and poloidal magnetic flux contained within each flux rope are different but approximately of the same order of magnitude. However, the relative magnetic helicity contained in each flux rope differs significantly. They discussed the causes of such differences, taking into account the underestimate of the area of the flux rope at *Ulysses* and the effect of magnetic cloud evolution that may not be fully addressed by 2-D models.

A double discontinuity is a rarely observed compound structure composed of a slow shock layer and an adjoining rotational discontinuity layer in the downstream region. Zuo and Feng (2007) reported the observations of a double discontinuity detected by *WIND* on May 15, 1997. This double discontinuity is found to be the front boundary of a magnetic cloud boundary layer. They strictly identify the shock layer and the rotational discontinuity layer by using the high-resolution plasma and magnetic field data from *WIND*. The observed jump conditions of the upstream and downstream region of the slow shock layer are in good agreement with the Rankine-Hugoniot relations. The flow speeds in the shock frame $U_n < V_A \cos \theta_{Bn}$ on both sides of the slow shock layer. In the upstream region, the slow Mach number $M_{s1} = U_{n1}/V_{s1}$ is 1.95 (above unity), and in the downstream region, the slow Mach number $M_{s2} = U_{n2}/V_{s2}$ is 0.31 (below unity). Here V_A and V_s represent the Alfvén speed and the local slow magnetosonic speed, respectively, and θ_{Bn} is the angle between the direction of the magnetic field and the shock normal. The magnetic cloud boundary layer observed by *WIND* was also detected by *Geotail* 48 min later when the spacecraft was located outside the bow shock of the magnetosphere. However, *Geotail* observations showed that its front boundary was no longer a double discontinuity and the rotational discontinuity layer disappeared, indicating that this double discontinuity was unstable when propagating from *WIND* to *Geotail*.

In August 2007, *Voyager 2* reached the termination shock and entered the heliosheath at a distance of about 83.6 AU. Due to the variations of the solar wind dynamic pressure or waves on the shock front, the termination shock moved back and forth, and *Voyager 2* crossed the termination shock multiple times. Li, Wang and Richardson (2008) used the best fit solution of the Monte-Carlo method to define the upstream and downstream conditions and determine the properties of

termination shock, such as the shock normal, speed, and strength. For the crossings on DOY 243.819-243.875 (shock 1) and DOY 243.99-244.012 (shock 2), the termination shock moved almost in the radial direction. The shock is nearly perpendicular, and the angle between the shock normal and the solar wind magnetic field is about 70° . In the case of the first crossing, the termination shock moved away from the Sun with a speed of about 100 km/s, whereas the termination shock moved toward Sun with a speed of about 30 km/s for the second crossing. The density ratios of the termination shock are 2.2 and 1.6, respectively. For both crossing events, the flow is found to be still supersonic with respect to the thermal ions downstream of the termination shock, probably due to the fact that most of the solar wind energy is transferred to the pickup ions.

Zhang et al. (2008) gives an investigation of the effects of corotating interaction regions (CIRs) in the heliosphere ($<1\text{AU}$) on geomagnetic disturbances during solar cycle 23 (1996–2005). Three kinds of interplanetary structures, “pure” CIR, interaction of CIR with ICME, and “pure” ICME by transient events, are identified by using the Hakamada-Akasofu-Fry (HAF) solar wind model. Yearly occurrence of 157 “pure” CIRs has a minimum value in 2001 and a peak value in 2003 at the declining phase during the 23rd solar cycle. The maximum correlation coefficient of the daily sum of Kp indices between consecutive Carrington Rotations indicates that recurrent geomagnetic disturbances are dominant during the declining phase near solar minimum. Eighty percent of storms that are related to “pure” CIRs belong to weak and moderate storms. The statistical analysis shows that about 50% of CIRs produce classical interplanetary shocks during the descending phase and 89% of the CIR-related shocks are followed by geomagnetic storms. These results demonstrate that CIR-related shock is not a necessary condition for generating a magnetic storm, but most CIR-related shocks are related to a storm. The Dst index that corresponds to CIR-related storms has a better linear relationship with IMF B_z , E_y , and the coupling function (ϵ) when the Dst indices are higher than -100 nT. Finally, the geoeffectiveness of CIRs appears clearly to have a seasonal variation.

Liu et al. (2008a) examine the upstream meridional deflection flows of interplanetary coronal mass ejections (ICMEs) in an effort to investigate their cross-sectional shape and the magnetic field orientation in their sheath regions. Eight out of 11 magnetic clouds (MCs) near solar minimum identified for the

curvature study are concave outward as indicated by the elevation angle of the MC normal with respect to the solar equatorial plane; an inverse correlation is observed between the meridional deflection flow and the spacecraft latitude for these concave-outward MCs, which suggests that the upstream plasma is deflected toward the equatorial plane. MHD simulations, however, show that the meridional deflection flow moves poleward for a concave-outward CME. The poleward flow deflection is observed only ahead of convex-outward MCs. Possibilities leading to this discrepancy are discussed. The deflection flow speed in sheath regions of ICMEs increases with the ICME speed relative to the ambient solar wind, which together with the coupling between the meridional magnetic field and deflection flow yields a positive linear correlation between the sheath meridional field and the ICME relative speed. This empirical relationship could predict the sheath meridional field based on the observed CME speed, which may be useful for space weather forecasting as ICME sheaths are often geoeffective. Implications of the deflection flows and ICME curvature are also discussed in terms of magnetic reconnection and particle acceleration in ICME sheaths.

Coronal mass ejections (CMEs) are often assumed to be magnetic flux ropes, but direct proof has been lacking. A key feature, resulting from the translational symmetry of a flux rope, is that the total transverse pressure as well as the axial magnetic field has the same functional form over the vector potential along any crossing of the flux rope. Liu et al. (2008b) test this feature (and hence the flux-rope structure) by reconstructing the 2007 May 22 magnetic cloud (MC) observed at *STEREO-B*, *WIND/ACE*, and possibly *STEREO-A* with the Grad-Shafranov (GS) method. The model output from reconstruction at *STEREO-B* agrees fairly well with the magnetic field and thermal pressure observed at *ACE/WIND* the separation between *STEREO-B* and *ACE/WIND* is about 0.06 AU, almost half of the MC radial width. For the first time, they reproduce observations at one spacecraft with data from another well separated spacecraft, which provides compelling evidence for the flux-rope geometry and is of importance for understanding CME initiation and propagation. They also discuss the global configuration of the MC at different spacecraft on the basis of the reconstruction results.

Wang et al. (2009) perform a statistical survey of geospace magnetic field responses, including the geosynchronous magnetic field and the sudden impulses

on the ground, to interplanetary shocks (IP shocks) between 1998 and 2005. The magnitude of the geosynchronous magnetic field (dBz) responses to IP shocks depends strongly on local time, which peaks near the noon meridian; however, the relative magnitude of the responses depends only weakly on local time. These results are similar to those obtained from the static study of the responses to solar wind dynamic pressure pulses. However, negative responses (where dBz is negative) were sometimes observed in the nightside of the magnetosphere even though the IP shocks always caused increases in the solar wind dynamic pressure, a new phenomenon not widely reported in the literature. Their analysis shows that ~75% of negative responses in the midnight sector are associated with southward interplanetary magnetic field. For a moderately compressed magnetosphere, the amplitude of the geosynchronous response dBz could be determined by the average value of the background local magnetic field. As the magnitude of the upstream solar wind dynamic pressure increases, the rate of response increases correspondingly. The dBz at the geosynchronous orbit near local noon and the amplitude of sudden impulses (dSYM-H) on the ground are highly correlated.

The plasma and magnetic-field instruments on the Helios 2 spacecraft, which was on 3 April 1979 located at 0.68 AU, detected an interplanetary coronal mass ejection (ICME) that revealed itself by the typical signature of magnetic field rotation. The solar wind flow speed ranged between 400 and 500 km/s. Marsch et al. (2009) present here some detailed proton velocity distributions measured within the ICME. These cold distributions are characterized by an isotropic core part with a low temperature, $T \leq 10^5$ K, but sometimes reveal a broad and extended hot proton tail or beam propagating along the local magnetic field direction. These beams lasted only for about an hour and were unusual as compared with the normal ICME protons distributions that were comparatively isotropic. Furthermore, they looked into the velocity and field fluctuations in this ICME and found signatures of Alfvén waves, which might be related to the occurrence of the hot proton beams. However, it cannot be excluded that the beam originated from the Sun.

A generic self-similar flux rope model is proposed by Wang, Zhang and Shen (2009) to probe the internal state of CMEs in order to understand the thermodynamic process and expansion of CMEs in interplanetary space. Using this model, three physical parameters and their variations with heliocentric distance can be inferred based on coronagraph observations of CMEs' propagation and

expansion. One is the polytropic index Γ of the CME plasma, and the other two are the average Lorentz force and the thermal pressure force inside CMEs. By applying the model to the 8 October 2007 CME observed by *STEREO/ SECCHI*, they find that (1) the polytropic index of the CME plasma increased from initially 1.24 to more than 1.35 quickly and then slowly decreased to about 1.34; it suggests that there be continuously heat injected/converted into the CME plasma and the value of Γ tends to be $4/3$, a critical value inferred from the model for a force-free flux rope; (2) the Lorentz force directed inward while the thermal pressure force outward, and both of them decreased rapidly as the CME moved out; the direction of the two forces reveals that the thermal pressure force is the internal driver of the CME expansion, whereas the Lorentz force prevented the CME from expanding. Some limitations of the model and approximations are discussed meanwhile.

Li et al. (2009a) introduce a new definition of the quantity, residue, based on all field line invariants of a specified flux rope model to measure the deflection between the assumed axis and the true flux rope axis. Then, a new minimum residue (MR) method is proposed to infer the axial orientation of IFR with the observational data from a single spacecraft. For an arbitrarily assumed flux rope axis, the natural coordinate system can be constructed, then a magnetic flux function, A , and each invariant of the specified flux rope model can also be concurrently calculated under this coordinate system. The direction corresponding to the minimum residue is expected to be the real axial orientation. In previous study, the residue was first defined with A and a single invariant P_i of a static equilibrium flux rope model. Here, the new MR method is tested with simulated magnetic cloud data sets constructed from the analytical model outputs of two different flux rope models with “trend noise” added. It shows that the new MR method is applicable in real case analysis and the inferring results are acceptable for cases with small closest approach distance and proper noise level. Compared with results from traditional methods, accuracy of the inferred axial orientation is improved by the new method. The new MR method is also applied to a typical in situ event observed by *WIND* spacecraft. The comparison of the inferring results from different models indicates that application of a more accurate flux rope model is useful for inferring techniques.

Li et al. (2009b) report two MC events observed by *WIND* spacecraft with good examples of field- aligned residual flow inside the MC structure. For both

events, the co-moving frames are determined through the deHoffman-Teller (HT) analysis and the axial orientations are inferred by the newly developed minimal residue (MR) method. The nature coordinate system for both events are constructed with velocity of the HT frame and the inferred MC axis, the field and flow remaining in the HT frame are analyzed at this coordinate system. As a result, they find that the residual flows in the co-moving HT frame of the two MC events are almost anti-parallel to the helical magnetic field. They speculate that the field-aligned residual flows are large scale coherent hydrodynamic vortices co-moving with the MCs at the supersonic speed near 1 AU. Data analyses show that the event in slow ambient solar wind is expanding at 1 AU and another one in fast solar wind does not show apparent expansion. Proton behaviors for both events are quasi-isothermal. Accelerated HT analysis shows that both events have no suitable HT frame with constant accelerations, which suggests that both events may be moving at the constant speed near 1 AU under the assumptions of the HT analysis. For both events, the ratio of the dynamic pressure to the magnetic pressure is larger than that of the thermal pressure to magnetic pressure, which suggests that the dynamic effects due to the plasma flows remaining in the co-moving HT frame are more important than the thermal effects in the study of MC evolution and propagation.

Interplanetary (IP) shocks disturb the magnetosphere-ionosphere system resulting in geosynchronous magnetic field changes and sudden impulses observed by ground-based magnetometers. Wang et al. (2010a) extended the implications of a previous statistical study and show that sudden impulses (SIs) can be used to estimate some parameters at the L1 point and geosynchronous orbit, including the change of the square root of solar wind dynamic pressure across the shock and the associated geosynchronous magnetic field changes near the subsolar region. It should be pointed out that the relationship between magnetospheric field change and SIs amplitude and the solar wind dynamic pressure is not a single valued one, but a statistical relationship is useful in cases when interplanetary data are not available. Empirical formulae deduced from observations can be used to estimate certain IP shock characteristics and geosynchronous magnetic field changes from sudden impulse data observed on the ground, with the prediction efficiency as high as 90% and 86%, respectively. These estimates are useful for studying historic, pre-space era data or if the L1 and geosynchronous data are not available at some

future time.

Voyager 2 (V2) has observed heliosheath plasma since 2007 August. The plasma flux decreases by 25% before the termination shock (TS), then, as V2 moved into the heliosheath, the plasma density, temperature, and flux all decreased by an additional factor of 2. Richardson and Wang (2010) suggest three effects combine to cause these decreases. (1) V2 moved into the lower-flux transition region between the low- and high-speed solar wind. This hypothesis is consistent with *Ulysses* observations of the transition location, explains the 25% decrease in solar wind flux observed before the TS crossing, and can reconcile discrepancies between the V2 and Voyager 1 heliosheath speeds and between the V2 speeds and model results. (2) The weaker source at the Sun. (3) The heliosheath plasma turning and flowing toward the heliotail.

Observations show that the geosynchronous magnetic field in midnight sector sometimes decreases when an interplanetary (IP) fast forward shock (FFS) passes Earth, even though the magnetosphere is always compressed. Wang et al. (2010b) perform case studies of the response observed by the *GOES* spacecraft at geosynchronous orbit near midnight to two IP shocks passing Earth. One shock produces a decrease in B_z (a negative response) and the other an increase in B_z (a positive response). A global 3D MHD code is run to reproduce the responses at geosynchronous orbit, and to further provide information on the initiation and development of B_z variations in the entire magnetosphere. The model reveals that when a FFS sweeps over the magnetosphere, there exist mainly two regions, a positive response region caused by the compressive effect of the shock and a negative response region which is probably associated with the temporary enhancement of earthward convection in the nightside magnetosphere. The spacecraft may observe an increase or decrease of the magnetic field depending on which region it is in. The numerical results reproduce the main characters of the geosynchronous magnetic field response to IP shocks for these two typical cases.

On 9 November 2004, the *WIND* spacecraft detected a magnetic cloud boundary layer (MCBL) during the interval from 19:07 UT to 20:30 UT. Within the MCBL, there is intense southward magnetic field and the dynamic pressure is rather high, which makes it much geoeffective. Twenty-three minutes later, the MCBL arrived on the magnetopause. An intense geomagnetic storm main phase was driven by the sustaining strong southward magnetic field within the MCBL.

During the passage of the MCBL, a typical magnetospheric substorm was triggered. The substorm onset was synthetically identified by the aurora breakup, magnetic dipolarization, dispersionless particle injection, Pi2 pulsation, and the polar bay onset. The substorm triggering is related to the special magnetic and plasma structure within the MCBL. The MCBL accompanying adjacent sheath region formed a dynamic pressure enhancement region, which strongly compressed the magnetosphere and even pushed the magnetopause into the geosynchronous orbit so that two dayside spacecraft *GOES-10* and *GOES-12* were directly exposed in the magnetosheath for a long interval during the passage of the MCBL. In terms of Shue et al. (1998) model, the closest subsolar standoff distance even reached 5.1 RE during the passage of the MCBL. It can be inferred that the strong dynamic pressure and the strong discontinuities within the MCBL determine the intense compression effect. In addition, a very intense geomagnetically induced current (GIC) event was directly caused by the MCBL. Similar to this case, majority of MCBLs are dynamic pressure enhancement regions, and there are strong southward magnetic field and several strong discontinuities inside these regions, which can potentially drive large-scale magnetospheric activities. In the work of Zuo et al. (2010), they take a case study to discuss the magnetospheric activities and the space weather effects caused by MCBLs.

Guo et al. (2010) examine and compare the statistical properties of interplanetary coronal mass ejections (ICMEs) and their sheath regions in the near-Earth space, mainly focusing on the distributions of various physical parameters and their geoefficiency. The 53 events studied are a subset of events responsible for intense ($Dst \leq -100$ nT) geomagnetic storms during the time period from 1996 to 2005. These events all fall into the single-type category in which each of the geomagnetic storms was caused by a well-isolated single ICME, free of the complexity of the interaction of multiple ICMEs. For both sheaths and ICMEs, they find that the distributions of the magnetic field strength, the solar-wind speed, the density, the proton temperature, the dynamic pressure, the plasma beta, and the Alfvén Mach number are approximately lognormal, while those of the Bz component and the Y component of the electric field are approximately Gaussian. On the average, the magnetic field strengths, the Bz components, the speeds, the densities, the proton temperatures, the dynamic pressures, the plasma betas, and the Mach numbers for the sheaths are 15, 80, 4, 60, 70, 62, 67, and 30% higher than

the corresponding values for ICMEs, respectively, whereas the Y component of the electric field for the sheaths is almost 1 s of that for ICMEs. The two structures have almost equal energy transfer efficiency and comparable Newell functions, whereas they show statistically meaningful differences in the dayside reconnection rate, according to the Borovsky function.

Using 141 CME-interplanetary shock (CME-IPS) events and foF2 from eight ionosonde stations from January 2000 to September 2005, from the statistical results Li, Wei, Feng and Zhao (2010) find that there is a “same side-opposite side effect” in ionospheric negative storms, *i.e.*, a large portion of ionospheric negative disturbances are induced by the same-side events (referring to the CMEs whose source located on the same side of the heliospheric current sheet (HCS) as the Earth), while only a small portion is associated with the opposite-side events (the CMEs source located on the opposite side of the HCS as the Earth); the ratio is 128 *vs.* 46, and it reaches 41 *vs.* 14 for the intense ionospheric negative storms. In addition, the ionospheric negative storms associated with the same-side events are often more intense. A comparison of the same-side event (4 April 2000) and the opposite-side event (2 April 2001) shows that the intensity of the ionospheric negative storm caused by the same-side event is higher than that by the opposite-side event, although their initial conditions are quite similar. Their preliminary results show that the HCS has an “impeding” effect to CMEIPS, which results in a shortage of energy injection in the auroral zone and restraining the development of ionospheric negative perturbations.

As far as the role of the interplanetary magnetic field (IMF) in the solar windmagnetosphere-ionosphere (SMI) coupling is concerned, the role of the IMF B_x has more or less been ignored. Recent studies have shown that the IMF B_x plays an important role in the geometry of the bow shock under low Alfvén Mach numbers. Using global MHD simulations, Peng et al. (2010) presents a further examination of the effects of the IMF B_x on the geometry of the magnetopause, the ionospheric transpolar potential, and the magnetopause reconnection rate, which quantify the SMI coupling process, under low Alfvén Mach numbers. The role of the IMF B_x manifests itself in three aspects: (1) the magnetopause shifts toward either north or south, depending on whether the $B_x \cdot B_z$ is negative or positive, whereas the bow shock expands in the opposite direction; (2) during southward IMF, the magnetic merging line shifts northward (southward) on the day side and

southward (northward) on the night side for $B_x > 0$ ($B_x < 0$); (3) both the ionospheric transpolar potential and the magnetopause reconnection rate decrease with increasing B_x , and the relative reduction may reach as high as 20% under extreme cases. The physical mechanism for this reduction is attributed to the change in the width of the magnetosheath, which is sensitive to the variation of B_x under low Alfvén Mach numbers.

Yao et al. (2010) presented in situ solar wind observations of three magnetic clouds (MCs) that contain cold high-density material when Helios 2 was located at 0.3 AU on 9 May 1979, 0.5 AU on 30 March 1976, and 0.7 AU on 24 December 1978. In the cold high-density regions embedded in the interplanetary coronal mass ejections they find (1) that the number density of protons is higher than in other regions inside the magnetic cloud, (2) the possible existence of He^+ , (3) that the thermal velocity distribution functions are more isotropic and appear to be colder than in the other regions of the MC, and the proton temperature is lower than that of the ambient plasma, and (4) that the associated magnetic field configuration can for all three MC events be identified as a flux rope. This cold high-density region is located at the polarity inversion line in the center of the bipolar structure of the MC magnetic field (consistent with previous solar observation work that found that a prominence lies over the neutral line of the related bipolar solar magnetic field). Specifically, for the first magnetic cloud event on 8 May 1979, a coronal mass ejection (CME) was related to an eruptive prominence previously reported as a result of the observation of *Solwind* (P78-1). Therefore, they identify the cold and dense region in the MC as the prominence material. It is the first time that prominence ejecta were identified by both the plasma and magnetic field features inside 1 AU, and it is also the first time that the thermal ion velocity distribution functions were used to investigate the microstate of the prominence material. Moreover, from their three cases, they also found that this material tended to fall behind the magnetic cloud and become smaller as it propagated farther away from the Sun, which confirms speculations in previous work. Overall, their in situ observations are consistent with three-part CME models.

IV. ENERGETIC PARTICLES

Zhang (2007) pointed out that the behavior of energetic charged particles

accelerated by a continuous plasma compression profile is explored in the framework of diffusion. At high enough energies, the accelerated particles have a power-law spectrum with a slope generally steeper than a shock spectrum with the same compression ratio. The spectral slope depends on the ratio of the diffusion coefficient to the product of the upstream plasma speed and the thickness of the compression region. In the limit of large diffusion, the spectrum becomes identical to that of diffusive shock acceleration, and when diffusion is small enough, it is consistent with adiabatic acceleration by a single passage through the compression region. For particles with a diffusion coefficient that increases with energy, the spectral shape of the accelerated particles changes from an adiabatic compressional acceleration spectrum at low energies to a shock spectrum at high energies. The flux level of the high energy asymptotic shock spectrum is generally lower than that from a calculation with diffusive shock acceleration. When this result is applied to particles accelerated to high energies by shocks, the particle injection energy and efficiency can be determined once the energy dependence of the diffusion coefficient and the spectrum of the source particles are known. A threshold criterion for particle injection to shock acceleration can be set from the injection efficiency calculation.

Current sheets are common structures in the solar wind and possibly the boundaries of individual flux tubes. Observations show that magnetic field directions often change abruptly upon crossing these structures. The presence of these structures introduces a new source of solar wind turbulence intermittency and can affect the transport of energetic particles. Previous studies of energetic-particle transport in the solar wind often assume a uniform large-scale background magnetic field, with a turbulent field superposed. With the existence of flux tubes in the solar wind, this picture needs to be changed. Qin and Li (2008) study the effects of flux tubes on the transport of energetic particles in the solar wind. They construct a model turbulence of the solar wind by including explicitly flux-tube-like structures. In their model, the solar wind is composed of many individual cells with a local uniform mean magnetic field chosen randomly. The turbulence in each cell is modeled by either a slab and/or 2D type. They then calculate numerically the particle diffusion coefficients by following single particle trajectories. Their results show that flux tubes in the solar wind can lead to stronger scatterings of particles in directions both parallel and perpendicular to the

large-scale background magnetic field. In particular, a true diffusion in the large-scale perpendicular direction (with respect to B_0) is obtained even when the local intrinsic turbulence in individual cells is of pure slab type.

The behavior of solar energetic particles (SEPs) in a shock-magnetic cloud interacting complex structure observed by the *ACE* spacecraft on 5 November 2001 is analyzed by Shen et al. (2008). A strong shock causing magnetic field strength and solar wind speed increases of about 41 nT and 300 km/s, respectively, propagated within a preceding magnetic cloud (MC). It is found that an extraordinary SEP enhancement appeared at the high-energy (≥ 10 MeV) proton intensities and extended over and only over the entire period of the shock-MC structure passing through the spacecraft. Such SEP behavior is much different from the usual picture that the SEPs are depressed in MCs. The comparison of this event with other top SEP events of solar cycle 23 (2000 Bastille Day and 2003 Halloween events) shows that such an enhancement resulted from the effects of the shock-MC complex structure leading to the highest ≥ 10 MeV proton intensity of solar cycle 23. Their analysis suggests that the relatively isolated magnetic field configuration of MCs combined with an embedded strong shock could significantly enhance the SEP intensity; SEPs are accelerated by the shock and confined into the MC. Further, they find that the SEP enhancement at lower energies happened not only within the shock-MC structure but also after it, probably owing to the presence of a following MC-like structure. This is consistent with the picture that SEP fluxes could be enhanced in the magnetic topology between two MCs, which was proposed based on numerical simulations by Kallenrode and Cliver.

Xiao et al. (2008) utilize a recently introduced relativistic kappa-type (KT) distribution function to model the omnidirectional differential flux of energetic electrons observed by the SOPA instrument on board the 1989-046 and LANL-01A satellites at geosynchronous orbit. They derive a useful correlation between the differential flux and the distribution of particles which can directly offer those best fitting parameters (e.g., the number density N , the thermal characteristic speed q and the spectral index k) strongly associated with evaluation of the electromagnetic wave instability. They adopt the assumption of a nearly isotropic pitch angle distribution (PAD) and the typical LMFIT function in the program IDL to perform a non-linear least squared fitting, and find that the new

KT distribution fits well with the observed data during different universal times both in the lower and higher energies. They also carry out the direct comparisons with the generalized Lorentzian (κ) distribution and find that κ distribution fits well with observational data at the relatively lower energies but display deviations at higher energies, typically above hundreds of keV. Furthermore, the fitting spectral index k basically takes 4, 5 or 6 while the fitting parameters N and q are quite different due to different differential fluxes of electrons at different universal times. These results, which are applied to the case of a nearly isotropic PAD, demonstrate that the particle flux satisfies the power law not only at the lower energies but also at the relativistic energies, and the new KT distribution may present valuable insights into the dynamical features in those space plasmas (e.g., the Earth's outer radiation belts and the inner Jovian magnetosphere) where highly energetic particles exist.

Pitch-angle diffusion is a key process in the theory of charged particle scattering by turbulent magnetic plasmas. This process is usually assumed to be diffusive and can, therefore, be described by a pitch-angle diffusion or Fokker-Planck coefficient. This parameter controls the parallel spatial diffusion coefficient as well as the parallel mean free path of charged particles. Qin and Shalchi (2009) determine pitch-angle diffusion coefficients from numerical computer simulations. These results are then compared with results from analytical theories. Especially, they compare the simulations with quasilinear, second-order, and weakly nonlinear diffusion coefficients. Such a comparison allows the test of previous theories and will lead to an improved understanding of the mechanism of particle scattering.

Zhang, Qin and Rassoul (2009) present a model calculation of solar energetic particle propagation in a three-dimensional interplanetary magnetic field. The model includes essentially all the particle transport mechanisms: streaming along magnetic field lines, convection with the solar wind, pitch-angle diffusion, focusing by the inhomogeneous interplanetary magnetic field, perpendicular diffusion, and pitch-angle dependent adiabatic cooling by the expanding solar wind. They solve the Fokker-Planck transport equation with simulation of backward stochastic processes in a fixed reference frame in which any spacecraft is roughly stationary. As an example they model the propagation of those high-energy ($E \geq 10$ MeV) solar energetic particles in gradual events that are accelerated by large

coronal mass ejection shocks in the corona and released near the Sun into interplanetary space of a Parker spiral magnetic field. Modeled with different scenarios, the source of solar energetic particles can have a full or various limited coverages of latitude and longitude on the solar surface. They compute the long-term time profiles of particle flux and anisotropy at various locations in the heliosphere up to 3 AU, from the ecliptic to high latitudes. Features from particle perpendicular diffusion are revealed. Their simulation reproduces the observed reservoir phenomenon of solar energetic particles with constraints on either solar particle source or the magnitude of perpendicular diffusion.

Wang, Wei et al. (2010) reported in situ observation of energetic electrons (~100-500 keV) associated with magnetic reconnection in the solar wind by the *ACE* and *WIND* spacecraft. The properties of this magnetic cloud driving reconnection and the associated energetic electron acceleration problem are discussed. Further analyses indicate that the electric field acceleration and Fermi-type mechanism are two fundamental elements in the electron acceleration processes and the trapping effect of the specific magnetic field configuration maintains the acceleration status that increases the totally gained energy.

The analytical nonlinear theory of magnetic field line random walk predicts the existence of nondiffusive transport for certain forms of the turbulence spectrum. Shalchi and Qin (2010) use computer simulations to test these predictions made for well-established one-and two dimensional models of magnetic field fluctuations. For the first time it is shown by using simulations, that for a whole family of spectra a non-diffusive behavior of field line wandering can be found.

The issue of the influence of coronal holes (CHs) on coronal mass ejections (CMEs) in causing solar energetic particle (SEP) events is revisited by Shen, Yao, et al. (2010). It is a continuation and extension of their previous work, in which no evident effects of CHs on CMEs in generating SEPs were found by statistically investigating 56 CME events. This result is consistent with the conclusion obtained by Kahler in 2004. They extrapolate the coronal magnetic field, define CHs as the regions consisting of only open magnetic field lines and perform a similar analysis on this issue for 76 events in total by extending the study interval to the end of 2008. Three key parameters, CH proximity, CH area and CH relative position, are involved in the analysis. The new result confirms the previous conclusion that CHs did not show any evident effect on CMEs in causing SEP events.

V. MHD SIMULATIONS

The space time conservation element and solution element (CESE) method is applied to three dimensional magnetohydrodynamics (MHD) equations in Cartesian coordinates for solar wind plasma, with the purpose of modeling the steady state solar atmospheric study. To illustrate this newly developed scheme Feng et al. (2007) have studied two examples: (1) two-dimensional coronal dynamical structure with multi-pole magnetic fields and (2) three dimensional coronal dynamical structure, using measured solar surface magnetic fields and the empirical values of the plasma properties on the solar surface as the initial conditions for the set of MHD equations and then the relaxation method to achieve a quasi-steady state. From these examples they have shown that the newly developed modified space time CESE scheme possesses the ability to model the Sun-Earth environment and other astrophysical flows.

A newly developed hybrid code, HAFv.2+3DMHD, that combines two simulation codes, Hakamada-Akasofu-Fry code version 2 (HAFv.2) and a fully three-dimensional (3-D), time-dependent MHD simulation code, is used by Wu et al. (2007) to study the global interplanetary coronal mass ejection (ICME) from the 12 May 1997 solar event. The solar wind structure is first simulated from the photosphere (1 solar radius, R_s) out to 2.5 R_s . The first step is derived from daily solar magnetograms. The HAFv.2 code is then used from 2.5 R_s to provide input at 18 R_s (0.08 AU) for the three-dimensional MHD code that calculates the evolution of solar wind plasma and interplanetary magnetic field beyond this distance into the heliosphere. A dynamic disturbance, mimicking the flare's energy output from the 12 May 1997 solar event, is then delivered to this quiescent nonuniform heliospheric structure to model the evolution and interplanetary propagation of the ICME (including its shock). They compare the derived ICME velocity and number density with the *WIND* spacecraft observations near Earth. They integrate the line-of-sight density in the plane of sky to compare with the white light brightness data observed by *LASCO* instrument on *SOHO*. This simulation will provide a tool to link the general cases of ICME at 1 AU to their solar sources, as well as to identify the possible origins of shock formation due to CMEs and CME/corotating interaction region interactions. In the case of complex or interacting ejecta, model

interpretation is often required to accurately determine the solar sources of the ejecta at 1 AU. Because this newly developed model is performed using 3-D MHD, its results can be extended to simulate coronal and heliospheric observations, including the ambient medium's nonuniformity provided by the HAFv.2 model, from the recently launched Solar Terrestrial Relations Observatory (*STEREO*) mission.

A three-dimensional time-dependent, numerical magnetohydrodynamic (MHD) model is used by Shen et al. (2007) to investigate the propagation of coronal mass ejections (CMEs) in the nonhomogenous background solar wind flow. On the basis of the observations of the solar magnetic field and K-coronal brightness, the self-consistent structure on the source surface of 2.5 Rs is established with the help of MHD equations. Using the self-consistent source surface structures as initial-boundary conditions, they develop a three-dimensional MHD regional combination numerical model code to obtain the background solar wind from the source surface of 2.5 Rs to the Earth's orbit (215 Rs) and beyond. This model considers solar rotation and volumetric heating. Time-dependent variations of the pressure and velocity configured from a CME model at the inner boundary are applied to generate transient structures. The dynamical interaction of a CME with the background solar wind flow between 2.5 and 215 Rs (1 AU) is then investigated. They have chosen the well-defined halo-CME event of 6–12 January 1997 as a test case. Because detailed observations of this disturbance at 1 AU (by *WIND* spacecraft) are available, this event gives us an excellent opportunity to verify their MHD methodology and to learn about the physical processes of the Sun-Earth connection. They find that this three-dimensional MHD model, with the self-consistent structures on the source surface as input, provides a relatively satisfactory comparison with the *WIND* spacecraft.

Numerical studies of the interplanetary “multiple magnetic clouds (Multi-MC)” are performed by a 2.5-dimensional ideal magnetohydrodynamic (MHD) model in the heliospheric meridional plane by Xiong et al. (2007). Both slow MC1 and fast MC2 are initially emerged along the heliospheric equator, one after another with different time intervals. The coupling of two MCs could be considered as the comprehensive interaction between two systems, each comprising of an MC body and its driven shock. The MC2-driven shock and MC2 body are successively involved into interaction with MC1 body. The momentum is

transferred from MC2 to MC1. After the passage of MC2-driven shock front, magnetic field lines in MC1 medium previously compressed by MC2-driven shock are prevented from being restored by the MC2 body pushing. MC1 body undergoes the most violent compression from the ambient solar wind ahead, continuous penetration of MC2-driven shock through MC1 body, and persistent pushing of MC2 body at MC1 tail boundary. As the evolution proceeds, the MC1 body suffers from larger and larger compression, and its original vulnerable magnetic elasticity becomes stiffer and stiffer. So there exists a maximum compressibility of Multi-MC when the accumulated elasticity can balance the external compression. This cutoff limit of compressibility mainly decides the maximally available geoeffectiveness of Multi-MC because the geoeffectiveness enhancement of MCs interacting is ascribed to the compression. Particularly, the greatest geoeffectiveness is excited among all combinations of each MC helicity, if magnetic field lines in the interacting region of Multi-MC are all southward. Multi-MC completes its final evolutionary stage when the MC2-driven shock is merged with MC1-driven shock into a stronger compound shock. With respect to Multi-MC geoeffectiveness, the evolution stage is a dominant factor, whereas the collision intensity is a subordinate one. The magnetic elasticity, magnetic helicity of each MC, and compression between each other are the key physical factors for the formation, propagation, evolution, and resulting geoeffectiveness of interplanetary Multi-MC.

Zhou et al. (2008) used a newly developed CESE MHD model to simulate sun-earth connection event with the well-studied 12 May 1997 CME event as an example. The main features and approximations of their numerical model are as follows: (1) The modified conservation element and solution element (CESE) numerical scheme in spherical geometry is implemented in their code. (2) The background solar wind is derived from a 3D time-dependent numerical MHD model by input measured photospheric magnetic fields. (3) Transient disturbances are derived from solar surface by introducing a mass flow of hot plasma. The numerical simulation has enabled us to predict the arrival of the interplanetary shock and provided us with a relatively satisfactory comparison with the *WIND* spacecraft observations.

Based on the space-time conservation element and solution element (CESE) method, Hu et al. (2008) have recently developed a novel 3D

magnetohydrodynamic (MHD) model for the solar corona and interplanetary study. Their aim is to describe the application of this new MHD model to study the global coronal magnetic structures by using the observed line-of-sight photospheric magnetic field from the Wilcox Solar Observatory (WSO) as boundary conditions. With this model, the magnetic structures of the global corona are obtained for fifteen Carrington Rotations (CRs) spanning solar cycle 23. The results illustrate how the shape and location of the heliospheric current sheet (HCS) and the coronal magnetic field configuration evolve during the course of the solar cycle. Comparison between their numerical results for the coronal magnetic structures and those from the standard potential field source surface (PFSS) model, with, in addition, white light observations further validates this new MHD model. The source surface neutral lines calculated from the MHD and PFSS models generally match each other closely; however, differences occur at different phases in the solar cycle. The location of the HCS shows good overall agreement with the bright structures in the observed white-light intensity pattern, especially around solar minimum or well after solar maximum, and this result confirms that the observed white-light streamer structures originate from a single, large scale plasma sheet located near the HCS.

Zhou and Feng (2008) present the solar-terrestrial transit process of three successive coronal mass ejections (CMEs) of November 4-5, 1998 originating from active region 8375 by using a time-dependent three-dimensional magnetohydrodynamics (MHD) simulation. These CMEs interacted with each other while they were propagating in interplanetary space and finally formed a “complex ejecta”. A newly developed SIP-CESE MHD model was applied to solve MHD equations numerically. The quiet solar wind was started from Parker-like 1D solar wind solution and the magnetic field map was calculated from the solar photospheric magnetic field data. In their simulation, the ejections were initiated using pulse in the real active region 8375. The interplanetary disturbance parameters, such as speed, direction and angular size of the expanding CME, were determined from the *SOHO/LASCO* data with the cone-model. They discussed the three-dimensional aspects of the propagation, interaction and merging of the three ejections. The simulated interplanetary shocks were compared with the nearby-Earth measurement. The results showed that their simulation could reproduce and explain some of the general features observed by satellite for the

“complex ejecta”.

An asynchronous and parallel time-marching method for three-dimensional (3D) time-dependent magnetohydrodynamic (MHD) simulation is used by Shen, Feng and Song (2009) for large-scale solar wind simulation. It uses different local time steps in the corona and the heliosphere according to the local Courant-Friedrichs-Levy (CFL) conditions. The solar wind background with observed solar photospheric magnetic field as input is first presented. The simulation time for the background solar wind by using the asynchronous method is $<1/6$ of that by using the normal synchronous time-marching method with the same computation pre-cision. Then, they choose the coronal mass ejection (CME) event of 13 November, 2003 as a test case. The time-dependent variations of the pressure and the velocity configured from a CME model at the inner boundary are applied to generate transient structures in order to study the dynamical interaction of a CME with the background solar wind flow between 1 and 230 Rs. This time-marching method is very effective in terms of computation time for large-scale 3D time-dependent numerical MHD problem. In this validation study, they find that this 3D MHD model, with the asynchronous and parallel time-marching method, provides a relatively satisfactory comparison with the ACE spacecraft observations at L1 point.

The numerical studies of the interplanetary coupling between multiple magnetic clouds (MCs) are continued by Xiong et al. (2009) by a 2.5-dimensional ideal magnetohydrodynamic (MHD) model in the heliospheric meridional plane. The interplanetary direct collision (DC)/oblique collision (OC) between both MCs results from their same/different initial propagation orientations. Here the OC is explored in contrast to the results of the DC. Both the slow MC1 and fast MC2 are consequently injected from the different heliospheric latitudes to form a compound stream during the interplanetary propagation. The MC1 and MC2 undergo contrary deflections during the process of oblique collision. Their deflection angles of $|\delta\theta_1|$ and $|\delta\theta_2|$ continuously increase until both MC-driven shock fronts are merged into a stronger compound one. The $|\delta\theta_1|$, $|\delta\theta_2|$, and total deflection angle $\Delta\theta$ ($\Delta\theta = |\delta\theta_1| + |\delta\theta_2|$) reach their corresponding maxima when the initial eruptions of both MCs are at an appropriate angular difference. Moreover, with the increase of MC2's initial speed, the OC becomes more intense, and the enhancement of $\delta\theta_1$ is much more sensitive to $\delta\theta_2$. The $|\delta\theta_1|$ is generally far less than the $|\delta\theta_2|$, and the unusual case of

$|\delta\theta_1| \approx |\delta\theta_2|$ only occurs for an extremely violent OC. But because of the elasticity of the MC body to buffer the collision, this deflection would gradually approach an asymptotic degree. As a result, the opposite deflection between the two MCs, together with the inherent magnetic elasticity of each MC, could efficiently relieve the external compression for the OC in the interplanetary space. Such a deflection effect for the OC case is essentially absent for the DC case. Therefore, besides the magnetic elasticity, magnetic helicity, and reciprocal compression, the deflection due to the OC should be considered for the evolution and ensuing geoeffectiveness of interplanetary interaction among successive coronal mass ejections.

A constant dawn-dusk B_y component is set as an interplanetary magnetic field (IMF) condition in the global MHD simulations of Guo and Wang (2010) to investigate the effects of IMF B_y on the closure of the field-aligned current (FAC) in the magnetosphere. On the basis of the steady state magnetosphere results, they trace streamlines of FAC from the ionosphere to draw the global geometry of current streamlines in the magnetosphere. Unlike those cases in which the IMF is purely northward or southward, the introduction of the dominant IMF B_y significantly changes the topologies of the current streamlines. Cusp and mantle currents arise, and the symmetry of the FAC across the noon-night meridional plane breaks in the ionosphere. In addition to the self-closed currents in the Northern or Southern hemispheres, three more types of current streamlines connecting the two ionospheres are shown from the simulation results. The first current, including the cusp current, originates from the southern ionosphere and flows into the northern ionosphere. The second current, mainly the mantle current, and the tail current are connected to form a single current system, threading most of the magnetosphere along a spiral-like path and closing through the two lobes in the far magnetotail. The third current flowing out of the southern and into the northern ionosphere connects the two ionospheres by finally closing through the bow shock instead of the magnetopause. Quantitative results are presented and discussed for the four types of current streamlines and indicate that for the dominant IMF B_y conditions the bow shock current should be included among the magnetosphere-ionosphere current system.

The Kelvin-Helmholtz (K-H) instability is found to occur at the low - latitude magnetopause through global magnetohydrodynamic simulations during a period of northward interplanetary magnetic field. The simulation results of Guo, Wang

and Hu (2010) present the global picture of the nonlinear evolution of the K-H instability at the magnetopause. At the low-latitude boundary layer (within the latitude of about 30°), vortices are generated by the K-H instability at the dayside magnetopause and transported to the far distant magnetotail region along the flank of the magnetosphere; two modes of surface waves propagate along the inner and outer edge of the magnetopause boundary layer, respectively, from the initial point to the tail region; the wavelengths of the inner and outer modes are estimated to vary from 1 to $8 R_E$ as the longitude increases. The vortices are initiated at a longitude of about 28° relative to the Sun-Earth line in the equatorial plane, and their evolution along the magnetopause boundary is studied in detail. They present the characteristics of the inner and outer mode surface waves near the magnetopause boundary layer and find different behaviors of the fast-mode surface waves on the two sides of the magnetopause boundary: the variations of the density and the magnetic field strength of the quasi-fast mode waves are in phase on the magnetosphere side (inner mode), while they are out of phase on the magnetosheath-side (outer mode). The obtained period of the surface waves coincides with the generation period of the vortex at the dayside magnetopause, which is considered to be the intrinsic period of the magnetopause for the corresponding interplanetary condition.

Jiang et al. (2010) present new extensions of the space- time conservation element and solution element (CESE) method for simulations of magnetohydrodynamic (MHD) problems in general curvilinear coordinates by using an adaptive mesh refinement (AMR) grid system. By transforming the governing MHD equations from the physical space (x, y, z) to the computational space (ξ, η, ζ) while retaining the form of conservation, the CESE method is established for MHD in the curvilinear coordinates. Utilizing the parallel AMR package PARAMESH, they present the first implementation of applying the AMR CESE method for MHD (AMR-CESE-MHD) in both Cartesian and curvilinear coordinates. To show the validity and capabilities of the AMR-CESE-MHD code, a suite of numerical tests in two and three dimensions including ideal MHD and resistive MHD are carried out, with two of them in both Cartesian and curvilinear coordinates. Numerical tests show that their results are highly consistent with those obtained previously by other authors, and the results under both coordinate systems confirm each other very well.

The objective of Feng et al. (2010) is to explore the application of a six-component overset grid to solar wind simulation with a three-dimensional (3D) Solar-InterPlanetary Conservation Element/Solution Element MHD model. The essential focus of their numerical model is devoted to dealing with: (1) the singularity and mesh convergence near the poles via the use of the six-component grid system, (2) the $\nabla \cdot \mathbf{B}$ constraint error via an easy-to-use cleaning procedure by a fast multigrid Poisson solver, (3) the Courant–Friedrichs–Levy number disparity via the Courant-number insensitive method, (4) the time integration by multiple time stepping, and (5) the time-dependent boundary condition at the subsonic region by limiting the mass flux escaping through the solar surface. In order to produce fast and slow plasma streams of the solar wind, they include the volumetric heating source terms and momentum addition by involving the topological effect of the magnetic field expansion factor f_S and the minimum angular distance θ_b (at the photosphere) between an open field foot point and its nearest coronal hole boundary. These considerations can help them easily code the existing program, conveniently carry out the parallel implementation, efficiently shorten the computation time, greatly enhance the accuracy of the numerical solution, and reasonably produce the structured solar wind. The numerical study for the 3D steady-state background solar wind during Carrington rotation 1911 from the Sun to Earth is chosen to show the above-mentioned merits. Their numerical results have demonstrated overall good agreements in the solar corona with LASCO on board the *SOHO* satellite and at 1 AU with *WIND* observations.

In terms of global magnetohydrodynamic (MHD) simulations of the solar wind-magnetosphere-ionosphere system, this paper investigates the rotational asymmetry of the Earth’s bow shock with respect to the Sun-Earth line. Hu et al. (2010) are limited to simple cases in which the solar wind is along the Sun-Earth Line, and both the Earth’s magnetic dipole moment and the interplanetary magnetic field (IMF) are perpendicular to the Sun-Earth line. It is shown that even for the case of vanishing IMF strength the bow shock is not rotationally symmetric with respect to the Sun-Earth line: the east-west width of the cross section of the bow shock exceeds the north-south width by about 9%-11% on the terminator plane (dawn-dusk meridian plane) and its sunward side, and becomes smaller than the north-south width by about 8% on the tailward side of the terminator plane. In the presence of the IMF, the configuration of the bow shock is affected by both the

shape of the magnetopause and the anisotropy of fast magnetosonic wave speed. The magnetopause expands outward, being stretched along the IMF, and the extent of its expansion and stretch increases when the IMF rotates from north to south. In the magnetosheath, the fast magnetosonic wave speed is higher in the direction perpendicular to the magnetic field than that in the parallel direction. Therefore, the stretch direction of the magnetopause is perpendicular to the maximum direction of the fast magnetosonic wave speed, and their effects on the bow shock position are exactly opposite. The eventual shape of the bow shock depends on which effect dominates. On the tailward side of the terminator plane, the anisotropy of fast magnetosonic wave speed dominates, so the cross section of the bow shock is wider in the direction perpendicular to the IMF. On the terminator plane and its sunward side, the shape of the bow shock cross section depends on the orientation of the IMF: the bow shock cross section is still wider in the direction perpendicular to the IMF under generic northward or dawn-dusk IMF cases, but it becomes narrower in the direction perpendicular to the IMF instead under generic southward IMF cases. In light of the intimate relationship between the shape of the bow shock and the orientation of the IMF, it is proposed to take the IMF as the datum direction so as to extract the parallel half width $R_{b\parallel}$ and the perpendicular half width $R_{b\perp}$ as the scale parameters. In comparison with the commonly used east-west half width y_b and the north-west half width z_b , these parameters provide a more reasonable description of the geometry of the bow shock. Simulation data show that under the assumption of isotropic orientation of the IMF, the statistical averages of y_b/z_b and $R_{b\parallel}/R_{b\perp}$ are both smaller than 1 on the terminator plane, which agrees with relevant observational conclusions.

Hu and Wang (2010) presents a brief summary of their recent work based on global MHD simulations of the Solar wind-Magnetosphere-Ionosphere (SMI) system with emphasis on the electrodynamic coupling in the system. The main conclusions obtained are summarized as follows. (1) As a main dynamo of the SMI system, the bow shock contributes to both region 1 Field-Aligned Current (FAC) and cross-tail current. Under strong interplanetary driving conditions and moderate Alfvén Mach numbers, the bow shock's contribution may exceed more than fifty percent of the total of either region 1 or cross-tail currents. (2) In terms of more than 100 simulation runs with due southward Interplanetary Magnetic Field (IMF),

they have found a combined parameter $f = E_{sw} P_{sw} M_A^{-1/2}$ (E_{sw} , P_{sw} , and M_A are the solar wind electric field, ram pressure, and Alfvén Mach number, respectively): both the ionospheric transpolar potential and the magnetopause reconnection voltage vary linearly with f for small f , but saturate for large f . (3) The reconnection voltage is approximately fitted by $\sin^{3/2}(\theta_{IMF}/2)$, where θ_{IMF} is the IMF clock angle. The ionospheric transpolar potential, the voltage along the polar cap boundary, and the electric fields along the merging line however defined they may be, respond differently to θ_{IMF} , so it is not justified to take them as substitutes for the reconnection voltage.

The basic characteristics of the global distribution for the corona plasma and magnetic field near 2.5 Rs are analyzed with the statistical and numerical methods for 136 Carrington Rotations (CRs) covering four different phases of solar activity. By using the observational data and the velocity distribution model in the corona, the statistical average distribution of the magnetic field, density and the coronal mass outputs are analyzed by Shen et al. (2010) for the four different phases. Then, a numerical study of the global distribution near 2.5 Rs has been made by solving a self-consistent MHD system. Finally, the solar wind speed at 1 AU is given by mapping the speed at 2.5 Rs to that near 1 AU, and the comparison of the numerical results with the observational measurements and the simulation result of the Wang-Sheeley-Argue (WSA) model are made during more than 5 years. The numerical results indicate that the global distributions on the source surface of 2.5 Rs at different phases of solar activity could be used to predict the change of the solar wind in interplanetary space.

VI. SPACE PLASMA

Lu and Li (2007) reported a new physical mechanism that enables the heating of ions by a low-frequency parallel propagating Alfvén wave of finite amplitude in a low beta plasma. The heating does not rely on ion cyclotron resonance. The process has two stages: First, ions, whose initial average velocity is zero, are picked up in the transverse direction by the Alfvén wave and obtain an average transverse velocity. Second, at a given location the parallel thermal motions of ions produce phase differences (randomization) between ions leading to the heating of

ions. The randomization (or heating) process saturates when phase differences are sufficiently large. The time scale over which ions are significantly heated is $\sim \pi / (kv_{th})$ (v_{th} is the initial ion thermal speed and k is the wave number). The heating is dominant in the perpendicular (to the background magnetic field) direction. Subsequently, a large ion temperature anisotropy is produced. During the heating process, ions are also accelerated in the parallel direction and obtain a bulk flow speed along the background magnetic field.

Two scenarios of possible ion heating due to finite amplitude parallel propagating Alfvén waves in the solar atmosphere are investigated by Li, Lu and Li (2007) using a one-dimensional test particle approach. (1) A finite amplitude Alfvén wave is instantly introduced into a plasma (or equivalently, new ions are instantly created). (2) New ions are constantly created. In both scenarios, ions will be picked up by the Alfvén wave. In case 1, the wave scatters ions in the transverse direction leading to a randomization (or heating) process. This process is complete when a phase shift of $\pm \pi$ in the ion gyrospeed is produced between particles with characteristic parallel thermal speed and particles with zero parallel speed. This corresponds to $t = \pi / kv_{th}$ (k is the wavenumber, and v_{th} is the ion thermal speed). A ring velocity distribution can be produced for a large wave amplitude. The process yields a mass-proportional heating in the transverse direction, a temperature anisotropy, and a bulk flow along the background magnetic field. In case 2, continuous ion creation represents a continuing phase shift in the ion gyrospeed leading to heating. New particles are picked up by the Alfvén wave within one ion gyroperiod. It is speculated that the mechanism may operate in the chromosphere and active regions where transient events may generate finite amplitude Alfvén waves.

The electron surfing acceleration in the current sheet with perpendicular propagating electrostatic waves is studied using analytical theories and test particle simulations. The trapped electron moving with the phase velocity v_p of wave may be accelerated effectively in the outflow direction by $(ev_p/c) \times B_z$ force until the electron is de-trapped from the wave potential. A criterion $K > 0$ for the electron surfing acceleration is obtained. The electron will escape from the boundary of current sheet quickly, if this criterion does not hold. The maximum velocity of surfing acceleration is about the same as the electric drift velocity. Superposed longitudinal magnetic field along the wave propagation is favorable for the

electron surfing acceleration in the current sheet.

Wavelength dependence of laser ablation of silicon was investigated by Lu et al. (2008a) with nanosecond ultraviolet, visible, and infrared laser pulses in the irradiance range from 3×10^{10} to 1×10^{12} W/cm². For 266 and 532 nm laser pulses, the depth of laser-produced crater shows a dramatic increase at a laser irradiance threshold of approximately 2×10^{10} and 4×10^{11} W/cm² respectively, above which, large micron-sized particulates were observed to eject from the target about 300-400 ns after the laser pulse. In contrast, for 1064 nm pulse, this dramatic increase was not observed. The underlying mechanism for the observed threshold phenomenon is presented in this study, which can be attributed to the thermal diffusion and subsequent explosive boiling after the completion of the interaction between the nanosecond laser pulse and silicon. Based on their delayed phase explosive model, the ablation depths were calculated for different wavelengths and compared to experimental results. Plasma shielding during laser irradiation was included in the model, which plays a key role to the coupling of laser energy to the irradiated material

Electron acceleration by the inductive electric field near the X point in magnetic reconnection is an important generation mechanism for energetic electrons. Particle simulations have revealed that most of energetic electrons reside in the magnetic field line pileup region, and a depletion of energetic electrons can be found near the centre of the diffusion region. Wang, Lu et al. (2008) report direct measurement of energetic electron in and around the ion diffusion region in near-Earth tail by the cluster, and their observations confirm the above predictions: a depletion of the high-energy electron fluxes is detected near the centre of the diffusion region. At the same time, the plasma temperature has a similar profile in the diffusion region.

Previous multi-dimensional particle simulations have shown that electron phase-holes can be formed during the nonlinear evolution of bi-stream instability. In these holes, the parallel cut of the parallel electric field (E_{\parallel}) has bipolar structures while the parallel cut of the perpendicular electric field (E_{\perp}) has unipolar structures. Two-dimensional (2D) electrostatic particle-in-cell simulations are performed by Lu et al. (2008b) to investigate the evolution of E_{\perp} in such electron holes for different plasma conditions, and the generation mechanism of the unipolar structures of E_{\perp} is also discussed. The electrons trapped in electron holes

bounce in the parallel direction, which leads to transverse instability (Muschiatti et al., 2000). At the same time, they gyrate in the background magnetic field, which tends to stabilize electron holes. In this way, the trapped electrons are forced to accumulate locally, and the charge density has variations along the perpendicular direction inside the electron holes. The balance between these two effects leads to the following results: in weakly magnetized plasma ($\Omega_e < \omega_{pe}$, but Ω_e is comparable to ω_{pe} . Where Ω_e and ω_{pe} are the electron cyclotron frequency and electron plasma frequency, respectively), electron holes have two-dimensional structures (isolated along both the parallel and perpendicular directions). Within such holes the parallel cut of E_{\perp} has unipolar structures. In strongly magnetized plasma ($\Omega_e > \omega_{pe}$), electron holes have one-dimensional structures along the direction perpendicular to the background magnetic field within which a series of islands (with alternate positive and negative E_{\perp}) develop because of the variations of the charge density along the perpendicular direction. Therefore one recovers that a parallel cut of E_{\perp} has unipolar structures at the location of the holes. Present results show that the unipolar structure of E_{\perp} in electron holes is attributed to the balance between the electron transverse instability and the stabilization of the background magnetic field. The unipolar structures of E_{\perp} in electron holes last for hundreds to thousands of electron plasma periods. They are destroyed and the streaked structures are formed in the whole simulation domain after the electrostatic whistler waves are excited and have sufficiently large amplitude. The influences of the initial perpendicular thermal velocity of electrons (via temperature anisotropy) and the drift speed of electron beam on the structures of E_{\perp} are also analyzed in details. At last, the relevance between their simulation results and the unipolar structures of the parallel cut of E_{\perp} observed in the auroral region is discussed.

Zheng et al. (2008) develop a two-dimensional momentum and pitch angle code to solve the typical Fokker-Planck equation which governs wave-particle interaction in space plasmas. They carry out detailed calculations of momentum and pitch angle diffusion coefficients, and temporal evolution of pitch angle distribution for a band of chorus frequency distributed over a standard Gaussian spectrum particularly in the heart of the Earth's radiation belt $L=4.5$, where peaks of the electron phase space density are observed. They find that the Whistler-mode chorus can produce significant acceleration of electrons at large pitch angles, and can enhance the phase space density for energies of 0.5~1MeV by a factor of 10 or

above after about 24 h. This result can account for observation of significant enhancement in flux of energetic electrons during the recovery phase of a geomagnetic storm.

Previous particle-in-cell simulations have evidenced that quasi-perpendicular shocks are nonstationary and suffer a self-reformation on gyro scale of the incoming ions due to the accumulation of reflected ions. Yang et al. (2009) investigate the detailed mechanisms of ion acceleration in a nonstationary perpendicular shock by separating the incoming ions into reflected and directly transmitted parts. Test particle simulations are performed where the shock profiles are issued from self-consistent one-dimensional full particle-in-cell simulations. Both shell and Maxwellian incoming ion distributions are used. In both cases, most energetic particles correspond to reflected ions, and the associated acceleration mechanisms include both shock drift acceleration (SDA) and shock surfing acceleration (SSA). Two types of results are obtained. First, if they fix the shock profiles at different times within a self-reformation cycle, the mechanisms of particle acceleration are different at different profiles. SDA process appears as the dominant acceleration mechanism when the width of the ramp is broad (and overshoot amplitude is low) whereas both SDA and SSA contribute as the width of the ramp is narrow (and overshoot amplitude is high). For the different shock profiles concerned herein, SDA process is more efficient (higher resulting ion energy gain) than the SSA process. Second, in order to investigate ion acceleration in self-reforming shocks, not only the ramp but also the variations of the whole shock front need to be included. In the continuously time-evolving shock, SDA remains a dominant acceleration mechanism whereas SSA mechanism becomes more and more important with the increase of the initial particle energy. The percentage of reflected ions cyclically varies in time with a period equal to the self reformation cycle, which is in agreement with previous full particle simulations. The reflected ions not only come from the distribution wings of the incoming ions but also from the core part, in contrast with previous results based on stationary shocks.

In the solar wind, alpha particles are observed to flow faster than the core protons. Lu et al. (2009a) perform two dimensional hybrid simulations to investigate the nonlinear evolution of oblique Alfvén waves excited by an alpha/proton beam instability in a low beta plasma. The propagation angles of the

excited waves are within a finite range suggesting the generation of oblique Alfvén waves. During the nonlinear evolution, both the wave numbers and frequencies of the waves drift to smaller values, and the propagation angles decrease. At the same time, the propagation angle of the dominant mode also changes. Eventually the plasma system reaches a marginally stable state according to linear theory.

Ion pickup by a monochromatic low-frequency Alfvén wave, which propagates along the background magnetic field, has recently been investigated in low beta plasma. In the study of Lu et al. (2009b) the monochromatic Alfvén wave is generalized to a spectrum of Alfvén waves with random phase. It finds that the process of ion pickup can be divided into two stages. First, ions are picked up in the transverse direction, and then phase difference (randomization) between ions due to their different parallel thermal motions leads to heating of the ions. The heating is dominant in the direction perpendicular to the background magnetic field. The temperatures of the ions at the asymptotic stage do not depend on individual waves in the spectrum, but are determined by the total amplitude of the waves. The effect of the initial ion bulk flow in the parallel direction on the heating is also considered in this paper.

With one-dimensional (1-D) hybrid simulations Guo et al. (2009) investigate the nonlinear evolution of the ion cyclotron waves excited by the H^+ and He^{2+} temperature anisotropies, and analyze the evolution by using the wavelet analysis method. The results show that the proton cyclotron waves with the dominant frequency higher than the helium gyro-frequency ($\Omega_{He} = 0.5\Omega_p$, with Ω_p and Ω_{He} the proton and helium gyro-frequencies respectively) are firstly excited, and then the helium cyclotron waves with the dominant frequency lower than the helium gyro-frequency are excited. The relation of their simulation results to the BIF (bifurcated) (there are two peaks in the wave spectrum: one above and one below Ω_{He}) and CON (continuous) (continuous spectrum from $0.1 \Omega_p$ to $1.0 \Omega_p$) wave spectra observed in the magnetosheath are discussed.

The possibility of heating of protons via Alfvén waves is a topic that stimulates much discussion in both plasma physics and astrophysics. Conventional thinking is that dissipation is essential for heating. In two recent discussions it is shown that turbulent Alfvén waves can enhance stochastic particle motion via scattering. This process can lead to a higher proton temperature. In the study of Wang and Wu (2009) two essential points are stressed: First, there is no dissipation; second,

physically the temperature increment is “apparent” rather than genuine, and consequently the heating is spurious. If the turbulent wave field should diminish, the proton temperature returns to its original value. The purpose of this communication is to elucidate and explain the above points.

Ion heating due to turbulent Alfvén waves via nonresonant wave-particle interaction is discussed to complement a preceding work. Wang and Wang (2009) claim that newborn ions can get extra energy from turbulent Alfvén waves. Since in plasmas newborn ions are created continuously and intrinsically via ionization and recombination, heating associated with these newborn ions may be significant. The heating rate is proportional to the creation rate of newborn ions and the total wave field energy density without dependence on the profile of the wave spectrum. Based on observed nonthermal velocities, they estimate the energy density of the wave field and the corresponding heating rate in the solar atmosphere. The results show that such a heating process could be significant in the upper chromosphere and transition region of the sun.

Ion stochastic heating by a monochromatic Alfvén wave, which propagates obliquely to the background magnetic field, has been studied by Chen et al. It is shown that ions can be resonantly heated at frequencies a fraction of the ion cyclotron frequency when the wave amplitude is sufficiently large. In the study of Lu and Chen (2009), the monochromatic wave is extended to a spectrum of left-hand polarized Alfvén waves. When the amplitude of the waves is small, the components of the ion velocity have several distinct frequencies, and their motions are quasi-periodic. However, when the amplitude of the waves is sufficiently large, the components of the ion velocity have a spectrum of continuous frequencies near the ion cyclotron frequency due to the nonlinear coupling between the Alfvén waves and the ion gyromotion, and the ion motions are stochastic. Compared with the case of a monochromatic Alfvén wave, the threshold of the ion stochastic heating by a spectrum of Alfvén waves is much lower. Even when their frequencies are only several percent of the ion cyclotron frequency, the ions can also be stochastically heated. The relevance of this heating mechanism to solar corona is also discussed.

In collisionless reconnection, the magnetic field near the separatrix is stronger than that around the X-line, so an electron-beam can be formed and flows toward the X-line, which leads to a decrease of the electron density near the separatrix.

Having been accelerated around the X-line, the electrons flow out along the magnetic field lines in the inner side of the separatrix. A quadruple structure of the Hall magnetic field B_y is formed by such a current system. A 2D particle-in-cell (PIC) simulation code is used by Huang et al. (2009) to study the collisionless magnetic reconnection without an initial guide field. The current system described above is proved by the simulations. Furthermore, the position of the peak of the Hall magnetic field B_y is found to be between the separatrix and the center of the current sheet, which is verified by Cluster observations.

Lu, Hu and Zank (2009) perform two-dimensional hybrid simulations to investigate the interaction of Alfvén waves with a perpendicular shock self-consistently. The perpendicular shock is formed by reflecting the particles in the right boundary, and it propagates to the left. The Alfvén waves are injected from the left boundary, and they are convected toward the right. The results show that the injected Alfvén waves have no obvious effects on the propagation speed of the shock. However, after the upstream Alfvén waves are transmitted into the downstream, their amplitude is enhanced about 10-30 times. The transmitted waves can be separated into two parts, and both of them are left-hand polarized Alfvén waves: one propagates along the $+y$ direction and the other along the $-y$ direction. Obvious ripples in the shock front are also found due to the interaction of the Alfvén waves with the shock. The great enhancement of the amplitude of the Alfvén waves by the shock is verified by the satellite observations. The implications of the simulation results to the influences on the diffusive shock acceleration are also discussed in their study.

Satellite observations clearly reveal that superthermal electrons in space plasma generally possess a pronounced non-Maxwellian distribution that can be well modeled by a κ distribution. Lu, Zhou and Wang (2010) perform one dimensional (1D) particle in-cell simulations to investigate the evolution of whistler waves driven by superthermal electrons with a typical κ distribution in the presence of a cold plasma population. The results obtained from the linear theory are first confirmed: with the increase of the spectral index κ for the κ distribution, the linear growth rate of the excited waves increases and instability threshold for the temperature anisotropy ($A=T_{\perp}/T_{\parallel}-1$) decreases. Then they further find that with the increase of κ , the fluctuating magnetic field energy density at the saturation stage also increases. Therefore, from both the linear growth rate and the fluctuating

magnetic field energy density at the saturation stage, they can find that a bi-Maxwellian distribution ($\kappa \rightarrow \infty$) overestimates the importance of whistler waves, since the observed value of κ lies in the range $2 \leq \kappa \leq 6$. They also find that the κ values of the electron distributions become smaller with the excitation of the whistler waves.

Previous particle-in-cell simulations have evidenced that supercritical, quasi-perpendicular shocks are non-stationary. By separating the incident ions into reflected (R) and directly transmitted (DT) parts, Yang, Lu and Wang (2010) investigate the ion distributions in a non-stationary perpendicular shock. The upstream ion distributions have two parts corresponding to the R and incident ions respectively, while the R ions have higher energy. The downstream ions have a corering distribution. The core and ring parts correspond to the DT and R ions, respectively. The ion distributions depend largely on the non-stationary shock structure. The percentage of the reflected ions cyclically varies in time with a period equal to the shock self-reformation cycle, and the number of the R ions increases with the steepness of the shock ramp.

Two-dimensional particle-in-cell simulations are performed by Huang, Lu and Wang (2010) to investigate electron dynamics in antiparallel and guide field (in the presence of a strong guide field) magnetic reconnection, and the mechanisms of electron acceleration are compared. In the antiparallel reconnection, the dominant acceleration occurs in the vicinity of the X line, where the magnetic field is weak. Most of these electrons come from the regions just outside of the separatrices, which move into the vicinity of the X line along the magnetic field lines. Electrons can also be nonadiabatically accelerated in the pileup region by the reconnection electric field, where the gyroradii of the electrons are comparable to the curvature radii of the magnetic field lines. Most of these electrons come from the regions inside of the separatrices, which move into the pileup region along the magnetic field lines. In the guide field reconnection, electrons are accelerated by the parallel electric field. They are firstly accelerated when moving toward the X line along the magnetic field lines, and then are further accelerated when they are funneled into the vicinity of the X line. Most of energetic electrons come from the region outside of the pair of the negative separatrices. The efficiency of such an acceleration mechanism is obviously higher than that in the antiparallel reconnection. In both the antiparallel and guide field reconnection, the mechanisms of electron

acceleration favor the electrons with higher initial energy.

Using one-dimensional test particle simulations, the effect of a kinetic Alfvén wave on the velocity distribution function (VDF) of protons in the collisionless solar wind is investigated. Li, Lu, et al. (2010) first use linear Vlasov theory to numerically obtain the property of a kinetic Alfvén wave (the wave propagates in the direction almost perpendicular to the background magnetic field). They then numerically simulate how the wave will shape the proton VDF. It is found that Landau resonance may be able to generate two components in the initially Maxwellian proton VDF: a tenuous beam component along the direction of the background magnetic field and a core component. The streaming speed of the beam relative to the core proton component is about 1.2-1.3 Alfvén speed.

A multidimensional electron phase-space hole (electron hole) is considered to be unstable to the transverse instability. Wu, Lu et al. (2010) perform two-dimensional (2D) particle-in-cell (PIC) simulations to study the evolution of electron holes at different plasma conditions; they find that the evolution is determined by combined actions between the transverse instability and the stabilization by the background magnetic field. In very weakly magnetized plasma ($\Omega_e \ll \omega_{pe}$, where Ω_e and ω_{pe} are the electron gyrofrequency and plasma frequency, respectively), the transverse instability dominates the evolution of the electron holes. The parallel cut of the perpendicular electric field (E_{\perp}) has bipolar structures, accompanied by the kinking of the electron holes. Such structures last for only tens of electron plasma periods. With the increase of the background magnetic field, the evolution of the electron holes becomes slower. The bipolar structures of the parallel cut of E_{\perp} in the electron holes can evolve into unipolar structures. In very strongly magnetized plasma ($\Omega_e \gg \omega_{pe}$), the unipolar structures of the parallel cut of E_{\perp} can last for thousands of electron plasma periods. At the same time, the perpendicular electric field (E_{\perp}) in the electron holes can also influence electron trajectories passing through the electron holes, which results in variations of charge density along the direction perpendicular to the background magnetic field outside of the electron holes. When the amplitude of the electron hole is sufficiently strong, streaked structures of E_{\perp} can be formed outside of the electron holes, which then emit electrostatic whistler waves because of the interactions between the streaked structures of E_{\perp} and vibrations of the kinked electron holes.

In collisionless magnetic reconnection, the in-plane Hall currents are carried

mainly by the magnetized electrons. The in-plane Hall currents are directed toward the X line along the magnetic field lines just inside the separatrices and away from the X line along the separatrices. Such a current system leads to the quadrupole out-of-plane magnetic field with the peaks between the regions carrying the in-plane currents. Simultaneously, the electron flow toward the X line along the separatrices causes electron density depletions along the separatrices. In the work of Lu, Huang et al. (2010), the features of separatrix regions in magnetic reconnection and the relations between the electron density depletions and the out-of-plane magnetic field are investigated with both two-dimensional particle-in-cell simulations and Cluster observations. They conclude that the electron density depletions are formed because of the magnetic mirror, and they are outside the peaks of the out-of-plane magnetic field. Such a theoretical prediction is confirmed by both simulations and observations.

VII. PREDICTION METHODS

Turner and Li (2008) discussed a strong correlation between the behavior of low-energy (tens to hundreds of keV) and high-energy (>1 MeV) electron fluxes measured at geosynchronous orbit, and this correlation is further enhanced when a time offset is taken into account. A model has been developed incorporating this delay time between similar features in low-and high-energy electron fluxes to forecast the logarithm of daily averaged, 1.1-1.5 MeV electron flux at geosynchronous orbit several days in advance. The model uses only the current and previous days' daily averaged fluxes of low-and high-energy electrons as input. Parameters in the model are set by optimizing prediction efficiency (PE) for the years 1995-1996, and the optimized PE for these 2 years is 0.81. The model is run for more than one full solar cycle (1995-2006), and it consistently performs significantly better than a simple persistence model, where tomorrow's forecasted flux is simply today's value. Model results are also compared with an inward radial diffusion forecast model, in which the diffusion coefficient is a function of solar wind parameters. When the two models are combined, the resulting model performs better overall than each does individually.

Li et al. (2008) investigate methods to improve the predictions of Shock Arrival Time (SAT) of the original Shock Propagation Model (SPM). According to

the classical blast wave theory adopted in the SPM, the shock propagating speed is determined by the total energy of the original explosion together with the background solar wind speed. Noting that there exists an intrinsic limit to the transit times computed by the SPM predictions for a specified ambient solar wind, they present a statistical analysis on the forecasting capability of the SPM using this intrinsic property. Two facts about SPM are found: (1) the error in shock energy estimation is not the only cause of the prediction errors and they should not expect that the accuracy of SPM to be improved drastically by an exact shock energy input; and (2) there are systematic differences in prediction results both for the strong shocks propagating into a slow ambient solar wind and for the weak shocks into a fast medium. Statistical analyses indicate the physical details of shock propagation and thus clearly point out directions of the future improvement of the SPM. A simple modification is presented here, which shows that there is room for improvement of SPM and thus that the original SPM is worthy of further development.

In recent years remarkable advances have been made in the development of physics based models of various parts of the solar-terrestrial system. Wu et al. (2008) focus their discussions in a specific region of the Sun to the Earth's environment (i.e. 1 AU). It is well-known that geomagnetic storms are caused by solar eruptions. The consequences of these storms include particle acceleration, solar wind impact on the Earth's magnetosphere and ionosphere, UV-EUV radiation effects on the lower atmosphere, etc. One of the main challenges is to predict the arrival time at 1 AU of the solar disturbance. The prospects look good for an accurate, real-time forecast scheme built on the acquisition of solar, heliosphere and the near-Earth data and large-scale models. However, the accuracy of these models still needs improvement. They discuss the present status of the models and challenges to improve the simulation models.

A practical database method for predicting the interplanetary shock arrival time at L1 point is given by Feng et al. (2009a). First, a shock transit time database (hereinafter called Database-I) based on HAFv.1 (version 1 of the Hakamada-Akasofu-Fry model) is preliminarily established with hypothetical solar events. Then, on the basis of the prediction test results of 130 observed solar events during the period from February 1997 to August 2002, Database-I is modified to create a practical database method, named Database-II, organized on a

multidimensional grid of source location, initial coronal shock speed, and the year of occurrence of the hypothetical solar event. The arrival time at L1 for any given solar event occurring in the 23rd solar cycle can be predicted by looking up in the grid of Database-II according to source location, the initial coronal shock speed, and the year of occurrence in cycle 23. Within the hit window of ± 12 h, the success rate of the Database-II method for 130 solar events is 44%. This could be practically equivalent to the shock time of arrival (STOA) model, the interplanetary shock propagation model (ISPM), and the HAFv.2 model. To explore the capability of this method, it is tested on new data sets. These tests give reasonable results. In particular, this method's performance for a set of events in other cycles is as good as that of the STOA and ISPM models. This gives us confidence in its application to other cycles. From the viewpoint of long-term periodicity for solar activity, it is expected that the Database-II method can be applicable to the next solar cycle 24.

With the purpose of operational real-time forecasting for arrival times of flare/coronal mass ejection associated shocks in the vicinity of the Earth, Feng et al. (2009b) establish a one-dimensional hydrodynamic (HD) shock propagation model by a novel numerical scheme, the space-time conservation element and solution element (CESE) method. The required observational data inputs to this new one-dimensional CESE-HD model are the low coronal radio Type II drift speed, the duration estimation, and the background solar wind speed for a solar eruptive event. Applying this model to 137 solar events during the period of February 1997 to August 2002, it is found that their model could be practically equivalent to the STOA, ISPM, HAFv.2, and SPM models in forecasting the shock arrival time. The absolute error in the transit time from their model is not larger than those of the other four models for the same set of events. These results may demonstrate the potential capability of their model in terms of improving real-time forecasting because the CESE method can be extended to three-dimensional magnetohydrodynamics (3D-MHD) from the solar photosphere to any heliospheric position.

Real-time prediction of the arrival times at Earth of shocks is very important for space weather research. Recently, various models for shock propagation are used to forecast the shock arriving times (SATs) with information of initial coronal shock and flare from near real-time radio and X-ray data. Qin, Zhang and Rassoul

(2009) added the use of solar energetic particles (SEP) observation to improve the shock arrival time (SAT) prediction. High-energy SEPs originating from flares move to the Earth much faster than the shocks related to the same flares. They develop an SAT prediction model by combining a well-known shock propagation model, STOA, and the analysis of SEPs detected at Earth. They demonstrate that the SAT predictions are improved by the new model with the help of 38-53 keV electron SEP observations. In particular, the correct prediction to false alarm ratio is improved significantly.

A 1D-HD shock propagation model is established to predict the arrival time of interplanetary shocks at 1 AU. Applying this model to 68 solar events during the period of February 1997 to October 2000, it is found that their model could be practically equivalent to the STOA, ISPM and HAFv.2 models in forecasting the shock arrival time. The absolute error in the transit time from their model is not larger than those of the other three models for the same sample events. Also, the prediction test shows that the relative error of their model is $\leq 10\%$ for 31% of all events, $\leq 30\%$ for 75%, and $\leq 50\%$ for 84%, which is comparable to the relative errors of the other models. These results might demonstrate a potential capability of their model in terms of real-time forecasting.

Song (2010) presents an analytical model to predict the arrival time of coronal mass ejections (CMEs). All related calculations are based on the expression for the deceleration of fast CMEs in the interplanetary medium (ICMEs), $\tilde{v} = -(v - V_{sw})^2 / 15700$, where V_{sw} is the solar wind speed. The results can reproduce well the observations of three typical parameters: the initial speed of the CME, the speed of the ICME at 1 AU and the transit time. This simple model reveals that the drag acceleration should be really the essential feature of the interplanetary motion of CMEs.

References:

- Chen, A. Q., Chen, P. F. and Fang, C. (2006), On the CME velocity distribution, *A&A* 456, 1153-1158
- Chen, F., Ding, M. D. and Chen, P. F. (2010), Spectroscopic analysis of an EIT wave/dimming observed by Hinode/EIS, *Astrophys. J.*, 720:1254-1261
- Chen, P. F. (2006), The relation between EIT waves and solar flares, *Astrophys. J.*, 641: L153-L156
- Chen, P. F. (2009), The relation between EIT waves and coronal mass ejections, *Astrophys. J.*,

698:L112-L115

- Chen, Y., Hu, Y. Q. and Sun, S. J. (2007), Catastrophic eruption of magnetic flux rope in the corona and solar wind with and without magnetic reconnection, *Astrophys. J.*, 665:1421-1427
- Chen, Y., Li, X., Song, H. Q., Shi, Q. Q., Feng, S. W. and Xia, L. D. (2009), Intrinsic instability of coronal streamers, *Astrophys. J.*, 691:1936-1942
- Chen, Y., Song, H. Q., Li, B., Xia, L. D., Wu, Z., Fu, H., Li, X. (2010), Streamer Waves Driven by coronal mass ejections, *Astrophys. J.*, 2010, 714:644-651
- Du, D., Wang, C. and Hu, Q. (2007), Propagation and evolution of a magnetic cloud from ACE to Ulysses, *J. Geophys. Res.*, 112, A09101, doi:10.1029/2007JA012482
- Fang, C., Tang, Y. H., Xu, Z., Ding, M. D. and Chen, P. F. (2006), Spectral analysis of ellerman bombs, *Astrophys. J.*, 643:1325-1336
- Feng, X. S., Yang, L. P., Xiang, C. Q., Wu, S. T., Zhou, Y. F. and Zhong, D. K. (2010), Three-dimensional solar wind modeling from the Sun to Earth by a SIP-CESE MHD model with a six-component grid, *Astrophys. J.*, 723:300-319
- Feng, X. S., Zhang, Y., Sun, W., Dryer, M., Fry, C. D. and Deehr, C. S. (2009a), A practical database method for predicting arrivals of “average” interplanetary shocks at Earth, *J. Geophys. Res.*, 114, A01101, doi:10.1029/2008JA013499
- Feng, X. S., Zhang, Y., Yang, L. P., Wu, S. T. and Dryer, M. (2009b), An operational method for shock arrival time prediction by one-dimensional CESE-HD solar wind model, *J. Geophys. Res.*, 114, A10103, doi:10.1029/2009JA014385
- Feng, X. S., Zhou, Y. F. and Wu, S. T. (2007), A novel numerical implementation for solar wind modeling by the modified conservation element/solution element method *Astrophys. J.*, 655:1110-1126
- Guo, J., Feng, X., Zhang, J., Zuo, P. and Xiang C. (2010), Statistical properties and geoefficiency of interplanetary coronal mass ejections and their sheaths during intense geomagnetic storms, *J. Geophys. Res.*, 115, A09107, doi:10.1029/2009JA015140.
- Guo, J., Yang, Z. W., Lu, Q. M. and Wang, S. (2009), The nonlinear evolution of ion cyclotron waves in the Earth's magnetosheath. *Plasma Science and Technology*, 2009, 11(3):274-278
- Guo, X., C. and Wang, C. (2010), Effect of the dawn-dusk interplanetary magnetic field By on the field-aligned current system, *J. Geophys. Res.*, 115, A01206, doi:10.1029/2009JA014590
- Guo, X. C., Wang, C. and Hu Y. Q. (2010), Global MHD simulation of the Kelvin - Helmholtz instability at the magnetopause for northward interplanetary magnetic field, *J. Geophys. Res.*, 115, A10218, doi:10.1029/2009JA015193
- He, J. S., Marsch, E., Tu, C.-Y., Guo, L.-J. and Tian, H. (2010), Intermittent outflows at the edge of an

- active region – a possible source of the solar wind? *A&A* 516, A14, DOI: 10.1051/0004-6361/200913712
- He, J. S., Marsch, E., Tu, C. Y. and Tian, H. (2009), Excitation of Kink Waves Due to Small-Scale Magnetic Reconnection in the Chromosphere? *Astrophys. J.*, 705(2):L217-L222
- He, J. S., Marsch, E., Tu, C. Y., Tian, H. and Guo, L. J. (2010), Reconfiguration of the coronal magnetic field by means of reconnection driven by photospheric magnetic flux convergence, *A&A*, 510, 10.1051/00046361/200913059
- He, J. S., Tu, C.-Y. and Marsch, E. (2007), Can the solar wind originate from a quiet Sun region? *A&A* 468: 307-312, DOI: 10.1051/0004-6361:2006642
- He, J. S., Tu, C. Y. and Marsch, E. (2008), Modeling of Solar Wind in the Coronal Funnel with Mass and Energy Supplied at 5 Mm, *Solar Phys.*, 250(1):147-158
- Hu, Y. Q., Feng, X. S., Wu, S. T., Song, W. B. (2008), Three-dimensional MHD modeling of the global corona throughout solar cycle 23, *J. Geophys. Res.*, 113, A03106, doi: 10.1029/2007JA012750
- Hu, Y. Q. and Wang, C. (2010), Electrodynamic coupling in the solar wind-magnetosphere-ionosphere system, *Chinese Journal of Space Science*, 30(4): 321-332
- Hu, Y. Q., Zhong, P. and Wang, C. (2010), Rotational asymmetry of Earth's bow shock, *Chinese Journal of Geophysics*, 53(2): 198-208
- Huang, C., Lu, Q. M. and Wang, S. (2010), The mechanisms of electron acceleration in antiparallel and guide field magnetic reconnection, *Phys. Plasma*, 17, 072306
- Huang, C., Wang, R. S., Lu, Q. M. and Wang, S. (2009), Electron density hole and quadruple structure of By during collisionless magnetic reconnection, *Chinese Sci Bull*, 55(8):718-722, doi: 10.1007/s11434-009-0538-z
- Jiang, C. W., Feng, X. S., Zhang, J. and Zhong, D. K. (2010), AMR Simulations of Magnetohydrodynamic Problems by the CESE Method in Curvilinear Coordinates, *Solar Phys.*, 267: 463-491
- Jin, M., Ding, M. D., Chen, P. F., Fang, C. and Imada, S. (2009), Coronal mass ejection induced outflows observed with Hinode/EIS, *Astrophys. J.*, 702:27-38
- Li, H., Wang, C. and Kan, J. R. (2010), Midday magnetopause shifts earthward of geosynchronous orbit during geomagnetic superstorms with $Dst \leq -300$ nT, *J. Geophys. Res.*, 115, A08230, doi:10.1029/2009JA014612
- Li, H., Wang, C. and Richardson, J. D. (2008), Properties of the termination shock observed by Voyager 2, *Geophys. Res. Lett.*, 35, L19107, doi:10.1029/2008GL034869
- Li, H. J., Feng, X. S., Zuo, P. B., Xie, Y. Q. (2009a), Inferring interplanetary flux rope orientation with the minimum residue method. *J. Geophys. Res.*, 114, A03102, doi:10.1029/2008JA 013331.

- Li, H. J., Feng, X. S., Zuo, P. B., Xie, Y. Q. (2009b), Observations of the field-aligned residual flow inside magnetic cloud structure. *Sci. China (E)*, 52(9):2555-2566
- Li, H. J., Wei, F. S., Feng, X. S. and Xie, Y. Q. (2008), On improvement to the Shock Propagation Model (SPM) applied to interplanetary shock transit time forecasting, *J. Geophys. Res.*, 113, A09101, doi:10.1029/2008JA013167.
- Li, X., Lu, Q. M., Chen, Y., Li, B. and Xia, L. D. (2010), A kinetic Alfvén wave and the proton distribution function in the fast solar wind, *Astrophys.*, 719:L190-L193
- Li, X., Lu, Q. M. and Li, B. (2007), Ion pickup by finite amplitude parallel propagating Alfvén waves, *Astrophys. J.*, 661: L105-L108
- Li, Z., Wei, F. S., Feng, X. S. and Zhao, X. H. (2010), The “Same Side–Opposite Side Effect” of the Heliospheric Current Sheet in Ionospheric Negative Storms, *Solar Phys*, 263: 263-273
- Liu, Y., Luhmann, J. G., Huttunen, K. E. J., Lin, R. P., Bale, S. D., Russell, C. T. and Galvin, A. B. (2008b), Reconstruction of the 2007 May 22 magnetic cloud: how much can we trust the flux-rope geometry of CMEs? *Astrophys. J.*, 677:L133-L136
- Liu, Y., Manchester, IV W. B., Richardson, J. D., Luhmann, J. G., Lin, R. P. and Bale, S. D. (2008a), Deflection flows ahead of ICMs as an indicator of curvature and geoeffectiveness, *J. Geophys. Res.*, 113, A00B03, doi:10.1029/2007JA012996.
- Lu, Q. M. and Chen, L. (2009), Ion heating by a spectrum of obliquely propagating low-frequency Alfvén waves, *Astrophys. J.*, 704:743-749
- Lu, Q. M., Du, A. M., Li, X. (2009a), Two-dimensional hybrid simulations of the oblique electromagnetic alpha/proton instability in the solar wind, *Phys. Plasmas*, 16, 042901
- Lu, Q. M., Hu, Q. and Zank, G. P. (2009), The interaction of Alfvén waves with perpendicular shocks, *Astrophys. J.*, 706:687-692
- Lu, Q., Huang, C., Xie, J., Wang, R., Wu, M., Vaivads, A. and S. Wang (2010), Features of separatrix regions in magnetic reconnection: Comparison of 2-D particle-in-cell simulations and Cluster observations, *J. Geophys. Res.*, 115, A11208, doi:10.1029/2010JA015713.
- Lu, Q. M., Lembege, B., Tao, J. B. and Wang, S. (2008b), Perpendicular electric field in two-dimensional electron phaseholes: A parameter study. *J. Geophys. Res.*, 113, A11219, doi:10.1029/2008JA013693.
- Lu, Q. M. and Li, X. (2007), Heating of ions by low-frequency Alfvén waves, *PHYSICS OF PLASMAS* 14, 042303, DOI: 10.1063/1.2715569
- Lu, Q. M., Li, X., Dong, C. F. (2009b), Ion pickup by intrinsic low-frequency Alfvén waves with a spectrum. *Chin. Phys. B*, 18(5):2101-2108.
- Lu, Q. M., Mao, S. S., Mao, X. L. and Russo, R. E. (2008a), Theory analysis of wavelength dependence of laser-induced phase explosion of silicon. *J. Appl. Phys.*, 104, 083301

- Lu, Q. M., Zhou, L. H. and Wang, S. (2010), Particle-in-cell simulations of whistler waves excited by an electron κ distribution in space plasma, *J. Geophys. Res.*, 115, A02213, doi:10.1029/2009JA014580
- Marsch, E., Yao, S., Tu, C. Y. (2009), Proton beam velocity distributions in an interplanetary coronal mass ejection, *Annales Geophysicae*, 27(2):869-875
- Peng, Z., Wang, C. and Hu Y. Q. (2010), Role of IMF Bx in the solar wind-magnetosphere-ionosphere coupling, *J. Geophys. Res.*, 115, A08224, doi:10.1029/2010JA015454.
- Qin, G. and Li, G. (2008), Effect of flux tubes in the solar wind on the diffusion of energetic particles, *Astrophys. J.*, 682:L129-L132
- Qin, G. and Shalchi, A. (2009), Pitch-angle diffusion coefficients of charged particles from computer simulations, *Astrophys. J.*, 707:61-66.
- Qin, G., Zhang, M. and Rassoul, H. K. (2009), Prediction of the shock arrival time with SEP observations, *J. Geophys. Res.*, 114, A09104, doi:10.1029/2009JA014332.
- Richardson, J. D. and Wang, C. (2010), Plasma near the heliosheath: observations and interpretations, *Astrophys. J.*, 711:L44-L47
- Shalchi, A. and Qin, G. (2010), Random walk of magnetic field lines: analytical theory versus simulations, *Astrophys Space Sci* DOI 10.1007/s10509-010-0397-8
- Shen, F., Feng, X. S. and Song, W. B. (2009), An asynchronous and parallel time-marching method: Application to three-dimensional MHD simulation of solar wind, *Sci. in China (E)*, 52(10):2895-2902
- Shen, F., Feng, X. S., Wu, S. T., and Xiang, C. Q. (2007), Three-dimensional MHD simulation of CMEs in three-dimensional background solar wind with the self-consistent structure on the source surface as input: Numerical simulation of the January 1997 Sun-Earth connection event, *J. Geophys. Res.*, 112, A06109, doi:10.1029/2006JA012164
- Shen, F., Feng, X. S., Xiang, C. Q. and Song, W. B. (2010), The statistical and numerical study of the global distribution of coronal plasma and magnetic field near 2.5 Rs over a 10-year period, *Journal of Atmospheric and Solar-Terrestrial Physics* 72:1008-101
- Shen, C. L., Wang, Y. M., Ye, P. Z. and Wang, S. (2008), Enhancement of Solar Energetic Particles During a Shock-Magnetic Cloud Interacting Complex Structure, *Solar Phys.*, 252:409-418
- Shen, C. L., Wang, Y. M., Ye, P. Z., Zhao, X. P., Gui, B. and Wang, S. (2007), Strength of coronal mass ejection-driven shocks near the Sun and their importance in predicting solar energetic particle events, *Astrophys. J.*, 670:849-856
- Shen, C. L., Yao, J., Wang, Y. M., Ye, P. Z., Zhao, X. P. and Wang, S. (2010), Influence of coronal holes on CMEs in causing SEP events, *Research in Astron. Astrophys.* 10(10): 1049-1060
- Song, H. Q., Chen, Y., Liu, K., Feng, S. W. and Xia, L. D. (2009), Quasi-periodic releases of streamer

- blobs and velocity variability of the slow solar wind near the Sun, *Solar Phys.*, 258:129-140
- Song, W. B. (2010), An analytical model to predict the arrival time of interplanetary CMEs, *Solar Phys.*, 261:311-320
- Song, W. B., Feng, X. S. and Hu Y. Q. (2007), Solar Cycle variation of real CME latitudes, *Astrophys. J.*, 667: L101-L104
- Song, W. B., Feng, X. S. and Shen, F. (2008), A solar eruption triggered by merge interactions of different helicity loops, *A&A*, 485:L13-L16
- Song, W. B., Feng, X. S. and Shen, F. (2010), The heating of the solar transition region, *Research in Astron Astrophys.* 10(6): 529-532
- Song, W. B., Feng, X. S., Shen, F., and Zhang, Y. Z. (2009), Variability of Extended Bipolar Regions, *Solar Phys.*, 257:83-90
- Sun, S. J., Hu, Y. Q. and Chen, Y. (2007), Influence of photospheric magnetic flux distribution on coronal flux rope catastrophe, *Astrophys. J.*, 654: L167-L170,
- Tian, H., Marsch, E., Tu, C. Y., Xia, L. D. and He, J. S. (2008b), Sizes of transition-region structures in coronal holes and in the quiet Sun, *A&A*, 482(1):267-272
- Tian, H., Tu, C.-Y., Marsch, E., He, J. S. and Kamio, S. (2010), The nascent fast solar wind observed by the EUV imaging spectrometer on board Hinode, *Astrophys. J.*, 709:L88-L93
- Tian, H., Tu, C. Y., Marsch, E., He, J. S. and Zhou, G. Q. (2008c), Signature of mass supply to quiet coronal loops, *A&A*, 478(3):915-919
- Tian, H., Tu, C. Y., Xia, L. D. and He, J. S. (2008a), Radiance and Doppler shift distributions across the network of the quiet Sun, *A&A*, 489(3):1297-1306
- Turner, D. L., Li, X. L. (2008), Quantitative forecast of relativistic electron flux at geosynchronous orbit based on low-energy electron flux, *Space Weather*, 6, S05005, doi:10.1029/2007SW000354
- Wang, B. and Wang, C. B. (2009), Heating rate of ions via nonresonant interaction with turbulent Alfvén waves with ionization and recombination, *Phys. Plasmas*, 16, 082902
- Wang, C., Li, H., Richardson, J. D. and Kan J. R. (2010a), Interplanetary shock characteristics and associated geosynchronous magnetic field variations estimated from sudden impulses observed on the ground, *J. Geophys. Res.*, 115, A09215, doi:10.1029/2009JA014833
- Wang, C., Liu, J. B., Li, H., Huang, Z. H., Richardson, J. D. and Kan, J. R. (2009), Geospace magnetic field responses to interplanetary shocks. *J. Geophys. Res.*, 114, A05211, doi:10.1029/2008JA013794
- Wang, C., Sun, T. R., Guo, X. C. and Richardson J. D. (2010b), Case study of nightside magnetospheric magnetic field response to interplanetary shocks, *J. Geophys. Res.*, 115, A10247, doi:10.1029/2010JA015451.
- Wang, C. B. and Wu, C. S. (2009), Pseudoheating of protons in the presence of Alfvénic turbulence,

Phys. Plasmas, 16, 020703

- Wang, D. Y. and Lu, Q. M. (2007), Electron surfing acceleration by electrostatic waves in current sheet, *Astrophys Space Sci* (2007) 312: 103-111, DOI 10.1007/s10509-007-9658-6
- Wang, R. S., Lu, Q. M., Guo, J., Wang, S. (2008), Spatial Distribution of Energetic Electrons during Magnetic Reconnection. *Chin. Phys. Lett.*, 25(8):3083-3085
- Wang, Y., Wei, F. S., Feng, X. S., Zhang, S. H., Zuo, P. B. and Sun, T. R. (2010), Energetic electrons associated with magnetic reconnection in the magnetic cloud boundary layer, *Physical Review Letters*, 105, 195007
- Wang, Y. M., Cao, H., Chen, J. H., Zhang, T. F., Yu, S. J., Zheng, H. N., Shen, C. L., Zhang, J. and Wang, S. 2010, Solar limb prominence catcher and tracker (slipcat): an automated system and its preliminary statistical results, *Astrophys. J.*, 717:973-986
- Wang, Y. M., Ye P. Z. and Wang, S. (2007), The Dependence of the Geoeffectiveness of Interplanetary Flux Rope on Its Orientation, with possible Application to Geomagnetic Storm Prediction, *Solar Phys*, 240: 373-386
- Wang, Y. M. and Zhang, J. (2007), A comparative study between eruptive X-Class flares associated with coronal mass ejections and confined X-Class flares, *Astrophys. J.*, 665:1428-1438
- Wang, Y. M. and Zhang, J. (2008), A statistical study of solar active regions that produce extremely fast coronal mass ejections, *Astrophys. J.*, 680:1516-1522
- Wang, Y. M., Zhang, J. and Shen, C. L. (2009), An analytical model probing the internal state of coronal mass ejections based on observations of their expansions and propagations, *J. Geophys. Res.*, 114, A10104, doi:10.1029/2009JA 014360
- Wu, C.-C., Fry, C. D., Wu, S. T., Dryer, M. and Liu, K. (2007), Three-dimensional global simulation of interplanetary coronal mass ejection propagation from the Sun to the heliosphere: Solar event of 12 May 1997, *J. Geophys. Res.*, 112, A09104, doi:10.1029/2006JA012211
- Wu, M. Y., Lu, Q. M., Huang, C. and Wang, S. (2010), Transverse instability and perpendicular electric field in twodimensional electron phase-space holes, *J. Geophys. Res.*, 115, A10245, doi:10.1029/2009JA015235.
- Wu, S. T., Wang, A. H., Fry, C. D., Feng, X. S., Wu, C. C. and Dryer, M. (2008), Challenges of modeling solar disturbances' arrival times at the Earth, *Sci. China (E)*, 51(10):1580-1588
- Xiao, F. L., Shen, C. L., Wang, Y. M., Zheng, H. N. and Wang, S. (2008), Energetic electron distributions fitted with a relativistic kappa-type function at geosynchronous orbit. *J. Geophys. Res.*, VOL. 113, A05203, doi:10.1029/2007JA 012903
- Xiong, M., Zheng, H. N. and Wang, S. (2009), Magneto hydrodynamic simulation of the interaction between two interplanetary magnetic clouds and its consequent geoeffectiveness: 2. Oblique

- collision, *J. Geophys. Res.*, 2009, 114, A11101, doi:10.1029/2009JA014079.
- Xiong, M., Zheng, H., Wu, S. T., Wang, Y. and Wang, S. (2007), Magnetohydrodynamic simulation of the interaction between two interplanetary magnetic clouds and its consequent geoeffectiveness, *J. Geophys. Res.*, 112, A11103, doi:10.1029/2007JA012320
- Yao, S., Marsch, E., Tu, C.-Y. and Schwenn, R. (2010), Identification of prominence ejecta by the proton distribution function and magnetic fine structure in interplanetary coronal mass ejections in the inner heliosphere, *J. Geophys. Res.*, 115, A05103, doi:10.1029/2009JA014914.
- Yang, H. Q. and Chen, P. F. (2010), The dependence of the EIT wave velocity on the magnetic field strength, *Solar Phys.* DOI 10.1007/s11207-010-9595-3
- Yang, Z. W., Lu, Q. M., Lembege, M. and Wang, S. (2009), Shock front nonstationarity and ion acceleration in supercritical perpendicular shocks, *J. Geophys. Res.*, 114, A03111, doi:10.1029/2008JA013785.
- Yang, Z. W., Lu, Q. M. and Wang, S. (2010), Ion Velocity Distributions in a Non-Stationary Perpendicular Shock, *Chin. Phys. Lett.* 27(1), 019601
- Zhang, M. (2007), Diffusive compression acceleration of energetic particles with an application to shock acceleration near injection energies, *Astrophys. J.*, 665:1159-1163
- Zhang, M., Qin, G. and Rassoul, H. (2009), Propagation of solar energetic particles in three-dimensional interplanetary magnetic fields, *Astrophys. J.*, 692:109-132
- Zhang, M., Xia, L. D., Tian, H. and Chen, Y. (2007), Signatures of transition region explosive events in hydrogen Ly β profiles, *A&A* 520, A37, DOI: 10.1051/0004-6361/201014240
- Zheng, H. N., Su, Z. P. and Xiong, M. (2008), Pitch Angle Distribution Evolution of Energetic Electrons by Whistler-Mode. *Chin. phys. lett.*, 25(9):3515-3518
- Zhang, Y., Chen, J. Y. and Feng, X. S. (2010), Predicting the shock arrival time using 1D-HD solar wind model, *Chinese Science Bulletin*, 55(11): 1053-1058
- Zhang, Y., Sun, W., Feng, X. S., Deehr, C. S., Fry, C. D. and Dryer, M. (2008), Statistical analysis of corotating interaction regions and their geoeffectiveness during solar cycle 23, *J. Geophys. Res.*, 113, A08106, doi:10.1029/2008JA013095
- Zhao, X. H., Feng, X. S., Xiang, C. Q., Liu, Y., Li, Z., Zhang, Y. and Wu, S. T. (2010), Multi-spacecraft observations of the 2008 January 2 CME in the inner heliosphere, *Astrophys. J.*, 714:1133-1141
- Zhao, X. H., Feng, X. S. and Wu, C.-C. (2007), Influence of solar flare's location and heliospheric current sheet on the associated shock's arrival at Earth, *J. Geophys. Res.*, 112, A06107, doi:10.1029/2006JA012205
- Zhou, Y. F. and Feng, X. S. (2008), Numerical study of successive CMEs during November 4-5, 1998, *Sci. China (E)*, 51(10):1-11

- Zhou, Y. F., Feng, X. S. and Wu, S. T. (2008), Numerical Simulation of the 12 May 1997 CME Event, *Chin.Phys.Lett*, 25(2): 790-793
- Zuo, P. B. and Feng, X. S. (2007), The plasma and magnetic field characteristics of a double discontinuity in interplanetary space, *Solar Phys.* 240: 347-357
- Zuo, P. B., Wei, F. S., Feng, X. S., Xu, X. J. and Song, W. B. (2010), Magnetic cloud boundary layer of 9 November 2004 and its associated space weather effects, *J. Geophys. Res.*, 115, A10102, doi:10.1029/2009JA014815
- Zuo, P. B., Wei, F. S., Feng, X. S. and Yang, F. (2007), The relationship between the magnetic cloud boundary layer and the substorm expansion phase, *Solar Phys.*, DOI 10.1007/s11207-007-0407-3